Lattice Boltzmann simulation of liquid water transport in gas diffusion layers of proton exchange membrane fuel cells

Von der Fakultät Energie-, Verfahrens- und Biotechnik der Universität Stuttgart
zur Erlangung der Würde eines Doktors der
Ingenieurwissenschaften (Dr.-Ing.) genehmigte Abhandlung

Vorgelegt von

Patrick Sarkezi-Selsky

aus Filderstadt

Hauptberichter:	Prof. Dr. K. Andreas Friedrich
Mitberichter:	Prof. Dr. Rainer Helmig
2. Mitberichter:	Prof. Dr. Arnulf Latz

Tag der mündlichen Prüfung: 12.07.2024

Institut für Gebäudeenergetik, Thermotechnik und Energiespeicherung
der Universität Stuttgart

2024

Declaration of Authorship

I hereby declare that I have written the underlying thesis with the title

"Lattice Boltzmann simulation of liquid water transport in gas diffusion layers of proton exchange membrane fuel cells"

independently and that I have not used sources other than indicated.

Ich erkläre hiermit, dass ich die vorliegende Arbeit mit dem Titel

"Lattice Boltzmann simulation of liquid water transport in gas diffusion layers of proton exchange membrane fuel cells"

selbständig verfasst und keine anderen als die angegebenen Quellen verwendet habe.

Place, Date

Patrick Sarkezi-Selsky

Contents

Nomenclature

Abbreviations

AFC	Alkaline fuel cell
AFM	Atomic force microscopy
AST	Accelerated stress test
BEV	Battery-electric vehicle
BGK	Bhatnagar-Gross-Krook
BPP	Bipolar plate
CCL	Cathode catalyst layer
CFD	Computational fluid dynamics
CFM	Cluster based full morphology
CGM	Color-gradient model
CL	Catalyst layer
CR	Compression ratio
DAFC	Direct alcohol fuel cell
DI	Deionized
EDX	Energy dispersive x-ray spectroscopy
EV	Electric vehicle
FC	Fuel cell
FCEV	Fuel cell-electric vehicle
FEM	Free-energy model
FEP	Fluorinated ethylene propylene
FIB-SEM	Focused ion beam-scanning electron microscopy
FM	Full morphology
GC	Gas channel
GDB	Gas diffusion backing
GDL	Gas diffusion layer
GHG	Greenhouse gas
gPSD	Geometric pore size distribution
HEV	Hybrid-electric vehicle

HOR	Hydrogen oxidation reaction
LB	Lattice Boltzmann
LBE	Lattice Boltzmann equation
LBM	Lattice Boltzmann method
LGA	Lattice gas automata
LSM	Level-set method
MCFC	Molten carbonate fuel cell
µCT	X-ray micro-computed tomography
MPL	Microporous layer
MPS	Macroporous substrate
MRT	Multi relaxation time
OCV	Open circuit voltage
ORR	Oxygen reduction reaction
PAFC	Phosphoric acid fuel cell
PEM	Polymer electrolyte membrane
PEMFC	Polymer electrolyte membrane fuel cell
PFPE	Perfluoropolyether
PFSA	Perfluorosulfonic acid
PHEV	Plug-in hybrid-electric vehicle
PM	Pore morphology
PNM	Pore network modeling
PSD	Pore size distribution
PSM	Pore-scale modeling
PTFE	Polytetrafluoroethylene
PVDF	Polyvinylidene difluoride
px	Pixel
REA	Representative elementary area
REV	Representative elementary volume
RK	Rothman-Keller
SC	Shan-Chen
SEM	Scanning electron microscopy
SOFC	Solid oxide fuel cell
SPH	Smoothed particle hydrodynamics
SRT	Single relaxation time
SUSD	Startup/shutdown
var	variable
VoF	Volume-of-Fluid

vol	volume
vx	Voxel
WBC	Wetting boundary condition
wt	weight
XTM	X-ray tomographic microscopy

Greek symbols

Symbol	Description	Unit
α_k	Compressibility parameter for phase k	
α_p	Local pore wall angle	°
β	Parameter to control the interface thickness	
Δ_R	Half offset between throat and pore radius	m
$\Delta\rho$	Phase density difference	$\mathrm{kg\,m^{-3}}$
Δt	Time interval	s
Δx	Lattice spacing	m
Δx^{phys}	Spatial resolution	µm/px or µm/vx
ϵ	Porosity	
ζ_i	Lattice weight for galilean invariance	
γ	Ratio of initial fluid densities	
θ	Contact angle	°
ϑ_i	Angle between $\mathbf{F}$ and $\mathbf{c}_i$	°
κ	Permeability	$\mathrm{m^2}$
λ	Mean free path	nm
λ	Parameter for the secant method in the WBC	
μ	Dynamic viscosity	$\mathrm{Pa\,s}$
ν	Kinematic viscosity	$\mathrm{m^2\,s^{-1}}$
$\boldsymbol{\xi}$	Particle velocity vector	$\mathrm{m\,s^{-1}}$
ρ	Density	$\mathrm{kg\,m^{-3}}$
σ	Surface tension	$\mathrm{N\,m^{-1}}$
σ_{ij}	Interfacial energy between phases i and j	$\mathrm{N\,m^{-1}}$
τ	Relaxation time	s
τ	Tortuosity	
φ	Color-field parameter	
Φ_i^k	Correction term for galilean invariance	
ϕ_i^k	Compressibility parameter for phase k	
ϕ_{PTFE}	PTFE loading	vol% or wt%
Φ_s	Particle sphericity	

χ	PTFE fiber surface coverage	
ψ_i	Lattice weight for galilean invariance	
Ω	Collision operator	$\mathrm{kgs^2m^{-6}}$
ω_i	Relaxation coefficient	$\mathrm{s^{-1}}$

Roman symbols

Symbol	Description	Unit
A	Cross-sectional area	$\mathrm{m^2}$
A_k	Perturbation operator parameter for phase k	$\mathrm{N\,m^{-1}}$
B_i	Lattice weight in the perturbation operator	
c	Lattice speed	$\mathrm{m\,s^{-1}}$
$\mathbf{c}_i$	Discrete lattice velocity vector	$\mathrm{m\,s^{-1}}$
c_j	Molar concentration of species j	$\mathrm{mol\,m^{-3}}$
c_s	Isothermal speed of sound	$\mathrm{m\,s^{-1}}$
D	Diffusion coefficient	$\mathrm{m^2\,s^{-1}}$
d	Number of spatial dimensions	
d_f	Fiber diameter	µm
d_p	Pore diameter	µm
$d_{p(X)}$	Pore diameter larger than X% of a distribution	µm
F	External force	N
f	Particle distribution function	$\mathrm{kgs^3m^{-6}}$
$\mathbf{F}$	Color-gradient	
g	Gravitational acceleration	$\mathrm{m^2\,s^{-1}}$
h	Height	m
$\mathbf{h}$	Binary void-solid matrix	
I	Current	A
i	Current density	$\mathrm{A\,cm^{-2}}$
$\boldsymbol{J}_j$	Diffusive flux of species j	$\mathrm{mol\,m^{-2}\,s^{-1}}$
$\mathbf{K}$	Relaxation matrix	$\mathrm{s^{-1}}$
k_K	Kozeny constant	
L	Length	m
l	Capillary filling length	m
m	Mass	kg
$M_{\mathrm{H_2O}}$	Molar mass of water	$\mathrm{g\,mol^{-1}}$
$\dot{m}_{\mathrm{H_2O}}$	Mass flow rate of water	$\mathrm{kg\,s^{-1}}$
$\mathbf{M}$	Moment transformation matrix	
$\boldsymbol{m}$	Vector of discrete particle distribution moments	

n_{H_2O}	Amount of substance of water	mol
$\dot{n}_{H_2O}$	Molar flow rate of water	$\mathrm{mol\,s^{-1}}$
N_i	Domain size along spatial coordinate i	vx
p	Pressure	Pa
Q	Electrical charge	C
q	Number of discrete lattice velocity vectors	
R	Radius	m
r_p	Local pore radius	m
S	Saturation	
t	Time	s
$\mathbf{u}$	Macroscopic velocity vector	$\mathrm{m\,s^{-1}}$
u_k	Velocity of species or phase k	$\mathrm{m\,s^{-1}}$
$\dot{V}$	Volumetric flow rate	$\mathrm{m^3\,s^{-1}}$
W_i	Lattice weight	
$\mathbf{x}$	Particle position vector	m
x	First principal spatial coordinate	m
y	Second principal spatial coordinate	m
z	Third principal spatial coordinate	m
z_{H_2O}	Charge number of water	

Subscripts, indices and superscripts

(l)	liquid
(m)	mass
$*$	dimensionless
0	Initial state
app	apparent
b	blue
B	Bottom
B	Bubble point
BC	Boundary condition
BT	Breakthrough
c	capillary
CF	Carbon fiber
char	characteristic
compr	compressed
D	Defending

Drain	Drainage
eff	effective
eq	equilibrium
est	estimated
f	fluid
G	Gravitational
g	gas
h	hydrostatic
H14	Carbon fiber felt GDL by Freudenberg
H14impr	PTFE-impregnated H14
H_2O	Water
$\tilde{i}$	Lattice direction opposite to i
I	Invading, Inlet
Intr	Intrusion
l	liquid
macro	macroporous
nw	nonwetting
O	Outlet
phys	physical
p	pore
r	red
ref	reference
rel	relative
res	residual
s	solid
T	Top
t	throat or tube
trans	Transition zone
visc	viscous
w	wetting

Physical constants

Symbol	Description	Value
$\mathcal{F}$	Faraday constant	$96\,485\,\mathrm{C\,mol^{-1}}$

Dimensionless Numbers

Symbol	Description	Definition
Bo	Bond number	$\mathrm{Bo} = \dfrac{\Delta\rho R^2 g}{\sigma}$
Ca	Capillary number	$\mathrm{Ca} = \dfrac{\mu u}{\sigma}$
Kn	Knudsen number	$\mathrm{Kn} = \dfrac{\lambda}{L_{\mathrm{char}}}$
La	Laplace number	$\mathrm{La} = \dfrac{\sigma\rho R}{\mu^2}$
M	Dynamic viscosity ratio	$M = \dfrac{\mu_I}{\mu_D}$
Re	Reynolds number	$\mathrm{Re} = \dfrac{\rho u d_p}{\mu}$

Abstract

Polymer electrolyte membrane fuel cells (PEMFCs) offer a compelling powertrain solution for the e-mobility sector and in particular for heavy-duty applications. Generating electrical energy by electrochemical reaction of hydrogen and oxygen to water, these fuel cells present (when using green hydrogen) a climate-friendly technology in support of reducing overall greenhouse gas emissions.

During cell operation, the reactand gases are consumed at the electrodes and water is produced in the cathode catalyst layer (CCL). In dependence of the operating conditions, this product water can condensate and block as a liquid phase available transport paths for the reactand gases. In order to prevent advancing liquid water accumulation and therewith flooding of the cell, the product water has to be therefore removed efficiently. Thus, stable fuel cell (FC) operation is only possible with an appropriate water management. In this context, the porous gas diffusion layer (GDL) plays a pivotal role by ensuring both homogeneous reactand gas distribution to the electrodes and efficient water removal from the cathode catalyst layer. Consequently, optimal water management is only achievable with an appropriate design of the GDL material properties, which requires a profound understanding of the capillary transport phenomena on the pore scale. In long-term operation, the GDL is furthermore in general subject to different aging processes, due to the harsh conditions typically present in automotive applications. With proceeding material degradation, the water removal capabilities of the GDL can decrease over time, leading to a progressively deteriorated gas transport and increasing cell performance losses upon aging. In order to achieve the component durability needed to meet the lifetime requirements for long-term fuel cell operation, degradation phenomena and their repercussions on the water management therefore have to be fully understood. Owing to the complexity of multiphase transport mechanisms in porous media, however, conventional experimental testing can be expensive, time-consuming and with limited depth of detail. In recent years, pore-scale modeling (PSM) has therefore gained increasing popularity as a comparatively fast and inexpensive technique for investigation of porous media transport processes directly at the pore scale.

In this work, liquid water transport through a carbon felt GDL was thoroughly investigated using multiphase PSM simulations and real microstructural data. At first, a 3D

Color-Gradient Lattice-Boltzmann model was developed and validated against analytical references. GDL microstructures of a plain and an impregnated carbon fiber substrate of a Freudenberg H14 GDL were then reconstructed via segmentation of high-resolution X-ray micro-computed tomography (µCT) images. For the microstructure reconstruction of the impregnated GDL, an in-house algorithm was furthermore developed to distinguish a hydrophobic additive component (polytetrafluoroethylene (PTFE)) from the support material (carbon fibers). Subsequently, a first computational domain for the simulation of GDL liquid water transport was generated according to the experimental boundary conditions of a test bench for measuring capillary pressure-saturation ($p_c - S$) relations. Here, special attention was paid to the GDL surface regions by explicit consideration of two semipermeable membranes according to the experimental setup. Starting from an initially dry GDL, liquid water intrusion was then simulated by gradually decreasing the gas pressure until full saturation was reached. Whereas the obtained $p_c - S$ relation is not unique but dependent on the wetting history of the GDL, drainage of liquid water was simulated as well, thereby recovering the complete capillary hysteresis. Parametric studies then showed that the obtained $p_c - S$ characteristics are significantly affected by boundary effects owing to the highly porous GDL surface regions. In addition, microstructure-resolved simulations require a high resolution of the porous medium in order to predict capillary behavior reasonably. Assuming uniform wettability with a carbon fiber contact angle of $\theta_{\mathrm{CF}} = 65°$ for the plain fiber substrate, the simulated $p_c - S$ curves were furthermore in good agreement with the experimental reference. Considering mixed wettability for the impregnated fiber substrate, on the other hand, the simulations showed an expected shift of the $p_c - S$ characteristics towards higher capillary pressures owing to the hydrophobicity of the additive (PTFE) but could otherwise not reproduce the experimentally observed significant enlargement of the capillary hysteresis. This discrepancy was primarily related to a measurement artifact. After validation of the simulated capillary hystereses, novel $pc-S$ relations were furthermore derived for both the intrusion and drainage of liquid water in the plain and impregnated H14 fiber substrate. On the other hand, the widely-used Leverett relation was found to be incapable to describe the capillary characteristics of the plain and impregnated carbon felt GDL appropriately.

In order to investigate the impact of aging on the GDL water management, a second computational domain was generated, mimicking the *operando* conditions during fuel cell operation. For this purpose, the GDL microstructure reconstruction was virtually compressed corresponding to a typical cell assembly clamping pressure. In addition, a microporous layer (MPL) was considered as well by reconstruction of its macropores via segmentation of µCT images of an impregnated and MPL-coated Freudenberg H14 GDL. Generating a computational setup, the GDL/MPL assembly was then sandwiched between

a liquid and a gas buffer zone representing the catalyst layer (CL) and the gas channel (GC) according to *operando* conditions. In order to investigate aging effects, the microstructure reconstructions were furthermore degraded virtually assuming PTFE loss from the GDL and increase of the MPL macroporosity as the main aging scenarios. Corresponding to stationary cell operation, liquid water transport through the partially aged GDL and MPL was then simulated with a constant inlet velocity. Once the liquid phase percolated through to the gas channel (i.e., at breakthrough), the simulations were halted and the invasion patterns were then characterized by means of local and overall saturation. In order to investigate mass transport limitations due to liquid water accumulation in the pore space, effective gas transport properties were furthermore determined for the partially saturated and aged GDLs and MPLs. Subsequent simulations then showed that with the MPL in the pristine state loss of PTFE had no measureable effect on the liquid water transport through the degraded GDL. This observation was related to the dominant impact of the MPL on the capillary transport by strongly restricting the liquid water invasion sites into the GDL. Upon aging of the MPL, on the other hand, significant degradation effects were observed, as indicated by rising breakthrough saturations and an increasingly disturbed gas transport. Once the MPL was already degraded, aging of the GDL was then found to impact the liquid water transport and consequently the effective gas transport as well.

Kurzfassung

Polymerelektrolytmembranbrennstoffzellen (PEMFCs) bieten eine vielversprechende Antriebslösung für den Elektromobilitätssektor und insbesondere für Schwerlastanwendungen. Mit der Bereitstellung elektrischer Energie durch die elektrochemische Reaktion von Wasserstoff und Sauerstoff zu Wasser stellen diese Brennstoffzellen (bei Einsatz von grünem Wasserstoff) eine klimafreundliche Technologie zugunsten der Reduktion globaler Treibhausgasemissionen dar.

Während des Zellbetriebs werden die Reaktandengase an den Elektroden verbraucht und Wasser in der Kathodenkatalysatorschicht (CCL) produziert. Dieses Produktwasser kann in Abhängigkeit der Betriebsbedingungen auskondensieren und als Flüssigphase die verfügbaren Transportpfade für die Reaktandengase blockieren. Um fortschreitende Flüssigwasseransammlung und dadurch ein Fluten der Zelle zu verhindern, muss das Produktwasser daher effizient entfernt werden. Somit kann ein stabiler Brennstoffzellenbetrieb nur mit einem angemessenen Wassermanagement erreicht werden. In diesem Kontext spielt die poröse Gasdiffusionsschicht (GDL) eine entscheidende Rolle, da sie sowohl eine homogene Reaktandengasverteilung auf die Elektroden als auch einen effizienten (Flüssig-)Wasserabtransport von der Kathodenkatalysatorschicht sicherstellen muss. Ein optimales Wassermanagement ist folglich nur mit einem geeigneten Design der Materialeigenschaften von GDLs möglich, welches ein tiefgreifendes Verständnis der Kapillartransportphänomene auf der Porenskala erfordert. Im Dauerbetrieb ist die GDL des Weiteren aufgrund der in Automobilanwendungen typischerweise harschen Betriebsbedingungen im Allgemeinen von verschiedenen Alterungsvorgängen betroffen. Mit fortschreitender Materialdegradation kann sich die Effizienz des Wasserabtransports durch die GDL über die Zeit verschlechtern, was zu einer zunehmenden Störung des Gastransports und damit verbundenen zunehmenden Verlusten in der Zellleistung führen kann. Um die Komponentenbeständigkeit zu erreichen, welche für die Erfüllung der Lebensdaueranforderungen im Langzeitbetrieb von Brennstoffzellen benötigt wird, müssen daher Degradationsphänomene und ihre Auswirkungen auf das Wassermanagement vollständig verstanden werden. Allerdings ist die konventionelle Erprobung durch Experimente aufgrund der Komplexität von Mehrphasentransportmechanismen in porösen Medien im Allgemeinen teuer, zeitintensiv und mit begrenzter Detailtiefe. In den vergangenen Jahren hat daher die Porenskalenmodellierung

zunehmende Popularität erlangt, da sie einen vergleichsweise schnellen und kostengünstigen Alternativansatz darstellt, welcher zudem die Untersuchung von Transportprozessen poröser Medien direkt auf der Porenskala erlaubt.

Im Rahmen dieser Arbeit wurde der Flüssigwassertransport durch eine Kohlefaservlies-GDL mithilfe von Mehrphasensimulationen auf der Porenskala und unter Verwendung realer Mikrostrukturdaten tiefgreifend untersucht. Zu Beginn wurde dafür ein mehrphasiges (Color-Gradient) Lattice-Boltzmann-Modell entwickelt und gegen analytische Referenzen validiert. Anschließend wurden die GDL-Mikrostrukturen eines unbehandelten und eines imprägnierten Kohlefasersubstrates einer Freudenberg H14 GDL durch Segmentierung hochaufgelöster Röntgen-Mikrotomographieaufnahmen (µCT) rekonstruiert. Für die Mikrostrukturrekonstruktion der imprägnierten GDL wurde zudem ein hausinterner Algorithmus entwickelt, welcher die Unterscheidung einer hydrophoben Additivkomponente (Polytetrafluoroethylen (PTFE)) vom Stützmaterial (Kohlefasern) ermöglicht. Nachfolgend wurde eine erste Berechnungsdomäne für die Simulation des GDL-Wassertransports erzeugt, welche die experimentellen Randbedingungen eines Prüfstands zur Bestimmung von Kapillardruck-Sättigungsbeziehungen $p_c - S$ nachahmte. Hierbei wurde durch die explizite Berücksichtigung von zwei semipermeablen Membranen gemäß experimentellen Aufbaus besonderes Augenmerk auf die Oberflächenregionen der GDL gelegt. Beginnend mit einer anfänglich trockenen GDL wurde dann das Eindringen von flüssigem Wasser durch die stufenweise Reduktion des Gasdrucks simuliert bis sich vollständige Sättigung einstellte. Da die so erhaltene Kapillardruck-Sättigungsbeziehung jedoch nicht einzigartig sondern abhängig von der Benetzungsvergangenheit der GDL ist, wurde anschließend auch die Verdrängung von Wasser simuliert um letztlich die vollständige Kapillarhysterese zu erhalten. Anschließende Parameterstudien zeigten dann, dass die erhaltenen $p_c - S$-Charakteristika aufgrund der hochporösen GDL-Oberflächenregionen maßgeblich von Randeffekten beeinflusst werden. Darüber hinaus benötigen mikrostrukturaufgelöste Simulationen eine hohe Auflösung des porösen Mediums, sodass diese die Kapillarhysterese angemessen vorhersagen können. Unter Annahme einheitlicher Benetzbarkeit mit einem Kohlefaserkontaktwinkel von $\theta = 65°$ für das unbehandelte Fasersubstrat waren die simulierten $p_c - S$-Kurven des Weiteren in guter Übereinstimmung mit der experimentellen Referenz. Bei Berücksichtigung gemischter Benetzbarkeit für das imprägnierte Fasersubstrat zeigten die Simulationen auf der anderen Seite die aufgrund der Hydrophobizität des Additivs (PTFE) erwartete Verlagerung der $p_c - S$-Charakteristika hin zu höheren Kapillardrücken aber konnten darüber hinaus die experimentell beobachtete starke Vergrößerung der Kapillarhysterese nicht reproduzieren. Diese Diskrepanz wurde in erster Linie auf ein Messartefakt zurückgeführt. Im Anschluss an die Validierung der simulierten Kapillarhysteresen wurden abschließend neue $p_c - S$-Beziehungen für sowohl

das Eindringen als auch die Verdrängung von Wasser im unbehandelten und imprägnierten H14-Kohlefasersubstrat abgeleitet. Die weitverbreitete Leverett-Beziehung wurde auf der anderen Seite für untauglich befunden, die Kapillarcharakteristika der unbehandelten und imprägnierten Kohlefaservlies-GDL adäquat zu beschreiben.

Zur Untersuchung der Auswirkungen von Alterung auf das GDL-Wassermanagement wurde eine zweite Berechnungsdomäne generiert, welche die Bedingungen während des Brennstoffzellenbetriebs imitierte. Hierfür wurde die GDL-Mikrostrukturrekonstruktion virtuell und entsprechend eines typischen Anpressdrucks im Zellaufbau komprimiert. Zusätzlich wurde eine mikroporöse Schicht (MPL) anhand der Rekonstruktion ihrer Makroporen durch die Segmentierung von µCT-Aufnahmen einer imprägnierten und MPL-beschichteten Freudenberg H14 GDL berücksichtigt. Zur Erzeugung einer Berechnungsdomäne wurden anschließend GDL und MPL zwischen eine Flüssigphasen- und eine Gasphasenpufferzone geschichtet, welche die Katalysatorschicht (CL) und den Gaskanal (GC) gemäß gewöhnlicher Betriebsbedingungen repräsentieren sollte. Des Weiteren wurden für die Untersuchung von Alterungsvorgängen Mikrostrukturrekonstruktionen virtuell degradiert. Hierfür wurde angenommen, dass der Verlust von PTFE und eine Zunahme der MPL-Makroporosität die Hauptalterungsszenarien darstellen. Anschließend wurde der Wassertransport durch die partiell gealterte GDL und MPL mit einer konstanten Eintrittsgeschwindigkeit gemäß stationärem Zellbetrieb simuliert. Sobald die Flüssigphase zum Gaskanal durchgetreten war (d.h. bei Breakthrough), wurden die Simulationen dann gestoppt und die Eindringmuster anhand von lokaler Wasserverteilung und Gesamtsättigung charakterisiert. Des Weiteren wurden zur Untersuchung von Massentransportlimitierungen durch die Flüssigwasseransammlung im Porenraum effektive Gastransporteigenschaften für die partiell gesättigten und gealterten GDLs und MPLs bestimmt. Nachfolgende Simulationen zeigten dann, dass mit einer MPL im ungealterten Zustand der Verlust von PTFE keinen messbaren Einfluss auf den Flüssigwassertransport durch die degradierte GDL hatte. Diese Beobachtung wurde auf den dominanten Einfluss der MPL auf den Kapillartransport in der GDL durch die starke Beschränkung der Wassereintrittsstellen zurückgeführt. Mit Alterung der MPL konnten auf der anderen Seite allerdings signifikante Degradationseffekte registriert werden, welche sich in steigenden Breakthrough-Sättigungen und einem zunehmend gestörten Gastransport äußerten. Sobald die MPL einmal degradiert war, dann hatte die auch Alterung der GDL durch PTFE-Verlust einen merklichen Einfluss auf den Flüssigwassertransport und folglich auch auf den effektiven Gastransport.

1 Introduction

1.1 Motivation

Increasing global mean temperatures and rising sea levels are just two of many indicators for proceeding climate change [1], alerting mankind to take action. In order to attenuate advancing global warming, one of the primary objectives is a massive reduction of greenhouse gas (GHG) emissions. According to recent studies, the transportation sector is estimated to be responsible for more than 15 % of the global GHG emissions [2, 3], and thus represents a major contributor to anthropogenic global warming. Therefore, automakers are currently urged to a massive development of the e-mobility sector to accomplish a rapid technological transition from conventional fossil fuel-based internal combustion engines towards emission-free electrical motors. In search of cleaner powertrain solutions, different types of electric vehicles (EVs) have been developed over the years. Depending on the propulsion system, these can be categorized as battery-electric (BEVs), hybrid-electric (HEVs), plug-in hybrid-electric (PHEVs) or fuel cell-electric vehicles (FCEVs). For a review of the aforementioned EV technologies, the interested reader is referred to Verma et al. [4]. Polymer electrolyte membrane fuel cells (PEMFCs) are currently the most widely employed type of fuel cells in FCEVs, owing to several advantages such as low operating temperature, short refueling, high power density and efficiency [5–7]. Together with furthermore good scalability, PEMFCs have in recent years attracted increasing attention with regard to future heavy-duty applications such as trucks and busses, aircraft, trains or ships [8]. However, large-scale commercialization of PEM fuel cells is still obstructed by the remaining technological barriers of cost, reliability and durability [9–11].

In a PEM fuel cell, electrical energy is generated by the electrochemical reaction of hydrogen (H_2) and oxygen (O_2) to water (see Figure 1.1). In order to sustain stable operation, the reactand gases have to be continuously fed to the electrodes (H_2 to the anode and O_2 to the cathode) to prevent performance losses due to fuel starvation. As a result of the electrochemical reaction consuming the reactand gases, water is furthermore produced in the cathode catalyst layer (CCL). Depending on the conditions within the cell (e.g., pressure, temperature or relative gas humidity), the product water may be present either as vapor or in the liquid state (or at sub-zero temperatures also as ice).

Occupying pore space in the cathode CL (and adjacent porous layers), liquid water blocks available paths for the effective oxygen transport to the CCL and thereby reduces the cell performance due to mass transport limitations. In order to ensure reliable cell performance, liquid water accumulation has to be therefore prevented by efficient removal of product water from the cell. Otherwise, advancing accumulation may lead to *flooding* of the cathode, resulting in a complete blockage of the gas transport and ultimately operation failure. On the other hand, however, a certain water content has to be preserved in the cell in order to maintain a high proton conductivity of the polymer electrolyte membrane [12]. In summary, stable and efficient long-term cell operation can be only achieved with a well-balanced water management, which prevents both catalyst flooding and membrane dehydration while maximizing the effective reactand transport to the electrodes.

Here, the gas diffusion layer (GDL) acts as a key component present at both the anode and cathode side electrode. On the one hand, the GDL has to distribute the reactand gases homogeneously from the gas channels to the catalyst layer of the respective electrode. On the other hand, the cathode side GDL additionally has to transport the liquid product water efficiently from the CCL to the gas channels, where it is then expelled from the cell. In addition, the GDL is also vital to the conduction of electrons to and from the electrodes as well as the removal of reaction heat from the cathode CL. Furthermore, gas diffusion layers also act as supporting structures for the catalyst layers and thereby assist in preserving the mechanical stability of the cell assembly.

GDLs typically consist of a (carbon-based) macroporous fibrous structure with a high porosity (see also Figure 2.2), facilitating efficient gas distribution to the CL. In order to promote its water discharge capabilities, the GDL is therefore usually impregnated with a hydrophobic additive such as PTFE [14]. As the impregnation reduces the average pore size in the GDL, however, excessive additive contents can lead to a deterioration of the effective gas transport [15]. In recent years, the GDL is also increasingly coated with a microporous layer (MPL), as the latter is observed to further enhance the water removal significantly [16]. However, an overly hydrophobic MPL may as well also completely prevent water discharge via the GDL, thereby causing flooding of the catalyst layer [17, 18]. Evidently, optimal GDL water management requires an appropriate GDL design with well-balanced structural (e.g., porosity, pore sizes, tortuosity) and wetting properties (hydrophobicity). In long-term operation, however, these properties may be subject to degradation owing to the harsh conditions present in automotive applications. Hence, the water removal capabilities of the GDL can decrease upon aging, thereby reducing the effective gas transport and consequently the cell performance over operation lifetime.

Over the past decades, researchers have conducted numerous *ex situ* experiments to characterize the capillary behavior of GDLs by, e.g., contact angle measurements [19, 20]

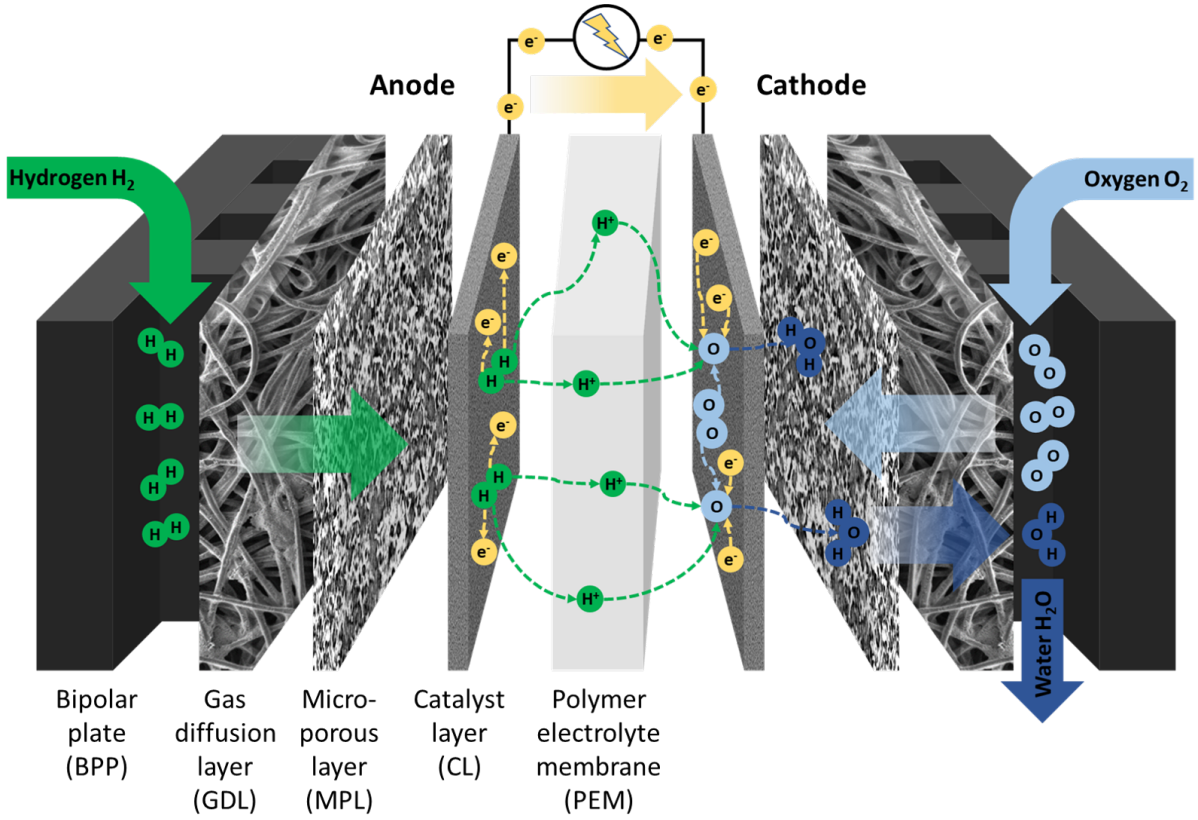

Figure 1.1: Schematic illustration of a PEM fuel cell (inspired by ref. [13]).

or derivation of capillary pressure-saturation ($p_c - S$) relations [21, 22]. While these studies provide interesting insight on the hydrophobicity and capillary behavior of GDLs, the derived characteristics are in general dependent on the boundary conditions (as will be also illustrated in Section 4.4.2). Consequently, the experimental observations at an *ex situ* test bench may have limited transferability to real fuel cell operation, owing to the different *in situ* boundary conditions in cell assembly. In recent years, researchers have therefore also increasingly investigated the water management under *in situ* conditions by, e.g., conducting water breakthrough experiments [23] or visualization of *operando* liquid water transport via neutron radiography [24, 25]. However, such experiments require test benches, which are expensive and difficult to operate but may nonetheless be limited in their depth of detail.

Aging processes are in general expected to occur during long-term cell operation, however, the degradation rates can be low, requiring durability tests to run for thousands of hours [26]. In order to investigate the impact of aging phenomena on the cell performance in a reduced amount of time, researchers have therefore conducted accelerated stress tests (ASTs) to speed-up degradation under extreme operating conditions during, e.g, idling [27–29] or startup/shutdown (SUSD) phases [30, 31]. Whereas such *in situ* experiments

enable to induce specific aging processes under *operando* conditions, they usually do not allow to differentiate between the degradation phenomena of different cell components but present a superposition thereof. Moreover, these *in situ* ASTs are often still time-consuming and expensive. In order to isolate the aging effects of the GDL from other cell components, researchers have therefore conducted numerous *ex situ* experiments to exclusively degrade the GDL under accelerated stress conditions by, e.g., immersion in oxidizing solutions [32–36] or freeze-thaw cycling [37–40]. While these *ex situ* tests in fact allow to isolate the degradation phenomena of the GDL from other cell components, accelerated aging is typically achieved under very extreme test conditions. Eventually, this rises again the question about the transferability of *ex situ* observations to actual fuel cell operation.

Given the aforementioned limitations of experimental studies on transport processes in pristine and aged GDLs, researchers have in recent years increasingly turned towards modeling and simulation as an inexpensive and more rapid means of investigation. With the advent of larger computational resources, in particular pore scale methods (PSMs) have gained increasing popularity, as they allow to study complex multiphase capillary transport phenomena directly at the pore scale. Over the years, researchers have therefore employed pore scale approaches such as Pore Network Modeling (PNM), the Volume-of-Fluid (VoF) or the Lattice Boltzmann method (LBM) to simulate amongst others steady-state capillary pressure-saturation characteristics [41] or dynamic liquid water transport in fresh [42] and aged GDLs [43]. In order to further optimize the GDL design and thereby the water management of PEM fuel cells, however, more research is required to determine key influencing parameters for capillary behavior and the impact of aging on the GDL liquid water transport. Eventually, those novel insights will also further advance the understanding of complex multiphase transport phenomena in porous media.

1.2 Scope of the thesis

In this work, the liquid water transport characteristics in fresh and aged GDLs are thoroughly studied using 3D pore scale simulations and real GDL microstructural tomographic data. By this, the investigations of the underlying thesis contribute to a better understanding of capillary transport characteristics of GDLs in general. In addition, novel insights are provided for the impact of microstructural aging on the GDL liquid water transport and the repercussions on the effective gas transport. The findings of this study thus help to establish a link between water management and cell performance and may thereby support further optimization of GDL designs and future health monitoring during cell operation.

At first, Chapter 2 introduces into the fundamentals of PEM fuel cells and their water management to lay out the foundations for the subsequent investigations of this work. In Chapter 3, different pore scale methods are then reviewed and a 3D multiphase Lattice Boltzmann model (color-gradient model (CGM)) is introduced and validated against analytical references in three numerical test cases. In Chapter 4, the capillary behavior of a plain and impregnated Freudenberg H14 GDL is then analyzed by simulative derivation of capillary pressure-saturation ($p_c - S$) relations. For this purpose, liquid water intrusion is simulated for GDL microstructure reconstructions from high-resolution X-ray micro-computed tomography (µCT) images. Whereas $p_c - S$ characteristics are non-uniquely dependent on the wetting history of the GDL, complementary drainage simulations are conducted as well to derive the complete capillary hysteresis. Moreover, key influencing parameters for this capillary hysteresis are identified by performing simulations for both liquid water intrusion and drainage under variation of several model and simulation parameters. Eventually, the derived capillary characteristics are furthermore also validated against the $p_c - S$ curves of an experimental reference. Whereas in the aforementioned chapter the capillary behavior of the GDL is investigated under test bench conditions, Chapter 5 focuses on the liquid water transport as it may occur during fuel cell operation and how it may change under degradation in long-term operation. For the simulations, the GDL is therefore assumed to be in the compressed state and sandwiched between the cathode side catalyst layer and gas channel, corresponding to typical *in situ* conditions of cell assembly. A microporous layer is furthermore considered by a reconstruction of representative macropores. Mimicking *operando* conditions of stationary cell operation, invasion of liquid water from the catalyst layer is then simulated until it breaks through to the gas channel. In order to investigate the impact of microstructural degradation on the *operando* liquid water transport, virtually aged microstructures are furthermore generated assuming loss of PTFE and increase in macroporosity as the primary degradation mechanisms for the GDL and MPL, respectively. Based on invasion simulations for proceeding stages of aging, the degradation effect on the liquid water transport is then evaluated by means of capillary pressure and local as well as overall saturation at breakthrough. Repercussions on the effective gas transport due to pore blockage by liquid water are furthermore analyzed by calculation of effective diffusivities and permeabilities for the partially saturated and aged GDL and MPL. Chapter 6 lastly summarizes all investigations on the GDL water management in the frame of this work as well as their respective findings and concludes with a perspective on the potentials of future research works in this field.

2 Fuel cell fundamentals

2.1 Basic working principle

A fuel cell is an energy conversion device, which converts the chemical energy of a fuel into usable electrical energy by electrochemical reaction with an oxidant component. In contrast to batteries, however, fuel cells do not store convertible chemical energy but have to be constantly supplied with the reactands to sustain stable operation and thereby provide continuous electrical power. A fuel cell basically consists of two electrochemical half-cells (i.e., electrode and electrolyte) with a separator in between. Whereas the half-cells provide the electrodes for the respective electrochemical half-cell reactions, the separator acts as both an electrical insulator and ionic conductor. In succession to the half-cell reactions, protons are then transferred through the separator and electrons flow through an external circuit, providing electrical power to be used by a consumer. To this day, different types of fuel cells have been developed, which differ amongst others in their fuel component, electrolyte material and/or operating temperature. Classified by the type of electrolyte, the most common fuel cells can be divided into alkaline fuel cells (AFCs), direct alcohol fuel cells (DAFCs), molten carbonate fuel cells (MCFCs), phosphoric acid fuel cells (PAFCs), polymer electrolyte membrane fuel cells (PEMFCs) and solid oxide fuel cells (SOFCs) [44]. Given their respective characteristics, these common-type fuel cells have by now found their way into various stationary and mobile applications [45]. In the automotive sector, PEMFCs are considered to be the most promising fuel cell technology, amongst others, due to low operating temperature, short refueling, dynamic response, high power density and energy efficiency [5–7, 12].

2.2 Polymer electrolyte membrane fuel cells (PEMFCs)

Polymer electrolyte membrane fuel cells provide electrical energy by the electrochemical conversion of hydrogen (H_2, fuel) and oxygen (O_2, oxidant) to water (H_2O). Operating at temperatures below 100 °C, these low temperature fuel cells use a proton conducting polymer membrane as both the electrolyte and separator. In a PEM fuel cell (Figure 2.1), this polymer electrolyte membrane (PEM) is sandwiched between the anode and cathode

to form the membrane electrode assembly (MEA). The electrodes typically consist of the catalyst layers (CLs), microporous layers (MPLs) and gas diffusion layers (GDLs) and are enclosed by bipolar plates (BPPs), which provide flow fields for the gas supply to the MEA.

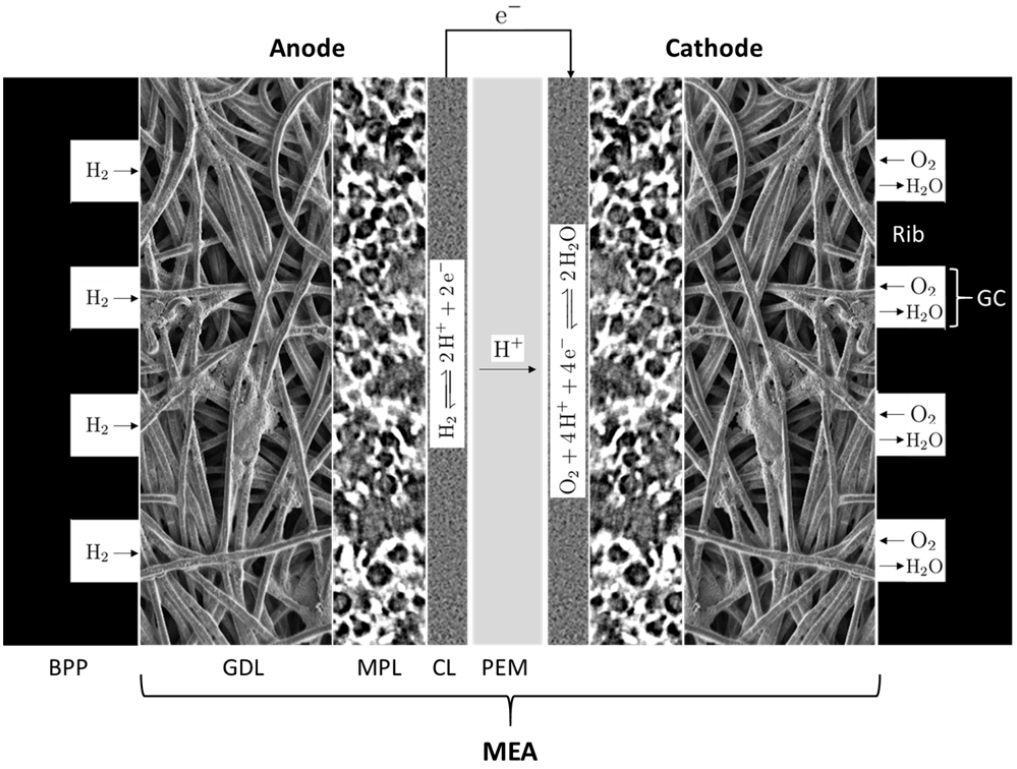

Figure 2.1: Working principle of a PEM fuel cell.

During operation, the reactand gases are fed to the electrodes (H_2 to the anode and O_2 to the cathode) via the gas channels (GCs) of the BPP flow fields. For reasons of practicability, the oxygen is typically supplied by feeding air to the cell. Permeating through the adjacent GDL and MPL, the gases are then distributed homogeneously to the respective catalyst layers, where the electrochemical half-cell reactions occur. In the anode CL, hydrogen is split into protons and electrons, according to the hydrogen oxidation reaction (HOR):

$$\mathrm{H_2} \rightleftharpoons 2\,\mathrm{H^+} + 2\,\mathrm{e^-} \tag{2.1}$$

The protons then move directly through the polymer electrolyte membrane to the cathode CL, whereas the electrons have to pass through an external electrical circuit. Upon arrival at the CCL, the protons and electrons then react with oxygen under formation

of water, according to the oxygen reduction reaction (ORR):

$$O_2 + 4\,H^+ + 4\,e^- \rightleftharpoons 2\,H_2O \tag{2.2}$$

Combining the oxidation half-cell reaction of the anode and reduction half-cell reaction of the cathode, the overall redox reaction of a PEM fuel cell then equals:

$$2\,H_2 + O_2 \rightleftharpoons 2\,H_2O \tag{2.3}$$

As the water is produced at the CCL, it interferes with the oxygen transport to the catalyst layer and therefore has to be removed from the cathode CL to prevent flooding. At the same time, however, the PEM requires a sufficient amount of water to remain hydrated and thus maintain a high protonic conductivity. Consequently, stable PEM fuel cell operation is only achievable with a proper water management.

2.2.1 Water management in PEM fuel cells

The polymer electrolyte membrane has to provide high protonic conductivity, high electronic resistivity and low gas permeability. The PEM is commonly made of a perfluorosulfonic acid (PFSA) ionomer such as Nafion®, as the latter offer high ionic conductivities and chemical as well as mechanical stability [46].
However, the properties, and in particular the proton conductivity, of the PEM are strongly dependent on the membrane water content. Therefore, the reactand gases are usually humidified when supplied to the cell in order to maintain the PEM hydrated [47]. Associated with the proton conduction through the membrane, however, water can be transported from the anode to the cathode via electro-osmotic drag [48], causing dehydration of the PEM. A counteracting process is the water production in the CCL, which will lead to back-diffusion of membrane water from the cathode to the anode. Depending on the local saturation conditions, the product water in the CCL can be furthermore present in both the gas and liquid phase (or partly as ice at sub-zero temperatures). As vapor, the product water may then diffuse along concentration gradients through the MPL and GDL towards the gas channel to be expelled from the cell. Liquid water, on the other hand, will block portions of the cathode catalyst surface from the reactand gases, thereby reducing the cell performance. Primarily driven by capillary forces, liquid water may furthermore percolate through the MPL and GDL until breaking through to the cathode GC to be dragged off as droplets [49, 50]. In order to prevent flooding, however, the liquid product water has to be efficiently removed from the cathode. This requires an appropriate design of the capillary transport characteristics of the GDL and MPL.

2.2.2 The gas diffusion layer (GDL)

Gas diffusion layers are highly porous structures typically made from carbon fibers of approximately 7 to 14 µm in diameter, which can be grouped into woven cloths and nonwoven fiber substrates [51]. Depending on the manufacturing process, nonwoven GDLs can be further subdivided into papers or felts, according to the procedure of fiber fixation. In carbon paper GDLs, straight fibers are interconnected by a binder component (usually carbonizable resin) to form rather ordered quasi-planar structures [52]. In carbon felts, on the other hand, loose fibers are mechanically intertwined in a hydro-entangling process [53–55], yielding rather disordered 3D fibrous structures. For a comparison of the structural properties of carbon paper and felt GDLs the interested reader is at this point referred to elsewhere, e.g., [56] or [57]. In the frame of this work, all subsequent investigations focus on a carbon felt GDL by Freudenberg, as shown in Figure 2.2.

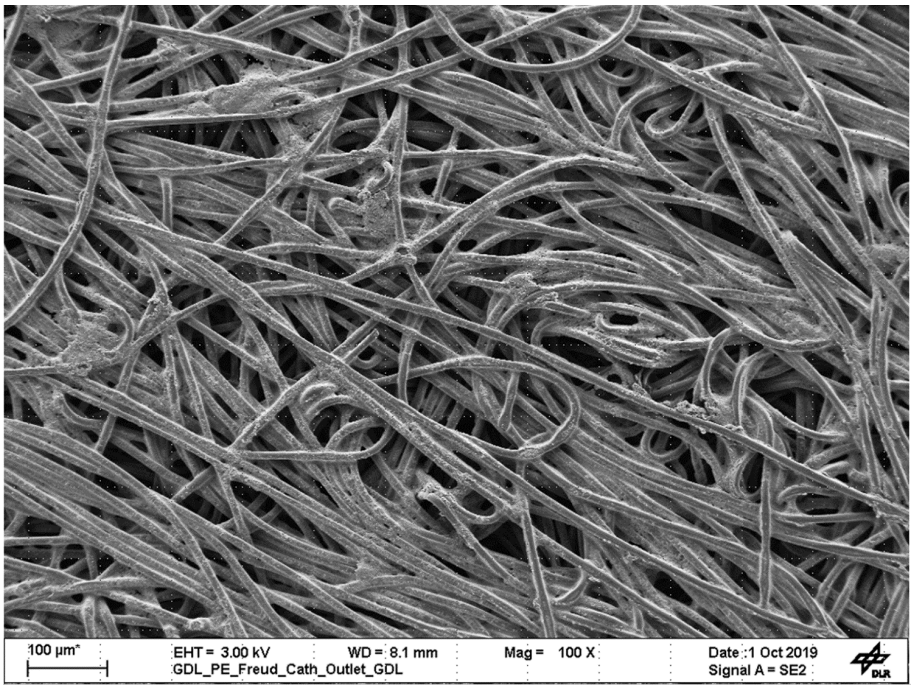

Figure 2.2: Scanning electron microscopy (SEM) image of a carbon felt GDL by Freudenberg. Image recorded by Pia Aßmann (Department for Electrochemical Energy Technology, Institute of Engineering Thermodynamics, DLR Stuttgart) in the frame of the EU project ID-FAST.

With thicknesses of 100 to 400 µm, GDLs typically exhibit large average pore diameters of 10 to 100 µm and high porosities of 60 to 90 % to facilitate efficient gas transport to the CL [19]. Owing to their pore sizes, GDLs are therefore also often referred to as macroporous substrates (MPSs). In order to promote their water removal ability as well, GDLs are commonly wet-proofed with a hydrophobic additive such as polytetrafluoroethylene

(PTFE). Untreated fiber substrates are therefore typically impregnated via dip-coating in aqueous dispersions of a hydrophobic component followed by a finalizing drying procedure. As will be discussed in more detail in Section 4.2.4, the latter can have a non-negligible impact on the eventual additive distribution in the GDL. While considered to be beneficial for the water discharge from the GDL, the hydrophobic agent also reduces the average pore size, which is disadvantageous for the effective gas transport [15]. Typical additive loadings therefore usually range from 5 to 30 wt% [51]. In addition to efficient gas transport and water removal, the GDL also has to fulfill further essential tasks. On the one hand, the GDL has to establish good electrical contact between the bipolar plate and the CL, and should therefore exhibit a high electrical conductivity [58, 59]. On the other hand, the GDL has to remove waste heat from the CL to maintain a stable operating temperature (thermal management), thus requiring a high thermal conductivity [60, 61]. Lastly, the GDL also has to provide mechanical support for the CL/PEM and should hence possess sufficient mechanical strength [62–64].

In recent years, GDLs have been also increasingly coated with a microporous layer (MPL), as the latter was observed to improve PEM fuel cell performance in different ways. MPLs are composed of a carbonaceous powder (e.g., carbon black or graphite) mixture with a hydrophobic agent (mostly PTFE), which is coated onto the GDL [65]. Additive loadings are furthermore reported to range from 5 to 35 wt% [66]. With thicknesses of typically less than 50 µm, MPLs exhibit average pore sizes around 100 to 500 nm and can be thus considered as a primarily nanoporous structure [51]. As a result of the coating procedure, MPLs typically penetrate the GDL at varying depths, oftentimes obviating a clear distinction of the respective diffusion layers [67–72] due to a rather smooth transition zone (see also Section 5.3). In addition, the MPL is found to enhance the electrical contacting between the GDL and CL [73, 74]. Furthermore, the MPL is also reported to increase the stiffness of the coated GDL due to a larger elastic modulus [62, 75, 76]. Moreover, MPLs are also reported to be in particular beneficial for the water management. Owing to their low pore sizes and high hydrophobicity, MPLs provide a high capillary barrier for the liquid water transport to the GDL. As a result of this water retention capability, the MPL can help to prevent GDL flooding and promote back-diffusion to the anode, thereby maintaining sufficient membrane hydration [73, 74, 77]. On the other hand, however, the MPL also has to possess certain water discharge capabilities, as an overly high capillary resistance may as well cause flooding [66]. While many MPLs exhibit cracks or fractures either from manufacturing [78] or from compression in cell assembly [79], these are observed to provide preferential water pathways to the GDL [80–82], owing to a lower capillary resistance. In summary, a MPL should possess well-balanced water retention and discharge capabilities in order to provide an optimal water management. In

Chapter 5 of this work, a MPL is considered as well by reconstruction of its macroporous features, which will be used to define inlet locations for the subsequent GDL liquid water invasion simulations. At this point, however, it is emphasized that this work focuses on the capillary transport phenomena in the GDL and not the MPL. The latter is therefore disregarded in all subsequent sections prior to Chapter 5.

2.2.3 Liquid water transport in the GDL

In PEM fuel cell operation, water is constantly produced by the ORR (see eq. (2.2)) in the cathode catalyst layer. According to Faraday's law, the amount $n_{\mathrm{H_2O}}$ of product water is with

$$n_{\mathrm{H_2O}} = \frac{Q}{z_{\mathrm{H_2O}}\mathcal{F}} \tag{2.4}$$

proportional to the transferred electrical charge Q, the charge number $z_{\mathrm{H_2O}} = 2$ and the Faraday constant $\mathcal{F} = 96\,485\,\mathrm{C/mol}$ [83]. With the current $I = dQ/dt$ as the charge per time, the water production rate $\dot{n}_{\mathrm{H_2O}}$ then furthermore equals

$$\dot{n}_{\mathrm{H_2O}} = \frac{d}{dt}\left(n_{\mathrm{H_2O}}\right) = \frac{d}{dt}\left(\frac{Q}{z_{\mathrm{H_2O}}\mathcal{F}}\right) = \frac{I}{z_{\mathrm{H_2O}}\mathcal{F}}. \tag{2.5}$$

As previously discussed in Section 2.2.1, the product water will be in general present in different states (liquid, vapor, ice), depending on the local saturation conditions in the cathode CL. However, under the assumption that the gas phase in the CCL is fully saturated at an ordinary operating temperature above zero and below the boiling point, the product water can be expected to be completely in the liquid state, i.e., $\dot{n}_{\mathrm{H_2O}} = \dot{n}_{\mathrm{H_2O(l)}}$. Such a scenario is likely to occur in PEMFC operation at high relative gas humidities and/or high current densities and will be investigated in the subsequent GDL liquid water transport studies of this work. Presuming furthermore stationary operation with a completely hydrated PEM and zero net flux of water through the membrane, the liquid product water has to be removed from the CCL via the GDL to prevent flooding and to maintain stable operation. At this point, however, it is aknowledged that the assumption of a zero net flux of water through the PEM presents a strong simplification, as the membrane water balance is in general dependent on the operating conditions (e.g., relative gas humidity or current density, see also Section 2.2.1). Consequently, the amount of liquid product water (as a function of the current) being transported through the cathode GDL is in this work only roughly estimated. Provided that the liquid water is produced homogeneously across the cross-sectional area A_{cell} of the cell, an average GDL inlet velocity

$$u_{\mathrm{H_2O(l)}} = \frac{\dot{V}_{\mathrm{H_2O(l)}}}{A_{\mathrm{cell}}} = \frac{\dot{m}_{\mathrm{H_2O(l)}}}{\rho_{\mathrm{H_2O(l)}} A_{\mathrm{cell}}} = \frac{M_{\mathrm{H_2O}}}{\rho_{\mathrm{H_2O(l)}} A_{\mathrm{cell}}} \dot{n}_{\mathrm{H_2O(l)}} = \frac{M_{\mathrm{H_2O}}}{\rho_{\mathrm{H_2O(l)}} A_{\mathrm{cell}}} \frac{I}{z_{\mathrm{H_2O}} \mathcal{F}} = \frac{M_{\mathrm{H_2O}}}{\rho_{\mathrm{H_2O(l)}} z_{\mathrm{H_2O}} \mathcal{F}} i, \tag{2.6}$$

can then be associated with the current density $i = I/A_{\mathrm{cell}}$, the molar mass $M_{\mathrm{H_2O}}$ and density $\rho_{\mathrm{H_2O(l)}}$. In favor of enhanced readability, water will be from here on referred to as the liquid phase for the remainder of this work, e.g., $\rho_{\mathrm{H_2O(l)}} = \rho_{\mathrm{H_2O}} = \rho_l$.

According to equation (2.6) and with current densities of commonly $i < 3\,\mathrm{A/cm^2}$ [84, 85], the average GDL liquid flow velocity is on the order of $u_l \sim 10^{-6}\,\mathrm{m/s}$ or even below. Assuming an average GDL pore diameter of $d_p = 10 - 30\,\mu\mathrm{m}$ [19], the Reynolds number can be then estimated to

$$\mathrm{Re} := \frac{\text{inertial forces}}{\text{viscous forces}} = \frac{\rho_l u_l d_p}{\mu_l} \sim 10^{-5} - 10^{-4} [86, 87] \tag{2.7}$$

with μ_l as the liquid dynamic viscosity. For $\mathrm{Re} << 1$ inertial effects become negligible and the liquid water motion can be classified as creeping (Stokes) flow. Due to the presence of the reactand gas in the pores, the liquid water is furthermore subject to capillary action. With the surface tension σ of the water-air two-fluid system, the Capillary number is on the order of

$$\mathrm{Ca} := \frac{\text{viscous forces}}{\text{capillary forces}} = \frac{\mu_l u_l}{\sigma} \sim 10^{-8} - 10^{-5} [23, 88] \tag{2.8}$$

and the liquid water transport through the GDL can be thus considered as dominated by capillary forces. According to Lenormand et al. [89], the invasion pattern of a nonwetting fluid into a porous medium can be classified as stable displacement, viscous fingering or capillary fingering in dependence of Ca and the ratio

$$M := \frac{\mu_I}{\mu_D} \tag{2.9}$$

of the dynamic viscosities μ_{I} and μ_{D} for an invading and defending fluid. Corresponding to Figure 2.3 and with $M = \mu_l/\mu_g \sim 17.5$ [90], GDL liquid water invasion patterns are thus typically described as capillary fingering [88, 90]. In this flow regime, which has been also reported by experimental studies [91], the invading fluid percolates the porous medium via single capillary fingers along paths of least capillary transport resistance.

Once percolated through the entire GDL thickness, the liquid water then breaks through to the gas channel and forms droplets. After growing to a certain size, the droplets then detach from the GDL surface and are then dragged off by the convective gas flow along the GC to be ultimately expelled from the cell. Several studies have reported that the liquid

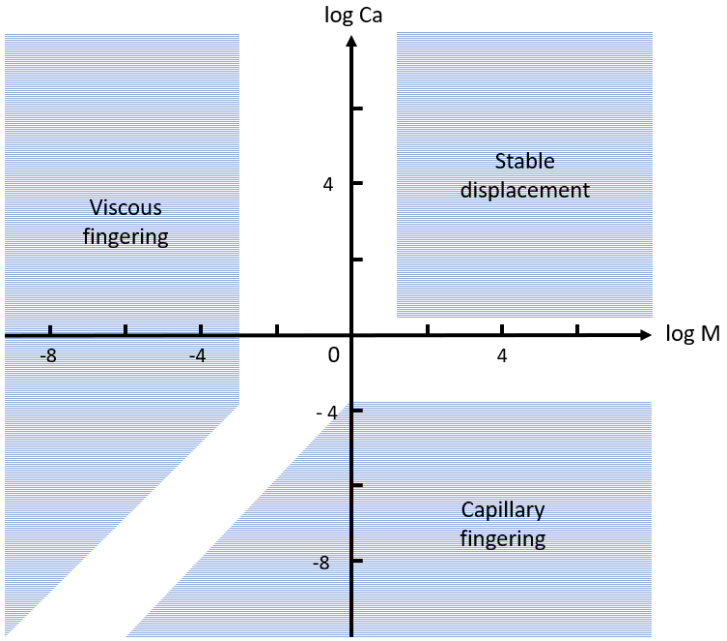

Figure 2.3: Flow regime characterization for the invasion of a nonwetting fluid into a porous medium in dependence of the capillary number Ca and the ratio $M = \mu_I/\mu_D$ of invading and defending fluid's dynamic viscosity. Qualitatively adopted from the phase-diagram by Lenormand et al. [89].

water distribution in the GDL is rather stable once breakthrough has occurred [86, 92, 93], in particular in the presence of a MPL [23]. Consequently, the breakthrough liquid water distribution can be regarded as representative for the water management in stationary cell operation. This circumstance will be exploited in Chapter 5, where the impact of GDL aging on the liquid water invasion behavior is investigated and characterized by means of time to breakthrough, saturation at breakthrough and capillary pressure required for breakthrough.

2.2.4 Capillary phenomena

In porous media, capillary forces arise from different interfacial energies of the participating fluids with the pore surfaces. In Figure 2.4, these circumstances are illustrated for a sessile liquid drop on a flat solid surface, where σ_{sl} and σ_{sg} are the surface energies of the solid-liquid and solid-gas interface and σ_{lg} represents the liquid-gas interfacial energy (or more commonly surface tension σ). In thermodynamic equilibrium, an energy minimum is then obtained at the three-phase contact line, according to Young's equation [94] with

$$\sigma_{sg} = \sigma_{sl} + \sigma_{lg} \cos(\theta) \tag{2.10}$$

and the contact angle θ. The latter is a measure for the tendency of a fluid to wet a solid surface, a property which is commonly referred to as wettability. Hence, a fluid is considered as wetting (w) for a contact angle smaller than 90°, or as nonwetting (nw) for $\theta > 90°$.

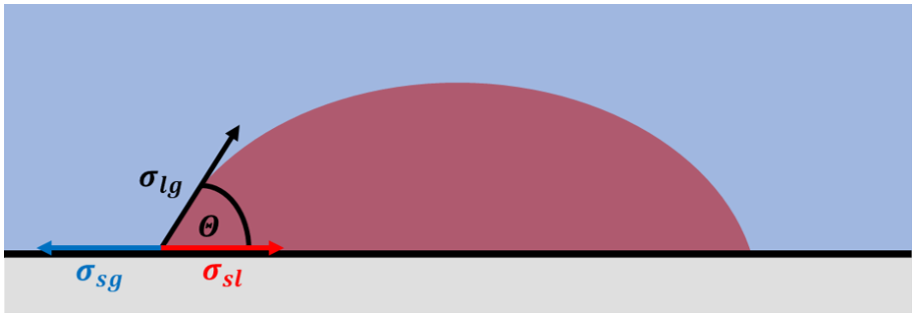

Figure 2.4: A liquid droplet wetting a solid surface. At the three-phase contact line, the different surface energies σ_{sl} and σ_{sg} for the solid-liquid and solid-gas interface are balanced by the surface tension bending the droplet surface by a contact angle θ.

Due to their different wetting properties, two immiscible fluids will experience capillary forces resulting in a capillary pressure

$$p_c = p_{nw} - p_w = f(\theta) \tag{2.11}$$

as the difference of the nonwetting and wetting phase pressure. For a circular capillary tube as shown in Figure 2.5, p_c is given by the well-known Young-Laplace equation [95] with

$$p_c = \frac{2\sigma}{R} \tag{2.12}$$

and the radius R of a sphere describing the meniscus of the fluid-fluid interface. The meniscus is a result of the fluid's wettability and the sphere radius can be expressed with

$$R = \frac{R_t}{\cos\theta} \tag{2.13}$$

as a function of the contact angle θ and throat radius R_t of the capillary tube. Combining equations (2.13) and (2.12) yields

$$p_c = \frac{2\sigma\cos\theta}{R_t} \tag{2.14}$$

for the capillary pressure in dependence of the contact angle and capillary tube radius. Driven by capillary forces, a wetting fluid ($\theta < 90°$) will be thus spontaneously imbibed into a capillary tube unless p_c is counteracted. For a vertical tube under the effect of gravitational forces (Figure 2.5), capillary ascension will proceed until the capillary pressure

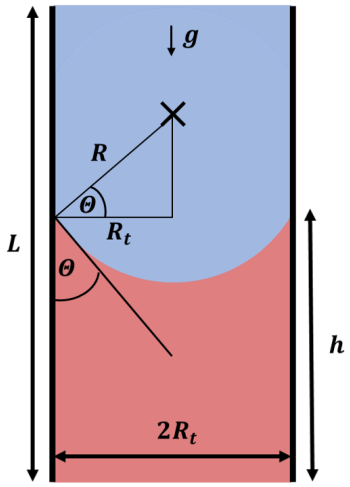

Figure 2.5: Capillary ascension of a wetting fluid (red) in a circular tube of radius R_t and length L. Driven by capillary forces, a wetting fluid with a contact angle of $\theta < 90°$ invades the tube and displaces a nonwetting fluid (blue) against gravitational acceleration g. According to Jurin's law [96], capillary ascension stops at a height h, where the capillary pressure is balanced by the hydrostatic pressure.

$$p_c = \frac{2\sigma \cos\theta}{R_t} = p_h = \Delta\rho g h \tag{2.15}$$

is balanced by the hydrostatic pressure p_h. In equation (2.15), $\Delta\rho = \rho_w - \rho_{nw}$ represents the difference in phase densities from which the hydrostatic pressure arises. According to Jurin's law [96], the capillary ascension height in the tube is given as

$$h = \frac{2\sigma \cos\theta}{R\Delta\rho g} = \frac{p_c}{\Delta\rho g}. \tag{2.16}$$

With an overall tube length L, a wetting phase saturation S_w can be associated to the capillary ascension height with

$$S_w = \frac{V_w}{V_t} = \frac{h}{L} \tag{2.17}$$

as the fraction of wetting fluid volume V_w to the overall tube volume V_t. Comparing equations (2.16) and (2.17), the saturation can be then related to the capillary pressure, i.e.,

$$S_w = \frac{p_c}{\Delta\rho g L} = f\left(p_c\right). \tag{2.18}$$

Such a constitutive capillary pressure-saturation ($p_c - S$) relation is a basic characteristic of capillary systems, which expresses the saturation as a function of the capillary driving forces. Hence, $p_c - S$ relations are an important measure for the multiphase transport

properties of capillary systems. Furthermore, the derived functions can be employed in modeling and simulation of multiphase transport phenomena in porous media, e.g., liquid water transport in PEM fuel cells [97]. However, while the $p_c - S$ relation for a single capillary tube can be derived analytically, this is a disparately more difficult task for porous media of higher geometric complexity. Whereas a generalized Young-Laplace equation [95] can be formulated for arbitrary geometries as

$$p_c = \sigma \left(\frac{1}{R_1} + \frac{1}{R_2} \right) \tag{2.19}$$

with R_1 and R_2 as the principal radii of curvature of any fluid-fluid interface, p_c may vary locally inside the pores of a capillary system. Furthermore, the principal radii of curvature are in general also a function of the contact angle, i.e., $R_i = f(\theta)$ and thus additionally dependent on the local wettability within the porous medium. As a result, analytical derivation of $p_c - S$ relations is in general beyond feasibility for complex microstructures such as the GDL. Over the past decades, numerous efforts were therefore made to derive empirical $p_c - S$ relations for various porous media. One of these (in PEMFC modeling presumably most popular) empirical relations was proposed by Leverett [98] with

$$\frac{\Delta \rho g h}{\sigma} \sqrt{\frac{\kappa}{\epsilon}} = \frac{p_c}{\sigma} \sqrt{\frac{\kappa}{\epsilon}} = f(S_w) \tag{2.20}$$

for the permeability κ, porosity ϵ and wetting phase saturation S_w of the porous medium. Based on Leverett's work, Udell [99] later on presented with the *Leverett J-function*

$$J(S_w) = 1.417 (1 - S_w) - 2.120 (1 - S_w)^2 + 1.263 (1 - S_w)^3 \tag{2.21}$$

an expression for the saturation dependence. Introducing furthermore a contact angle to account for different wettabilities, a formulation for the capillary pressure was then suggested with

$$p_c = \sigma \cos\theta \sqrt{\frac{\epsilon}{\kappa}} J(S_w) \tag{2.22}$$

known as the Leverett-Udell correlation. Over the past decades, equation (2.22) has been extensively employed in various modeling works on multiphase transport in porous media. However, originally derived for soils with uniform wettability, Leverett's relation was repeatedly reported to have limited predictive capabilities for the capillary characteristics of structurally different porous media such as GDLs [100–102]. Therefore, Kumbur and coworkers proposed modified Leverett-type approaches with a *K-function* including previously neglected aspects such as mixed wettability [103], compression [104] or temperature [105] and demonstrated that these extensions provided improved predictions for different

types of GDLs. In addition to Leverett's approach, also other relations have been derived and widely employed in research fields associated with capillary transport phenomena. Defining an effective saturation

$$S_w^{\text{eff}} = \frac{S_w - S_w^{\text{res}}}{1 - S_w^{\text{res}}} \tag{2.23}$$

with the residual wetting phase saturation S_w^{res} retained at large p_c, Brooks and Corey [106] proposed

$$S_w^{\text{eff}} = \left(\frac{p_c}{p_c^{\text{B}}}\right)^{-\lambda} \qquad \text{for } p_c > p_c^{\text{B}} \tag{2.24}$$

using the fit parameters λ and p_c^{B}. The latter can be physically interpreted as the *bubble pressure* required to sustain at least one nonwetting phase percolation path through the porous medium. Van Genuchten [107] modified the approach of Brooks and Corey to

$$S_w^{\text{eff}} = \left(1 + \left(\frac{p_c}{p_c^{\text{B}}}\right)^{n}\right)^{-m} \qquad \text{for } p_c > 0, \tag{2.25}$$

suggesting to use three fit parameters m, n and p_c^{B}. Despite their popularity, the aforementioned three $p_c - S$ relations are known to have their limitations depending on the porous medium and saturation range. Therefore, numerous later studies have worked on the derivation of new (semi-)empirical relations for the capillary transport characteristics of the GDL (or other porous media). For a comprehensive summary of mainly experimental investigations on $p_c - S$ characteristics of GDLs, the reader is referred to the extensive review by Si et al. [21]. In addition to these experimental studies, few works have also employed pore-scale modeling (PSM) and simulation to derive new $p_c - S$ relations for GDLs, as will be reviewed in Section 4.1.

Chapter 4 of this work provides a novel contribution to PSM studies on $p_c - S$ characteristics of GDLs. For this purpose, liquid water transport through GDL microstructure reconstructions are modeled and simulated using the Lattice Boltzmann method. Whereas oftentimes neglected, capillary hysteresis is recovered by simulation of both the intrusion and drainage process. By variation of model and simulation parameters, new insights are furthermore provided on key influencing parameters for the capillary transport characteristics and ther relation between capillary pressure and saturation. Based on the simulation results, new $p_c - S$ relations are then eventually derived.

3 Modeling of multiphase flows in porous media

3.1 Pore-scale modeling

Multiphase transport phenomena of porous systems much larger than the pore scale can be conveniently described on the continuum scale using volume-averaged transport properties. However, these effective medium approaches require constitutive relations for the description of volume-averaged transport properties. Here, typical examples are a porosity-dependent permeability ($\epsilon - \kappa$) and capillary pressure-saturation ($p_c - S$) relations.

While such dependencies have been traditionally studied and derived in experiments ever since attaining relevance, pore-scale modeling (PSM) has increasingly approached researcher's interest over the past decades as an alternative means of investigation. Beyond the sole derivation of constitutive relations, the latter is in particular interesting as it allows to study multiphase flows directly at the pore scale in order to gain a deeper understanding of the underlying transport phenomena. Over the past decades, different pore-scale modeling approaches have therefore been developed with varying model complexity, accuracy and computational expense. To this day, a multitude of different concepts have been developed and utilized. However, whereas an in-depth description of this large variety of models is beyond the scope of this work, the interested reader is at this point referred to the more comprehensive overview by Szűcs et al. [108]. In general, the different PSM concepts can be classified into pore network modeling (PNM), direct numerical simulation (DNS) techniques and hybrid approaches, which combine the former two approaches.

In PNM, the pore space geometry is approximated by an idealized network typically consisting of pores interconnected by throats. By using simpler geometric entities such as spheres and circular tubes for these basic structural elements, fluid flow through the capillary system can then be described (semi-)analytically using, e.g., the Lucas-Washburn equation (2.14)). As a result of this geometric simplification, PNM is a computationally very efficient pore-scale modeling approach. The foundations for PNM were already laid out in 1956 by Fatt [109] with a simple network of regular circular capillary tubes. Since then, many research works were devoted to the generation of improved pore space

representations by network construction from regular cubic or square lattices [110–113] in order to recover certain structural properties (e.g., porosity or pore size distribution). Later on, more realistic pore networks were increasingly extracted from random sphere packs using mathematical methods such as Delaunay or Voronoi tesselations [114–118]. With the continuous improvement of experimental imaging techniques in recent years, direct extraction from 3D volumetric pore space data has also gained increasing attention and researchers have developed new pore network extraction routines employing methods such as the maximal ball [119], medial axis [120] or watershed algorithm [121, 122]. For a more comprehensive overview on the history of pore network construction and extraction approaches, the interested reader is at this point referred to the comprehensive reviews provided in [123, 124]. Complementary to the aforementioned concepts for pore network generation, researchers have also increasingly employed different cross-sectional shapes for the pore elements (angularity and irregularity) in order to achieve desired capillary flow phenomena such as film flow, phase trapping and hysteresis [125–128]. Furthermore, also dynamic pore network models have been developed in parallel to above quasi-static approaches in order to account for viscous effects and transient flow characteristics in porous media [129–131]. As evident from these and many more developments, pore network modeling has been an active field of PSM research over the last decades owing to its predictive power at low computational expense. In spite of all improvements in the past, however, one of the major drawbacks of PNM remains the limited accuracy due to the strong simplifications inherent to the approach [132, 133]. Moreover, the predictive power for single- and multiphase transport characteristics (e.g., effective diffusivities, permeabilities or capillary pressure-saturation relations) is in general also dependent on the validation/calibration of *a priori* unknown parameters for the modeling of the pore geometry [134, 135].

In order to overcome this parametric uncertainty in the representation of the pore space, Hazlett [136] proposed in 1995 with the Full Morphology (FM) method a concept, which utilizes real microstructural data. Based on the same idea, Hilpert and Miller [137] published with the Pore Morphology (PM) method a few years later a very similar but slightly improved approach. Employing a morphological opening operator to binarized pore/solid tomographic images of a porous microstructure, this approach determines for each individual pore the largest sphere, which can be still inscribed without touching the pore walls. Similar to PNM, a radius-dependent capillary pressure can be then associated with each of these spheres representing pore sizes (see Young-Laplace equation (2.14) and capillary fluid distribution can then be modeled (semi-)analytically by account of the pore size distribution and pore interconnectivity. The FM method is reported to provide predictions with accuracy similar to PNM, while it has the advantage over the latter that

no additional parameters are required for the representation of the pore network [138]. At the same time, the approach comes along with an acceptable increase in the computational cost as compared to PNM [132]. According to Hazlett [136], however, the FM method also suffers from inherent limitations such as overestimation of phase trapping amongst others due to the assumption of a sphere-shaped meniscus of the fluid interface. Moreover, the predictions are limited to static equilibrium phase distributions, as the approach is purely morphological and has no sound physical base (e.g, no momentum conservation) [139]. Eventually, as the pore morphology is approximated by whole geometric entities (i.e., spheres), transport phenomena at the sub-pore scale remain unresolved in FM (as well as in PNM), thus prohibiting further investigation. With the advent of high-performance computing, pore scale-resolving direct numerical simulation methods have gained increasing attention in the field of PSM. These modeling techniques can be generally sub-divided into grid-based and particle-based methods.

In grid-based CFD methods, macroscopic fluid behavior is modeled by dividing the fluid's continuum domain into smaller (volumetric) subdomains for which the Navier-Stokes equations are then solved numerically. For these calculations, the governing equations have to be discretized on a computational grid using specific discretization schemes. Among these, the Finite Volume method (FVM) [140] represents one of the most widely used in the field of computational fluid dynamics. Whereas in general the simulation of multiphase flows is possible with the FVM alone, the latter *per se* provides no capability to resolve and capture fluid-fluid interfaces. For applicability to the field of pore-scale methods, the set of underlying model equations therefore has to be extended. One of such approaches is the Volume-of-Fluid method (VoF), which was proposed in 1976 by Noh and Woodward [141]. In this approach, an indicator variable is introduced as a phase volume fraction to capture the fluid-fluid interface. The temporal evolution of the interface position is then governed by an advective transport equation for the indicator function, which has to be solved in addition to the Navier-Stokes equations. Amongst others due to the ease of implementation for this simple and mass-conserving modeling approach, VoF has gained increasing popularity over the past decades. As a result, the method has found its way into a variety of different applications such as the modeling of free surface flows [142], bubble dynamics [143], phase-change phenomena [144] and multiphase flows in porous media [145, 146]. However, one of the major remaining challenges of this method is a non-physical smearing of the interface due to numerical diffusion [147]. A grid-based pore-scale model, which is capable of inherently providing a sharp interface is the Level Set (LS) method originally proposed by Osher and Sethian [148] in 1988. In this method, an indicator variable is introduced and described with a transport equation similar to the VoF approach. As opposed to defining the indicator variable as a phase volume fraction,

however, the LS method uses a continuous signed distance function to preserve an interface of high sharpness. While the latter is considered as one of the main advantages of the LS method, mass conservation is on the other hand amongst others a general issue yet to be completely resolved [149]. In order to overcome some of the disadvantages of the VoF and the LS method, also hybrid approaches have been developed in recent years, which combine the strengths of both methods [150].

In particle-based CFD methods, a fluid continuum is discretized into sets of particles or particle distributions. On the mesoscale, motion and interaction of the particles are then modeled such that the correct fluid behavior is recovered at the macroscale. Among these particle-based PSMs, Smoothed Particle Hydrodynamics (SPH) is a modeling approach, which was first proposed in 1977 [151–153]. Originally developed to describe gasdynamic phenomena in astrophysics, this mesh-free method has been over the past decades employed to a large variety of different problems such as solid mechanics, free surface flows, multiphase flows, coastal wave dynamics or fluid-solid interactions [154–156]. The basic concept of SPH is the lagrangian description of a fluid as a set of particles with point masses, which discretize the continuum scale. Using a gaussian-like kernel, particle-averaged properties (e.g., density, velocity or pressure) are then smoothened around the point masses to recover the fluid behavior. Over the past decades, SPH has gained increasing popularity due to strengths such as mass conservation, galilean invariance and the applicability to arbitrary geometries, owing to its mesh-free formulation [157, 158]. In particular the latter two aspects have rendered SPH an interesting method for PSM applications, as multiphase flows in complex porous media can be simulated without the requirement for explicit interface tracking [159, 160]. In addition, whereas earlier models did not guarantee conservation of linear and angular momentum, this model limitation was resolved in later SPH formulations as well. [161, 162]. Apart from all these benefits of the method, however, there remain certain challenges such as high computational cost, convergence behavior or local refinement of spatial resolution (adaptivity) [163–165].
A second widely used particle-based approach is the Lattice Boltzmann Method (LBM), which originated from the Lattice-Gas Automata (LGA), where the motion and interaction of discrete gas particles is modeled on a computational lattice [166]. Whereas the original LGA suffers from statistical noise, McNamara and Zanetti [167] resolved this issue for the LBM using particle distributions instead of discrete numbers. The basic concept of LBM is the description of a fluid continuum as a set of particle distributions, whose temporal evolution is governed by the Boltzmann equation. In the LBM formalism, the latter is then discretized on a lattice to recover the fluid behavior, according to the Navier-Stokes equations. As a particle-based mesh-free modeling approach similar to SPH, one of the major strengths of LBM is also the applicability to simulation geometries of arbitrary

complexity. Over the past decades, different single- and multiphase LB models have been therefore developed and successfully employed to a variety of different problems in fields such as single- and multiphase flows [168, 169], heat transfer [170, 171] and phase-phase phenomena [172, 173]. Furthermore, the LBM has proved to be very suitable for the modeling of multiphase flows in porous media [174]. As opposed to SPH, however, galilean invariance is in general not provided in the original LBM formulation and higher-order correction terms had to be introduced [175–177]. In addition, the simulation of fluid flows at high density and viscosity ratios remained for a longer time a major challenge to many multiphase LB models due to numerical instabilities. Over the years, however, the aforementioned limitations have been largely addressed and increasingly resolved in newer model extensions [178–180]. Lastly, the accuracy of multiphase LB models traditionally suffers from spurious currents near curved interfaces due to discretization errors [181–183]. In more recent works, however, researchers were able to successfully suppress these parasitic fluid velocities using higher-order discretization schemes or alternative formulations thereof [184–186]. In spite of all these improvements, the LBM remains in general a pore-scale modeling technique with high computational cost (even though less than compared to SPH [187]). With good parallelizability of the LB formulation and increasing capacities for high-performance computation, however, this bottleneck is prospected to be further mitigated in the upcoming future.

In this work, the LBM is employed to model and simulate the two-phase transport through porous GDL microstructures. For this purpose, a preexisting in-house LB code [188] is adopted, which allows for multiphase flow simulations using the Color-Gradient model (CGM) [189, 190]. In the frame of the underlying thesis, the numerical framework is then extended by implementation of model improvements, as they have been developed in literature over the past years. Here, it is emphasized that actual theoretical development of new LB models is not part of this work, as the latter focuses on the investigation of capillary transport phenomena in GDLs by employment of preexisting multiphase models. In order to provide a sound theoretical basis for the subsequent studies of this work, the following sections of this chapter are dedicated to an in-depth description of the theoretical foundations of the LBM, the model formulations and the corresponding numerical scheme for single phase simulations. Then, a multiphase model (the Color-Gradient model (CGM) [189, 190]) is introduced and thoroughly validated in Section 3.2.5 before it will be later on utilized for the simulative studies on capillary flow phenomena of liquid water transport through porous GDL microstructures.

3.2 The Lattice Boltzmann method (LBM)

3.2.1 Fundamentals

A classical model for the description of the thermodynamic behavior of fluid systems is the kinetic theory of gases. One of the principal assumptions in this approach is that a fluid consists of many indistinguishable molecules. The state of such a system can be determined on the microscopic scale by tracking the motion of every single molecule. For a large number of particles, however, this becomes a tedious and beyond a certain point an even unfeasible endeavour. Thus, kinetic theory takes another path in modeling not discrete molecules but their distributions instead. The fundamental quantity in this mesoscale approach is the particle distribution function

$$f\left(\mathbf{x}, \boldsymbol{\xi}, t\right), \tag{3.1}$$

which represents a probability density for particle presence at a time t in 6-dimensional phase space, i.e., at position $\mathbf{x} = (x, y, z)$ and velocity $\boldsymbol{\xi} = (\xi_x, \xi_y, \xi_z)$. As the number of particles in the considered fluid systems is assumed to be very large, it is well justified that the overall system behavior can be described statistically. Thus, macroscopic properties such as density $\rho\left(\mathbf{x}, t\right)$ and velocity $\mathbf{u}\left(\mathbf{x}, t\right)$ can be recovered by statistical moments

$$\rho\left(\mathbf{x}, t\right) = \int f\left(\mathbf{x}, \boldsymbol{\xi}, t\right) \mathrm{d}^3\xi \tag{3.2}$$

$$\rho\left(\mathbf{x}, t\right) \mathbf{u}\left(\mathbf{x}, t\right) = \int \boldsymbol{\xi} f\left(\mathbf{x}, \boldsymbol{\xi}, t\right) \mathrm{d}^3\xi \tag{3.3}$$

of the distribution function. Whereas $f\left(\mathbf{x}, \boldsymbol{\xi}, t\right)$ represents the state of a fluid system, its temporal evolution is governed by the Boltzmann equation [191]:

$$\frac{\partial f}{\partial t} + \boldsymbol{\xi} \left(\frac{\partial f}{\partial \mathrm{x}}\right) + \frac{F}{m} \left(\frac{\partial f}{\partial \xi}\right) = \frac{\mathrm{d}f}{\mathrm{d}t} = \Omega\left(f\right) \tag{3.4}$$

In above formulation, the first two terms advect the distribution function with the particle velocity $\boldsymbol{\xi}$, which is in turn affected by the external forces F acting on the particles of mass m. The overall temporal evolution of f is balanced by a source term $\Omega\left(f\right)$, which accounts for particle collisions and is therefore generally referred to as the collision operator. Boltzmann originally derived an analytic solution for $\Omega\left(f\right)$ as a complex integro-differential form of equation (3.4). As can be shown by Chapman-Enskog expansion [192–194], the Boltzmann equation recovers the Navier-Stokes equations. In spite of originating in kinetic theory, this is in fact not solely valid for gases but in general for weakly compressible fluids as well.

In order to be able to predict fluid behavior, equation (3.4) has to be solved numerically, which requires discretization along its principal coordinates (t, $\mathbf{x}$, $\boldsymbol{\xi}$). In favor of introductory simplicity, however, this discretization is in the following demonstrated for the force-free Boltzmann equation:

$$\frac{\partial f}{\partial t} + \boldsymbol{\xi}\left(\frac{\partial f}{\partial \mathrm{x}}\right) = \Omega\left(f\right) \tag{3.5}$$

For the discretization of the Boltzmann equation in velocity space, the continuous distribution function f is replaced by a set of discrete distribution functions f_i

$$f\left(\mathbf{x}, \boldsymbol{\xi}, t\right) \Rightarrow \sum_{i=0}^{q-1} f_i\left(\mathbf{x}, \mathbf{c}_i, t\right) \tag{3.6}$$

for a limited number q of discrete velocities $\mathbf{c}_i = (\mathrm{c}_{ix}, \mathrm{c}_{iy}, \mathrm{c}_{iz})$. These velocity sets can vary in their spatial dimensionality d and number q of velocity directions, depending on the requirements for modeling accuracy. Categorized as DdQq, different models have been therefore developed in the past, such as D1Q3, D2Q9, D3Q15, D3Q19 and D3Q27. Among these, the most widely used velocity sets are the D2Q9 and D3Q19, whose connectivity vectors are illustrated in Figure 3.1.

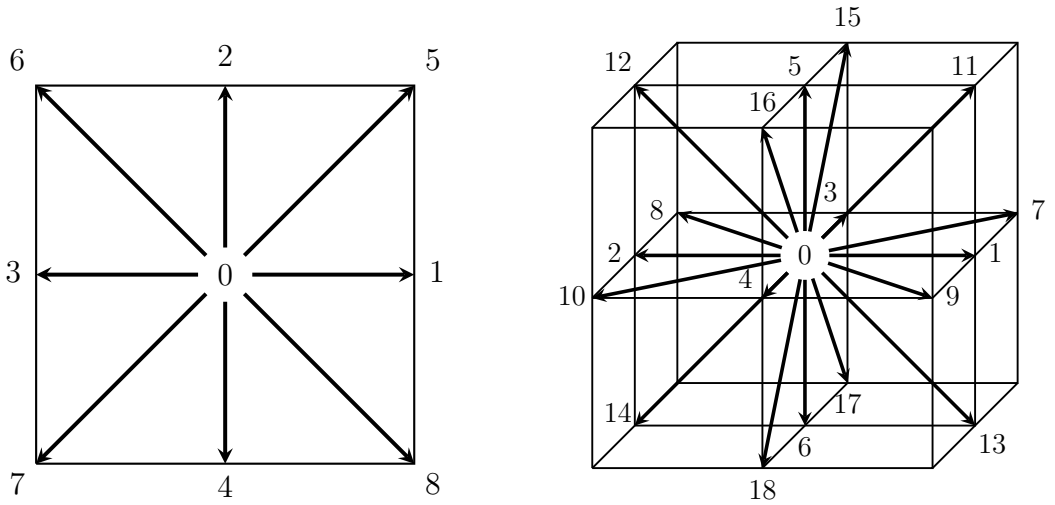

(a) D2Q9. (b) D3Q19.

Figure 3.1: Connectivity vectors on a lattice node for the most widely used DdQq velocity sets.

For any given velocity set, macroscopic properties are analogous to equations (3.2) and (3.3) obtained as statistical moments

$$\rho\left(\mathbf{x}, t\right) = \sum_{i=0}^{q-1} f_i\left(\mathbf{x}, \mathbf{c}_i, t\right) \tag{3.7}$$

$$\rho\left(\mathbf{x},t\right)\mathbf{u}\left(\mathbf{x},t\right)=\sum_{i=0}^{q-1}\mathbf{c}_i f_i\left(\mathbf{x},\mathbf{c}_i,t\right) \tag{3.8}$$

of the (now discrete) distribution functions f_i. In addition to the discretization in velocity space, the f_i can be furthermore discretized in physical space and time on square lattices. With a forward finite-difference scheme, the Lattice Boltzmann equation (LBE) can be then derived as an evolution equation for the f_i

$$\frac{f_i\left(\mathbf{x},t+\Delta t\right)-f_i\left(\mathbf{x},t\right)}{\Delta t}+c\frac{f_i\left(\mathbf{x}+\mathbf{c}_i\Delta t,t+\Delta t\right)-f_i\left(\mathbf{x},t+\Delta t\right)}{\Delta \mathrm{x}}=\Omega_i\left[f_i\left(\mathbf{x},t\right)\right] \tag{3.9}$$

on each individual lattice node. This approach of solving the Boltzmann equation on a lattice has been proposed by McNamara et al. [167], thereby extending the preexisting lattice-gas automaton (LGA) models [166]. With respect to the latter, however, the LBE has the advantage to not suffer from statistical noise. In equation (3.9), the resolution is defined on the spatial and temporal scale with $\Delta \mathrm{x}$ as the distance between neighboring lattice nodes and time increments of Δt. The constant $c={}^{\Delta \mathrm{x}}/_{\Delta t}$ sets the basic speed on the lattice and thus equation (3.9) can be further simplified to

$$f_i\left(\mathbf{x}+\mathbf{c}_i\Delta t,t+\Delta t\right)=f_i\left(\mathbf{x},t\right)+\Delta t\Omega_i\left[f_i\left(\mathbf{x},t\right)\right]. \tag{3.10}$$

According to above equation, the particle distributions $f_i\left(\mathbf{x},t\right)$ at lattice position $\mathbf{x}$ and time t first undergo a local collision step through $\Delta t\Omega_i\left(\mathbf{x},t\right)$. For this collision operator Ω_i, different approaches exist, of which the most simple was originally proposed by Bhatnagar, Gross and Krook (BGK) [195]:

$$\Omega_i^{\mathrm{BGK}}\left[f_i\left(\mathbf{x},t\right)\right]=\Omega_i^{\mathrm{SRT}}=-\frac{f_i\left(\mathbf{x},t\right)-{f_i}^{\mathrm{eq}}\left(\mathbf{x},t\right)}{\tau} \tag{3.11}$$

In above formulation, the distributions f_i are approaching local equilibrium in a given relaxation time τ. As the same time constant is assigned to all collision processes, the BGK operator is also commonly referred to as single relaxation time (SRT) operator. The local equilibrium distributions

$${f_i}^{\mathrm{eq}}\left(\mathbf{x},t\right)=\rho W_i\left[1+\frac{\mathbf{c}_i\cdot\mathbf{u}}{{c_s}^2}+\frac{\left(\mathbf{c}_i\cdot\mathbf{u}\right)^2}{2{c_s}^4}-\frac{\mathbf{u}\cdot\mathbf{u}}{2c_s^2}\right] \tag{3.12}$$

are Maxwellian distributions as derived from statistical mechanics [191] and under conservation of mass and momentum, i.e., $\rho=\rho^{\mathrm{eq}}$ and $\rho\mathbf{u}=\left(\rho\mathbf{u}\right)^{\mathrm{eq}}$. The lattice weights W_i are specific for the respective DdQq velocity set. c_s denotes the isothermal speed of sound with ${c_s}^2={}^{1}/_{3}\,{}^{\Delta x^2}/_{\Delta t^2}$ and is linked to the fluid pressure via

$$p = \rho c_s^2 \tag{3.13}$$

in the isothermal equation of state. According to Chapman-Enskog analysis [191], the relaxation time τ is furthermore linked with

$$\tau = \frac{\nu}{c_s^2} + \frac{\Delta t}{2} \tag{3.14}$$

to the kinematic viscosity ν of the fluid. In succession to the collision process, the distributions are streamed out in the direction $\mathbf{c}_i \Delta t$ to a neighboring lattice node at position $\mathbf{x} + \mathbf{c}_i \Delta t$ and time $t + \Delta t$. The streaming of the post-collision distributions is a linear operation on f_i and can be thus carried out subsequent to and independent of the collision process. The basic numerical scheme for the Lattice Boltzmann equation can be then summarized as two separate steps:

- Collision

$$f_i\left(\mathbf{x}, t^*\right) = f_i\left(\mathbf{x}, t\right) + \Delta t \Omega_i\left[f_i\left(\mathbf{x}, t\right)\right] \tag{3.15}$$

- Streaming

$$f_i\left(\mathbf{x} + \mathbf{c}_i \Delta t, t + \Delta t\right) = f_i\left(\mathbf{x}, t^*\right) \tag{3.16}$$

The fact that the collision operation can be conducted locally and independently on the individual lattices nodes makes above numerical scheme most suitable for massive parallelization. Over the last decades, this strength motivated the development of a multitude of different Lattice Boltzmann methods (LBM) for the modeling and simulation of fluid flows in various fields of application.

3.2.2 Single-phase LBM

Single relaxation time (SRT)

In this work, the Lattice Boltzmann method is employed for a D3Q19 model with the velocity set $\mathbf{c}$ (see Section 3.2.1) given as

$$\mathbf{c} = c \begin{pmatrix} 0 & 1 & -1 & 0 & 0 & 0 & 0 & 1 & -1 & 1 & -1 & 1 & -1 & 1 & -1 & 0 & 0 & 0 & 0 \\ 0 & 0 & 0 & 1 & -1 & 0 & 0 & 1 & 1 & -1 & -1 & 0 & 0 & 0 & 0 & 1 & -1 & 1 & -1 \\ 0 & 0 & 0 & 0 & 0 & 1 & -1 & 0 & 0 & 0 & 0 & 1 & 1 & -1 & -1 & 1 & 1 & -1 & -1 \end{pmatrix}. \tag{3.17}$$

In favor of numerical simplicity, it is in general convenient to switch from the standard physical SI unit system to an arbitrary system of lattice units. For this, conversion factors have to be defined, as will be described in more detail in Section 3.2.4. Following the most

common choice, the lattice spacing and the time step are set to $\Delta x = 1$ and $\Delta t = 1$ in this work. This simplifies the LBE from equation (3.10) further to

$$f_i\left(\mathbf{x} + \mathbf{c}_i, t+1\right) = f_i\left(\mathbf{x}, t\right) + \Omega_i\left[f_i\left(\mathbf{x}, t\right)\right]. \tag{3.18}$$

and the single relaxation time BGK operator (equation (3.11)) to

$$\Omega_i^{\mathrm{BGK}}\left[f_i\left(\mathbf{x}, t\right)\right] = \Omega_i^{\mathrm{SRT}} = -\frac{f_i\left(\mathbf{x}, t\right) - {f_i}^{\mathrm{eq}}\left(\mathbf{x}, t\right)}{\tau}. \tag{3.19}$$

For the D3Q19 lattice, the equilibrium distributions are given as

$${f_i}^{\mathrm{eq}}\left(\mathbf{x}, t\right) = \rho W_i\left[1 + 3\mathbf{c}_i \cdot \mathbf{u} + \frac{9}{2}\left(\mathbf{c}_i \cdot \mathbf{u}\right)^2 - \frac{3}{2}\mathbf{u} \cdot \mathbf{u}\right] \tag{3.20}$$

with an isothermal speed of sound $c_s = \sqrt{1/3}$ and the lattice-specific weights W_i

$$W_i = \begin{cases} 1/3 & i = 0 \\ 1/18 & i = 1...6 \\ 1/36 & i = 7...18 \end{cases}. \tag{3.21}$$

Multi relaxation time (MRT)

While the SRT operator convinces through simplicity, it comes along with deficiencies such as spurious velocities [196], a viscosity-dependent permeability [197] and limited numerical stability [177]. Depending on the case of application, it might be therefore also necessary to take a more sophisticated approach for the collision operator. In order to mitigate the shortcomings of the SRT, other operators have been developed in the past by employing different relaxation rates for different moments of the particle distributions. The general expression of such multiple relaxation time operators (MRT) requires a reformulation of equations (3.18) and (3.19) in vector notation

$$\boldsymbol{f}\left(\mathbf{x} + \mathbf{c}, t+1\right) = \boldsymbol{f}\left(\mathbf{x}, t\right) + \boldsymbol{\Omega}^{\mathrm{MRT}}\left[\boldsymbol{f}\left(\mathbf{x}, t\right)\right] \tag{3.22}$$

$$\boldsymbol{\Omega}^{\mathrm{MRT}}\left[\boldsymbol{f}\left(\mathbf{x}, t\right)\right] = -\mathbf{M}^{-1}\mathbf{K}\mathbf{M}\left[\boldsymbol{f}\left(\mathbf{x}, t\right) - \boldsymbol{f}^{\mathrm{eq}}\left(\mathbf{x}, t\right)\right]. \tag{3.23}$$

MRT operators are conceptually different to the SRT scheme, as not the fluid distributions $\boldsymbol{f} = \left(f_0, ..., f_{18}\right)^T$ themselves but their moments $\boldsymbol{m} = \left(m_0, ..., m_{18}\right)^T$ are relaxed towards local equilibrium. For this, a matrix $\mathbf{M}$ transforms the system from distribution space to moment space

$$\mathbf{M}\left[\boldsymbol{f}\left(\mathbf{x},t\right)-\boldsymbol{f}^{\mathrm{eq}}\left(\mathbf{x},t\right)\right]=\boldsymbol{m}\left(\mathbf{x},t\right)-\boldsymbol{m}^{\mathrm{eq}}\left(\mathbf{x},t\right) \tag{3.24}$$

in which the moments are then relaxed with the diagonal matrix $\mathbf{K}=\mathrm{diag}\left(\omega_0,...,\omega_{18}\right)$

$$\mathbf{K}\left[\boldsymbol{m}\left(\mathbf{x},t\right)-\boldsymbol{m}^{\mathrm{eq}}\left(\mathbf{x},t\right)\right]=\boldsymbol{m}\left(\mathbf{x},t^{*}\right)-\boldsymbol{m}^{\mathrm{eq}}\left(\mathbf{x},t^{*}\right), \tag{3.25}$$

according to the relaxation coefficients $\omega_i={}^{1}\!/_{\tau_i}$. The inverse $\mathbf{M}^{-1}$ eventually transforms the system back to distribution space

$$\mathbf{M}^{-1}\left[\boldsymbol{m}\left(\mathbf{x},t^{*}\right)-\boldsymbol{m}^{\mathrm{eq}}\left(\mathbf{x},t^{*}\right)\right]=\boldsymbol{f}\left(\mathbf{x},t^{*}\right)-\boldsymbol{f}^{\mathrm{eq}}\left(\mathbf{x},t^{*}\right). \tag{3.26}$$

For the construction of an invertible transformation matrix $\mathbf{M}$, researchers have commonly used a Hermite polynomial approach or the Gram-Schmidt procedure [191]. In the LBM community, the latter represents the more popular approach and was also employed by D'Humieres et al. [198], whose transformation matrix is adopted in this work with

$$\mathbf{M}=\begin{bmatrix}
1 & 1 & 1 & 1 & 1 & 1 & 1 & 1 & 1 & 1 & 1 & 1 & 1 & 1 & 1 & 1 & 1 & 1 & 1\\
-30 & -11 & -11 & -11 & -11 & -11 & -11 & 8 & 8 & 8 & 8 & 8 & 8 & 8 & 8 & 8 & 8 & 8 & 8\\
12 & -4 & -4 & -4 & -4 & -4 & -4 & 1 & 1 & 1 & 1 & 1 & 1 & 1 & 1 & 1 & 1 & 1 & 1\\
0 & 1 & -1 & 0 & 0 & 0 & 0 & 1 & -1 & 1 & -1 & 1 & -1 & 1 & -1 & 0 & 0 & 0 & 0\\
0 & -4 & 4 & 0 & 0 & 0 & 0 & 1 & -1 & 1 & -1 & 1 & -1 & 1 & -1 & 0 & 0 & 0 & 0\\
0 & 0 & 0 & 1 & -1 & 0 & 0 & 1 & 1 & -1 & -1 & 0 & 0 & 0 & 0 & 1 & -1 & 1 & -1\\
0 & 0 & 0 & -4 & 4 & 0 & 0 & 1 & 1 & -1 & -1 & 0 & 0 & 0 & 0 & 1 & -1 & 1 & -1\\
0 & 0 & 0 & 0 & 0 & 1 & -1 & 0 & 0 & 0 & 0 & 1 & 1 & -1 & -1 & 1 & 1 & -1 & -1\\
0 & 0 & 0 & 0 & 0 & -4 & 4 & 0 & 0 & 0 & 0 & 1 & 1 & -1 & -1 & 1 & 1 & -1 & -1\\
0 & 2 & 2 & -1 & -1 & -1 & -1 & 1 & 1 & 1 & 1 & 1 & 1 & 1 & 1 & -2 & -2 & -2 & -2\\
0 & -4 & -4 & 2 & 2 & 2 & 2 & 1 & 1 & 1 & 1 & 1 & 1 & 1 & 1 & -2 & -2 & -2 & -2\\
0 & 0 & 0 & 1 & 1 & -1 & -1 & 1 & 1 & 1 & 1 & -1 & -1 & -1 & -1 & 0 & 0 & 0 & 0\\
0 & 0 & 0 & -2 & -2 & 2 & 2 & 1 & 1 & 1 & 1 & -1 & -1 & -1 & -1 & 0 & 0 & 0 & 0\\
0 & 0 & 0 & 0 & 0 & 0 & 0 & 1 & -1 & -1 & 1 & 0 & 0 & 0 & 0 & 0 & 0 & 0 & 0\\
0 & 0 & 0 & 0 & 0 & 0 & 0 & 0 & 0 & 0 & 0 & 0 & 0 & 0 & 0 & 1 & -1 & -1 & 1\\
0 & 0 & 0 & 0 & 0 & 0 & 0 & 0 & 0 & 0 & 0 & 1 & -1 & -1 & 1 & 0 & 0 & 0 & 0\\
0 & 0 & 0 & 0 & 0 & 0 & 0 & 1 & -1 & 1 & -1 & -1 & 1 & -1 & 1 & 0 & 0 & 0 & 0\\
0 & 0 & 0 & 0 & 0 & 0 & 0 & -1 & -1 & 1 & 1 & 0 & 0 & 0 & 0 & 1 & -1 & 1 & -1\\
0 & 0 & 0 & 0 & 0 & 0 & 0 & 0 & 0 & 0 & 0 & 1 & 1 & -1 & -1 & -1 & -1 & 1 & 1
\end{bmatrix}. \tag{3.27}$$

Since some of the distribution moments represent conserved quantities, they don't have to be considered in the MRT scheme, because they are already in equilibrium, i.e., $m_i=m_i{}^{\mathrm{eq}}$. This applies to the density $m_0=\rho$ and the momentum fluxes $m_3=\rho u_x$, $m_5=\rho u_y$, $m_7=\rho u_z$ in the respective spatial directions. The relaxation matrix $\mathbf{K}$ is then simplified to

$$\mathbf{K} = \mathrm{diag}\left(0, \omega_1, \omega_2, 0, \omega_4, 0, \omega_6, 0, \omega_8, \omega_9, \omega_{10}, \omega_{11}, \omega_{12}, \omega_{13}, \omega_{14}, \omega_{15}, \omega_{16}, \omega_{17}, \omega_{18}\right). \quad (3.28)$$

For all nonzero coefficients, different sets can be found in literature. In this work, the choice of Pan et al. [197] is adopted with

$$\omega_9 = \omega_{11} = \omega_{13} = \omega_{14} = \omega_{15} = 1/\tau, \quad (3.29)$$

which is the same as for the BGK operator (see eq. (3.14)). At this point, it is worth noting that assignment of $\omega_i = 1/\tau$ to all coefficients would turn the MRT operator into the SRT operator, as only one single relaxation time would be used for all moments m_i and hence all distribution functions f_i. For the remaining coefficients ($i \in [1, 2, 4, 6, 8, 10, 12, 16, 17, 18]$), the entries are defined as

$$\omega_i = 8\frac{(2-\omega_9)}{(8-\omega_9)}. \quad (3.30)$$

The MRT operator provides numerical stability as well as modeling accuracy superior to the SRT operator. In spite of numerically efficient implementations, however, it also comes along with a computational overhead of at least 15 to 20 % [177, 198], as compared to the simple BGK formulation. Depending on the case of application, it is therefore advisable to assess, if the MRT collision operator is required, as it comes with a higher computational expense. In this work, the MRT operator is solely employed for validation purposes in the frame of test cases.

To this point, all above derivations are made under the assumption of a force-free Boltzmann equation (3.5). In the general case, however, it is of interest to include external forces such as gravity as well. Starting from the full Boltzmann equation (3.4) and following a similar discretization route as presented in Section 3.2.1, LBM formulations can be derived for the inclusion of forces. In the general case, the presence of an external force leads to an additional source term in equation (3.23), resulting in

$$\boldsymbol{f}\left(\mathbf{x} + \mathbf{c}, t+1\right) = \boldsymbol{f}\left(\mathbf{x}, t\right) + \boldsymbol{\Omega}^{\mathrm{MRT}}\left[\boldsymbol{f}\left(\mathbf{x}, t\right)\right] + \boldsymbol{F}. \quad (3.31)$$

In the past, different formulations have been developed for $\boldsymbol{F}$, as comprehensively reviewed by Krueger et al. [191]. In this work, external forces are only considered in the form of gravity and exclusively for validation purposes. According to Leclaire et al. [199], a gravitational force

$$\boldsymbol{F}_G = \mathbf{M}^{-1}\Delta\boldsymbol{m}. \quad (3.32)$$

can be modeled with an additional term $\Delta \boldsymbol{m}$, in which the only nonzero entries correspond to the momenta along the three spatial dimensions. For the D3Q19 lattice, the nonzero entries are thus given as

$$\Delta m_3 = \rho \mathrm{u}_x = \rho g_x, \tag{3.33}$$

$$\Delta m_5 = \rho \mathrm{u}_y = \rho g_y, \tag{3.34}$$

$$\Delta m_7 = \rho \mathrm{u}_z = \rho g_z \tag{3.35}$$

with $\boldsymbol{g} = (g_x, g_y, g_z)^T$ as the gravitational acceleration. For the single-phase D3Q19 Lattice Boltzmann model, the numerical scheme is then again summarized as a collision step

$$f_i(\mathbf{x}, t^*) = f_i(\mathbf{x}, t) + \Omega_i [f_i(\mathbf{x}, t)] \tag{3.36}$$

followed by a streaming step

$$f_i(\mathbf{x} + \mathbf{c}_i, t + 1) = f_i(\mathbf{x}, t^*). \tag{3.37}$$

Boundary conditions

In pore-scale modeling, two types of boundary conditions have to be considered:

- Internal boundary conditions for the fluid-solid interactions near solid surfaces.
- External boundary conditions for the borders of the computational domain.

In the former case, it is common to model solid surfaces as impermeable by employing a no-slip condition. For this, bounce-back schemes are usually implemented, in which particle distributions f_i are bounced back from a solid surface

$$f_{\tilde{i}} = f_i \tag{3.38}$$

in the opposite direction $\mathbf{c}_{\tilde{i}} = -\mathbf{c}_i$. In the most common approaches, the actual fluid-solid interface is assumed to be located halfway between a fluid and a solid lattice node. In recent years, however, more sophisticated approaches with complex interpolation schemes have been developed as well [191, 200, 201]. In this work, the halfway bounce-back scheme [202] is employed due to its simplicity. As the fluid-solid interfaces are located halfway between the respective fluid and solid lattice nodes, fluid particles are bounced back and streamed back into the opposite direction within the same time step. In the numerical scheme, the bounce-back is thus carried out after the collision step (equation (3.36)) and

before the streaming step (equation (3.37)). An illustration of the halfway bounce-back scheme for the D2Q9 lattice is provided in Figure 3.2. With equation (3.38), the *a priori* unknown particle distributions are then obtained as $f_2 = f_4$, $f_5 = f_7$ and $f_6 = f_8$.

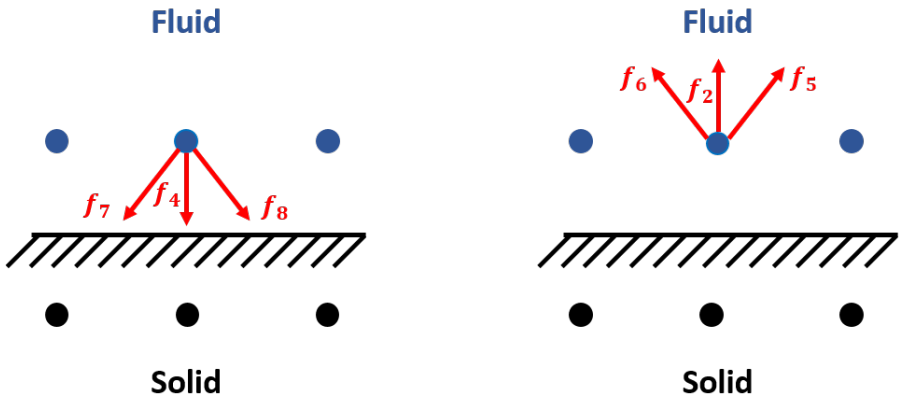

(a) Pre collision. (b) Post collision.

Figure 3.2: Halfway bounce-back scheme as internal boundary condition to account for fluid-solid interactions in LB simulations (D2Q9 lattice). Fluid distributions f_i which move from a fluid node towards solid surface nodes are bounced back in the opposite direction. In this no-slip condition, the fluid-solid interface is located halfway between the respective fluid and solid surface nodes. (Illustration inspired by T. Danner [188]).

Since the borders of the computational domain are finite and *a priori* undefined, external boundary conditions are required to obtain a physically determined system. In the simplest case, this can be achieved by periodic boundary conditions, in which the borders of the computational domain are extended by periodic images of itself. In this setup, fluid portions leave the domain at one border and reenter the system at the opposite end, resulting in a virtually borderless domain. However, caution is advised and a sufficiently large system size has to be selected in order to prevent correlated fluid interaction across opposite domain borders. Even though periodic boundary conditions ensure a determined and numerically stable system, applicability to different use cases is very limited. However, many applications require the definition of flow conditions at the boundaries, e.g., by imposing a specific fluid pressure or velocity at a domain boundary. One of the most widely used approaches for such boundary conditions was originally proposed by Zou and He [203] for the D2Q9 and the D3Q15 lattice. Later on, Hecht and Harting [204] extended and generalized the approach to the D3Q19 lattice. In the following, this boundary condition is described for a bottom boundary node at $z = 0$, as shown in Figure 3.3.

At this point, it is noted that the subscripts of the f_i in the subsequent paragraphs are different to Hecht and Harting [204], as this work uses a different column order in the velocity set $\mathbf{c}$ (equation (3.17)). In each time step, distributions are streamed across the

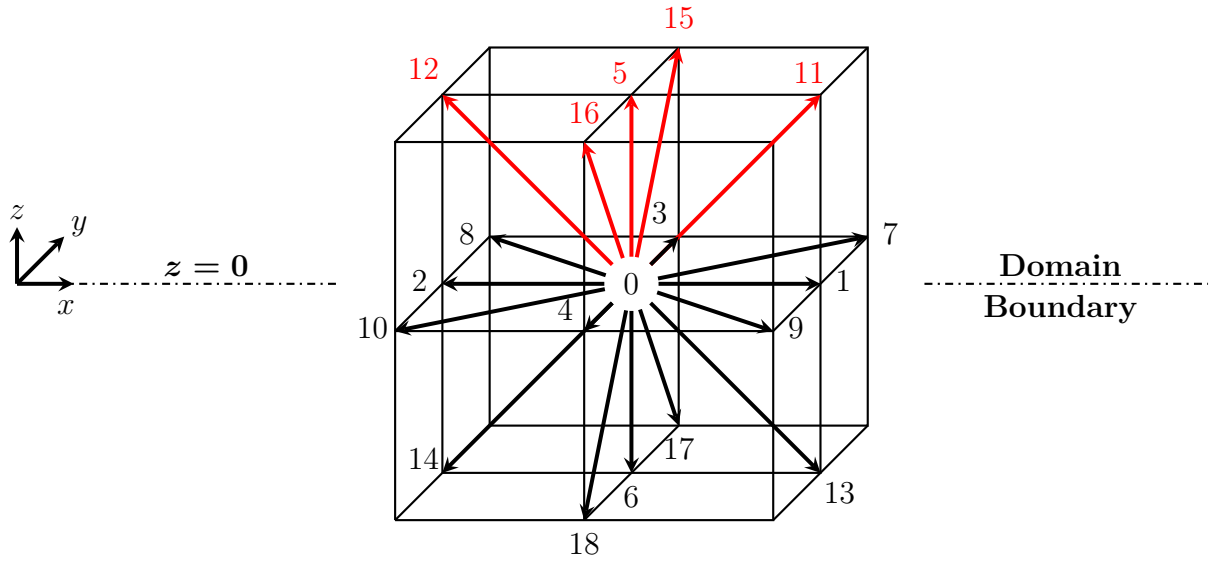

Figure 3.3: Schematic illustration of a bottom boundary node in the D3Q19 lattice at $z = 0$. As the in-streaming particle distributions (red) are in each time step *a priori* unknown, they have to be defined in a reasonable way, e.g., by an external boundary condition.

boundary, either out or into the system. In the former case, these distributions are known, as they are advected from adjacent lattice nodes within the domain. The distributions f_5, f_9, f_{13} and f_{15} are on the other hand undetermined, as they enter the domain via the boundary. In order to determine these unknown distributions, assumptions have to be made and further equations are needed. Starting point for the derivation of Zou and He's formulae are the equations for mass (eq. (3.7))

$$\rho = \sum_{i=0}^{q-1} f_i \tag{3.39}$$

and momentum balance (eq. (3.8))

$$\rho u_x = \sum_{i=0}^{q-1} e_{ix} f_i = f_1 + f_7 + f_9 + f_{11} + f_{13} - (f_2 + f_8 + f_{10} + f_{12} + f_{14}) \tag{3.40}$$

$$\rho u_y = \sum_{i=0}^{q-1} e_{iy} f_i = f_3 + f_7 + f_8 + f_{15} + f_{17} - (f_4 + f_9 + f_{10} + f_{16} + f_{18}) \tag{3.41}$$

$$\rho u_z = \sum_{i=0}^{q-1} e_{iz} f_i = f_5 + f_{11} + f_{12} + f_{15} + f_{16} - (f_6 + f_{13} + f_{14} + f_{17} + f_{18}) \tag{3.42}$$

in all three spatial dimensions. By fixing the tangential velocities (u_x, u_y) and combining equations (3.39) and (3.42), the velocity normal to the boundary plane is then given as

$$u_z = 1 - \frac{1}{\rho}\left[f_1 + f_2 + f_3 + f_4 + f_7 + f_9 + f_8 + f_{10} + f_0 + 2(f_6 + f_{13} + f_{14} + f_{17} + f_{18})\right]. \tag{3.43}$$

With the density ρ as an input parameter, above equation can be employed to impose a Neumann pressure boundary condition (see eq. (3.13) for the link between density and pressure). When instead a Dirichlet flux boundary condition is desired, equation (3.43) can be rewritten to

$$\rho = \frac{1}{1 - u_z}\left[f_1 + f_2 + f_3 + f_4 + f_7 + f_9 + f_8 + f_{10} + f_0 + 2(f_6 + f_{13} + f_{14} + f_{17} + f_{18})\right]. \tag{3.44}$$

in order to set a flow velocity u_z normal to the boundary plane. In both equations (3.43) and (3.43), the unknown distributions f_5, f_{11}, f_{12}, f_{15}, and f_{16} pointing into the domain do not appear. Nonetheless, these have to be specified, which leads to the requirement of additional equations.

Therefore, Hecht and Harting followed Zou and He by assuming that the non-equilibrium part $f_i^* = f_i - f_i^{\mathrm{eq}}$ of each particle distribution f_i is bounced back in the opposite direction $\mathbf{c}_{-i} = -\mathbf{c}_i$ at the boundary plane. With $f_i^* = f_{-i}^*$ and equation (3.12), 5 more equations are obtained

$$f_5 = f_6 + \frac{2W_5}{c_s^2}\rho u_z \tag{3.45}$$

$$f_{11} = f_{14} + \frac{2W_9}{c_s^2}\rho\left(u_z + u_x\right) \tag{3.46}$$

$$f_{12} = f_{13} + \frac{2W_{13}}{c_s^2}\rho\left(u_z - u_x\right) \tag{3.47}$$

$$f_{15} = f_{18} + \frac{2W_{15}}{c_s^2}\rho\left(u_z + u_y\right) \tag{3.48}$$

$$f_{16} = f_{17} + \frac{2W_{17}}{c_s^2}\rho\left(u_z - u_y\right). \tag{3.49}$$

In order to correct transverse momentum contributions in the $x-$ and $y-$direction, the additional terms N_x^z and N_y^z are added to equations (3.46)-(3.49). With the parameters specific for the D3Q19 lattice, above equations are then rewritten to

$$f_5 = f_6 + \frac{\rho}{6}\rho u_z \tag{3.50}$$

$$f_{11} = f_{14} + \frac{\rho}{6}\left(u_z + u_x\right) - N_x^z \tag{3.51}$$

$$f_{12} = f_{13} + \frac{\rho}{6}(u_z - u_x) + N_x^z \tag{3.52}$$

$$f_{15} = f_{18} + \frac{\rho}{6}(u_z + u_y) - N_y^z \tag{3.53}$$

$$f_{16} = f_{17} + \frac{\rho}{6}(u_z - u_y) + N_y^z. \tag{3.54}$$

The transverse momentum corrections can be furthermore derived by combining equations (3.51)-(3.54) with the momentum balances in the equations (3.40) and (3.41):

$$N_x^z = \frac{1}{2}\left[f_1 + f_7 + f_9 - (f_2 + f_8 + f_{10})\right] - \frac{1}{3}\rho u_x \tag{3.55}$$

$$N_y^z = \frac{1}{2}\left[f_3 + f_7 + f_8 - (f_4 + f_9 + f_{10})\right] - \frac{1}{3}\rho u_y \tag{3.56}$$

At this point, the set of equations is complete and all unknown particle distributions f_5, f_{11}, f_{12}, f_{15} and f_{16} can be determined. By definition of a tangential vector $\mathbf{t}_i = \mathbf{c}_i - (\mathbf{c}_i \cdot \mathbf{n})\,\mathbf{n}$ perpendicular to the normal vector $\mathbf{n}$ of the boundary plane, the unknown distributions can be lastly denoted in a generalized form

$$f_{-i} = f_i - \frac{\rho}{6}\mathbf{c}_i \cdot \mathbf{u} - \frac{\rho}{3}\mathbf{t}_i \cdot \mathbf{u} + \frac{1}{2}\sum_{j=0}^{18} f_j\,(\mathbf{t}_i \cdot \mathbf{c}_j)\,(1 - |\mathbf{c}_j \cdot \mathbf{n}|) \tag{3.57}$$

for all boundary planes.

3.2.3 Multiphase LBM - The color-gradient model

Modeling and simulation of multiphase flows is in general a challenging task, as the fluid behavior is governed by intra- and interphase interactions. This endeavour is even more difficult, when the flows occur on the pore scale where complex geometries have to be considered. Many conventional CFD simulation techniques are not suitable for microstructure-resolved simulations. However, LBM has proved to be very advantageous for PSM applications, owing to the applicability of the computational lattice domain to arbitrary geometries. Over the past decades, different multiphase LB methods have been therefore developed.

Based on the original work of Rothman and Keller [189] for lattice gases, the first multiphase LB model for two immiscible fluids was proposed in 1991 by Gunstensen et al. [190]. In this RK model or color-gradient model (CGM), two fluids are distinguished as of different color. In order to account for interactions between the two fluid phases, a color-gradient is defined. Surface tension and immiscibility are then modeled in employing a perturbation and a recoloring operator. The CGM offers several advantages such as local conservation of mass and momentum and independently adjustable fluid properties, e.g., surface tension, density and viscosity ratios [205]. However, one of the drawbacks is

that the CGM does in general not provide galilean invariance and correction terms have to be added when unequal phase densities are considered [206]. In 1993, Shan and Chen [207, 208] introduced the pseudopotential or SC model, in which an inter-particle potential is employed to account for fluid interactions. As surface tension and phase separation arise directly from the potential, the fluid interface does not have to be tracked. Owing to this simplicity, the SC model is computationally efficient and has thus become quite popular. However, not all fluid properties can be chosen independently and the basic approach suffers amongst others also from thermodynamic inconsistency and large spurious currents. Furthermore, the potential has to be calibrated *a priori* in numerical experiments in order to achieve the desired surface tension [209]. Swift et al. [210, 211] presented in 1995 the free-energy model (FEM), in which a free energy functional is utilized to model interfacial dynamics and phase separation. Advantages of the FEM are a thermodynamic consistent formulation and the local conservation of mass and momentum. Similar to the CGM, however, the original formulation also lacks in galilean invariance [174]. The phase-field (or mean-field) model was proposed in 1999 by He et al. [212]. In this model, two distribution functions are utilized to recover the Navier-Stokes equation and to establish phase separation. In order to track the interface location, an order parameter is introduced, whose evolution is governed by the Cahn-Hilliard equation [213, 214]. While convincing through robustness, this model also requires calibration of certain parameters similar to the SC model [215].

In this work, multiphase flow of two immiscible fluids is modeled using the color-gradient model on account of its aforementioned strengths. Originating from the formulations of Gunstensen et al. [190], the CGM benefited over the last decades from several major improvements. In 1993, Grunau et al. [216] extended the model to allow for variable density and viscosity ratios. As the original perturbation operator by Gunstensen et al. [190] did not recover the macroscopic capillary stress tensor correctly, Reis and Philips [217] proposed a new approach for the D2Q9 lattice. Later on, Liu et al. [218] generalized the modified operator to threedimensional lattices. Suffering from numerical artifacts such as lattice pinning and spurious currents in vicinity of the fluid-fluid interface, the original recoloring operator was reworked by Tölke [219], Latva-Kokko and Rothman [220] and Leclaire et al. [221]. Moreover, higher-order isotropic discretization schemes for the calculation of the color-gradient have been found to reduce parasitic currents significantly [222–225]. By increasing the local lattice resolution near the fluid-fluid interface with a grid refinement method, Leclaire et al. [226] were also able to suppress spurious currents even further.

As a result of aforementioned improvements, the CGM demonstrated in recent years to provide good physical accuracy and numerical stability in comparison to other common

Lattice Boltzmann methods [134, 227, 228]. In particular the introduction of MRT operators was observed to increase numerical robustness significantly, allowing for density ratios up to $\mathcal{O}(1000)$ [226, 229–231] and viscosity ratios up to $\mathcal{O}(100)$ [226, 232] for simpler numerical test cases. Employing higher-order isotropic discretization schemes, Leclaire et al. [225] even achieved a density ratio of $\mathcal{O}(10,000)$ for a steady bubble with low surface tension. However, most of such studies were limited to 2D test cases and simple geometries, as application of high density and viscosity ratios to complex 3D porous microstructures is still a challenging task [233]. However, depending on the flow regime this is also not strictly necessary, as will be discussed in Section 4.3.3 and shown in Section 4.4.5. The color-gradient model employed in this work is adopted from the publication by Leclaire et al. [199], mainly incorporating the model improvements by Liu et al. [218], Tölke [219] and Latva-Kokko and Rothman [220].

Single-phase collision

In the CGM, two phases are modeled as fluids of red (r) and blue (b) color

$$f_i(\mathbf{x},t) = {f_i}^r(\mathbf{x},t) + {f_i}^b(\mathbf{x},t)\,. \tag{3.58}$$

The location of the fluid-fluid interface is furthermore described by a phase-field parameter

$$\varphi(\mathbf{x},t) = \frac{\rho_r(\mathbf{x},t) - \rho_b(\mathbf{x},t)}{\rho_r(\mathbf{x},t) + \rho_b(\mathbf{x},t)} \tag{3.59}$$

with $\rho_k = \sum_i f_i^k$ as the fluid density of phase k. In analogy to the single-phase formulation in equation (3.36), both of the fluids first undergo single-phase collisions

$$f_i^k(\mathbf{x},t^*) = f_i^k(\mathbf{x},t) + \Omega_i^{k,1}\left[f_i^k(\mathbf{x},t)\right] \tag{3.60}$$

in each time step, driving the respective phases towards their local equilibrium.

With respect to the single-phase case (eq. (3.20)), the equilibrium distributions in the two-fluid system have to be slightly modified to

$${f_i}^{k,\mathrm{eq}} = \rho_k\left[\phi_i^k + W_i\left(1 + 3\mathbf{c}_i\cdot\mathbf{u} + \frac{9}{2}(\mathbf{c}_i\cdot\mathbf{u})^2 - \frac{3}{2}\mathbf{u}\cdot\mathbf{u}\right)\right] + \Phi_i^k \tag{3.61}$$

where $\mathbf{u}$ corresponds to the system velocity, according to equation (3.8) and the overall density $\rho = \rho_r + \rho_b$. The parameter ϕ_i^k accounts for the compressibility of the k-th fluid

$$\phi_i^k = \begin{cases} \alpha_k & i = 0 \\ (1-\alpha_k)/12 & i = 1...6 \\ (1-\alpha_k)/24 & i = 7...18 \end{cases} \tag{3.62}$$

where α_k is linked to the isothermal speed of sound c_s^k and the phase pressure p_k via

$$p_k = \rho_k \frac{1}{2}(1-\alpha_k) = \rho_k \left(c_s^k\right)^2. \tag{3.63}$$

In order to assure a stable interface, the initial phase pressures have to be equal, i.e., $p_r^0 = p_b^0$. Hence, the condition

$$\gamma = \frac{\rho_r^0}{\rho_b^0} = \frac{1-\alpha_b}{1-\alpha_r} \tag{3.64}$$

must be fulfilled depending on the ratio γ of the initial fluid densities ρ_k^0 [216]. Thus, only one α_k is a free parameter. Following Leclaire et al. [199], the blue fluid is defined as the least dense and the free parameter is set to $\alpha_b = W_0$. With this choice, the relation $0 < \alpha_b \leq \alpha_r < 1$ is respected in order to prevent the occurrence of negative pressures.

As can be shown by Chapman-Enskog expansion, the LBE provides *per se* no galilean invariance due to an unphysical velocity-dependent viscosity [175, 176, 234]. However, a correction term Φ_i^k can be added to mitigate this shortcoming. Based on the works of Holdych et al. [175], such a correction term was introduced by Leclaire et al. [232] for the D2Q9 lattice and later formulated in a generalized form [199] to

$$\Phi_i^k = \bar{\nu}\left[\psi_i \left(\mathbf{u} \cdot \nabla \rho_k\right) + \zeta_i \left(\mathbf{G} : \mathbf{c}_i \otimes \mathbf{c}_i\right)\right] \tag{3.65}$$

with

$$\mathbf{G} = \left(\mathbf{u} \cdot \nabla \rho_k\right) + \left(\mathbf{u} \cdot \nabla \rho_k\right)^T \tag{3.66}$$

for the tensor product $\otimes$ and the tensor contraction ':'. The lattice-dependent weights are given as

$$\psi_i = \begin{cases} -5/2 & i = 0 \\ -1/6 & i = 1...6 \\ 1/24 & i = 7...18 \end{cases} \tag{3.67}$$

and

$$\zeta_i = \begin{cases} 0 & i = 0 \\ 1/4 & i = 1...6 \\ 1/8 & i = 7...18 \end{cases} . \tag{3.68}$$

According to Leclaire et al. [235], above formulation improves galilean invariance by rendering the lower-order error terms of the Chapman-Enskog expansion independent of density variation. In the case of equal phase densities, the correction term Φ_i^k vanishes.

In addition to the densities, also the kinematic viscosities ν_k of the respective fluid phases are in general unequal. This leads to the requirement of defining an effective kinematic viscosity $\bar{\nu}$ and consequently an effective relaxation parameter (see eq. (3.14))

$$\tau_{\text{eff}} = 3\bar{\nu} + \frac{1}{2}. \tag{3.69}$$

In the bulk of the respective phases k, the effective kinematic viscosity is simply given as $\bar{\nu} = \nu_k$. Throughout the multiphase region near the fluid-fluid interface, on the other hand, an averaging scheme has to be employed to ensure a smooth transition from ν_r to ν_b and vice-versa. For this, different formulae have been developed, of which a harmonic density-averaged viscosity

$$\bar{\nu} = \left(\sum_k \frac{\rho_k}{\rho \nu_k} \right)^{-1} \tag{3.70}$$

is one of the most widely used due to its simplicity. A more sophisticated approach was proposed by Grunau et al. [216], in which the relaxation time (instead of the viscosity)

$$\tau_{\text{eff}} = \begin{cases} \tau_r, & \varphi > \delta, \\ g_r(\varphi), & \delta \geq \varphi > 0, \\ g_b(\varphi), & 0 \geq \varphi \geq -\delta, \\ \tau_b, & \varphi < -\delta, \end{cases} \tag{3.71}$$

is interpolated along the interface position given by φ. In order to recover the single-phase viscosity in the bulk of the respective phases, the relaxation time is set to $\tau_{\text{eff}} = \tau_k$ for $|\varphi| > \delta$, with the thickness of the interphase region controlled by the free parameter $0 \leq \delta \leq 1$. In the two-phase region ($|\varphi| \leq \delta$), two quadratic functions

$$g_r(\varphi) = \alpha + \beta\varphi + \kappa\varphi^2 \tag{3.72}$$

$$g_b(\varphi) = \alpha + \beta\varphi + \xi\varphi^2. \tag{3.73}$$

are utilized. A smooth transition from one bulk region to the other is furthermore established under the constraints of $g_r(\delta) = \tau_r$, $g_b(-\delta) = \tau_b$, $\partial\tau/\partial\varphi = 0$ for $|\varphi| = \delta$ and $g_r(0) = g_b(0) = \langle\tau\rangle$. The remaining parameters are then derived as

$$\alpha = 2\tau_r\tau_b/(\tau_r + \tau_b) \tag{3.74}$$

$$\beta = 2(\tau_r - \alpha)/\delta \tag{3.75}$$

$$\kappa = -\beta/(2\delta) \tag{3.76}$$

$$\xi = \eta/(2\delta) \tag{3.77}$$

with the harmonic average $\langle\tau\rangle = 2\tau_r\tau_b/(\tau_r + \tau_b)$.

Perturbation - Two-phase collision

In succession to the single-phase collisions, the distributions of the two fluids undergo inter-phase collisions as well. In the CGM, these multiphase events are realized in a two-step approach. First, surface tension is generated at the fluid-fluid interface by utilization of a perturbation operator [190, 217]

$$f_i^k(\mathbf{x}, t^{**}) = f_i^k(\mathbf{x}, t^*) + \Omega_i^{k,2}\left[f_i^k(\mathbf{x}, t^*)\right] \tag{3.78}$$

$$\Omega_i^{k,2}\left[f_i^k(\mathbf{x}, t^*)\right] = A_k|\mathbf{F}|\left[W_i\frac{(\mathbf{F}\cdot\mathbf{c}_i)^2}{|\mathbf{F}|^2} - B_i\right] \tag{3.79}$$

in which the orientation of the interface is approximated by

$$\mathbf{F} = \nabla\varphi = \nabla\left(\frac{\rho_r - \rho_b}{\rho_r + \rho_b}\right). \tag{3.80}$$

This color-gradient $\mathbf{F}$ can be calculated with different discretization schemes, which reduce spurious currents for increasing orders of isotropy. However, they also result in higher computational loads [223, 224]. In this work, a fourth-order isotropic discretization scheme [225] is employed with

$$\nabla\varphi = 3\sum_{i=0}^{18} W_i\mathbf{c}_i\varphi(\mathbf{x} + \mathbf{c}_i). \tag{3.81}$$

In the perturbation operator, a link to the surface tension is then established via

$$\sigma = \frac{2}{9}(A_r + A_b)\tau_{\text{eff}} \tag{3.82}$$

and the free parameters A_k, which are set as equal in this work, i.e., $A_r = A_b$. The weights B_i [217, 218] are lattice-dependent and are chosen to conserve mass and to recover the Navier-Stokes equations with

$$B_i = \begin{cases} -2/9 & i = 0 \\ 1/54 & i = 1...6 \\ 1/27 & i = 7...18 \end{cases} . \tag{3.83}$$

Recoloring - Two-phase collision

The perturbation operator redistributes the phases perpendicular to the fluid-fluid interface, but does not guarantee phase immiscibility. Thus, in a second multiphase collision step, a recoloring operator [220, 221] has to be employed with

$$f_i^r\left(\mathbf{x}, t^{***}\right) = \frac{\rho_r}{\rho} f_i\left(\mathbf{x}, t^{**}\right) + \beta \frac{\rho_r \rho_b}{\rho^2} \cos\left(\vartheta_i\right) f_i^{\mathrm{eq}}\left(\mathbf{x}_{\mathbf{u}=0}, t\right) \tag{3.84}$$

$$f_i^b\left(\mathbf{x}, t^{***}\right) = \frac{\rho_b}{\rho} f_i\left(\mathbf{x}, t^{**}\right) - \beta \frac{\rho_r \rho_b}{\rho^2} \cos\left(\vartheta_i\right) f_i^{\mathrm{eq}}\left(\mathbf{x}_{\mathbf{u}=0}, t\right) . \tag{3.85}$$

In the above two equations, $f_i = \sum_k f_i^k$ and $f_i^{\mathrm{eq}} = \sum_k f_i^{k,\mathrm{eq}}$ denote the color-blind distribution functions and their equilibrium states. The latter are determined for a resting fluid-fluid interface with a net velocity of $\mathbf{u} = 0$. The angle ϑ_i is spanned between the vectors of the color-gradient $\mathbf{F}$ and the lattice velocity direction $\mathbf{c}_i$ and the parameter β controls the thickness of the fluid-fluid interface.

In the streaming step, the new distributions of both fluid phases are lastly propagated to the lattice neighbors and similar to equation (3.16)

$$f_i^k\left(\mathbf{x} + \mathbf{c}_i \Delta t, t + \Delta t\right) = f_i^k\left(\mathbf{x}, t^{***}\right) . \tag{3.86}$$

The numerical scheme can then be eventually summarized as follows:

- Single-phase collision

$$f_i\left(\mathbf{x}, t^*\right) = f_i\left(\mathbf{x}, t\right) + \Omega^1\left[f_i\left(\mathbf{x}, t\right)\right] \tag{3.87}$$

- Two-phase collision (Perturbation)

$$f_i\left(\mathbf{x}, t^{**}\right) = f_i\left(\mathbf{x}, t^*\right) + \Omega^2\left[f_i\left(\mathbf{x}, t^*\right)\right] \tag{3.88}$$

- Two-phase collision (Recoloring)

$$f_i\left(\mathbf{x}, t^{***}\right) = f_i\left(\mathbf{x}, t^{**}\right) + \Omega^3\left[f_i\left(\mathbf{x}, t^{**}\right)\right] \tag{3.89}$$

- Streaming

$$f_i^k\left(\mathbf{x}+\mathbf{c}_i\Delta t, t+\Delta t\right) = f_i^k\left(\mathbf{x}, t^{***}\right). \tag{3.90}$$

Wetting boundary condition

As introduced in Section 2.2.4, the contact angle θ is a measure for the tendency of fluids to wet a solid surface. Depending on their interaction strength with the solid surface, fluids might thus experience either attractive or repulsive forces at the threephase contact line. In order to recover capillary phenomena appropriately in PSM simulations, fluid-solid interactions and thus contact angles have to be therefore modeled accurately. At this point, it is noted that the contact angle θ is in the modeling part of this work understood and defined as the static equilibrium contact angle θ^{eq} being a solid material property, i.e., $\theta = \theta^{\mathrm{eq}}$. In contrast to other studies, contact angle hysteresis is therefore not modeled explicitly but is expected to emerge from the simulations. In order to better understand this modeling assumption, it is helpful to distinguish different sources of contact angle hysteresis. In general, contact angles may vary temporally and locally due to flow field dynamics and/or non-ideality of the solid surface. In the former case, contact angle hysteresis arises from momentum-driven deformation of the three-phase contact line. A prime example for such a scenario would be a sliding liquid droplet on a flat solid surface. In this case, the droplet surface is deformed by its movement and the resulting effective contact angles are observed to be lower or higher ($\theta^{\mathrm{rec}} < \theta^{\mathrm{eq}} < \theta^{\mathrm{adv}}$) at the receding or advancing end of the three-phase contact line, respectively. Under the assumption that all flow field dynamics are appropriately modeled, these phenomena should then be recovered in the PSM simulations as well and without explicit consideration of any hysteretic behaviour in the fluid-solid interaction. In fact, this conjecture was confirmed amongst others by Liu et al. [236]. Apart from flow field dynamics, contact angle hysteresis might as well also result from inhomogeneity of the solid surface due to surface roughness or chemical composition. In this regard, however, one should recall that one of the strengths of LBM actually relies in the precise lattice-representation of arbitrary simulation geometries. With the possibility to impose different geometrical (void or solid) and material properties (ρ_k, ν_k, θ_k) locally and independently on every lattice node, structural heterogeneity can be therefore in principle accounted for straightforwardly. Notwithstanding preexisting works on the explicit modeling of contact angle hysteresis [237–239], it appears reasonable that structural effects should emerge directly from a sufficiently resolved simulation geometry and not from a LB model extension. Due to above reasons, an explicit modeling of contact angle hysteresis is thus not considered in the underlying work. In fact, both the emergence

of geometric effects and the importance of a sufficient lattice resolution will be illustrated in Section 3.2.5 and Section 4.4.6, respectively.

In multiphase LBM, different wetting behavior is modeled by imposition of a desired contact angle locally on each lattice node of the solid surface, employing a wetting boundary condition (WBC). In the CGM, the orientation of the fluid-fluid interface is given by the color-gradient $\mathbf{F}$ (see also eq. (3.80)). With regard to Figure 3.4, the contact angle of the red fluid is then given as the angle between the normal $\mathbf{n}_s$ of the solid surface and the normal $\mathbf{n_F} = \mathbf{F}/|\mathbf{F}|$ of the fluid-fluid interface. In order to impose a desired contact angle, $\mathbf{n_F}$ has to be modified on the fluid lattice sites neighboring the solid surface. As isotropic discretization schemes (see eq. (3.81)) for the calculation of the color-gradient take φ of the neighboring lattice sites into account, it is a common approach to assign fictitious fluid densities to the solid surface sites. Due to the proportionality to the surface tension, $\mathbf{F}$ is thus perturbed in order to enforce the desired contact angle. Based on Young's equation (see also eq. (2.10))

$$\sigma_{sb} = \sigma_{sr} + \sigma_{rb}\cos(\theta) \tag{3.91}$$

for the force balance (Figure 3.4) at the three-phase contact line, Latva-Kokko and Rothman [240] derived these fictitious densities as

$$\rho_r^s = \rho + \frac{1}{2}\rho\cos(\theta) \tag{3.92}$$

$$\rho_b^s = \rho + \frac{1}{2}\rho\cos(180° - \theta) \tag{3.93}$$

in dependence of the contact angle with respect to the red phase. However, the derivations were made under the assumption of equal fluid densities ($\rho = \rho_r = \rho_b$) and are thus only valid in the absence of density variation. Moreover, above formulae were found to lead to non-negligible numerical errors resulting in unphysical wall flow [235]. In this work, the standard wetting boundary condition was therefore only employed for validation purposes in Section 3.2.5.

In front of these shortcomings, Leclaire et al. [199] proposed a different approach for a wetting boundary condition. In their formulation, the contact angle is imposed locally on the fluid sites neighboring the solid surface by adjusting the angle between the fluid-fluid interface normal $\mathbf{n_F} = \mathbf{F}/|\mathbf{F}|$ and the normal $\mathbf{n}_s$ of the solid surface. (Nota bene: In ref. [199], the color-gradient is denoted as $\mathbf{n_c}$.) The adjustment is carried out for every time step by minimizing the objective function

$$g(\mathbf{v_F}) = \mathbf{v_F} \cdot \mathbf{n}_s - |\mathbf{v_F}|\cos(\theta) \stackrel{!}{=} 0 \tag{3.94}$$

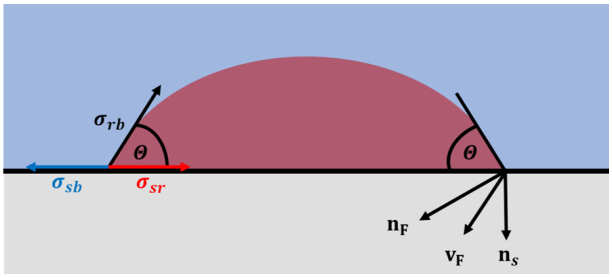

Figure 3.4: A sessile wetting droplet on a flat solid surface. Left: Arrows indicate the direction of action for the forces between the interacting phases. In equilibrium, these forces are balanced for a contact angle θ at the three-phase contact line. Right: θ is defined as the angle between the normal $\mathbf{n}_s$ of the solid surface and the normal $\mathbf{n_F}$ of the fluid-fluid interface. In multiphase LBM, the desired θ is enforced by readjusting $\mathbf{n_F}$ to a modified orientation $\mathbf{v_F}$ via a wetting boundary condition.

for the current orientation of the color-gradient $\mathbf{v_F}$, solid surface normal $\mathbf{n}_s$ and the desired contact angle θ. Equation (3.94) is solved iteratively

$$\mathbf{v_F}^{(0)} = \mathbf{n_F} \tag{3.95}$$

$$\mathbf{v_F}^{(1)} = \mathbf{n_F} - \lambda \left(\mathbf{n_F} - \mathbf{n}_s\right) \tag{3.96}$$

$$\mathbf{v_F}^{(n)} = \frac{\mathbf{v_F}^{(n-2)} g\left(\mathbf{v_F}^{(n-1)}\right) - \mathbf{v_F}^{(n-1)} g\left(\mathbf{v_F}^{(n-2)}\right)}{g\left(\mathbf{v_F}^{(n-1)}\right) - g\left(\mathbf{v_F}^{(n-2)}\right)} \tag{3.97}$$

using the secant method. Above scheme is illustrated for the contact angle of a droplet on a flat surface in Figure 2.4. In order to keep the computational expense at bay, the iteration is stopped after $n = 2$. Owing to the small time scales common to LBM, this is assumed to provide sufficient accuracy [199]. In addition to the number of iterations, also $\lambda = 1/2$ is adopted in this work. However, the formulation in equation (3.96) is chosen different to Leclaire's choice of $\mathbf{v_F}^{(1)} = \mathbf{n_F} - \lambda \left(\mathbf{n_F} + \mathbf{n}_s\right)$, as it proved to have slightly improved convergence. For the calculation of $\mathbf{n_F}$, fluid densities have to be provided on the solid surface. This is accomplished with the following scheme [235]

$$\rho_k \left(\mathbf{x}_s\right) = \frac{\sum_f W_f \left(\mathbf{x}_s\right) \cdot \rho_k \left(\mathbf{x}_s + \mathbf{c}_f \Delta t\right)}{\sum_f W_f \left(\mathbf{x}_s\right)} \tag{3.98}$$

extrapolating the fluid density ρ_k of the k-th phase from adjacent fluid sites (index f) to a solid surface site $\mathbf{x}_s$. The weights $W_f \left(\mathbf{x}_s\right)$ correspond to the standard lattice weights for the respective lattice direction $\mathbf{c}_f \Delta t$ to a neighboring fluid surface site. The solid surface normal $\mathbf{n}_s$ is calculated *a priori* by applying the isotropic gradient operator

$$\mathbf{n}_s = \nabla \mathbf{h}\,(x, y, z) \tag{3.99}$$

to the binary fluid-solid matrix $\mathbf{h}\,(x, y, z)$. In order to improve the staircase approximation of the solid surface, the matrix $\mathbf{h}\,(x, y, z)$ is furthermore smoothed beforehand the calculation of $\mathbf{n}_s$ with

$$\mathbf{h}\,(\alpha, \beta, \gamma)^{(n)} = \sum_{k=-1}^{k=1} \sum_{j=-1}^{j=1} \sum_{i=-1}^{i=1} w\left(i^2 + j^2 + k^2\right) \times \mathbf{h}\,(\alpha + i, \beta + k, \gamma + k)^{(n-1)} \tag{3.100}$$

using for w the standard D3Q19 lattice weights (see eq. (3.21)) and $n = 3$ iterations in accordance to ref. [199]. As will be shown in Section 3.2.5, above presented approach significantly improves the modeling of fluid-solid interaction over the standard wetting boundary condition.

3.2.4 Conversion factors

In LBM simulations, it is in general practicable to use a unit system which simplifies the numerical calculations. Most commonly, the lattice spacings in lattice units (*l.u.*), and lattice time (*l.t.*) are set to $\Delta x^{\mathrm{LBM}} = \Delta \mathrm{x} = 1$ and $\Delta t^{\mathrm{LBM}} = \Delta t = 1$, resulting in a lattice velocity of $c^{\mathrm{LBM}} = c = {}^{\Delta x^{\mathrm{LBM}}}/_{\Delta t^{\mathrm{LBM}}} = 1$ (cf. equations (3.10) and (3.18)). Another convenient choice is to set the initial fluid density to $\rho_0^{\mathrm{LBM}} = 1$.

In order to transfer the simulation results back into the physical SI unit system, conversion factors C_i have to be defined. Since a mechanical system is fully described by three independent physical units, the same number of independent conversion factors has to be declared. All other C_i are then derivable from these principal three conversion factors. For above lattice parameters, the conversion factors are then given as

- Length

$$C_l = \frac{\Delta x^{\mathrm{phys}}}{\Delta x^{\mathrm{LBM}}} \qquad [C_l] = \frac{\mathrm{m}}{\mathrm{l.u.}} \tag{3.101}$$

- Time

$$C_t = \frac{\Delta t^{\mathrm{phys}}}{\Delta t^{\mathrm{LBM}}} \qquad [C_t] = \frac{\mathrm{s}}{\mathrm{l.t.}} \tag{3.102}$$

- Density

$$C_\rho = \frac{\rho^{\mathrm{phys}}}{\rho^{\mathrm{LBM}}} \qquad [C_\rho] = \frac{{}^{\mathrm{kg}}/_{\mathrm{m}^3}}{{}^{\mathrm{l.m.}}/_{\mathrm{l.u.}^3}}. \tag{3.103}$$

At this point, it is noted that a direct definition of Δt^{phys} oftentimes appears cumbersome, as the physical time scale is eventually indirectly defined by a fluid's physical kinematic viscosity ν^{phys}. Since the relaxation parameter τ (equation (3.14)) is furthermore in general delimited by numerical stability (e.g., $t/\Delta t > \frac{1}{2}$ for the BGK operator [191]), it is often more convenient to define a conversion factor for the kinematic viscosity instead

- Kinematic viscosity

$$C_\nu = \frac{\nu^{\text{phys}}}{\nu^{\text{LBM}}} \qquad [C_\nu] = \frac{\text{m}^2/\text{s}}{\text{l.u.}^2/\text{l.t.}}. \tag{3.104}$$

The conversion factor C_t for the time scale can be then derived as $C_t = C_l^2/C_\nu$. In analogous fashion, the conversion factors for all other mechanical quantities of interest can be derived from above principal $\{C_l, C_t, C_\rho\}$ or $\{C_l, C_\nu, C_\rho\}$ as well:

- Mass

$$C_m = \frac{m^{\text{phys}}}{m^{\text{LBM}}} \qquad [C_m] = \frac{\text{kg}}{\text{l.m.}} \tag{3.105}$$

- Surface tension

$$C_\sigma = \frac{\sigma^{\text{phys}}}{\sigma^{\text{LBM}}} \qquad [C_\sigma] = \frac{\text{kg}/\text{s}^2}{\text{l.m.}/\text{l.t.}^2} \tag{3.106}$$

- Pressure

$$C_p = \frac{p^{\text{phys}}}{p^{\text{LBM}}} \qquad [C_p] = \frac{\text{kg}/\text{ms}^2}{\text{l.m.}/\text{l.m.}\cdot\text{l.t.}^2} \tag{3.107}$$

3.2.5 Model validation against theory

In order to ascertain the validity of the implemented multiphase Lattice Boltzmann model, three validation test cases are simulated beforehand all further simulative studies. As this work investigates the multiphase transport within porous media, the validation focuses on verifying the proper modeling of fluid-fluid, fluid-solid and fluid-fluid-solid interactions. Such as the color-gradient model, the validation test cases are adopted in major parts (Jurin's law and Washburn's law) from Leclaire et al. [199] as well.

Jurin's law

In a first case study, the steady state capillary ascension against gravity is simulated for a vertical tube, as shown in Figure 2.5). Given that the radius of the capillary tube is much smaller than its length ($R << L$), the capillary ascension height h can then be predicted according to Jurin's law [96] (see equation (2.16)) as

$$h = \frac{2\sigma \cos\theta}{R\Delta\rho g} \tag{3.108}$$

for the surface tension σ, the contact angle θ, density difference $\Delta\rho$ of the participating two fluids and gravitational acceleration g. By rearranging above equation, a relation can be obtained with

$$\frac{hR\Delta\rho g}{\sigma} = 2\cos\theta, \tag{3.109}$$

which is only a function on the contact angle. Introducing the characteristic Bond number

$$\mathrm{Bo} := \frac{\text{gravitational forces}}{\text{capillary forces}} = \frac{\Delta\rho R^2 g}{\sigma} \tag{3.110}$$

as the ratio of volume to surface forces, equation (3.109) is then further simplified to

$$\frac{h}{R}\mathrm{Bo} = 2\cos\theta. \tag{3.111}$$

Above equation presents a convenient relation for the validation of wettability modeling in the subsequent LB simulations, as for a constant Bond number the capillary ascension height becomes a sole function of the contact angle. However, the validity of Jurin's law is dependent on the dominance of capillary forces. In the subsequent study, this is ensured with a Bond number of $\mathrm{Bo} = 0.2$, which is according to Leclaire et al. [199] sufficiently low.

Figure 3.5a shows the computational domain for this first model validation test case, encompassing $160 \times 160 \times 162$ voxels in total. In the center of this computational box, a capillary tube with a radius of $R = 10$ voxels is embedded and aligned with its length of $L = 120$ voxels parallel to the z-axis. At this point, it is noted that in the subsequent model validation studies only lattice-based quantities are used. Conversion to physical counterparts (see Section 3.2.4) is irrelevant for the outcome of the studies and thus omitted in favor of brevity. The bottom and top domain boundaries are defined as solid walls, whereas periodic boundary conditions are employed for the remaining four in-plane domain boundaries. In the single-phase collision step, the SRT is utilized, as this test case focuses on the steady state capillary ascension height without consideration of flow dynamics. At the solid boundaries, fluid-solid interactions are governed by the halfway bounce-back scheme as described in Section 3.2.2 and as opposed to ref. [199], who employed a fullway bounce-back rule. Contact angles are imposed using the wetting boundary condition as proposed by Leclaire et al. [199] and as described in Section 3.2.3. On bulk lattice sites, the color-gradient $\mathbf{F}$ is calculated with the 3D fourth-order isotropic gradient operator

as presented in Section 3.2.3, whereas a 1D forward/backward/centered discretization scheme [241] is used on all fluid sites neighboring the solid surface. Corresponding to ref. [199], the fluid-fluid interface thickness is furthermore controlled using $\beta = 0.8219$ within the recoloring operator (see Section 3.2.3). The computational domain is filled with two immiscible fluids. A denser fluid with a density of $\rho_B^0 = 1000$ and a kinematic viscosity of $\nu_B = 1/20$ occupies the bottom half of the box. The top half is filled with a fluid of lower density with $\rho_T^0 = 100$ and $\nu_T = 1/200$, resulting in density and kinematic viscosity ratios of $\gamma = \rho_B^0/\rho_T^0 = 10$ and $\nu_B/\nu_T = 10$, respectively. By this, the initial ratio of dynamic viscosities equals

$$M = \frac{\mu_T}{\mu_B} = \frac{\rho_T^0 \nu_T}{\rho_B^0 \nu_B} = 100 \tag{3.112}$$

and the Bond number is set to

$$\mathrm{Bo} = \frac{(\rho_B^0 - \rho_T^0)\, R^2 g}{\sigma} = 0.2 \tag{3.113}$$

for a dominance of capillary over gravitational forces. In order to ensure negligence of viscous dissipation, a high Laplace number of

$$\mathrm{La} := \frac{\text{capillary forces} \cdot \text{inertial forces}}{\text{viscous forces}^2} = \frac{\sigma\,(\rho_B^0 R)}{\mu_B^2} = \frac{\sigma R}{\rho_B^0 \nu_B^2} = 10 \tag{3.114}$$

is furthermore set with a surface tension of $\sigma = 2.5$. With above computational setup, capillary ascension is then simulated for a range of different contact angles θ and stopped at steady state. The simulation results are then compared with the analytical solution.

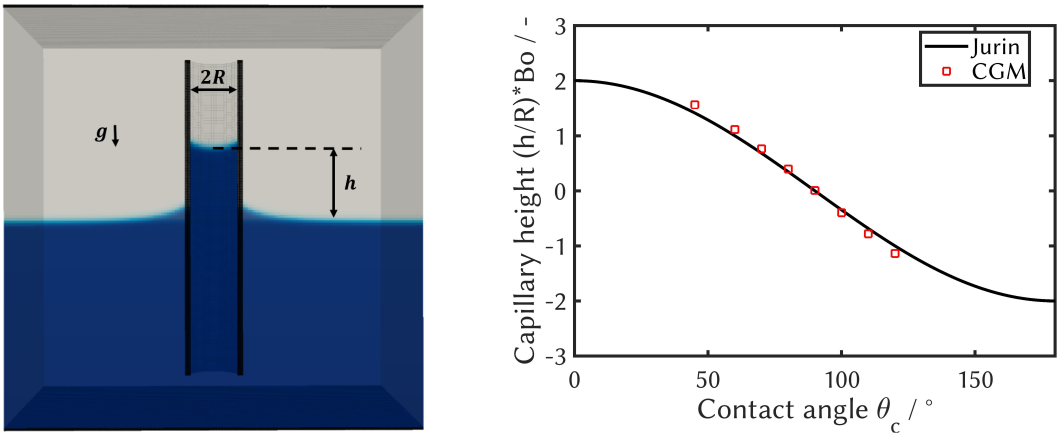

(a) Computational domain.

(b) Simulation results.

Figure 3.5: First test case for the validation of the 3D multiphase Lattice Boltzmann color-gradient model against theory: (a) Capillary ascension of a fluid against gravity g inside a capillary tube with a radius R. (b) In equilibrium, the capillary height h is a function of the contact angle θ (eq. (3.111)) and can be predicted by Jurin's law [96].

Figure 3.5b shows simulated capillary ascension heights for a wide range of contact angles ($\theta = [45°, 60°, 70°, 80°, 90°, 100°, 110°, 120°]$). The overall agreement with the analytical reference of Jurin's law (eq. (3.111) and [96]) is very good and only for the respectively lowest/highest contact angles slight deviations are observable. The latter may as well also stem from an inaccurate determination of the capillary ascension height due to the coarse lattice representation of the capillary tube. Overall, the simulation results demonstrate that the employed color-gradient LB model correctly accounts for the surface tension and the contact angle, even under inclusion of gravity as a body force. The underlying model is therefore considered to be successfully validated for fluid-fluid and fluid-solid interactions in steady state capillary-dominated multiphase systems. At this point, it is added that even though not the entire wettability range from 0° to 180° is covered in this first test case, model validity is nonetheless well ensured for the range of contact angles (65°–115°) expected to be relevant for the simulation of the GDL liquid water transport in the subsequent chapters of this work.

Washburn's law

This work aims at investigating multiphase transport processes in porous GDL microstructures under both stationary and dynamic conditions. In a second model validation test case, the CGM is thus validated for the time dependent invasion of a wetting fluid into a capillary tube, as illustrated in Figure 3.6a. According to Poiseuille's law [242], the volumetric flow rate $\dot{V}$ of a fluid in a circular capillary tube is given as

$$\dot{V} = \frac{dV}{dt} = \frac{\pi R^4}{8\mu}\frac{\Delta p}{l} \tag{3.115}$$

with the pressure drop Δp and dynamic viscosity of the fluid and radius R and length l of the tube. Replacing the differential volume by the product of cross-sectional area A and differential capillary length, i.e., $dV = Adl = \pi R^2 dl$ then yields

$$\frac{dl}{dt} = \frac{R^2}{8\mu}\frac{\Delta p}{l} \tag{3.116}$$

for the time derivative of the differential capillary filling length l. With $u = dl/dt$ as the average cross-sectional velocity, i.e., $dV/dt = uA$, above equation can be identified as a balance of driving forces Δp and viscous dissipation Δp_{visc}

$$\Delta p_{\text{visc}} = \frac{8\mu l}{R^2}\frac{dl}{dt} = \frac{8\mu l}{R^2}u = \Delta p. \tag{3.117}$$

Considering furthermore that the invading fluid has to displace a defending fluid, the viscous dissipation is extended to

$$\Delta p_{\text{visc}} = \frac{8\left[\mu_I l + \mu_D\left(L - l\right)\right]}{R^2} u \tag{3.118}$$

with μ_I and μ_D as the dynamic viscosity of the invading and defending fluid and the overall tube length L. Accordingly, equation (3.116) is then given with

$$\frac{dl}{dt} = \frac{R^2 \Delta p}{8\left[\mu_I l + \mu_D\left(L - l\right)\right]} \tag{3.119}$$

and separation of variables subsequently yields

$$\left[\mu_I l + \mu_D\left(L - l\right)\right] dl = \frac{R^2 \Delta p}{8} dt \tag{3.120}$$

and rearranging the viscous dissipation terms leads to

$$\left[\left(\mu_I - \mu_D\right) l + \mu_D L\right] dl = \frac{R^2 \Delta p}{8} dt. \tag{3.121}$$

Neglecting gravitation, the driving pressure difference can be furthermore denoted as the capillary pressure $\Delta p = p_c = 2\sigma \cos\theta / R$ (see eq. (2.14)) and equation (3.121) becomes

$$\left[\left(\mu_I - \mu_D\right) l + \mu_D L\right] dl = \frac{R^2 p_c}{8} dt = \frac{R\sigma \cos\theta}{4} dt. \tag{3.122}$$

By integration over $t = [0\ t]$ and $l = [0\ l]$, one obtains

$$\frac{1}{2}\left(\mu_I - \mu_D\right) l^2 + \mu_D L l = \frac{R\sigma \cos\theta}{4} t \tag{3.123}$$

and

$$l^2 + 2\frac{\mu_D L}{\left(\mu_I - \mu_D\right)} l = \frac{R\sigma \cos\theta}{2\left(\mu_I - \mu_D\right)} t. \tag{3.124}$$

Making use of the binomial theorem with

$$\left[l + \left(\frac{\mu_D L}{\mu_I - \mu_D}\right)\right]^2 = l^2 + 2\left(\frac{\mu_D L}{\mu_I - \mu_D}\right) l + \left(\frac{\mu_D L}{\mu_I - \mu_D}\right)^2, \tag{3.125}$$

equation (3.124) can be rewritten to

$$\left[l + \left(\frac{\mu_D L}{\mu_I - \mu_D}\right)\right]^2 = \left(\frac{\mu_D L}{\mu_I - \mu_D}\right)^2 + \frac{R\sigma \cos\theta}{2\left(\mu_I - \mu_D\right)} t. \tag{3.126}$$

Applying the square root and solving for the capillary filling length l then yields

$$l = -\left(\frac{\mu_D L}{\mu_I - \mu_D}\right) + \sqrt{\left(\frac{\mu_D L}{\mu_I - \mu_D}\right)^2 + \frac{R\sigma \cos\theta}{2\left(\mu_I - \mu_D\right)} t}. \tag{3.127}$$

With the dimensionless capillary length $l^* = l/L$ and time $t^* = \frac{\sigma}{(\mu_I - \mu_D)L}t$, a final expression is then obtained with

$$l^* = -\left(\frac{\mu_D}{\mu_I - \mu_D}\right) + \sqrt{\left(\frac{\mu_D}{\mu_I - \mu_D}\right)^2 + \left(\frac{1}{2}\frac{R}{L}\cos\theta\right)t^*}, \tag{3.128}$$

which is similar to ref. [199]. At this point, it is noted that the above equation differs from the most widely known relation

$$l = \sqrt{\frac{R\sigma\cos\theta}{2\mu_I}t} \tag{3.129}$$

commonly referred to as Washburn (or Lucas-Washburn) equation [243, 244], since it also includes the viscous flow resistance of the displaced fluid. As already pointed out by Leclaire et al. [199], however, equation (3.128) turns into equation (3.129) with $l^* \propto \sqrt{t^*}$ when viscous dissipation of the displaced fluid become negligible ($\mu_I >> \mu_D$). For the subsequent model validation simulations, the more complete Washburn relation (eq. (3.128)) will be used as an analytical reference.

In the computational domain, the tube has a radius of $R = 10$ voxels and a length of $L = 200$ voxels. Two rectangular basins ($24 \times 24 \times 22$ voxels) are appended to the bottom and top of the tube, which provide a fluid inlet and an outlet zone. In total, the simulation geometry thus exhibits a domain size of $24 \times 24 \times 244$ voxels. The in-plane domain boundaries are governed by periodic boundary conditions, whereas at the top of the outlet and bottom of the inlet zone, pressure (density) boundary conditions are imposed (see external boundary condition by Zou and He in Section 3.2.2). As this test case includes the dynamics of a capillary filling process, the MRT operator is employed in the single-phase collision step in favor of better physical accuracy with regard to time dependence. Since the capillary tube is positioned horizontally, gravitational influences are neglected in this test case. Solid boundaries at the tube walls are modeled with a no-slip condition using the halfway bounce-back scheme. The contact angle is imposed via the wetting boundary condition by Leclaire et al. [199]. For the calculation of the color-gradient, a 3D fourth-order isotropic gradient operator is utilized for the bulk and a 1D forward/backward/centered discretization scheme for all fluid surface sites. The thickness of the fluid-fluid interface is controlled with $\beta = 0.8219$. The capillary tube, the outlet zone and the top domain boundary are initially exclusively filled with the nonwetting fluid, whereas the wetting fluid occupies the bottom domain boundary and the inlet zone. The two immiscible fluids are then initialized with $\rho_I^0 = 998.2$ and $\nu_I^0 = 1/6$ for the wetting and invading fluid and with $\rho_D^0 = 661.32$ and $\nu_D^0 = 0.077\,95$ for the initially present nonwetting fluid. The ratios of density and kinematic viscosity are $\gamma = \rho_I/\rho_D = 1.5094$

and $\nu_I/\nu_D = 0.4676$, resulting in a dynamic viscosity ratio of $M = \mu_I/\mu_D = 3.2277$. The surface tension is chosen as $\sigma = 2.7728$ to set a Laplace number of La = 1 and thus a balance of viscous to capillary and inertial forces (see equation (3.114)). With the given computational setup, capillary invasion of a wetting fluid is then simulated for a wide range of contact angles θ.

Figure 3.6b shows the simulated capillary filling over time. For a large variety of contact angles, the simulation results agree very well with the analytical solution as provided by Washburn's law (equation (3.128) and [243]). These observations thus illustrate that the implemented CGM is also capable of modeling the correct time dependence for the capillary invasion of a wetting fluid into a capillary tube. This second test case proves that the underlying color-gradient LB model properly accounts for multiphase interactions such as surface tension and contact angle, not just in steady state but in unsteady flow regimes as well.

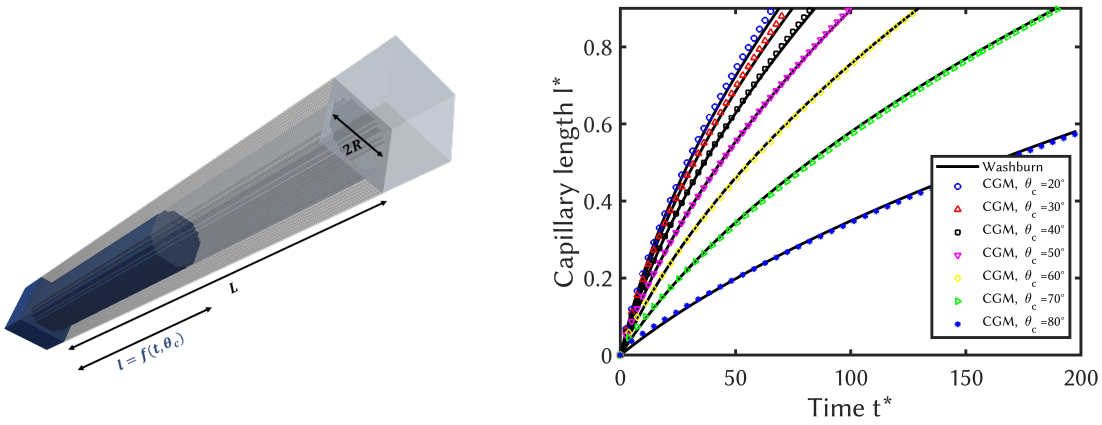

(a) Computational domain. (b) Simulation results.

Figure 3.6: Second test case for the validation of the 3D multiphase Lattice Boltzmann color-gradient model against an analytical reference: (a) Capillary filling of a tube with radius R and length L by a wetting fluid. (b) The time-dependent invasion length l is a function of the contact angle θ (eq. (3.128)) and can be described by Washburn's law [243].

Leclaire et al.'s wetting boundary condition [199] claims to provide significant improvements in physical accuracy over the standard wetting boundary condition by Latva-Kokko and Rothman [240]. However, the former also comes along with a higher computational expense. Seeking the best compromise between physical accuracy and computational efficiency, a comparison is therefore made between the simulation results for the improved and the standard wetting boundary condition. Figure 3.7a clearly shows that the standard wetting boundary condition is in fact incapable of modeling the fluid-solid interactions properly, resulting in major deviations from the predictions of Washburn's law. While for

a strongly wetting fluid ($\theta = 20°$), capillary filling proceeds delayed, it is found to be too fast for an almost neutrally wetting fluid ($\theta = 80°$). Both of these observations might be explained by the fact that the standard wetting boundary condition is known to cause unphysical mass transfer along the solid surface [235]. In summary, the standard wetting boundary condition is found to understate the overall wettability characteristics resulting from different contact angles. The wetting boundary condition by Leclaire et al., on the other hand, evidently achieves a very good agreement with the analytical solution. On account of the significantly improved physical accuracy, an increase in the computational expense is therefore well justified. In proving to be superior to the standard approach, Leclaire et al.'s wetting boundary condition is therefore used for all subsequent simulative studies of this work.

The MRT operator is known to result in improved numerical stability and a corrected time dependence in decoupling the different momenta of the particle distributions. However, even more than the wetting boundary condition, the MRT leads to a computational overhead of 15 to 20 % [191, 198] as compared to the SRT. Beforehand time consuming pore-scale simulations on complex GDL microstructures, the simple Washburn test case is therefore utilized to investigate, if application of the MRT operator leads to significantly different multiphase transport characteristics. As illustrated in Figure 3.7b, this is not the case as the simulation results for both the SRT and MRT collision operator lead to almost identical agreement with the theory. Only for $\theta = 80°$, the differences in the time dependence come into effect on longer time scales, resulting in marginally improved simulation results for the MRT operator. One explanation for this observation could be that the wetting dynamics on the solid surface are dominating the fluid-solid interaction such that the decoupling of the relaxation rates by the MRT operator has in general only a minor influence on the multiphase transport. Providing sufficient physical accuracy and in favor of computational cost reduction, the SRT operator is set as default for all subsequent simulative studies.

The ink-bottle or capillary valve effect

While both Jurin's and Washburn's law provide important analytical references for the validation of multiphase LB models, the considered simulation geometries of single capillary tubes are simple. Real porous media, however, typically have internal structures with a high geometric complexity. As a result, the modeling of capillary effects in such porous media becomes disparately more challenging, since according to the generalized Laplace law (compare eq. (2.19)) the internal capillary pressure

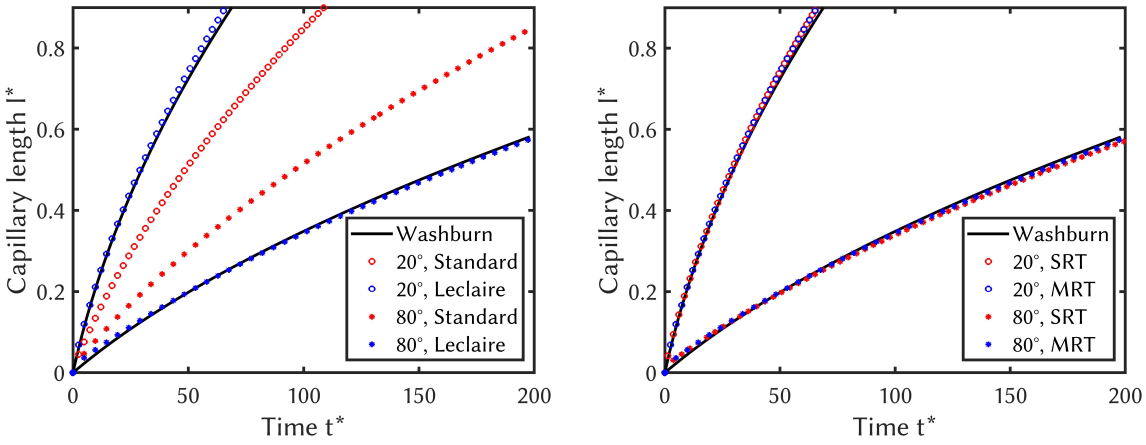

(a) Wetting boundary condition. (b) Collision operator.

Figure 3.7: Simulated time-dependent invasion of a wetting fluid into a capillary tube under parameter variation. (a) Comparison of different wetting boundary conditions by Latva-Kokko and Rothman [240] and Leclaire et al. [199]. (b) Comparison of the single relaxation time (SRT) and the multi relaxation time (MRT) operator for the single-phase collision step.

$$p_c = \sigma \left(\frac{1}{R_1} + \frac{1}{R_2} \right) \tag{3.130}$$

varies locally in dependence of the pore morphology represented by the two principal radii of curvature R_1 and R_2. Furthermore, as the latter are a function $R_i = f(\theta)$ of the contact angle θ, the internal capillary pressure is evidently also dependent on the local wettability within the porous medium. As a result of this increased complexity arising from the interplay between pore structure and wettability, also new capillary characteristics come into play.

While the imbibition of a wetting fluid ($\theta < 90°$) into a single circular capillary tube is a spontaneous self-driven process (recall Figure 3.5 and Figure 3.6), this is in general not necessarily the case for more complex capillary systems (such as GDLs) [245, 246]. Instead, oftentimes external pressure gradients have to be imposed in order to enforce full capillary invasion of a wetting phase. The reason for this phenomenon relies in the circumstance that real porous media generally exhibit irregular distributions of pore sizes and shapes. Moreover, these rather large pore spaces are typically interconnected by narrower capillary channels/throats. Hence, a pore-throat network (Figure 3.8) is formed with pore-space contours whose shape may be associated with those of ink-bottles. With their relatively smaller radii, the throats represent constrictions of the pore space and can be therefore interpreted as capillary bottlenecks. In general, however, the local resistance to capillary transport is not only dependent on the contact angles and the radii of the

individual pores and throats but on the radius transition between the aforementioned basic structural elements as well. The latter morphological characteristic gives rise to a phenomenon commonly referred to as ink-bottle or capillary valve effect [247, 248].

In the subsequent paragraphs, this phenomenon is illustrated with a simple 3D geometry of a larger pore connected to two narrower throats, as shown in Figure 3.8. Assuming that a wetting phase (red) is invading the capillary system against a defending fluid (blue) via the left-hand side throat, spontaneous imbibition is expected to occur due to the capillary pressure

$$p_c^t = \frac{2\sigma\cos\theta}{R_t} \tag{3.131}$$

inside the tube of constant radius R_t and length L_t. At the pore entry, however, the radius is not constant anymore but a function of the position x parallel to the flow direction, i.e., $r_p = f(x)$. Dependent on this pore space expansion, the orientation of the pore wall then develops in an angle $\alpha_p(x)$ relative to the flow direction and the invading wetting fluid forms an apparent contact angle $\theta^{\text{app}}(x) = \theta + \alpha_p(x)$ with the inclined solid surface. Consequently, the local capillary pressure inside the pore then equals

$$p_c^p(x) = \frac{2\sigma\cos\left[\theta^{\text{app}}(x)\right]}{r_p(x)} = \frac{2\sigma\cos\left[\theta + \alpha_p(x)\right]}{r_p(x)} \tag{3.132}$$

as a result of the spatially variable pore wall curvature [24, 246, 249] (see also Purcell's toroid model on converging-diverging pores [250]). As apparent from above equation (3.132), the spontaneous imbibition of the wetting fluid stops when $p_c^p(x) \leq 0$ for $\theta^{\text{app}}(x) \geq 90°$ and equivalently $\alpha_p(x) \geq 90° - \theta$. In other words, a strong enough pore wall curvature may counterbalance the wetting tendency of a fluid with $\theta < 90°$, eventually prohibiting further pore invasion. This somewhat counterintuitive phenomenon can be explained by the circumstance that the invading wetting fluid has to enlarge its surface (i.e., the fluid-fluid interface) against the defending nonwetting phase in order to proceed with the invasion process along an expanding pore radius. However, with the surface tension minimizing the fluid-fluid interface, additional work is required for this surface enlargement. In dependence on the local pore wall curvature, this energy barrier may then exceed the energetic surplus given by the tendency of the invading fluid to wet the solid pore surface. As a result, further advancement of the three-phase contact line would be halted, ultimately impeding capillary filling of the pore.

In the following, the capillary valve effect is demonstrated with a simple 3D pore-throat geometry, for which an analytical expression can be derived for the local capillary pressure. Afterwards, the latter will be used as an analytical reference for the further validation of the simulation results and thus of the underlying LB model. Recall Figure 3.8 with the

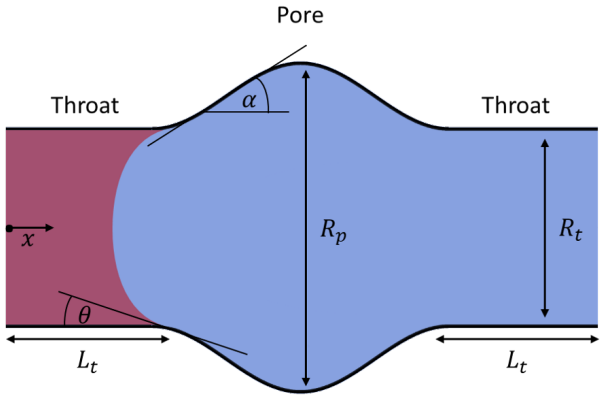

Figure 3.8: Schematic for a simple capillary system of a pore with a maximum radius R_p connected to two throats with radii R_t and lengths L_t. Along with the transition from throat to pore radius, the pore wall develops in an angle α to the flow direction x. In dependence of the contact angle θ, invasion of a wetting fluid (red) against a defending nonwetting phase (blue) may be stopped at the pore entry despite its wetting capabilities, a phenomenon known as ink-bottle or capillary valve effect.

simple capillary system of a single pore connected by two throats. Whereas the latter are assumed to have constant radii of $R_t = 12$ and a respective length of $L_t = 20$, the radius of the pore is defined by a cosine function

$$r_p(x) = R_t + \Delta_R \left[1 + \cos\left(x\frac{\pi}{R_p}\right)\right] \tag{3.133}$$

of the downstream position x, the maximum pore radius $R_p = 20$ and the constant $\Delta_R = (R_p - R_t)/2$. For the whole capillary pore-throat system, the position-dependent local radius is then given with

$$R(x) = \begin{cases} R_t & \text{for } 0 \leq x < L_t \\ r_p(x) & \text{for } L_t \leq x < L_t + 2R_p \\ R_t & \text{for } L_t + 2R_p \leq x < 2L_t + 2R_p, \end{cases} \tag{3.134}$$

as illustrated in Figure 3.9. With the radius of the pore given by equation (3.133), the angle $\alpha_p(x)$ is furthermore derived via the slope

$$\tan\left[\alpha_p(x)\right] = \frac{dr_p(x)}{dx} = -\frac{\pi}{R_p}\Delta_R \sin\left(x\frac{\pi}{R_p}\right) \tag{3.135}$$

of the pore wall to

$$\alpha_p(x) = \arctan\left[-\frac{\pi}{R_p}\Delta_R \sin\left(x\frac{\pi}{R_p}\right)\right], \tag{3.136}$$

as shown in Figure 3.9a. According to equation (3.132), the local capillary pressure in the pore is then given as

$$p_c^p(x) = \frac{2\sigma\cos\left[\theta + \alpha_p(x)\right]}{r_p(x)} = \frac{2\sigma\cos\left[\theta^{\text{app}}(x)\right]}{r_p(x)} \tag{3.137}$$

and via equation (3.134) a general expression

$$p_c(x) = \frac{2\sigma\cos\left[\theta^{\text{app}}(x)\right]}{R(x)} = \begin{cases} p_c^t & \text{for } 0 \le x < L_t \\ p_c^p(x) & \text{for } L_t \le x < L_t + 2R_p \\ p_c^t & \text{for } L_t + 2R_p \le x < 2L_t + 2R_p \end{cases} \tag{3.138}$$

is eventually obtained for the whole capillary pore-throat system. Figure 3.9b illustrates the resulting capillary pressure for three different contact angles of 40°, 60° and 80°. As expected, the lowest capillary pressure and thus highest capillary resistance for transport of the wetting phase does not reside in the throats exhibiting the smallest radii but instead at the pore entrance in between the transition from R_t to R_p. Whereas the capillary pressure for a strongly wetting fluid with $\theta = 40°$ remains positive at every downstream position, this is not anymore the case for contact angles of 60° and 80°, as the capillary system then exhibits regions with $p_c(x) < 0$. In these zones, the invading fluid can only proceed by an increase of its phase pressure in order to enforce a capillary pressure below a certain threshold. At a specific downstream position, $p_c(x)$ exhibits a global minimum which is dependent on the contact angle and the radii R_t and R_p (since $\theta^{\text{app}} = \theta + \alpha(x)$). Once this threshold capillary pressure for pore entry is reached, the wetting fluid then suddenly and rapidly flushes the pore, a phenomenon commonly referred to as Haines jump [245, 251–253]. At the end of complete pore filling, the wetting phase is then eventually imbibed again into the second capillary tube with a constant capillary pressure as given by equation (3.131).

In order to validate the underlying LB model against the previously described analytical reference for the capillary valve effect, a computational domain is generated accordingly. Figure 3.10a shows the computational domain of a centered pore with a maximum inner radius of $R_p = 20$ voxels connected to two capillary throats with inner radii of $R_t = 12$ voxels and length of $L_t = 20$ voxels. The local pore radius $r_p(x)$ is furthermore defined as a cosine function of the downstream position x according to equation (3.133). Rectangular basins with $42 \times 42 \times 11$ voxels are appended to the bottom of the lower and top of the upper tube in order to provide fluid inlet ($-L_I \le x < 0$) and outlet zones

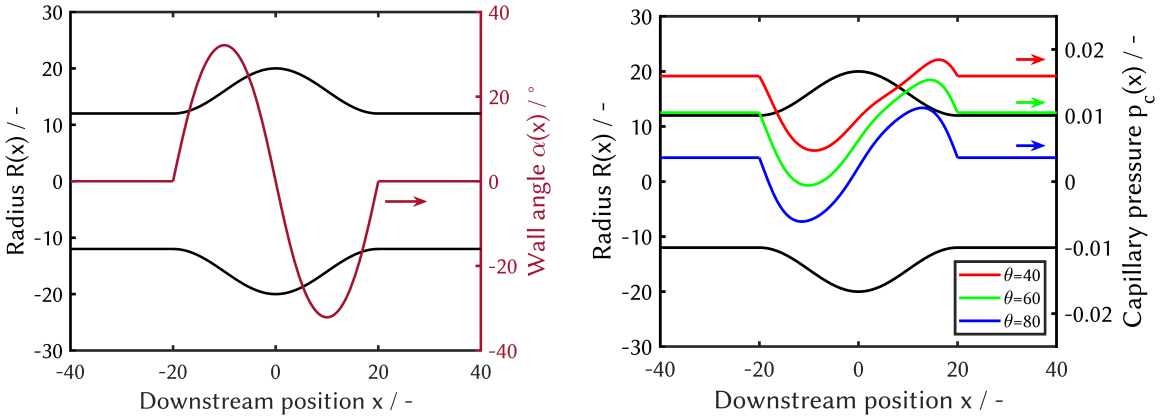

(a) Wall angle $\alpha\,(x)$. (b) Capillary pressure $p_c\,(x)$.

Figure 3.9: Simple 3D capillary system of a wider centered pore with a maximum radius R_p connected to two narrower throats with radii R_t and lengths L_t. Due to a spatially variable capillary radius $r_p(x)$, the pore wall develops in (a) an angle $\alpha\,(x)$ to the flow direction, resulting in (b) a position-dependent capillary pressure $p_c\,(x)$. Depending on the apparent contact angle $\theta^{\text{app}}\,(x) = \theta + \alpha\,(x)$, spontaneous imbibition of the pore may be eventually inhibited even for a wetting fluid, a phenomenon commonly referred to as ink-bottle or capillary valve effect.

$(2L_t + 2R_p \leq x < 2L_t + 2R_p + L_O)$, respectively. The simulation geometry thus comprises a total of $42 \times 42 \times 102$ voxels. Analogous to the previous computational domain of the Washburn validation test case, pressure boundary conditions (see Section 3.2.2 and Zhou and He [203, 204]) are imposed at the bottom of the inlet and top of the outlet zone. In-plane domain boundaries are again governed by periodic boundary conditions. As this test case does not focus on an accurate time dependence of the capillary filling process, the SRT operator is furthermore assumed to provide sufficient accuracy for the single-phase collision step. Gravitational effects are assumed to be negligible. Moreover, interior boundaries at the solid surfaces are modeled using the halfway bounce-back scheme and the contact angle is imposed via the wetting boundary condition by Leclaire et al. [199]. Analogous to the previous validation test cases, the color-gradient is calculated with the default 3D fourth-order isotropic gradient operator in the fluid bulk and with a 1D forward/backward/centered discretization scheme on all fluid surface sites. Due to a high sensitivity of the threshold capillary entry pressures, the fluid-fluid interface thickness is in this test case controlled with a slightly higher value of $\beta = 0.85$ providing a better compromise between numerical accuracy and numerical stability. Initially, the capillary pore-throat system is exclusively filled with a nonwetting defending fluid, whereas the invading wetting fluid is only present in the inlet zone $(-L_I \leq x < 0)$. The immiscible fluids are then initialized with phase densities of $\rho_I^0 = 1$ and $\rho_I^I = 1$ for the invading wetting and the defending nonwetting fluid, respectively. Kinematic viscosities are set to

$\nu_I^0 = 1/6$ and $\nu_D^0 = 1/12$, the ratios of density and viscosity thus equal $\gamma = \rho_I^0/\rho_D^0 = 1$ and $M = \mu_I/\mu_D = \rho_I^0\nu_I/(\rho_D^0\nu_D) = 2$. The surface tension is furthermore set to $\sigma = 0.125$ and the Laplace numbers for the throats and the pore thus equal $\mathrm{La}_t = \sigma R_t/(\rho_I^0\nu_I^2) = 54$ and $\mathrm{La}_p = \sigma R_p/(\rho_I^0\nu_I^2) = 90$, respectively. With the aforementioned computational setup, capillary invasion is then simulated analogously to the previous Washburn validation test case. In contrast to the latter, however, spontaneous imbibition of the capillary system by the wetting fluid is expected to be halted at the pore entry due to the capillary valve effect. Further progression of the capillary filling process is then enforced by increasing the invading fluid's density via the inlet pressure boundary condition in a stepwise fashion while keeping constant the density of the defending nonwetting phase at the outlet boundary. Thereby, an additional external pressure gradient is incrementally imposed until a certain threshold capillary pressure is reached and ultimately a complete filling of the capillary system occurs.

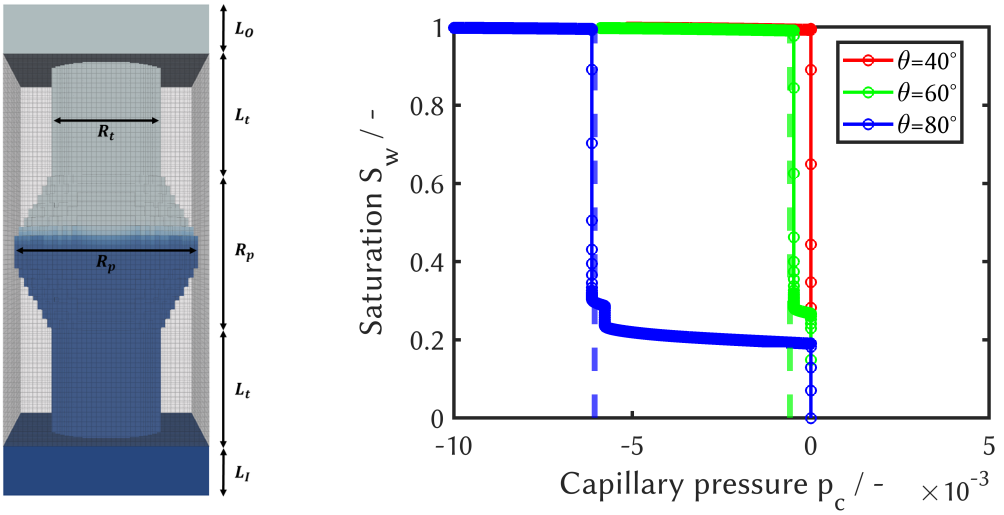

(a) Computational domain. (b) Simulation results.

Figure 3.10: Third test case for the validation of the 3D multiphase Lattice Boltzmann color-gradient model against an analytical reference: (a) Capillary invasion of a wetting fluid (blue) into a pore-throat system. (b) Simulated capillary pressure-saturation curves demonstrate the capillary valve effect during the intrusion process for three different contact angles θ. Dashed colored lines indicate the analytical reference for the capillary pressure threshold required for pore entry according to equation (3.138) and Figure 3.9b.

Figure 3.10b shows the simulated capillary valve effect on the wetting phase intrusion for three different contact angles of 40°, 60° and 80°. Representing the capillary filling progress, the wetting phase saturation of the capillary pore-throat system is plotted against the capillary pressure as imposed by the external pressure boundary conditions. Consistent with predictions, the wetting fluid is readily imbibed into the bottom capillary throat without the necessity of an external capillary pressure, as indicated by a sudden initial

saturation increase already at $p_c = 0$. In the scenario with the strongest wettability ($\theta = 40°$), the capillary filling process continues until the pore-throat system is completely saturated ($S_w = 1$) with the wetting phase. As expected, no capillary valve effect is visible in this case, which is in accordance with the analytical reference (Figure 3.9b). For a slightly higher invading phase wettability with $\theta = 60°$, on the other hand, spontaneous imbibition stops at a saturation of roughly one third, i.e., at the pore entry. Then, gradual increases of the wetting phase density leads to a barely notable saturation rise until the threshold capillary pressure is reached and the pore-throat system is rapidly and completely filled. Similar observations can be made for $\theta = 80°$, however, with a disparately higher threshold capillary pressure required for complete pore filling. In both simulation cases, the latter is in good agreement with the respective analytical reference as indicated with colored dashed vertical lines in Figure 3.10b. While the previous results demonstrate the capabilities of the LB model to describe the capillary valve effect for the intrusion of a wetting phase, the withdrawal of a fluid is in general affected by this phenomenon as well. However, as the drainage of a wetting phase is equivalent to the invasion of a nonwetting fluid, different capillary pressure thresholds have to be overcome to fill the capillary system. Assuming invasion from the right-hand side of the pore-throat system shown in Figure 3.8, the nonwetting phase first has to overcome the capillary pressure p_c^t (equation (3.131)) of the right-hand side throat in order to displace the defending wetting fluid. Analogous to the latter, however, the nonwetting fluid experiences the highest capillary resistance only after progressing to the pore entry, where the spatially variable capillary pressure of the pore (eq. (3.137) and Figure 3.9b) reaches its maximum value in the transition from R_t to R_p. In order to validate the underlying LB model for the capillary valve effect in the drainage process of the wetting phase as well, additional simulations are therefore conducted. Starting from an initially fully wetted capillary system ($S_w = 1$), withdrawal of the wetting fluid is then enforced by a stepwise increase of the capillary pressure via the pressure boundary conditions until the nonwetting fluid has filled the pore-throat system completely. Figure 3.11 shows the resulting simulated drainage curves for the given three contact angles in comparison to the respective intrusion curves. Similar to the invasion simulations, also the results for the withdrawal of the wetting phase are in good agreement with the analytical references. Furthermore, a comparison of the intrusion and drainage curves illustrates the non-uniqueness of the $p_c - S$ relation, as the latter is dependent on the flow direction. This hydrostatic capillary hysteresis [245, 246, 252, 254] (not to be confused with contact angle hysteresis [255]) is a well-known characteristic of porous media, which will be also extensively investigated in Chapter 4. With this third and final validation test case, the underlying color-gradient LB model is considered to be

successfully validated for the simulation of multiphase transport phenomena in porous media.

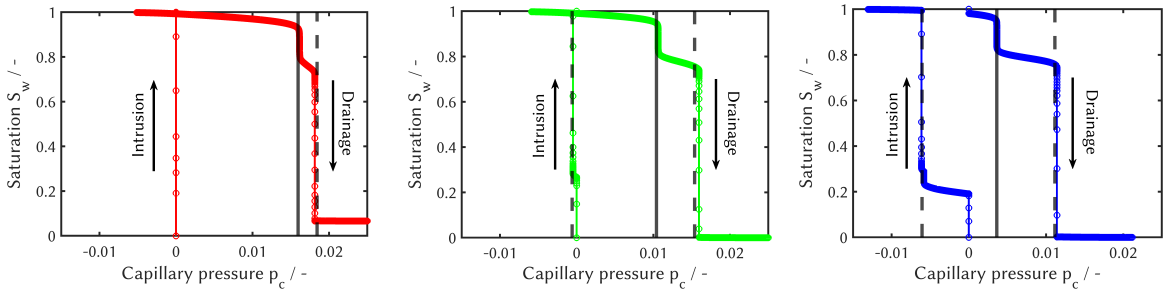

(a) $\theta = 40°$. (b) $\theta = 60°$. (c) $\theta = 80°$.

Figure 3.11: Simulated capillary pressure-saturation curves for the invasion and withdrawal of a wetting phase for a simple 3D pore-throat geometry (Figure 3.8) and variable contact angles θ of the wetting phase. The capillary valve effect impacts both the intrusion and drainage process, eventually causing a capillary hysteresis. Solid and dashed vertical lines indicate analytical references for the capillary pressure threshold for throat and pore entry, respectively.

4 Parametric studies on capillary hysteresis in carbon felt GDLs

4.1 Pore-scale modeling of capillary hysteresis

The relation between capillary pressure and saturation presents an important characteristic of porous media (see also Section 2.2.4). In order to characterize the capillary transport of liquid water in porous gas diffusion layers for PEM fuel cells, researchers have therefore conducted many experiments (typically porosimetry) to determine $p_c - S$ relations for a variety of GDL materials [100, 104, 256–264]. For more detailed information on such experimental studies the interested reader is at this point referred to the reviews in [20–22]. While these measurements yield valuable (volume-averaged) test bench data for the characterization of porous media, they do not provide any insights on the actual phase distribution within the samples. As discussed by García-Salaberri et al. [265], however, the same average GDL saturation can correspond non-uniquely to both rather homogeneous or heterogeneous phase distributions. In addition, experimental investigation of the underlying pore-scale processes is in general very difficulty and beyond a certain depth of detail not (yet) even feasible. In order to better understand capillary phenomena of liquid water transport during PEM fuel cell operation, researchers have over the past decades therefore increasingly employed pore-scale methods to derive $p_c - S$ relations for GDLs from simulations as well.

Schulz et al. [266] employed a full morphology model to study capillary pressure-saturation characteristics in stochastic reconstructions (see also Section 4.2) of Toray TPGH-90 and SGL 10BA carbon papers. Considering the primary drainage process of liquid water as the non-wetting phase with a contact angle of $\theta = 120°$, the simulations yielded $p_c - S$ curves which were similar for both GDLs and showed reasonable agreement with experimental data. Zamel et al. [101] also used the FM method to simulate the primary invasion of liquid water ($\theta = 130°$) into stochastic reconstructions of Toray TPGH-120 carbon papers and reported good agreement with measured $p_c - S$ curves. The empirical relation by van Genuchten (eq. (2.25)) was furthermore found to provide a good fit, whereas the classical Leverett J-function (eq. (2.22)) underestimated the capillary

pressure. Agaesse et al. [267] utilized both FM and PNM to model liquid water invasion ($\theta = 115°$) into pore space reconstructions of a SGL 24BA based on µCT imaging data. For both pore-scale methods, the authors reported simulated $p_c - S$ curves consistent with experimental data and concluded that FM and PNM present reliable approaches. Göbel et al. [55] examined with a pore network model the liquid water ($\theta = 95°$) invasion into a Freudenberg H14C7 carbon felt and a SGL 28BC carbon paper. The pore network was extracted from high-resolution tomographic data and the simulated $p_c - S$ curves revealed that liquid water invasion into the H14C7 required higher capillary pressures, which would promote enhanced water management. Palakurthi et al. [268] employed both the VoF and the FM method to predict primary drainage of liquid water ($\theta = 55°$) in a stochastically reconstructed fiber structure. Comparing the results of both methods, the simulated $p_c - S$ relations agreed well in the intermediate saturation range of 15 to 80 %. However, the FM was found to overpredict the capillary entry pressure at high saturations and to underestimate the residual saturation for high capillary pressures. These deviations were accounted to the reduced-order model neglecting capillary filling dynamics and contact line physics. Sabharwal et al. [139] developed a cluster-based FM model to investigate liquid water invasion into the µCT reconstruction of a Toray TGP-H-120. In a parametric study, liquid water invasion was then simulated under variation of the contact angle ($\theta = 90 - 120°$), resulting in linear shifts towards higher capillary pressures along with increasing hydrophobicity. Whereas this trend complies with expectations, the overall agreement of the simulated $p_c - S$ curves with an experimental reference was found to be rather poor. This discrepancy was related to the basic assumption of spherical pores in the FM method. Niu et al. [102] employed a VoF model to examine the liquid water transport inside a stochastic reconstruction of a Toray TGP-H-060. Imposing four different capillary pressures and setting a uniform contact angle of $\theta = 109°$, the simulations yielded average saturations which agreed well with the experimental reference from X-ray tomographic microscopy (XTM). The Leverett correlation was on the other hand found to strongly overestimate the saturation at higher capillary pressures. Satjaritanun et al. [269] investigated the transport of liquid water in a SGL 10BA using a free surface LB model. The GDL microstructure was directly reconstructed from µCT imaging data and non-wetting phase invasion was then simulated for different scenarios of liquid water injection points and varying contact angles. As expected, the simulations yielded higher saturations for increasing wettabilities. Furthermore, the simulated $p_c - S$ curve was found to agree well with the experiment for a contact angle of $\theta = 130°$. In another study, Niu et al. [270] utilized their VoF model again to investigate the $p_c - S$ relation of a Toray TGP-H-090. The GDL microstructure was reconstructed using a stochastic method and distributing two different PTFE loadings of 10 and 20 wt% either homogeneously or heterogeneously

along the GDL thickness, corresponding to different additive drying procedures in GDL manufacturing. Mixed wettability was then modeled by defining contact angles of $\theta_{\mathrm{CF}} = 80°$ and $\theta = 109°$) for the carbon fibers and PTFE, respectively. Predicting the process of liquid water invasion, the simulated $p_c - S$ curve agreed reasonably well with references from both experiment (Gostick et al. [261]) and LB simulation (Hao and Cheng [263]). In addition, the Leverett correlation was found to provide an acceptable description for the $p_c - S$ characteristics at a lower PTFE loading of 10 wt%, whereas it deviated significantly at the higher hydrophobic additive content. This observation was primarily related to the circumstance that the Leverett J-function assumes one uniform contact angle (in this case $\theta = 80°$, thereby neglecting mixed wettability. For the homogeneous PTFE distribution, the simulated $p_c - S$ curve was furthermore found to be closer to the experiment. Zhou et al. [271] also employed a VoF model to study the liquid water transport at different levels of GDL compression. A porous microstructure was therefore stochastically reconstructed and subsequently virtually compressed using the finite element method and assuming uniform deformation. Liquid water invasion ($\theta = 109°$) was then simulated for five different compression ratios and the resulting $p_c - S$ curves showed a general saturation decrease along with increasing compression, owing to smaller average pore sizes. Moreover, new capillary pressure-saturation relations were derived as exponential fit functions for each of the five compressive load cases. Based on a previous experimental study by Forner-Cuenca et al. [24] on GDLs with patterned wettability, Tranter et al. [272] performed liquid water invasion simulations using PNM. The pore networks for a Toray TGP-H-060, Freudenberg H23 and Sigracet SGL 24AA were extracted by watershed segmentation of µCT images and the pore throats were modeled as toroidal, according to Purcell's model [250]. Investigating four different pattern widths for the hydrophilic/hydropobic zones and two additive coating loads, the simulated $p_c - S$ curves agreed to a large extent well with the experiment. However, amongst others the model partly overpredicted phase separation, which was related to insufficient representation of the pore surface morphology and connectivity. Yang et al. [273] developed a pseudopotential LB model to investigate the two-phase capillary behavior of a Toray TGP-H-090. A GDL microstructure was reconstructed using stochastic methods and PTFE was distributed randomly. Mixed wettability was modeled with contact angles of $\theta_{\mathrm{CF}} = 95°$ and $\theta_{\mathrm{PTFE}} = 125°$ for carbon fibers and PTFE, respectively. Liquid water invasion was then simulated for two different additive loadings of 10 and 20 wt% and the results were in general qualitative agreement with experiments ([261, 263]) and simulations (LBM [263] and VoF [270]). Zhu et al. [274] combined solid mechanics simulations and a diffuse-interface Lattice Boltzmann model to study the effect of compression on the liquid water transport within a stochastically reconstructed GDL. Considering compression ratios of 0, 10 and 20 %, the simulated $p_c - S$

curves were found to be shifted towards higher capillary pressures, which can be related to increasing capillary transport resistance due to proceeding pore space constriction upon compression. A diffuse-interface LB model was also utilized by Zhang et al. [275], who investigated the capillary transport of liquid water in a Toray TGP-H-060 carbon paper and a Freudenberg H2315 carbon felt. The microstructures were reconstructed using a stochastic method in the former case and by segmentation of µimaging data in the latter case. A PTFE loading of 7 wt% was furthermore deployed to both samples and a binder component was additionally considered for the Toray GDL. Capillary invasion of liquid water was then simulated and the resulting $p_c - S$ curves indicated for the carbon paper a higher transport resistance along the GDL thickness as compared to the the in-plane direction. For the carbon felt GDL the trend was vice-versa, which was related to different internal pore structures.

As evident from the previous paragraph, over the past decades many PSM studies have been devoted to the investigation of $p_c - S$ characteristics in GDLs. Whereas these works provide interesting insights on influencing factors for the capillary liquid water transport in GDLs, most of them neglect mixed wettability in assuming uniform contact angles. Moreover, all of the aforementioned studies focus exclusively on the primary intrusion (or primary drainage [268]) and thereby neglect capillary hysteresis. However, the latter is an important characteristic of porous media, which can have non-negligible consequences in applications such as in PEM fuel cell water management. Amongst others, Shao et al. [276] showed that recurring liquid water intrusion and drainage cycles can lead to voltage hysteresis in operating PEM fuel cells. Therefore, capillary hysteresis of GDLs should not be neglected and further investigations are required to better understand the underlying multiphase transport phenomena and their influencing parameters. One study which considered capillary hysteresis was presented by Hao and Cheng [263]. In their work, the authors simulated liquid water transport through Toray TGP-H-090 carbon papers using a free-energy LB model. The GDL microstructures were stochastic reconstructions with 10 and 30 wt% of randomly distributed PTFE and mixed wettability was modeled with contact angles of $\theta_{\mathrm{CF}} = 80°$ and $\theta_{\mathrm{PTFE}} = 115°$. Simulating both intrusion and drainage of liquid water, the predicted $p_c - S$ curves were in reasonable agreement with experimental data for an intermediate saturation range between approximately 20 and 90 %. At both low and high saturations, however, the simulation results showed increasing deviation from the test bench data, which was related to limitations in the representativeness of the stochastic GDL reconstruction. Based on the predicted $p_c - S$ curves, a modified Leverett relation was furthermore derived, extending the J-function with two exponential functions. Tranter et al. [277] studied capillary hysteresis as well and utilized pore network modeling for injection and withdrawal of liquid water into and from a stochastic GDL reconstruction

of a Toray TGP-H-090 with 20 wt% PTFE. Assuming neutral wettability, the simulated $p_c - S$ curves for both injection and withdrawal agreed well with the experiment, but only when the capillary entry pressure was described with Purcell's toroidal model (see eq. (3.132) and [250]). When the standard PNM approach was used ($p_c - S$ according to eq. (2.14)), on the other hand, capillary hysteresis was found to be significantly underpredicted.

In the subsequent sections of this chapter, capillary hysteresis is thoroughly investigated for a carbon felt GDL by Lattice Boltzmann simulation of both liquid water intrusion and drainage under variation of several model and simulation parameters. For this purpose, GDL microstructures are reconstructed via segmentation of high-resolution µCT imaging data for a plain and additive-treated Freudenberg H14 carbon felt. Representative GDL subvolumes are then cut out from these base geometries by selection according to a novel approach based on the analysis of porosity profiles. For the impregnated GDL sample, the solid material in the binarized microstructure is furthermore differentiated into support material and additive component using an in-house developed algorithm. Subsequently, a computational model is set up according to the boundary conditions of an experimental test bench for the measurement of $p_c - S$ relations. Moreover, special attention is paid to ensure proper modeling of experimental surface effects. Employing the 3D color-gradient multiphase Lattice Boltzmann model from Chapter 3, both liquid water intrusion and drainage are then simulated to recover the capillary hysteresis for the reconstructions of the plain and additive-treated GDL. In addition, capillary characteristics are thoroughly investigated for different influencing factors by variation of several model and simulation parameters such as fluid properties, lattice resolution or wettability. Furthermore, the simulated $p_c - S$ curves and thus the LB model are also validated against experimental data. In addition, new $p_c - S$ relations are derived from the simulation results by curve fitting. Ultimately, the major outcomes of this chapter have been also published in Sarkezi-Selsky et al. [278].

4.2 Geometry generation for GDL microstructures

Microstructure reconstruction is an essential and yet challenging task for pore-scale simulations. Most commonly, the complex geometries are generated based on stochastic models or experimental imaging data, as reviewed by Shojaeefard et al. [279]. The former reconstruction approach offers the advantage of a parametric description for a structure consisting of geometric objects with well-defined shapes and surfaces. However, development of a sophisticated stochastic reconstruction method is difficult and calibration with real microstructural data is often necessary. Reconstruction from experimental imaging data such as X-ray micro-computed tomography (µCT) or Focused Ion Beam-

Scanning Electron Microscopy (FIB-SEM), on the other hand, in general requires neither a mathematical model nor *a priori* calibration. Based on real microstructural information, the geometry generation thus necessitates in principle less, if any, assumptions. However, a good reconstruction can only be accomplished for high-quality imaging data and utilizing an appropriate image segmentation procedure. In this work, GDL microstructures are reconstructed by segmentation of high-resolution µCT imaging data.

4.2.1 X-ray micro-computed tomography (µCT) of carbon felt GDLs

µCT imaging is conducted for a plain and a PTFE-treated fiber substrate of a Freudenberg H14 carbon felt. The scanning procedure is performed with a SkyScan 1172 desktop µCT by Bruker MicroCT (Belgium) and setting the experimental conditions as listed in Table 4.1. Single grayscale images are then reconstructed from raw imaging data with a resolution of 0.96 µm per pixel and using the software NRecon by Bruker MicroCT (Belgium). In order to achieve comparability across the different microstructures, the grayscale reconstruction is conducted with the same parameters and correction factors for all samples and as listed in Table 4.1. At this point, it is emphasized that all µCT imaging and subsequent greyscale image reconstruction (not to be confused with the GDL microstructure reconstruction, see Section 4.2.2) in the frame of this work has been conducted by Henrike Schmies (Department for Electrochemical Energy Technology, Institute of Engineering Thermodynamics, DLR Oldenburg).

Table 4.1: Experimental conditions of the µCT imaging and the subsequent grayscale reconstruction.

Parameter	**Value**	**Unit**
Acceleration voltage	54	kV
Current	85	µA
Rotation step	0.25	°
Random movement	4	–
Averaging frames	10	–
Resolution	0.96	µm/px
Exposure time	3015	ms
Stage temperature	23–25	°C
Reconstruction grayscale	−0.05 to 0.05	–
Beam hardening correction	15	%
Ring artifact correction	19	–

4.2.2 GDL microstructure reconstruction via binarization

X-ray micro-computed tomography provides microstructural information as grayscale image slices along a sample's thickness. Depending on the morphology of the sample and the imaging conditions, the pixel values within these images are characterized by a certain grayscale histogram. Hence, the raw imaging data does not provide a clear distinction between different materials (e.g., solid or void) and has to be further postprocessed by segmentation of the images into geometric objects to be used in subsequent microstructure analysis and simulation. While there exist different concepts for image segmentation [280, 281], one widely used approach is represented by thresholding methods. In these approaches, a grayscale image is segmented by definition of a threshold, beyond which pixels are identified and isolated into respective object classes according to their grayscale value. Depending on the number of classes, this thresholding process is also commonly referred to as binarization or trinarization. Appearing as a seemingly simple task, a reasonable choice of a grayscale threshold is yet oftentimes challenging. While in principle the threshold can be set to arbitrary values, images can be falsely segmented with ease. This circumstance poses in particular an issue, when properties of the geometric objects are *a priori* unknown, which is the general case. Moreover, the imaging data in general has to be considered as imperfect, amongst others due to limited spatial resolution and imaging artifacts deteriorating the structural information [282, 283]. Trying to alleviate these intricacies of image segmentation, several thresholding concepts have been developed in the past, among which Otsu's method [284] represents the most prominent approach. While many of these routines provide sophisticated object identification approaches, their performance oftentimes depends on the quality and characteristic of the raw image data [285]. In this work, grayscale µCT images are therefore binarized by manual thresholding using manufacturer specifications on the GDL structural properties.

GDL microstructures for a plain and a PTFE-impregnated carbon fiber substrate of a Freudenberg H14 are reconstructed from µCT imaging data obtained as described in Section 4.2.1. For this, sequential 2D grayscale image slices from µCT (Figure 4.1a) are imported into the commercial software suite GeoDict [286] to be further post-processed. During the import step, the µCT data is transferred from pixel-based image slices to a 2D image stack composed of voxels (volume elements). In order to sharpen and smoothen image contours, a sharpening [287] and a median filter [288] is then applied, each with a radius of one voxel. Subsequently, the image data is segmented into geometric objects of solid and void material via manual thresholding. For the plain carbon fiber substrate, this binarization is conducted using manufacturer specifications on the Freudenberg H14 [289]. With an areal weight of $m_{\mathrm{H14}} = 65\,\mathrm{g/m^2}$ and thickness of $L_{z,\mathrm{H14}} = 150\,\mu\mathrm{m}$, the overall porosity of the GDL can be estimated to

$$\epsilon_{\mathrm{H14}}^{\mathrm{est}} = \frac{V_p}{V_{\mathrm{H14}}} = 1 - \frac{V_{\mathrm{CF}}}{V_{\mathrm{H14}}} = 1 - \frac{\rho_{\mathrm{H14}}}{\rho_{\mathrm{CF}}} \approx 1 - \frac{m_{\mathrm{H14}}/L_{z,\mathrm{H14}}}{\rho_{\mathrm{CF}}} \approx 75\,\% \tag{4.1}$$

assuming a carbon fiber density of $\rho_{\mathrm{CF}} = 1.75\,\mathrm{g/cm^3}$ based on the measurements of Rashapov et al. [290]. Targeting a porosity of $\epsilon_{\mathrm{H14}}^{\mathrm{est}} = 75\,\%$ for the microstructure reconstruction, the binarization is then executed by selecting a threshold value accordingly. The resulting final binarized 3D microstructure of the H14 carbon fiber felt has a spatial resolution of $\Delta x^{\mathrm{phys}} = 0.96\,\mu\mathrm{m}$ per voxel (vx) and is visualized in Figure 4.1b.

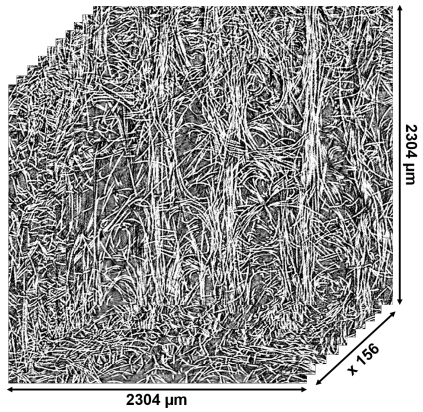

(a) 2D grayscale image stack (µCT).

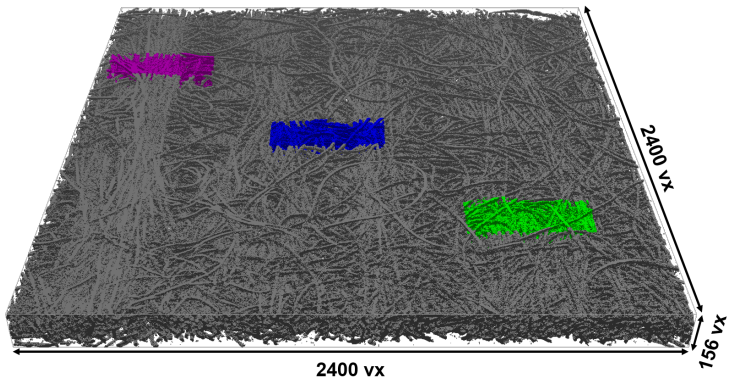

(b) Binarized 3D microstructure (0.96 µm per voxel).

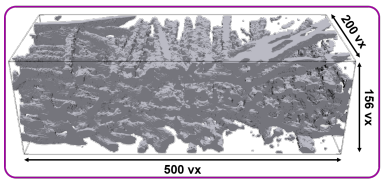

(c) Subvolume 2.

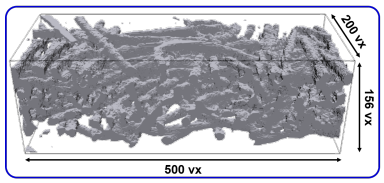

(d) Subvolume 1.

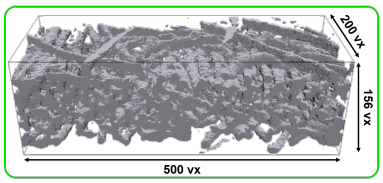

(e) Subvolume 3.

Figure 4.1: Microstructure reconstruction for the Freudenberg H14 carbon fiber substrate: (a) 2D grayscale image slices from µCT with a resolution of 0.96 µm per pixel are segmented via manual thresholding into (b) a binarized 3D microstructure with $\Delta x^{\mathrm{phys}} = 0.96\,\mu\mathrm{m}$ per voxel (vx). For the subsequent simulative studies, three GDL subvolumes (c)-(e) are selected, as indicated by colored patches in (b).

In analogous fashion, above segmentation approach via manual thresholding is also carried out for the microstructure reconstruction of the impregnated H14 carbon fiber felt. However, lacking structural information from both manufacturer and literature, a slightly different route has to be taken. Depending on the impregnation technique during the GDL manufacturing process, additives are observed to be distributed rather homogeneous or heterogeneous along the material thickness [51, 291, 292]. For the latter case, the additive is usually reported to accumulate primarily near the surface and rarely in the core region of the GDL [53, 54, 293]. Given that this assumption also holds for the impregnated

H14, the porosity in the GDL core region of the plain and impregnated fiber substrate is expected to be similar. Hence, the microstructure of the latter is binarized by manual thresholding such that it exhibits in the GDL core region a local porosity similar to the plain H14. Following the aforementioned modified reconstruction approach yields an overall porosity of $\epsilon^{\text{est}}_{\text{H14impr}} = 71.41\,\%$ for the binarized impregnated fiber microstructure shown in Figure 4.2a. At this point, it is noted that the presented segmentation approach so far only achieves a differentiation of void and solid material for the underlying GDL microstructure. Whereas further distinction between different solid phases (support and additive material) could be in general achieved with the selection of a second greyscale threshold value, this approach is in this case obstructed by similar phase contrasts (i.e., grey scale values) of the carbon fibers (support) and PTFE (additive) in µCT imaging [294–296]. Given their dissimilar wettability, on the other hand, differentiation of the two solid phases is a prerequisite for the appropriate modeling of multiphase transport in the GDL. Therefore, a novel approach for the segmentation of carbon fibers and additive is developed in this work and presented in Section 4.2.4 and Section 4.2.5.

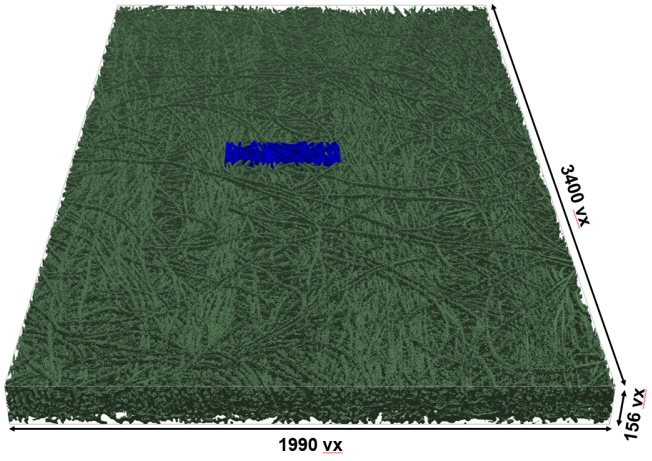

(a) Binarized 3D microstructure (0.96 µm per voxel).

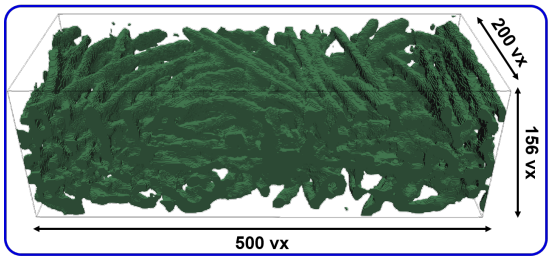

(b) Subset.

Figure 4.2: Microstructure reconstruction for the impregnated Freudenberg H14 carbon fiber substrate: From the (a) binarized 3D microstructure ($\Delta x^{\text{phys}} = 0.96\,\mu\text{m}$ per voxel), a (b) GDL subvolume is selected for the subsequent simulative studies, as indicated by a blue patch.

In a first microstructural analysis, the reconstructions of the plain and the impregnated fiber substrate are characterized by means of their through-plane porosity profiles and pore size distributions. The latter are determined with the GeoDict module Granulometry, which calculates geometric pore size distributions (gPSDs) by fitting spheres of varying diameters into the void volume of individual pores. As shown by comparison of the through-plane porosity profiles in Figure 4.3a, the additive (here assumed as pure PTFE)

appears in fact to be distributed heterogeneously along the thickness of the GDL. Moreover, the additive is found to be located primarily near the respective GDL surfaces, as indicated by two minima in the local porosity. In summary, the observed porosity profiles for the plain and impregnated fibers are characteristic for carbon felt GDLs and have been also reported in previous works [53, 297]. Another indication for the subsurface deposition of the additive can be found by comparison of the geometric pore size distributions (Figure 4.3b). Impregnation of the fibers apparently leaves the small- to medium-size pore space ($d_p^{\text{phys}} < 30\,\mu\text{m}$) in the GDL core region unaltered. Moreover, the characteristic peak of the distributions is for both microstructure reconstructions the same and the median resides around $d_{p,50}^{\text{phys}} \approx 21\,\mu\text{m}$, which is in accordance to literature [57, 275, 298]. Only for larger diameters beyond $d_p^{\text{phys}} > 30\,\mu\text{m}$ near the GDL surface, a reduction in the average pore size upon PTFE impregnation is observed.

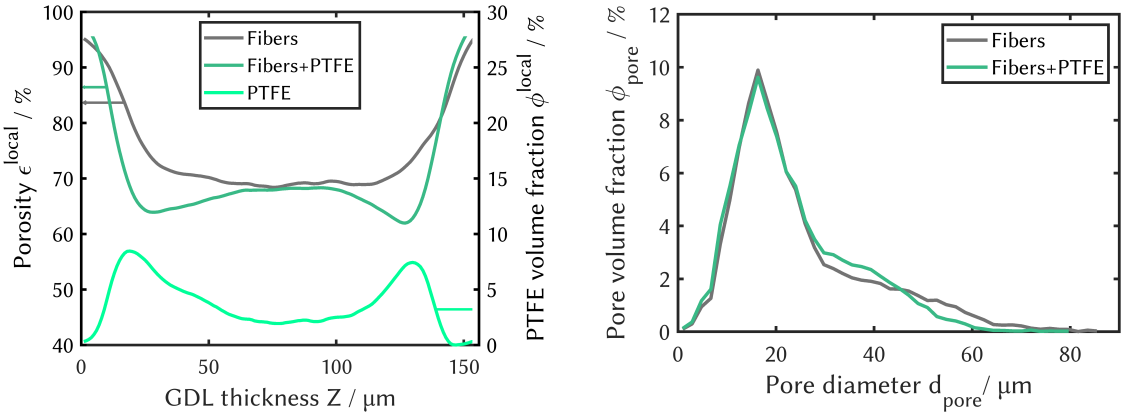

(a) Through-plane porosity profile.

(b) Pore size distribution.

Figure 4.3: Microstructural analysis of the reconstructions for the plain (Figure 4.1b) and impregnated fiber substrate (Figure 4.2a). (a) A decrease in the through-plane porosity profile indicates heterogeneous PTFE distribution along the GDL thickness. (b) Deviating for large pore diameters, the geometric pore size distributions (gPSDs) suggest additive deposition near the GDL surface.

4.2.3 Selection of representative GDL subvolumes

The µCT-scanned and binarized GDL microstructures (Figure 4.1b and Figure 4.1b) are with a base area of 4–7 mm^2 smaller than typical active area sizes of PEM fuel cells [299]. However, due to the geometric complexity requiring a high resolution, the domain sizes of the GDL reconstructions are still beyond accessibility for computationally expensive PSM simulations. In principle, this issue could be resolved straightforwardly by reducing the system size. Below a certain domain size, however, the subset does not recover the macroscopic structural properties of the overall GDL carbon felt anymore. Thus, in order

to conduct simulative studies of significance, a representative elementary volume (REV) has to be found, being the smallest microstructure subset which still recovers the overall macroscopic structural properties of the GDL [300–303]. Determination of such a REV is an omnipresent issue to microstructure-resolved simulations. However, as the macroscopic convergence limit depends on the porous medium and the structural property (e.g., porosity, pore size distribution, ...) [300, 303], researchers have come to different conclusions with regard to appropriate REV sizes. While the low GDL thickness of several hundredths of micrometers is usually entirely considered, REV studies mostly focus on finding a representative elementary area (REA). Based on the structural properties of dry GDLs, studies have derived a wide range for representative elementary areas of 0.5–2 mm^2 [293, 304–306]. Roth et al. [307] on the other hand reported that the REA of partially saturated GDLs varies from 0.35 to 1.6 mm^2, depending on the level of saturation. However, based on high-precision input data, some researchers also find lower representative elementary subsets. Hasanpour et al. [308] suggested that for GDL microstructure reconstructions from high-resolution µCT 1.167 µm per pixel, macroscopic properties can be already recovered with REA sizes of $500 \times 500\,\mu\mathrm{m}^2$. For the CFD transport modeling in stochastic GDL reconstructions with 0.8–0.64 µm per pixel, Bao et al. [76] even found a REV as small as $190 \times 190 \times 190\,\mu\mathrm{m}^3$. In this work, representative subvolumes are identified based on the analysis of porosity profiles for the GDL microstructure reconstructions. Subsequently, the representativeness of the REVs is validated with respect to their pore size distributions (PSDs) and capillary pressure-saturation characteristics (Section 4.4.8). This approach of REV selection for GDL microstructures presents to the author's knowledge a novelty to the field of microstructure-resolved modeling and simulations.

At first, a representative GDL subset is selected for the plain fiber substrate. Figure 4.4 shows the porosity profiles along the three spatial directions of the binarized microstructure (Figure 4.1b). In the first in-plane direction (Figure 4.4a), the porosity is found to exhibit periodic fluctuations with alternating local minima and maxima for roughly every $L_x^{\mathrm{char}} \sim 500\,\mu\mathrm{m}$. These observations are in accordance with literature findings [53, 297] for a similar Freudenberg H2315 GDL. With respect to Figure 4.1, these fluctuations can be identified with the bare eye as regions of denser fiber bundles and gaps of higher porosity. This characteristic is related to the GDL manufacturing technique of hydro-entangling [51, 53–55], in which loose carbon fibers are mechanically intertwined by water jet arrays to form carbon felt materials. Thus, the characteristic length $L_x^{\mathrm{char}} \sim 500\,\mu\mathrm{m}$ is a result of the distance between the individual water jets. Since the carbon fibers are aligned parallel to the production line, fiber bundling by hydro-entangling mainly occurs in the same direction, rendering the porosity profile in the second in-plane direction (Figure 4.4b)

rather uniform. Lastly, along the GDL thickness the porosity profile (Figure 4.4c) exhibits a shape with convex curvature, which is typical for carbon felt materials [297, 309].

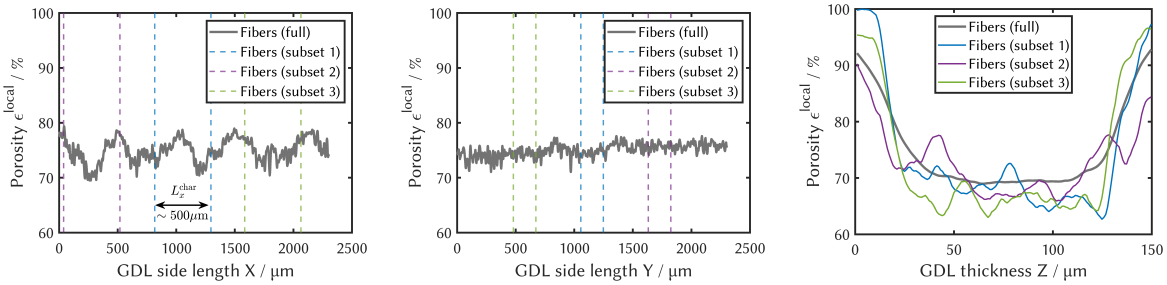

(a) In-plane X. (b) In-plane Y. (c) Through-plane Z.

Figure 4.4: Porosity profiles for the GDL microstructure reconstruction of the plain fiber substrate. In (a) and (b) dashed colored lines indicate the cutout positions of the GDL subvolumes shown in Figure 4.1. In (c), through-plane porosity profiles are compared for the full GDL microstructure reconstruction and its subvolumes.

Based on above analysis of the porosity profiles, a GDL subvolume is selected as REV in order to recover the characteristic structural features of the overall microstructure of the plain fibers. Corresponding to the characteristic length $L_x^{\text{char}} \sim 500\,\mu\text{m}$, the subvolume dimension in the first in-plane direction is therefore chosen to $N_x = 500$ voxel, with $\Delta x = 0.96\,\mu\text{m}$ per voxel. As in the second in-plane direction no characteristic in the porosity profile is detectable, the subvolume size is set to $N_y = 200$ voxel in order to reduce computational expense within the subsequent studies. The cutout positions for the GDL subvolume are set close to the center of the respective in-plane direction (blue dashed lines in Figure 4.4a and Figure 4.4b. Moreover, in the 'In-plane X' direction, the cutout is placed such that a porosity maximum is encompassed in the center of the domain. In the through-plane direction, the whole microstructure thickness of $L_{z,\text{H14}} = 150\,\mu\text{m}$ is considered in selecting $N_z = 156$ voxel for the third subset dimension. As a result, a REV is obtained with a GDL subvolume of the binarized plain fiber microstructure and a domain size of $500 \times 200 \times 156$ voxels. The latter is illustrated in Figure 4.1 and will be used as the default GDL subvolume for the plain fiber substrate in all subsequent studies of this work. Repeating this procedure of REV selection, two additional GDL subvolumes are generated in order to investigate structural heterogeneity for the chosen domain size. As visualized in Figure 4.1b, the additional subvolumes are chosen in order to cover different areas all across the full binarized GDL microstructure. This REV selection is again illustrated for the in-plane porosity profiles in Figure 4.4. In the 'In-plane X' direction (Figure 4.4a), the cutout positions are furthermore placed such that the respective GDL subvolumes encompass a porosity minimum in their domain center. As opposed to the centered porosity maximum for the default GDL subvolumes, these selections are

made intentionally in order to investigate possible boundary effects as well. Figure 4.4c shows the through-plane porosity profiles for all three GDL subvolumes in comparison to the full binarized microstructure of the plain H14 fiber substrate. Whereas the domain size reduction leads to a notable increase of fluctuations in the local porosity, all three GDL subvolumes appear to recover the macroscopic porosity profile of the full GDL microstructure well. Furthermore, the representativeness of the GDL subvolumes can be additionally confirmed by comparison of their pore size distributions, as shown in Figure 4.5a. While the pore size distributions of the subvolumes exhibit again increased fluctuations, they agree well with the PSD of the whole GDL microstructure reconstruction, thereby confirming the representativeness of the chosen REV sizes.

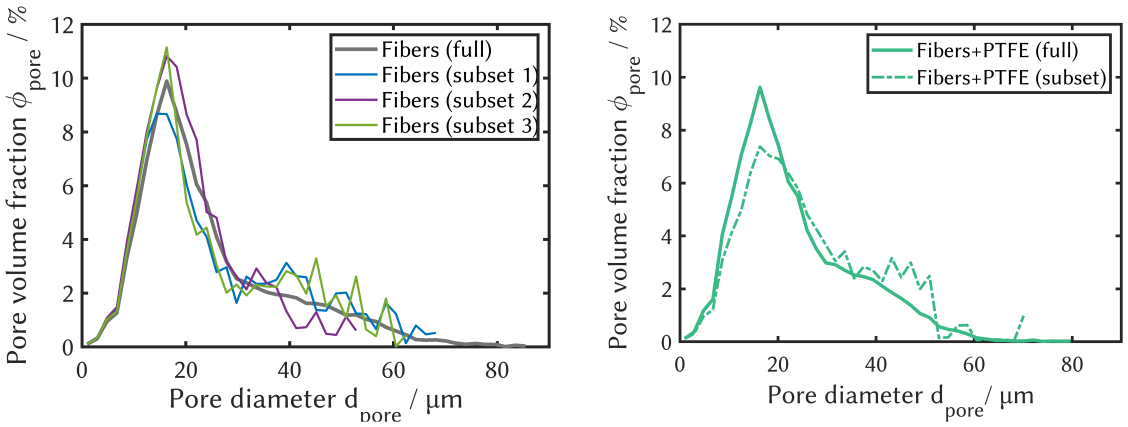

(a) Plain fiber substrate.

(b) Impregnated fiber substrate.

Figure 4.5: Comparison of geometric pore size distributions (gPSDs) for the full GDL microstructure reconstructions and their subvolumes.

With the previously described REV selection scheme, a representative elementary volume is selected for the binarized microstructure of the impregnated fibers (Figure 4.2) as well. The subvolume is taken from a centered position, as illustrated by the porosity profiles in Figure 4.6. In the 'In-plane X' direction, the GDL subvolume is positioned in order to encompass a porosity maximum (Figure 4.6b such as for the default plain fiber subset (see Figure 4.4b). Based on a comparison of the through-plane porosity profiles Figure 4.6c and pore size distributions Figure 4.5b, also the impregnated GDL subvolume is found to be representative for its overall microstructure. At this point, it is acknowledged that larger REVs may result in quantitatively even better agreement of the subvolume and the overall macroscopic properties. However, as this work primarily focuses on qualitative investigations of capillary transport phenomena in GDL microstructures, the author is convinced that a good compromise is found between computational expense and accuracy. Moreover, the chosen GDL subvolumes will prove in Section 4.4.8 to be representative for the macroscopic multiphase transport characteristics of the GDL as well.

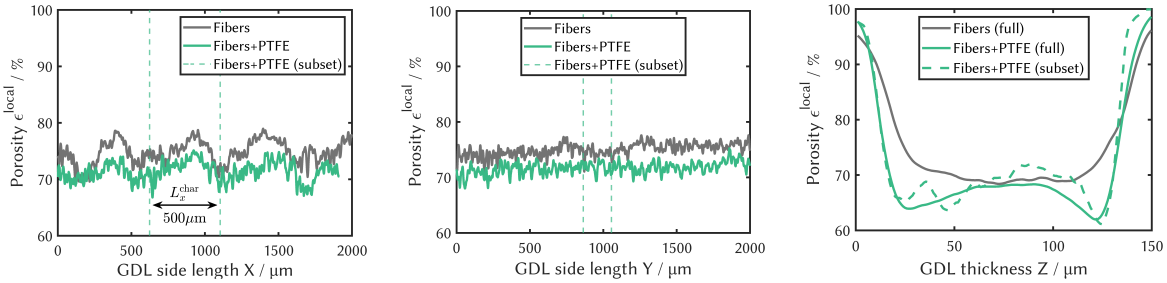

(a) In-plane X. (b) In-plane Y. (c) Through-plane Z.

Figure 4.6: Porosity profiles for the GDL microstructure reconstructions of the plain and impregnated fiber substrate. For the latter, a subvolume (see Figure 4.2) is selected with cutout positions as indicated by dashed colored lines in (a) and (b). In (c), the through-plane porosity profile of the subvolume is compared to the full GDL microstructure reconstructions of the plain and impregnated fiber substrate.

4.2.4 Derivation of a realistic PTFE loading profile

As introduced in Section 2.2.3, GDLs are typically wet-proofed by dip-coating with a hydrophobic agent such as polytetrafluoroethylene (PTFE) [51], fluorinated ethylene propylene (FEP) [310], perfluoropolyether (PFPE) or polyvinylidene difluoride (PVDF) [311] to improve their water removal capabilities. Depending on the type of the finalizing drying process (i.e., vacuum-drying or air-drying), additives are found to be distributed rather homogeneous or heterogeneous along the thickness of the GDL [270, 291, 292, 312]. Despite the non-negligible impact of different spatial additive distributions on the capillary transport characteristics, manufacturers usually don't provide detailed information on the hydrophobizing treatments of their GDL products. In this work, a heterogeneous through-plane additive loading profile is derived as a PTFE volume fraction $\phi_{\text{PTFE}} = V_{\text{PTFE}}/V_{\text{total}}$ by comparison of the through-plane porosity profiles for the microstructure reconstructions of the plain and impregnated fiber substrate. With an overall volume fraction of $\phi_{\text{PTFE}} = 3.68\,\text{vol}\%$, the local additive content is then determined as the through-plane porosity difference between the plain and impregnated fiber substrate, as shown in Figure 4.3a. Assuming a PTFE density of $\rho_{\text{PTFE}} = 2.15\,\text{g/cm}^3$ [313] ($\rho_{\text{CF}} = 1.75\,\text{g/cm}^3$ [290, 314]), this results in an overall weight-based additive loading of $\phi_{\text{PTFE}}^{(m)} = 16.36\,\text{wt}\%$, which is well in the range of 5–30 wt% commonly denoted in literature [22, 51, 308]. While this methodology provides information for the local and overall PTFE content in the GDL, the actual spatial distribution of the additive remains unknown. In favor of enhanced readability, the terms 'additive' and 'PTFE' will be used from here on interchangeably throughout the remainder of this work.

4.2.5 Segmentation of carbon fibers and PTFE in binarized microstructures

In grayscale images from µCT, differentiation of carbon fibers and PTFE is usually not possible due to similar phase contrasts [294–296]. In the past, spatial additive distributions within GDL microstructures have been therefore oftentimes investigated by experimental surface analysis methods such as atomic force microscopy (AFM) [315] or scanning electron microscopy (SEM) [53, 316]. However, these measurement techniques in general only allow for qualitative investigations. Moreover, the examination is restricted to sample surfaces and does not allow an in-depth analysis. In order to quantify local additive contents, researchers have combined SEM with energy dispersive x-ray spectroscopy (EDX) [292, 317–319] or Raman spectroscopy [320]. According to Manzi-Orezzoli et al. [294], however, these quantification methods suffer from limited sensitivity and lack of bulk information in being restricted to surface analysis. Lately, the aforementioned authors therefore combined high-resolution x-ray tomography and high-resolution neutron tomography to investigate the additive (FEP) fiber coverage in a Gadolinium-stained Freudenberg H23 GDL. While this new approach presents an interesting and potentially successful method for the experimental analysis of coating distributions in GDLs, such experimental efforts are beyond the scope of this work.

Since the experimental assessment of spatial additive distributions in the GDL microstructure is still a challenging task, the default PTFE coverage on the carbon fiber surfaces is for the subsequent parts of this work assumed with $\chi^{\mathrm{est}} = 50\,\%$ [321, 322]. Furthermore, a novel in-house algorithm is developed in this work to segment carbon fibers and PTFE in the binarized microstructure of the impregnated fiber substrate. Mimicking realistic additive distributions, the algorithm specifies PTFE predominantly in the vicinity of carbon fiber intersections, which is according to literature a preferential location for additive deposition [53, 54, 316, 317, 320]. At this point, it is noted that hydrophobic additives only affect the capillary transport in porous media when they are in direct contact with the pore space. For the subsequent modeling and simulation studies of this work, the PTFE surface coverage is therefore considered to provide a more appropriate parameter for the description of mixed wettability in the GDL than the additive loading.

Identification of fiber intersections: *OpeningPTFE*

In a first step, fiber intersections are located by application of a morphological opening operator [323] on the binarized GDL subvolume (Figure 4.2b) of the impregnated fiber substrate. For this, a sphere is used as a structuring element with a radius of six voxels. Figure 4.7 illustrates the identified fiber intersections for a cross-section halfway along the

GDL thickness. By assigning these fiber intersections as additive, the resulting PTFE loading and surface coverage add up to $\phi_{\mathrm{PTFE}} = 5.57\,\mathrm{vol\%}$ ($\phi^{(m)}_{\mathrm{PTFE}} = 24.38\,\mathrm{wt\%}$) and $\chi = 6.08\,\%$, respectively. After this first step, the obtained additive content is slightly higher than the target value of $\phi^{\mathrm{est}} = 3.68\,\mathrm{vol\%}$ derived in Section 4.2.4. The PTFE coverage on the fiber surfaces on the other hand is much lower than the desired estimate of $\chi^{\mathrm{est}} = 50\,\%$. The local additive distribution is furthermore illustrated in Figure 4.9.

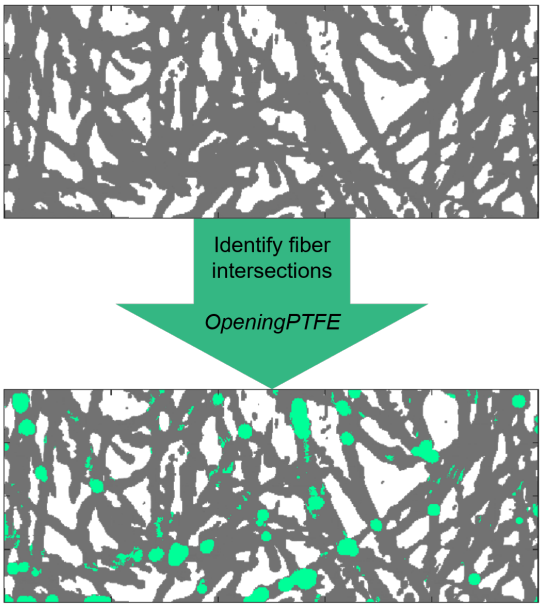

Figure 4.7: In-house algorithm for the segmentation of PTFE and carbon fibers in binarized GDL microstructures: A first subroutine *OpeningPTFE* identifies fiber intersections by applying a morphological opening operator [323] to the binarized microstructure of the impregnated fiber substrate.

Increase of the fiber surface coverage: *Bulk2SurfPTFE*

Assignment of the whole fiber intersections as additive apparently leads to bulky PTFE clusters with a fiber surface coverage of $\chi = 6.08\,\%$ much lower than the target value of $\chi^{\mathrm{est}} = 50\,\%$. In a second step, PTFE voxels are therefore redistributed by swapping bulk additive voxels with carbon fiber surface voxels in the vicinity of the fiber intersections. This methodology is carried out constrained by two conditions:

- In the through-plane direction, additive is reassigned with a probability based on the derived volume fraction profile (Figure 4.13b).
- PTFE is only redistributed to solid surface sites which are either part of a fiber intersection cluster or adjacent to an additive surface site. In this way, a branch-like propagation of superficial PTFE emanating from the fiber intersections is achieved.

The voxel-wise redistribution of additive from bulk to solid surface sites is then carried out until the desired PTFE surface coverage of $\chi^{\text{est}} = 50\,\%$ is reached. Since only the position but not the overall number of additive voxels is changed, the second subroutine *Bulk2SurfPTFE* maintains the overall PTFE content of $\phi_{\text{PTFE}} = 5.57\,\text{vol}\%$. Furthermore, both global and local porosity remain constant, as only different solid phases are reassigned. Figure 4.8 illustrates this redistribution for a cross-section halfway along the GDL thickness. Evidently, the local surface coverage is hereby significantly increased as well. As a result of the local porosity and additive loading profile (Figure 4.3a), χ^{local} is furthermore found to be more heterogeneous after the redistribution (Figure 4.9b). on the Other hand, The local PTFE volume fraction ϕ^{local} is found to be only slightly altered (Figure 4.9a).

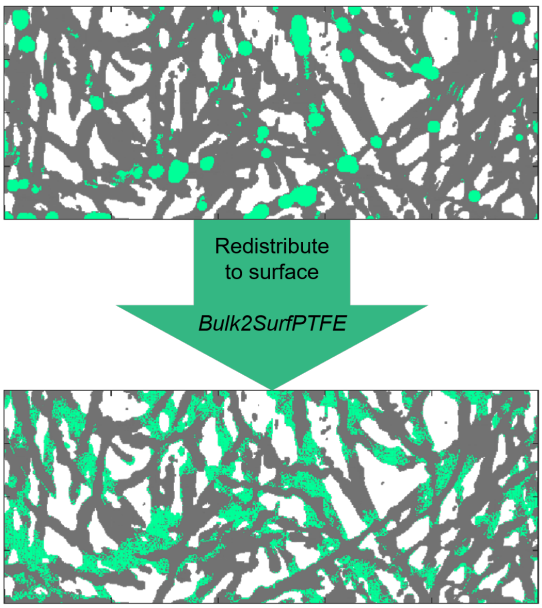

Figure 4.8: In-house algorithm for the segmentation of PTFE and carbon fibers in binarized GDL microstructures: A second subroutine *Bulk2SurfPTFE* redistributes additive by swapping PTFE voxels from solid bulk sites with carbon fiber voxels on solid surface sites near the identified fiber intersections.

Reduction of the overall PTFE loading: *DecreaseBulkPTFE*

As apparent from Figure 4.9a, neither the first nor the second step of the PTFE algorithm ensure that the desired additive loading is realized for the binarized GDL microstructure. In a third subroutine, solid bulk PTFE is therefore replaced by carbon fiber material until the target additive loading of $\phi^{\text{est}} = 3.68\,\text{vol}\%$ is reached. For this solid phase reassignment, solid bulk PTFE is selected along the GDL thickness with a probability based on the difference between the PTFE volume fraction profile after *Bulk2SurfPTFE* and the target profile (see Figure 4.9a). However, as the number of replaceable solid

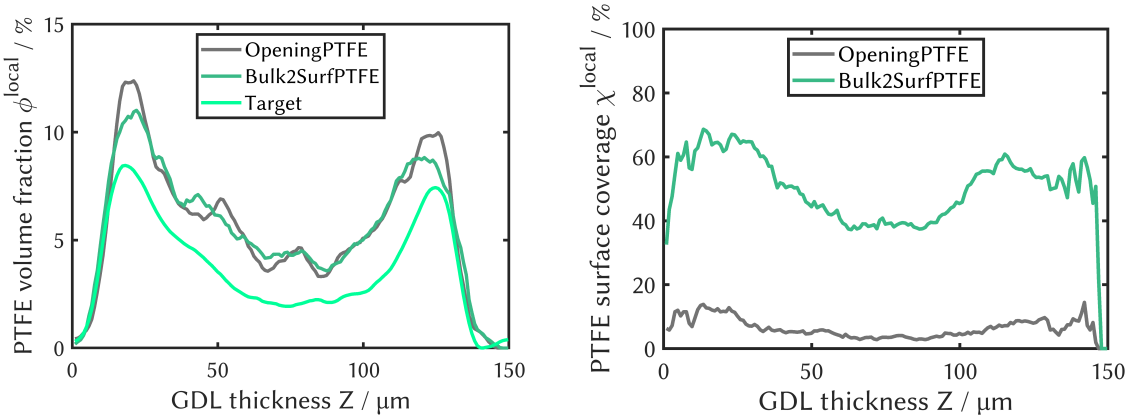

(a) PTFE loading.

(b) PTFE surface coverage.

Figure 4.9: In-house algorithm for the segmentation of PTFE and carbon fibers in binarized GDL microstructures: After identification of the fiber intersections (*OpeningPTFE*), the additive is redistributed from solid bulk to solid surface sites (*Bulk2SurfPTFE*) to increase the PTFE surface coverage χ^{local} (b). The target additive loading profile ϕ^{local} in (a) is derived as the difference in the local porosity ϵ^{local} of the plain and impregnated fiber substrate (Figure 4.3a).

bulk PTFE sites varies along the GDL through-plane direction, the local additive volume fraction ϕ^{local} in the GDL core region remains slightly above the desired value. With the target PTFE loading of $\phi^{est} = 3.68\,\text{vol}\%$ and the probabilistic nature of the third step, this is balanced by ϕ^{local} dropping below the desired value in the GDL surface regions as shown in Figure 4.10a. Since this adjustment of the PTFE loading only concerns additive in the bulk, neither the local nor the overall PTFE surface coverage is altered in this subroutine (Figure 4.10b).

Adjustment of the PTFE loading profile: *Surf2SurfPTFE*

The third subroutine realizes the desired overall PTFE loading of $\phi^{est} = 3.68\,\text{vol}\%$ but not the target profile for the local additive content. In a last step, PTFE is therefore redistributed on the solid surface to achieve the best possible match of ϕ^{local} and the target additive loading profile (Figure 4.3a). By only redistributing PTFE from one solid surface site to the other, *Surf2SurfPTFE* changes neither the overall additive loading nor the overall PTFE surface coverage. However, the local additive distribution embodied in ϕ^{local} and χ^{local} is altered. Ultimately, an almost perfect match with the target PTFE loading profile is achieved, as shown in Figure 4.11. The final binarized microstructure of the impregnated fiber substrate with segmented fibers and PTFE is visualized in Figure 4.12. An overview on the in-house algorithm and its two most characteristic subroutines *OpeningPTFE* and *Bulk2SurfPTFE* is furthermore provided in Figure 4.13.

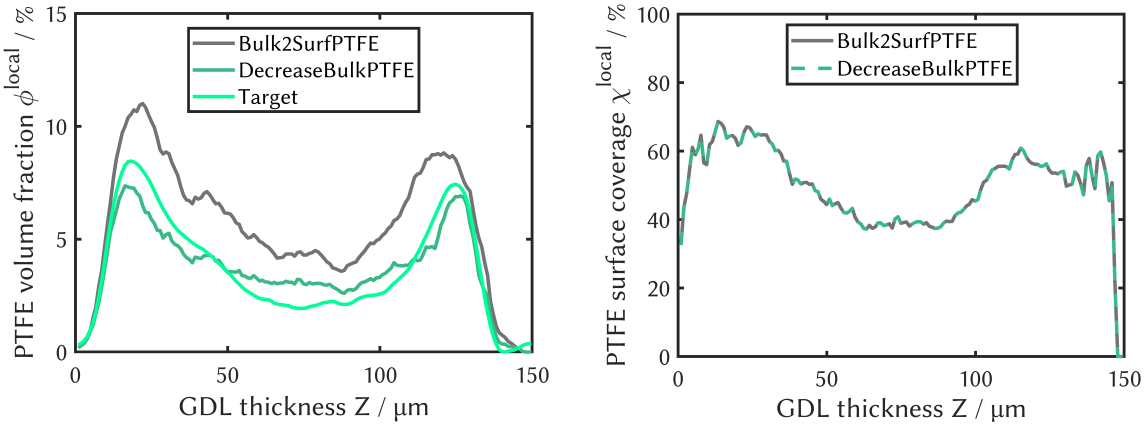

(a) PTFE loading. (b) PTFE surface coverage.

Figure 4.10: In-house algorithm for the segmentation of PTFE and carbon fibers in binarized GDL microstructures: After additive redistribution from solid bulk to solid surface sites (*Bulk2SurfPTFE*), solid bulk PTFE is replaced by carbon fiber material (*DecreaseBulkPTFE*) to realize the target additive loading of $\phi^{est} = 3.68\,\text{vol}\%$.

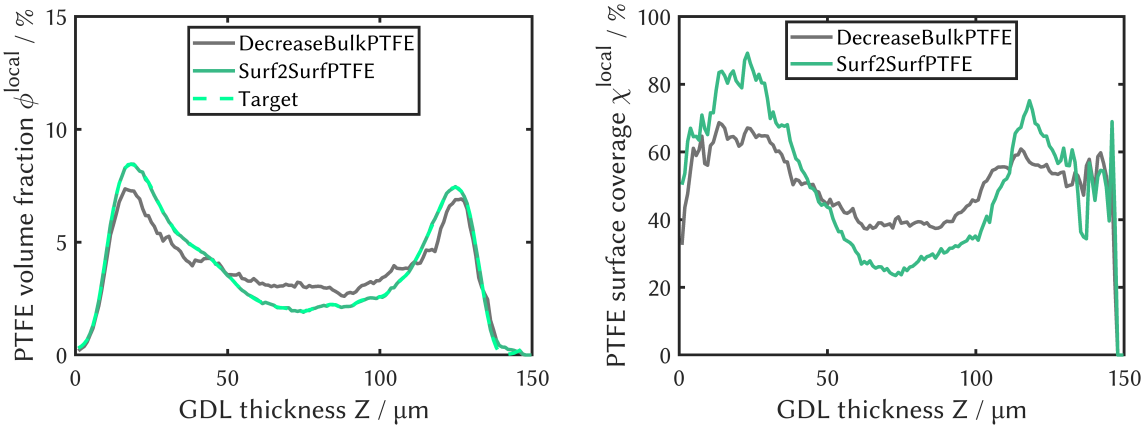

(a) PTFE loading. (b) PTFE surface coverage.

Figure 4.11: In-house algorithm for the segmentation of PTFE and carbon fibers in binarized GDL microstructures: After replacement of solid bulk additive by carbon fiber material (*DecreaseBulkPTFE*), PTFE is redistributed on the solid surface (*Surf2SurfPTFE*) to realize the target profile.

4.2.6 Variation of the spatial PTFE distribution

Acknowledging parametric uncertainty for the additive modeling, different PTFE distributions are subsequently generated to investigate the impact of wettability alteration on the capillary characteristics of the GDL. With the default case at $\chi = 50\,\%$ and employing the in-house algorithm (see Section 4.2.5 and Figure 4.13), the range of heterogeneous additive distributions is extended to microstructures with PTFE surface coverages of 25 and 75 %. These different PTFE distributions are realized in analogous fashion with the

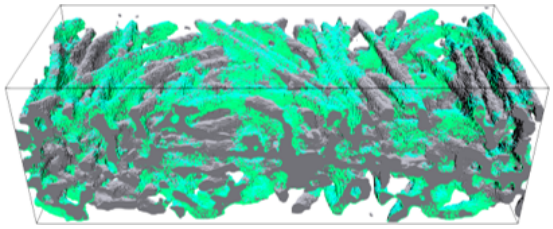

Figure 4.12: In-house algorithm for the segmentation of PTFE and carbon fibers in binarized GDL microstructures: Final impregnated fiber substrate reconstruction with segmented carbon fibers (gray) and PTFE (green). The overall additive loading and surface coverage equal $\phi_{\mathrm{PTFE}} = 3.68\,\mathrm{vol\%}$ ($\phi^{(m)}_{\mathrm{PTFE}} = 16.36\,\mathrm{wt\%}$) and $\chi = 50\,\%$, respectively.

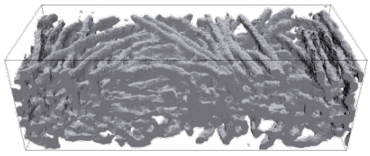

(a) Binarized fibers & PTFE.

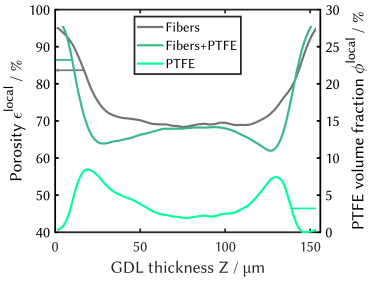

(b) PTFE loading.

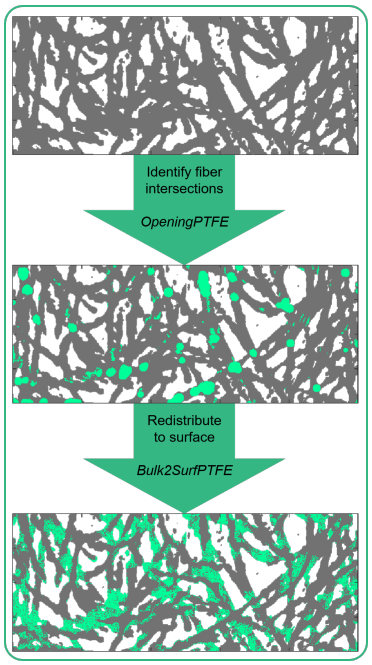

(c) Local distribution of PTFE.

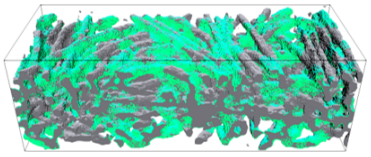

(d) Segmented fibers & PTFE.

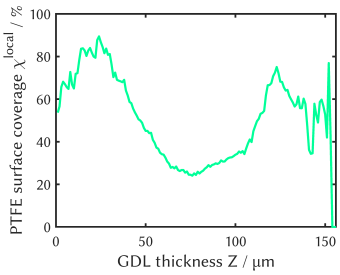

(e) PTFE surface coverage.

Figure 4.13: In-house algorithm for the segmentation of PTFE and carbon fibers in GDL microstructures: Fiber intersections in a binarized microstructure of impregnated fibers (a) are identified via a morphological opening operator (c). According to a desired additive loading profile (b), PTFE is then reassigned to the solid surface vicinal to the fiber intersections. The resulting microstructure (d) consists of carbon fibers and additive as two separate solid phases, of which the latter is distributed heterogeneously on the solid surface (e).

in-house algorithm as previously described in Section 4.2.5, but setting in *Bulk2SurfPTFE* different PTFE surface coverages accordingly. Figure 4.14 shows that the through-plane profiles of these heterogeneous additive distributions follow in general the same shape for both the loading (Figure 4.14a) and the surface coverage (Figure 4.14b). With respect to

the former, PTFE contents $\phi_{\mathrm{PTFE}}^{(m)}$ of 10.24 and 21.90 wt% are obtained for the additive surface coverages of 25 and 75 % (default: $\phi_{\mathrm{PTFE}}^{(m)} = 16.36$ wt%, $\chi = 50$ %). The GDL microstructure reconstructions of the impregnated fiber substrate for the three different heterogeneous PTFE surface coverages are illustrated in Figure 4.15.

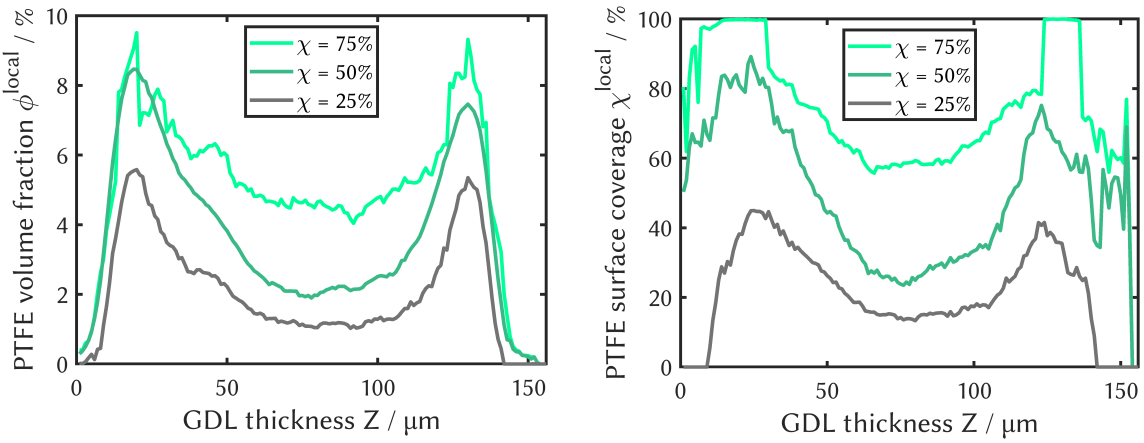

(a) PTFE loading profile.

(b) PTFE surface coverage profile.

Figure 4.14: Through-plane profiles of PTFE distributions with different surface coverages χ in GDL microstructure reconstructions of the impregnated fiber substrate. The heterogeneous additive distributions are realized with the in-house algorithm (Figure 4.13 and yield PTFE contents $\phi_{\mathrm{PTFE}}^{(m)}$ of 21.9, 16.36 and 10.24 wt%, respectively).

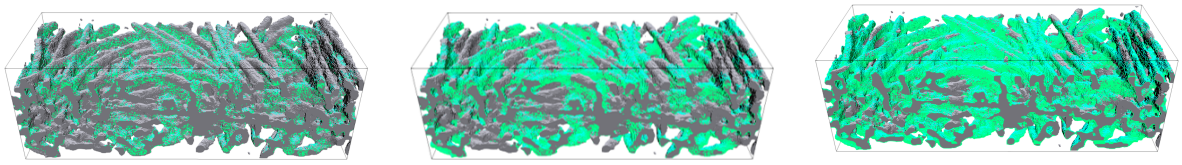

(a) $\chi = 25$ %.

(b) $\chi = 50$ %.

(c) $\chi = 75$ %.

Figure 4.15: GDL microstructure reconstructions of the impregnated fiber substrate with different PTFE surface coverages χ and additive contents $\phi_{\mathrm{PTFE}}^{(m)}$ of 21.9, 16.36 and 10.24 wt%, according to the heterogeneous through-plane profiles in Figure 4.14.

The aforementioned PTFE distributions with three different additive surface coverages exhibit qualitatively comparable profiles along the GDL thickness. In order to study PTFE distributions of varying heterogeneity as well, a fourth GDL microstructure reconstruction of impregnated fiber substrate is generated with a homogeneous PTFE distribution and $\phi_{\mathrm{PTFE}}^{(m)} = 16.36$ wt% and $\chi = 50$ %. Once again, the in-house algorithm (Section 4.2.5) is utilized, however, in this case two subroutines are slightly altered. Whereas in *Bulk2SurfPTFE* a heterogeneous additive loading profile (Section 4.2.4) is employed per default, the redistribution of PTFE is now conducted uniformly instead. In

addition, the target profile for the second redistribution of PTFE in *Surf2SurfPTFE* is not anymore the heterogeneous loading profile (Section 4.2.4), but a homogeneous additive surface coverage profile. Figure 4.16 shows the resulting through-plane profiles for the homogeneous PTFE distribution in comparison to the default heterogeneous case. As apparent from Figure 4.16b, the homogeneous PTFE surface coverage profile is realized very well and with only very minor deviations. On the other hand, the through-plane profile of the additive loading (Figure 4.16a) exhibits somewhat larger fluctuations along the GDL thickness. These can be traced back to the through-plane profile of the porosity (Figure 4.6c). The GDL microstructure reconstructions with the heterogeneous and homogeneous PTFE distributions are illustrated in Figure 4.17.

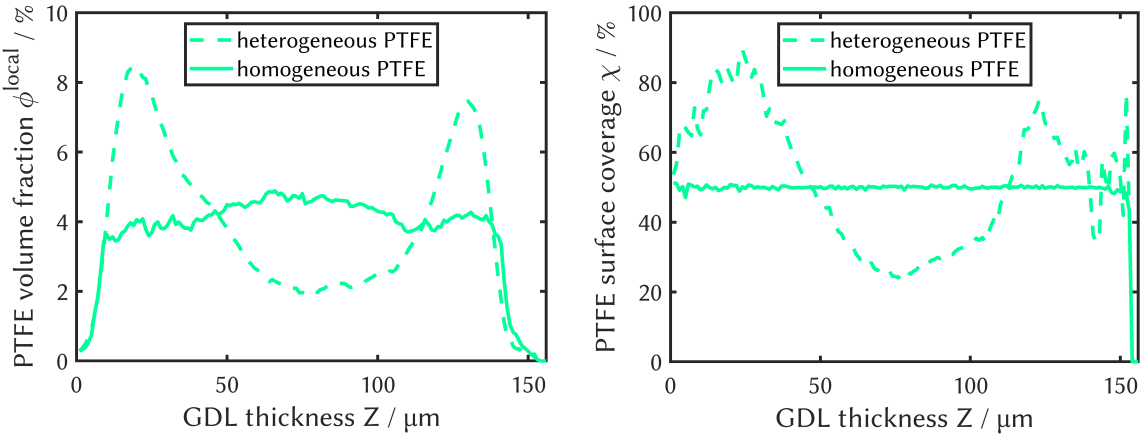

(a) PTFE loading profile.

(b) PTFE surface coverage profile.

Figure 4.16: Through-plane profiles of different spatial PTFE distributions in GDL microstructure reconstructions of the impregnated fiber substrate, as achieved with the in-house algorithm (Figure 4.13). Both distributions exhibit an additive loading of $\phi^{(m)}_{\mathrm{PTFE}} = 16.36\,\mathrm{wt\%}$ and a PTFE surface coverage of $\chi = 50\,\%$.

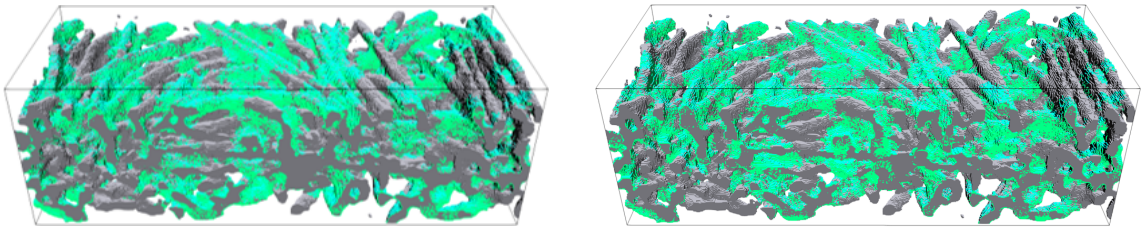

(a) Heterogeneous PTFE distribution.

(b) Homogeneous PTFE distribution.

Figure 4.17: GDL microstructure reconstructions of impregnated fiber substrate with homogeneous and heterogeneous spatial PTFE distributions, according to the through-plane profiles in Figure 4.16. The geometries exhibit an additive loading of $\phi^{(m)}_{\mathrm{PTFE}} = 16.36\,\mathrm{wt\%}$ and a PTFE surface coverage of $\chi = 50\,\%$.

4.3 Computational setup

In Section 3.2.5, the Lattice Boltzmann model is already successfully validated against the analytical solutions of Jurin's and Washburn's law as well as the capillary valve effect. However, these test cases considered only simpler geometries contrary to the complex microstructures of GDLs. As this thesis focuses on studying the capillary characteristics in carbon felt GDLs, the CGM is therefore also validated against experimentally measured $p_c - S$ curves of the plain and impregnated carbon fiber substrate. On the one hand, this additional validation is important to verify that the modeling of fluid-solid interactions (e.g., contact angles Section 3.2.3) also works properly for complex simulation geometries. On the other hand, GDL microstructure reconstruction has to be considered as imperfect with unknown errors. A comparison of simulated $p_c - S$ curves to experimental data can thus help to estimate, if significant systematic error sources are present in both the modeling and reconstruction approach. In this work, $p_c - S$ characteristics are therefore simulated and subsequently compared to test bench data. Following increasing levels of complexity, the additional model validation is first conducted for the simpler case of the plain H14 fiber substrate and then for the impregnated fiber substrate.

4.3.1 Test bench for capillary pressure-saturation relations

Whereas measurement of $p_c - S$ curves was not part of this thesis, the computational model for the simulation of capillary characteristics in the GDL was developed to mimic the boundary conditions of an experimental reference. As an introduction to the subsequent modeling and simulation work, the following subsection is therefore devoted to the detailed description of a test bench for the determination of $p_c - S$ relations. At this point, it is emphasized that in the frame of this work all experimental works related to the measurement of $p_c - S$ characteristics was conducted by A. Kube from the Department for Electrochemical Energy Technology at the Institute of Engineering Thermodynamics of the German Aerospace Center (DLR) in Stuttgart.

In order to serve as an experimental reference for the simulated capillary characteristics of the plain and impregnated fiber substrate, $p_c - S$ curves were measured for both the intrusion and drainage of liquid water using an in-house test bench as sketched in Figure 4.18a. In the test bench, a circular GDL sample ($d_{\text{sample}} = 18\,\text{mm}$) is sandwiched between a hydrophilic membrane (Merck Durapore Membrane Filter 0.45 µm HV) and a hydrophobic membrane (Whatman Membrane Filter 0.2 µm WTP Type) on the liquid water and air side, respectively. After sealing the microfluidic device with tightening screws, air pressure is then controlled using a syringe (Hamilton 1005TLL 5 mL) mounted onto a syringe pump (NE-500). A pressure transducer (DMP 311 from BD sensors, ±0.5 bar,

±0.1 %) is used with a data logger (Agilent 34970A Data Acquisition) to record the air pressure during the measurement. Homogeneity in the gas phase pressure across the sample surface is established using a gas distributor on top of the hydrophobic membrane. On the liquid water side, pressure is kept constant at 1 atm by providing the liquid via a basin which is sealed to prevent evaporation. This fluid container is placed on top of a balance (OHAUS Explorer EX225) to monitor the amount of liquid water intruding into the porous sample. By changing the volume inside the syringe with a constant rate of 50 µL/min, air pressure is then ramped between −25 kPa and 25 kPa to impose a capillary pressure equivalent to $p_c = p_g - p_l$ across the GDL sample and enforce subsequent intrusion and drainage of liquid water. In preliminary tests, a sufficiently low air pressure ramp rate was determined to obtain a quasi-stationary saturation for any given capillary pressure. With this experimental setup, capillary intrusion and drainage curves are then measured by recording the imposed capillary pressure and the intruded liquid water volume. In order to assure reproducibility, each measurement consists of five subsequent intrusion and drainage cycles.

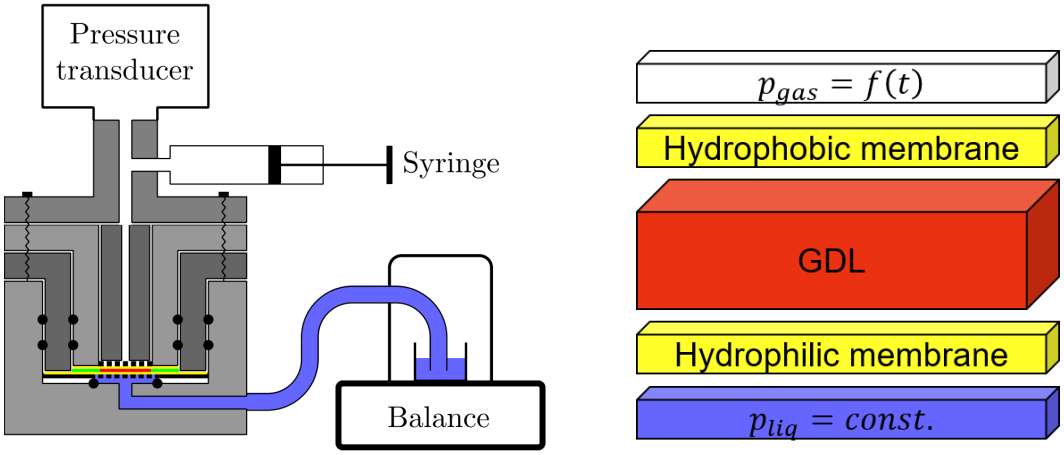

(a) Assembly. (b) Boundary conditions.

Figure 4.18: (a) Schematic view of the test bench used to measure $p_c - S$ curves (with permission from A. Kube, Department for Electrochemical Energy Technology, Institute of Engineering Thermodynamics, DLR Stuttgart). A GDL sample (red) is sandwiched between a hydrophobic and a hydrophilic semipermeable membrane (yellow). Liquid water intrusion and drainage are enforced by variation of the air pressure via a syringe. (b) Closeup of the experimental boundary conditions in the test bench.

Figure 4.19 shows the experimental intrusion and drainage curves for the plain and impregnated fiber substrate. For both samples, the first intrusion is found to be significantly different to the subsequent measurement cycles. With the capillary pressure given as $p_c = p_g - p_l$, a higher liquid phase pressure p_l is apparently required to enforce primary wetting of the carbon fibers and thus liquid water intrusion. According to Harkness et al.

[260], this observation may be related to residual liquid water in the GDL after primary drainage, which may facilitate subsequent intrusions. In addition, the initial wetting of the carbon fibers may also alter their solid surface properties, rendering them more hydrophilic. However, as this work focuses on the stationary capillary characteristics of GDL, primary intrusion phenomena are in general neglected in the frame of this study. Hence, and if not denoted otherwise, only the respective last cycles are considered for the subsequent simulative studies of this chapter. A comparison of the intrusion and drainage curves for the plain (Figure 4.19a) and impregnated fiber substrate (Figure 4.19b) furthermore reveals three major differences between the two investigated samples. First, impregnation of the fiber substrate leads to a shift of the intrusion and drainage curves towards lower capillary pressures. Hence, higher liquid pressures are required to enforce full saturation, which can be related to the impeding effect of hydrophobicity PTFE ($\theta_{\mathrm{PTFE}} > \theta_{\mathrm{CF}}$) on the liquid water transport. Secondly, a slightly higher maximum of the intruded volume V_l is measured for the impregnated fiber substrate. This appears counter-intuitive, as addition of PTFE leads to a reduction of the sample porosity. However, taking into account that GDLs are subject to production tolerances, this observation may be related to variations in the sample thickness [289, 324]. Lastly, the slope of the intrusion curve appears to have changed for the impregnated fiber substrate, as indicated by an intermediate change in curvature around $-5\,\mathrm{kPa} < p_c < 0\,\mathrm{kPa}$. As will be discussed in detail in Section 4.4.9, however, these observations may be related to measurement artifacts caused by the experimental boundary conditions.

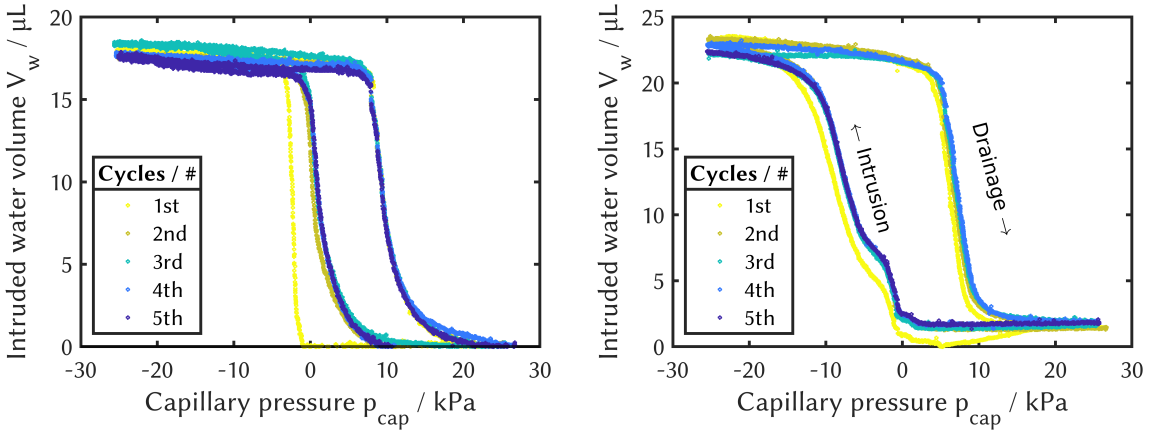

(a) Plain fiber substrate.

(b) Impregnated fiber substrate.

Figure 4.19: Experimental intrusion and drainage curves as measured with the $p_c - S$ test bench (Figure 4.18). Measurements from A. Kube, Department for Electrochemical Energy Technology, Institute of Engineering Thermodynamics, DLR Stuttgart)

Before the results of the subsequent simulation studies can be compared to the experimental data, the measured intruded liquid water volume V_l has to be converted into liquid saturations S_l by normalization

$$S_l = \frac{V_l}{V_p} \tag{4.2}$$

by the pore volume V_p of the GDL sample. While the latter can be in principle determined via the sample radius R_{sample} and height H_{sample} to

$$V_p = \pi R_{\text{sample}}^2 H_{\text{sample}} \epsilon_{\text{sample}}^{\text{eff}}, \tag{4.3}$$

the effective porosity $\epsilon_{\text{sample}}^{\text{eff}}$ of the GDL sample in the test bench is unknown and can only be estimated very roughly. Since the focus of the simulative studies in this work relies on the qualitative analysis of capillary characteristics in GDLs, the saturation is approximated to

$$S_l \approx \frac{V_l}{V_l^{\max}}. \tag{4.4}$$

Furthermore, whereas the remainder of this work will only consider the saturation of water as the only liquid phase, the subscript will be from here on omitted in favor of brevity, i.e., $S_l = S$.

4.3.2 Modeling of semipermeable membranes

With up to one fifth of the overall sample thickness, the GDL surface regions can have a significant influence on the overall structural properties. However, in air-tight assemblies such as in PEM fuel cell assembly or the $p_c - S$ test bench (Figure 4.18a), these highly porous surface regions are prone to compression, owing to their limited mechanical stiffness [306]. As pointed out by Fishman et al. [325], the surface regions may be therefore completely neglected in experimental studies, reducing the GDL to the bulk properties of its core region. In this chapter, however, special attention is paid to appropriately account for these surface regions, aiming for a most realistic computational setup according to experimental boundary conditions. Inside the $p_c - S$ test bench (Figure 4.18b), GDL samples are sandwiched between a hydrophilic and a hydrophobic semipermeable membrane on the liquid and gas side, respectively. In order to achieve a simulation setup similar to the experimental conditions, those membranes are considered explicitly in the subsequent simulative studies of this chapter. Following a first and simple approach, the membranes may be modeled by appending two monolayers to the GDL microstructure surfaces (Figure 4.20b). However, assuming that despite the absence of a nominal compression

pressure the membranes nonetheless face a certain bending force from the air-tight test bench sealing, they might be squeezed into the large surface pores of the GDL sample. Such a scenario would require a more sophisticated membrane model, which is therefore developed in this work. In order to identify and differentiate the large surface pores from smaller ones within the GDL core region, 2D geometric pore size distributions (2D-gPSDs) are determined for each individual layer along the through-plane direction of the respective GDL subvolume. At this point, it is helpful to recall that the GeoDict tool 'Granulometry' calculates geometric pore size distributions (gPSDs) by fitting spheres of maximum diameter into the pore space (see Section 4.2.2). When the investigated porous structure is reduced to a thickness of one single layer, however, the pore volume is essentially an area and the sphere of maximum diameter becomes a circular disk. For anisotropic porous media such as GDLs, the local 2D pore sizes (2D-gPSD) of single slices along the domain thickness might be thus significantly different to the overall pore size distribution (3D-gPSD) of the whole 3D structure. Towards the highly porous GDL surface regions, these 2D pore sizes may increase exceptionally and ultimately even exceed the overall thickness of the 3D microstructure. Figure 4.20a shows the 2D pore diameter profiles as well as the porosity profile along the thickness of the GDL subvolume for the plain fiber substrate (Figure 4.1d). In the GDL core region (between dashed vertical lines), the 2D pore sizes fluctuate around $d_{p(50)}^{\mathrm{phys,2D}} \approx 17 - 20\,\mu\mathrm{m}$ and $d_{p(90)}^{\mathrm{phys,2D}} \approx 40 - 80\,\mu\mathrm{m}$ for the median and the 90 % quantile, respectively. Towards the GDL surface, however, the 2D diameters increase strongly along with the local porosity. Based on the through-plane profile of the 2D maximum pore diameter, a threshold value of $d_{\mathrm{threshold}}^{\mathrm{phys}} = 75\,\mu\mathrm{m}$ is then defined above which pores are assumed be occupied with the respective semipermeable membrane. Application of this rule to the simple membrane monolayer approach (Figure 4.20b) results in the more sophisticated membrane model, as illustrated in Figure 4.20c. Even though the differences in the two geometries might appear minor, they play a crucial role for the capillary characteristics as will be discussed in Section 4.4.2. For the 3D pore size distribution of the plain fiber substrate subvolume (Figure 4.1d), the median is furthermore determined around $d_{p(50)}^{\mathrm{phys}} \approx 21\,\mu\mathrm{m}$, which is in the range of common literature values [57, 298].

4.3.3 Boundary conditions

The computational setup is developed with the aim to mimic the experimental setup by selection of boundary conditions similar to the $p_c - S$ test bench (Figure 4.18b). Therefore, the GDL microstructure reconstruction is sandwiched between a hydrophilic and a hydrophobic semipermeable membrane on the liquid water and air side, as described

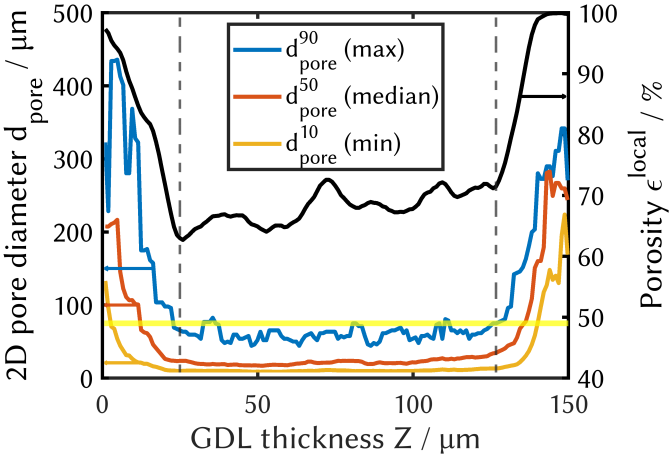

(a) Pore size distribution along GDL thickness.

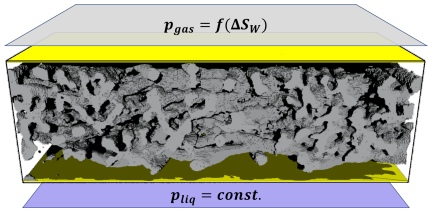

(b) Membranes on GDL surfaces.

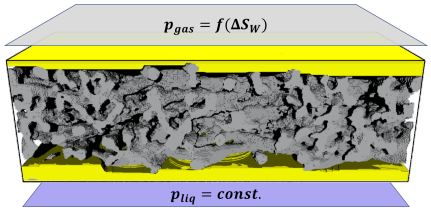

(c) Membranes in GDL pores.

Figure 4.20: Modeling of semipermeable membranes: (a) Local pore diameters given as 10/50/90% quantiles from 2D geometric pore size distributions (2D gPSDs) and porosity profile along the thickness of the plain fiber substrate subvolume (Figure 4.1d). A yellow solid line marks a threshold diameter of $d^{\text{phys}}_{\text{threshold}} = 75\,\mu\text{m}$, grey dashed lines indicate the GDL core area. (b) A simple approach models the membranes (Figure 4.18a) as monolayers on the GDL surfaces. (c) A more sophisticated model assumes that the membranes are partly squeezed into the GDL surface pores with diameters larger than $d^{\text{phys}}_{\text{threshold}}$.

in Section 4.3.2. In the default setup, the domain of the porous GDL sample encompasses $500 \times 200 \times 156$ voxels with a lattice resolution of $\Delta x^{\text{phys}} = 0.96\,\mu\text{m}$ per voxel. In the case of the simplified model (Figure 4.20b), the membranes are considered as monolayers on top of the respective GDL surfaces. In the more sophisticated membrane model (Figure 4.20c), they also occupy GDL surface pores with diameters larger than the threshold of 75 µm.

At the bottom and top boundaries of the computational domain, liquid and gas phase pressures are imposed using the pressure boundary condition originally proposed in 2D by Zou and He [203] and implemented by Hecht and Harting [204] for the D3Q19 lattice. In the two in-plane directions, the domain boundaries are governed by periodic boundary conditions. Both fluid phases are initialized with a density ratio

$$\gamma = \frac{\rho_l^0}{\rho_g^0} \tag{4.5}$$

of unity, i.e., $\rho_l^0 = \rho_g^0 = 1$. In favor of enhanced readability, the superscript 'LBM' is omitted here and in all subsequent paragraphs for all lattice-based quantities, e.g., $\rho_i := \rho_i^{\text{LBM}}$. Kinematic viscosities are chosen as $\nu_l = 1/6$ and $\nu_g = 1/12$ to set a dynamic viscosity ratio of

$$M = \frac{\mu_l}{\mu_g} = \frac{\rho_l \nu_l}{\rho_g \nu_g} = 2. \tag{4.6}$$

At this point, it is noted that the real ratios in the physical water-air system are with $\gamma^{\text{phys}}\,(20\,^\circ\text{C}) \sim 830$ [326, 327] and $M^{\text{phys}}\,(20\,^\circ\text{C}) \sim 55$ [328, 329] quite different but not accessible in the LB simulations, owing to numerical instabilities. On the other hand, application of these real ratios in the simulations is not strictly necessary, as inertial and viscous effects are negligible in the capillary-dominated regime [88, 330]. In the simulations, dominance of capillary forces is ensured by a high Laplace number of

$$\text{La} = \frac{\sigma \rho_l d_{p(50)}}{\mu_l^2} \approx 98 \tag{4.7}$$

for a surface tension of $\sigma = 0.125$ and a lattice-based median pore diameter $d_{p(50)} = d_{p(50)}^{\text{phys}}/\Delta x^{\text{phys}}$ (see Section 4.3.2). The Laplace number of the real physical system can be estimated to $\text{La}^{\text{phys}} \sim 1500$ [326, 327, 331], but is not realizable in the simulations due to numerical instabilities. As will be shown in Section 4.4.5, however both M and La will prove to be sufficiently high to recover an appropriate capillary characteristics in the simulations. In order to account for different wettability, the contact angles for the carbon fibers and PTFE were furthermore set to $\theta_{\text{CF}} = 65°$ [332] and $\theta_{\text{PTFE}} = 115°$ [312, 333, 334]. In the subsequent studies of this chapter, intrusion and drainage of liquid water is then simulated with above parameters and assuming initially dry GDL subvolumes. Similar to the test bench, the liquid phase pressure is therefore kept constant ($p_l = 1\,\text{atm}$) at the bottom domain boundary, while the gas phase pressure at the top domain end is varied over time using an adaptive ramp in the pressure boundary condition (Section 3.2.2). With above computational setup and assuming a standard laboratory temperature of 20 °C for the test bench operation (Section 4.3.1), the relevant conversion factors (see also Section 3.2.4) for the subsequent simulations in this chapter are furthermore given as listed in Table 4.2.

Table 4.2: Conversion factors (*cf.* Section 3.2.4) for the LB simulation of $p_c - S$ characteristics at a standard laboratory temperature of 20 °C.

Quantity X	**Value** phys	LBM	**Conversion factor** $C_X = {}^{X^{\text{phys}}}/_{X^{\text{LBM}}}$
Length l	0.96 µm	1	$C_l = 0.96\,\mu\text{m}$
Viscosity ν	$1\text{e}^{-6}\,\text{m}^2/\text{s}$ [326]	$1/6$	$C_\nu = 6\text{e}^{-6}\,\text{m}^2/\text{s}$
Time t	$1.53\text{e}^{-7}\,\text{s}$	1	$C_t = {}^{C_l^2}/_{C_\nu} = 1.53\text{e}^{-7}\,\text{s}$
Surface tension σ	$7.28\text{e}^{-2}\,\text{N/m}$ [331]	0.125	$C_\sigma = 5.82\text{e}^{-1}\,\text{N/m}$
Pressure p			$C_p = {}^{C_\sigma}/_{C_l} = 6.07\text{e}^{5}\,\text{Pa}$

4.3.4 Adaptive boundary pressure ramp

$p_c - S$ characteristics are in general nonlinear and can be often qualitatively described to follow an S-type curve, as illustrated in Figure 4.21. In fact, the test bench data show in Figure 4.19 similar characteristics for the plain and impregnated fiber substrate. Hence, $p_c - S$ relations typically exhibit regions of both very low and very high gradients. Such a characteristic poses a challenge for PSM studies due to two different reasons: At low and high saturations, GDLs are commonly insensitive to minor changes in the capillary pressure. In the intermediate saturation range, on the other hand, porous media usually show a strong sensitivity on changes in p_c, with sudden and strong saturation increases for even minor Δp_c. Whereas these equilibrium states significantly contribute to the $p_c - S$ characteristics, a good data coverage is difficult to obtain due to the high sensitivity of the saturation on pressure changes. In a simple simulation setup using a constant capillary pressure, derivation of a complete $p_c - S$ curve would therefore require a large number of separate equilibrium simulations. Such an approach is both computationally expensive and inefficient.

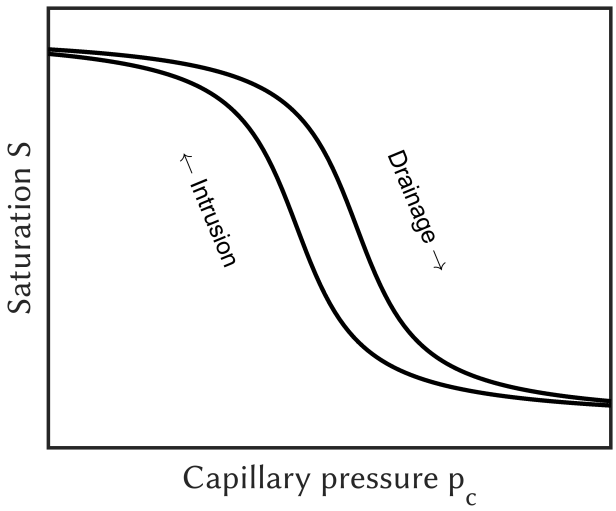

Figure 4.21: Typical S-shaped $p_c - S$ characteristic of a porous medium for the intrusion and drainage of a wetting fluid.

In the test bench, liquid water intrusion and drainage is enforced by variation of the air pressure using a syringe. For this, the piston in the syringe is moved continuously in small steps to adjust the gas phase pressure and thereby the capillary pressure $p_c = p_g - p_l$ imposed on the porous sample. In order to ensure a quasi-stationary ramping process, the step size is furthermore set to sufficiently low values, resulting in a measurement duration of several hours for each $p_c - S$ curve. Whereas this experimental procedure could be in principle realized in a computational setup, the mandated time scale would be inaccessible to LBM simulations, owing to the high computational expense. In addition,

this ramping process is also inefficient, as the same low ramp rate would be used in both low and high sensitivity regions. Therefore, an alternative approach is chosen this chapter by ramping the gas phase pressure adaptively in dependence of the saturation change. This procedure is computationally efficient, as low ramp rates would be only used where needed, which is primarily in the intermediate saturation range. In the low sensitivity regions of the saturation, on the other hand, the computation time can be significantly reduced by increasing the ramp rate. For the subsequent simulative studies, the adaptive ramp for the gas phase pressure is formulated as follows:

$$p_g^{\mathrm{BC}}\left(t+\Delta t\right)=p_g^{\mathrm{BC}}\left(t\right)+\Delta p_g^{\mathrm{BC}}\left(t\right) \tag{4.8}$$

In equation (4.8), the gas phase pressure at the top GDL boundary is incremented every time step with a ramp rate Δp_g^{BC}. After every $\Delta t_S = 1000$ time steps, this rate is adjusted to

$$\Delta p_g^{\mathrm{BC}}\left(t+\Delta t\right)=\Delta p_g^{\mathrm{BC}}\left(t\right)\cdot\frac{C_S}{\Delta S\left(t\right)/\Delta t_S} \tag{4.9}$$

by rescaling with the ratio of the target saturation change C_S and the average saturation change per time step

$$\frac{\Delta S\left(t\right)}{\Delta t_S}=\frac{S\left(t\right)-S\left(t-\Delta t_S\right)}{\Delta t_S} \tag{4.10}$$

for the previous time step interval $[t-\Delta t_S, t]$. In this chapter, the default target saturation change is set to $C_S = 10^{-6}$, which translates to achieving full saturation within 10^6 time steps. As will be shown in Section 4.4.4, this ramp speed is proven to be sufficiently low to ensure stationary capillary characteristics. With the local voxel-wise saturation as

$$S^{\mathrm{vx}}\left(x,y,z\right)=\frac{\rho_l\left(x,y,z\right)}{\rho_l\left(x,y,z\right)+\rho_g\left(x,y,z\right)}, \tag{4.11}$$

the overall saturation S is furthermore determined as the global average

$$S=\frac{1}{n_x^p n_y^p n_z^p}\sum_{ix}\sum_{iy}\sum_{iz}S^{\mathrm{vx}}\left(ix,iy,iz\right) \tag{4.12}$$

over all $n_x^p n_y^p n_z^p$ pore space voxels along the three spatial coordinates $(x,y,z)^T$ of the simulation domain. By comparison of equations (4.11) and (3.59), the local saturation can be furthermore linked to the local phase-field parameter with $\varphi^{\mathrm{vx}} = 2S^{\mathrm{vx}} - 1$.

4.4 Simulation of capillary hysteresis in porous GDL microstructures

4.4.1 Adaptive capillary pressure ramp

In the previous subsection, a new computational setup for the simulation of $p_c - S$ characteristics was presented, which utilizes an adaptive ramp for the gas phase boundary pressure to impose variable capillary pressures. The novel approach is prospected to be computationally significantly more efficient as one $p_c - S$ curve can be determined in one single LB simulation. Beforehand time consuming parametric studies, the adaptive boundary pressure ramp is therefore tested and compared to the conventional approach of imposing a constant capillary pressure. Figure 4.22 shows a simulated intrusion curve as derived with the adaptively ramped capillary pressure. Whereas in the conventional approach with a constant capillary pressure one separate simulation would be required for each data point along the $p_c - S$ curve, the entire capillary characteristic is obtained in one single LB simulation using the adaptive boundary pressure ramp. As a result, a significant reduction of computational cost is achieved with the novel approach. In addition, as the capillary characteristics in general has to be assumed as *a priori* unknown, the conventional approach would necessitate a 'blind' selection of constant capillary pressures for each simulation in order to eventually assemble an entire $p_c - S$ curve. Given furthermore the heavy computational expense of LBM and the often resulting requirement to minimize the number of simulations, these circumstances then can lead to rather poor recovery of capillary characteristics from only few simulated capillary pressures. With the novel adaptively ramped capillary pressure formulation, on the other hand, this issue is circumvented as the (still) *a priori* unknown capillary characteristic is approached in a staircase manner, ensuring good data coverage in one single simulation and all along the $p_c - S$ curve. Due to its proven superiority over the standard constant pressure approach, the adaptive boundary pressure ramp is from here on used as the default for all subsequent parametric studies on capillary hysteresis within this work.

4.4.2 Surface effects and membrane models

In Section 4.3.2, two models of different complexity were developed to explicitly consider semipermeable membranes from the $p_c - S$ test bench for the simulations, aiming to appropriately account for experimental boundary conditions. While the simulation geometries (Figure 4.20b and Figure 4.20c) for the plain fiber substrate appear similar at first sight, their capillary characteristics are yet to be studied. Therefore, liquid water

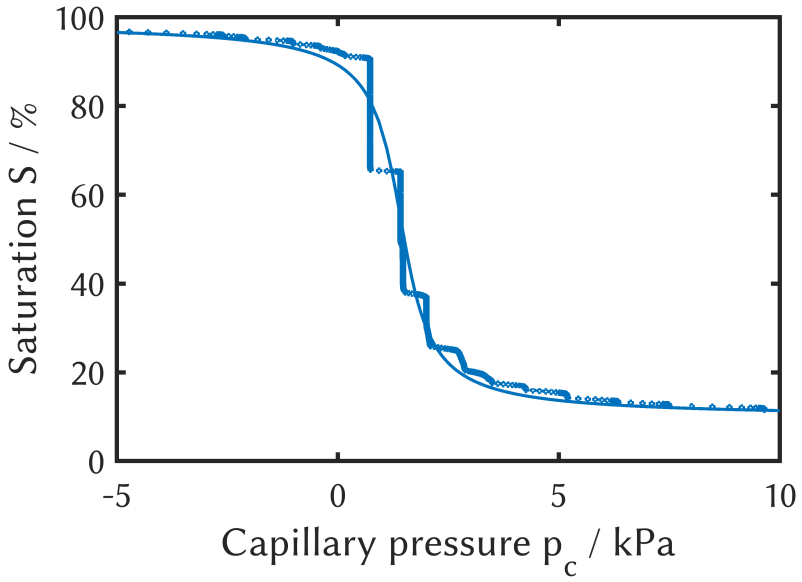

Figure 4.22: LB simulation of a capillary intrusion curve using an adaptively ramped capillary pressure $p_c = p_g - p_l$. A fit function (solid line) illustrates the $p_c - S$ characteristic to be recovered by the data points of the LB simulation.

intrusion and drainage are simulated for the plain fiber GDL subvolume (Figure 4.1d), thereby recovering the full capillary hysteresis. The LB simulations are carried out using the default computational setup as described in Section 4.3.3. Figure 4.23a shows the simulated $p_c - S$ curves in comparison to the test bench data. Similar to the experimental data, the simulated first intrusion (dashed colored lines) is observed to be significantly different to the subsequent cycles, owing to primary wetting phenomena in the initially dry GDL (see also Section 4.3.1 and ref. [260]). However, since the underlying work focuses on the investigation of stationary capillary characteristics, primary intrusion is from here on neglected. When the subsequent drainage and secondary intrusion curves of the two membrane modeling approaches are compared with the experiment, significant differences become apparent. For the more sophisticated model with the semipermeable membranes in the large GDL surface pores, a good match is obtained for the simulation results and the experimental data. Amongst others, this agreement is found in a similar residual saturation of around $S^{\text{res}} \approx 10\,\%$, which is in the range of approximately $4 - 13\,\%$ reported for various types of GDLs [257, 261]. Furthermore, the width of the capillary hysteresis is observed to be similar to the experiment. This indicates that the capillary valve effect (see Section 3.2.5) is appropriately recovered for the GDL microstructure reconstructions. Only in the low and high saturation range, minor deviations are observable, which may originate from unknown experimental boundary conditions such as sample compression [264]. When the simplified membrane model is employed, on the other hand, the simulation results deviate significantly from the experiment. While the width of the capillary hysteresis is

approximately similar, a slight shift towards lower capillary pressures is observed. Disparately more drastic, however, the simulated drainage is observed to result in a residual saturation of $S^{\text{res}} \approx 30\,\%$, which is about three times higher than for the sophisticated membrane model and the experiment.

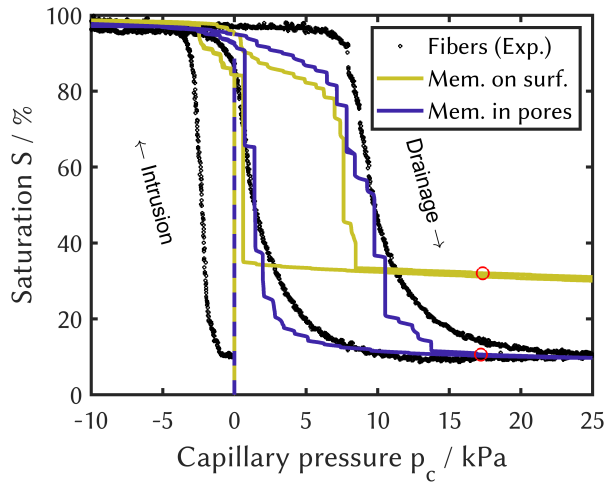

(a) $p_c - S$ curves.

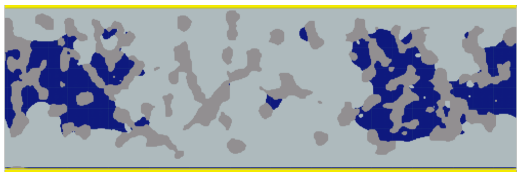

(b) Membrane on GDL surface.

(c) Membrane in GDL pores.

Figure 4.23: (a) Simulated liquid water intrusion and drainage for the plain fiber substrate using two different membrane models with dashed colored lines indicating the primary intrusion. (b)-(c) Through-plane cross-sections visualize the liquid water distribution at the end of the respective drainage curve, as indicated by red circles in (a). The different phases are colored as follows: Semipermeable membrane (yellow), carbon fiber (grey), gas (light-blue), liquid water (dark-blue).

In order to comprehend these vastly different residual saturations, the liquid water distributions near the end of the respective drainage curves are visualized in Figure 4.23b and Figure 4.23c. While for the sophisticated membrane model apparently only few smaller disconnected liquid water clusters are observed along the GDL thickness, larger amounts of water remain entrapped in the core area of the porous medium for the simplified membrane model. These deviating observations can be explained based on the equivalence of wetting phase drainage (liquid water with $\theta_{\text{CF}} = 65°$) and non-wetting phase intrusion (gas) and the 2D pore diameter profile in Figure 4.20a. As demonstrated in Section 3.2.5, a non-wetting phase invades a pore when the capillary pressure exceeds a certain threshold value. According to the Young-Laplace equation (2.19) with $p_c \propto 1/d_p$, preferential pathways for invasion of the (non-wetting) gas phase are thus found in the largest GDL pores offering the lowest capillary barriers. From the GDL surface at the gas inlet side towards the core region, capillary resistance to gas invasion is therefore on average increasing along with declining pore diameters (Figure 4.20a). Towards the GDL surface at the liquid inlet side, on the other hand, capillary barriers become progressively lower again due to the increasing

pore diameters. Once single percolation paths from the gas inlet side have reached the GDL core region, the gas phase then rapidly invades adjacent and successively larger pores towards the liquid inlet side. In addition, owing to the tortuosity and interconnectivity of the pores, the liquid phase is furthermore not just progressively drained along the GDL thickness but in the in-plane directions as well. At the same time, smaller pores of the GDL core region remain filled with liquid water, as the gas phase cannot overcome their capillary barrier. As a result, the wetting phase in the GDL pores eventually loses capillary contact to the liquid water inlet and remains in the GDL core region as isolated clusters. Such a wetting phase entrapment is found for the LB simulations using the simplified membrane model, as illustrated in Figure 4.23b. The preferential drainage pathway in the center of the GDL cross-section can be furthermore related to the high porosity zone (Figure 4.4a) in the gap between two fiber bundles (see also Section 4.2.3). According to the significantly lower residual saturation, a comparable liquid phase entrapment does not occur in the experiment, suggesting that GDL surface effects are suppressed by the boundary conditions of the $p_c - S$ test bench. This conjecture is confirmed by the simulation using the sophisticated membrane approach. By modeling the flexible semipermeable membranes as partly bent into the large surface pores, GDL boundary effects are attenuated and massive wetting phase entrapment is averted (Figure 4.23c). This investigation demonstrates that GDL surface effects can have a major impact on the capillary hysteresis, as the residual saturation is strongly influenced by the porosity and pore size gradients of the porous medium. Hence, a good agreement of simulated capillary hysteresis with test bench data can be only accomplished by proper accounting of experimental boundary conditions. Providing a more realistic representation of the test bench boundary conditions, the sophisticated membrane model is therefore set as default for all subsequent studies of this chapter.

4.4.3 Dependence on initial conditions

As previously mentioned in Section 4.3.1 and shown Section 4.4.2, the primary liquid water intrusion differs vastly from subsequent cycles and is therefore neglected in the subsequent sections of this chapter. In order to obtain a secondary intrusion curve for an initially dry GDL microstructure reconstruction, however, one has to simulate a primary intrusion and subsequent primary drainage beforehand. For computationally expensive PSM methods such as LBM, this results in a time-consuming task. A second study therefore investigates if the derived capillary hysteresis of the GDL is dependent on its initial state (i.e., dry or fully saturated). When the capillary characteristics of the GDL are invariant to the initial state, primary intrusion would not have to be simulated and the capillary hysteresis

could be recovered from an initial drainage and subsequent (secondary) intrusion process, resulting in a significant reduction of computational expense. In order to investigate, if the capillary characteristics are in fact independent of the initial state, capillary hysteresis is therefore simulated and compared for both an initially dry and fully saturated GDL microstructure. Figure 4.24 shows two full cycles of simulated capillary hysteresis starting with primary intrusion in an initially dry and primary drainage from an initially fully saturated GDL, respectively. Evidently, the resulting simulated $p_c - S$ curves are for both initial states of the GDL very similar, suggesting that the capillary characteristics of the GDL are in fact independent of its initial state. Based on this finding and in favor of reducing computational expense, capillary hysteresis is therefore from here on recovered by simulation of primary drainage and subsequent intrusion of liquid water for an initially fully saturated GDL.

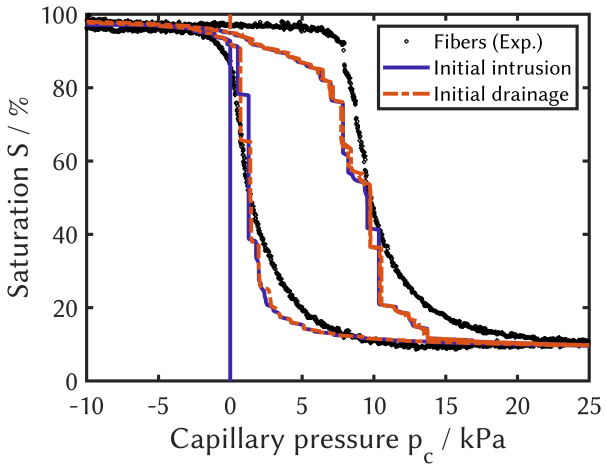

Figure 4.24: Simulated capillary hysteresis for the plain fiber substrate and comparison to experimental data. Starting from an initially dry and an initially wet plain fiber microstructure reconstruction respectively, capillary hysteresis is simulated for two complete cycles.

4.4.4 Impact of adaptive capillary pressure ramp speed

Even though the independence of the GDL capillary characteristics of the initial state support a reduction in computational expense, simulation of capillary hysteresis remains a task of high cost in time and computation. Therefore, another study aims at reduction of the computational expense by increasing the speed C_S of the adaptive capillary pressure ramp (Section 4.3.4). Higher ramp speeds evidently lead to shorter computation times, however, reasonable choice are bounded by an upper limit as the process has to be sufficiently slow to obtain a steady-state capillary hysteresis. A second study is therefore devoted to the identification of a maximum target saturation change given by C_S that still

warrants quasi-stationarity in the ramping procedure. In order to keep the computational expense of this study at bay, the investigation is restricted to the intrusion of liquid water. Moreover, as the invasion of a primarily wetting fluid ($\theta_{\mathrm{CF}} = 65°$) into a porous medium proceeds (promoted by attractive fluid-solid interactions) faster than its withdrawal, the maximum C_S for quasi-stationarity is expected to be delimited by the intrusion and not the drainage process. Starting from the end of the drainage curve shown in Figure 4.23a (red circle on dark velvet line), secondary intrusion is simulated for six different ramp speeds, as depicted in Figure 4.25a. In general, a higher C_S leads to larger saturation jumps during the ramping procedure in the capillary intrusion simulation. This observation can be explained by the fact that for higher C_S the pressure ramp rate is adjusted more rarely as the target saturation change is exceeded less frequently. Consequently, in the intermediate saturation range with high sensitivity on pressure changes, the ramp speed is reduced with increasing delay, resulting in a too high Δp_c^{BC}. As a result, the system becomes increasingly perturbed while having less relaxation time until the next ramp rate adjustment step. Whereas for $C_S = 1e^{-5}$ the simulated capillary intrusion curve is strongly deviating from the experimental data, a distinct convergence behavior is observed for $C_S \geq 3e^{-6}$. However, along with slower ramp speeds also the number of required simulation time steps increases with approximately $\Delta t^{\mathrm{sim}} \propto 1/C_S$. Furthermore, beyond $C_S \leq 1e^{-6}$ the intrusion curve does not anymore change significantly, even when the ramp speed is halved to $C_S = 5e^{-7}$. Providing a maximum in accuracy for still practicable computational expense, a ramp speed of $C_S = 1e^{-6}$ is therefore selected as default for all subsequent simulative studies of this chapter.

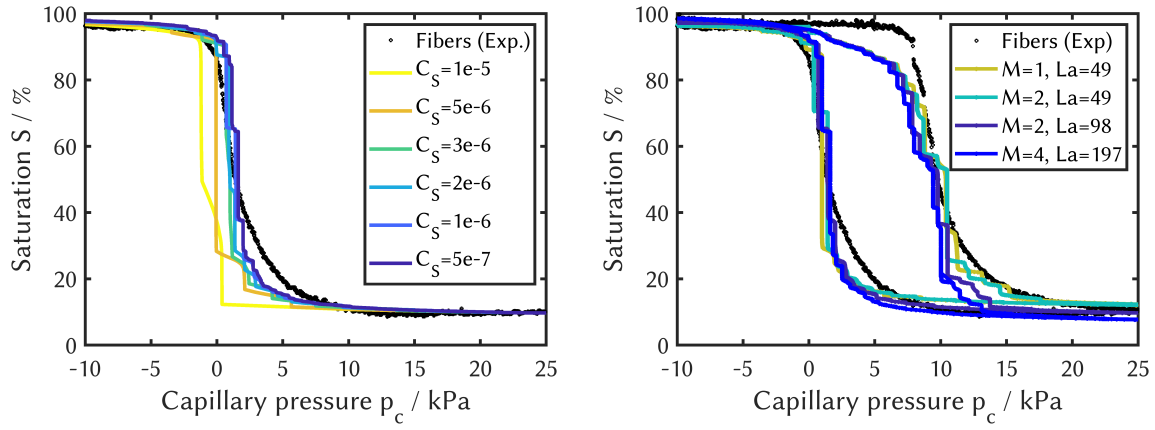

(a) Adaptive ramp speed.

(b) Fluid properties.

Figure 4.25: (a) Simulated capillary intrusion for the plain fiber substrate using varying ramp speeds C_S for the adaptive capillary pressure ramp. (b) Capillary hysteresis of the plain fiber substrate simulated for different dynamic viscosity ratios M and Laplace numbers La.

4.4.5 Sensitivity to fluid properties

Delimited by numerical stability, some fluid properties in the LB simulations have to be chosen different from the real physical air-water system. In the default computational setup (Section 4.3.3), the ratio of the dynamic viscosities is set to $M = 2$ instead of $M^{\text{phys}} \sim 50$ and the Laplace number equals approximately $\text{La} \approx 98$ as opposed to $\text{La}^{\text{phys}} \sim 1900$. However, since the liquid water transport in the GDL occurs in the capillary-dominated regime, application of these real physical ratios is not strictly necessary as long as dominance of capillary forces is assured. In order to verify the presence of a valid flow regime, a third study therefore investigates the sensitivity of the capillary characteristics on the dynamic viscosity ratio M and the Laplace number La. For this, capillary hysteresis is simulated for different values of M and La by variation of ν_g and σ (see equations (4.6) and (4.7)), respectively. Presuming that similar flow characteristics are obtained for a wider range of dynamic viscosity ratios and Laplace numbers, sufficiently high values in M and La are expected to provide the desired capillary-dominated regime of the real water-air fluid system. Figure 4.25b shows a comparison of simulated capillary intrusion and drainage curves for varying M and La with the experimental data. Apparently, the capillary hysteresis does not change considerably, even upon doubling of the dynamic viscosity ratio and the Laplace number. These observations indicate that already $M = 2$ and $\text{La} \approx 98$ prove to be sufficiently high to ensure a capillary-dominated hysteresis. In favor of numerical robustness in the LB simulations, the dynamic viscosity ratio and the Laplace number are chosen with $M = 2$ and $\text{La} = 98$ in all subsequent parametric studies.

4.4.6 Influence of lattice resolution

In dependence of the geometric complexity of a porous microstructure, pore-scale methods may require high spatial resolutions of the simulation geometries in order to account for all relevant structural details. At the same time, the computational domain has to be sufficiently large to recover the macroscopic structural properties of the porous sample (see REV in Section 4.2.3). For computationally expensive simulation techniques such as the LBM, the aforementioned PSM aspects lead to a practical dilemma as both demand for large lattice domains containing high numbers of voxels. Eventually, a compromise often has to be found between depth of structural detail and domain size. In another study, capillary hysteresis is therefore simulated and compared for the default and doubled lattice spacing of $\Delta x^{\text{phys}} = 0.96\,\mu\text{m}$ and $\Delta x^{\text{phys}}_{\text{coarse}} = 2\Delta x^{\text{phys}} = 1.92\,\mu\text{m}$ per voxel, respectively. If the lattice resolution turned out to yield similar capillary characteristics in the simulations, unnecessary depth of detail could then be traded in for a significant reduction of computation time. Beforehand the simulations, the GeoDict tool 'Rescale' is

therefore employed to coarsen the lattice geometry of the GDL subvolume for plain fiber substrate reconstruction. By this procedure, the original domain size of $500 \times 200 \times 156$ voxels is reduced by a factor of 8 to $250 \times 100 \times 78$ voxels (Figure 4.1d). In order to assure La ≈ 98 also for the simulations on the coarse lattice (see eq. (4.7)), the surface tension has to be furthermore adjusted to $\sigma^{\text{coarse}} = 0.25$, due to $d_p^{\text{coarse}} = d_p^{\text{phys}} / \Delta x_{\text{coarse}}^{\text{phys}} = d_p^{\text{phys}} / 2\Delta x^{\text{phys}}$. Figure 4.26a shows the simulated capillary hysteresis curves for the coarse and fine lattice geometry. While the intrusion curves for both resolutions agree qualitatively for $S < 50\,\%$, a significantly steeper saturation increase is observed for the coarse lattice towards higher saturations. Vice-versa, the opposite is observed for the drainage curves and simulation results deviate increasingly for saturations below 50 %. Based on the 2D through-plane pore diameter profile (Figure 4.20a), one may thus deduce that a highly resolved pore geometry is in particular important when the invading fluid is beyond the highest capillary barriers in the GDL core region and proceeding towards the increasingly larger surface pores. As a result, the capillary hysteresis is found to be underrepresented for the coarse simulation geometry, with a narrower width of the capillary hysteresis as compared to the fine lattice and the experimental data. Furthermore, the residual saturation is with $S^{\text{res}} \approx 5\,\%$ approximately halved for the coarser resolution. These observations can be explained with the lack of structural detail in the lattice representation of the pore-throat geometry. Moreover, by halving the spatial discretization the time scale is increased by a factor of 4 to $\Delta t_{\text{coarse}}^{\text{phys}} \approx 1.69e^{-6}\,\text{s}$ as well (see $C_t = C_l^2 / C_\nu$ in Section 3.2.4). Therefore, also the dynamics of pore filling events are covered much less accurately. In summary, a lattice resolution of approximately 2 µm per voxel is found to be too coarse to provide all relevant structural details to recover the capillary hysteresis of the plain fiber substrate appropriately. As a result of this investigation, the fine lattice with $\Delta x^{\text{phys}} = 0.96\,\mu\text{m}$ per voxel is chosen as the default for all subsequent studies within this chapter. At this point, it is noted that this study does not ensure a sufficiently high voxel resolution for 0.96 µm per voxel but only demonstrates the necessity for a spatial discretization of at least $\Delta x^{\text{phys}} < 2\,\mu\text{m}$, which is consistent with the findings of Wang et al. [335]. However, an investigation of GDL microstructures with even higher resolutions was in the frame of this work not possible due to the resolution limitations of the µCT imaging device. Whereas other comparable works [263, 270, 273–275] derive lower minimum resolutions from their mesh or grid independence studies [263, 270, 273], these studies usually only consider the intrusion or drainage process and thereby neglect to appropriately recover the capillary hysteresis.

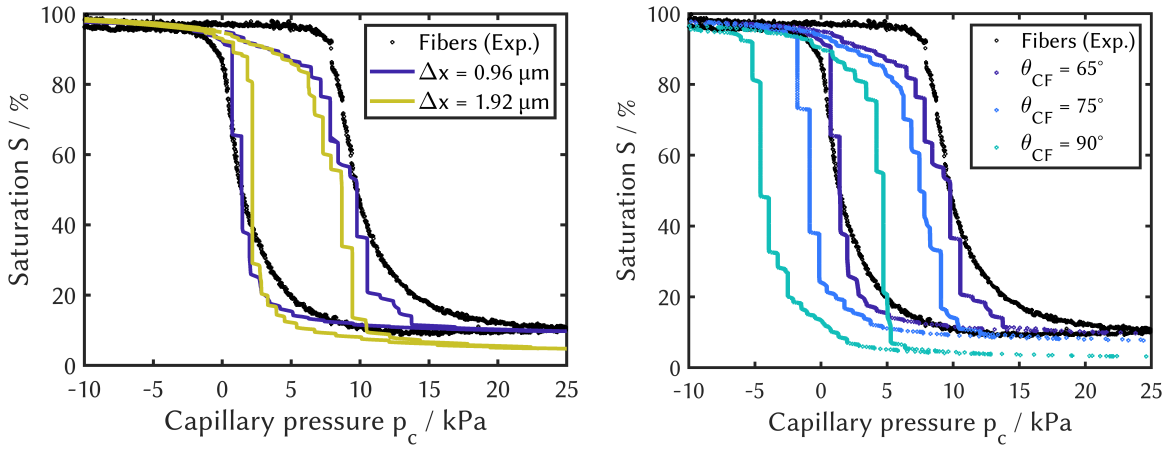

(a) Lattice resolution.

(b) Contact angle.

Figure 4.26: Simulated capillary hysteresis of the plain fiber substrate for varying resolutions of the lattice geometry and different carbon fiber wettabilities.

4.4.7 Variation of the carbon fiber wettability

Contact angle measurement is a standard procedure for characterization of GDL wettability, for which the sessile drop, Wilhelmy-Plate or the capillary rise method are the most commonly employed measurement techniques [66, 336]. However, all of these experimental approaches have in common that they determine the outer contact angle on the GDLs exterior surface. Thus, the measured values are effective quantities as they not only represent the wetting properties of the solid surfaces *per se* but also include the roughness and porosity of the exterior GDL surface [20, 337]. As a result, reported external GDL contact angles for liquid water are generally higher ($\theta > 90°$)[19, 338–340] than expected for a material structurally similar to graphite ($\theta \approx 60 - 90°$) [312, 341]. In recent decades, research works were therefore also dedicated to experimental assessment of inner contact angles within the GDLs interior pore structure, seeking for a more representative measure for wettability characterization [296, 342, 343]. While these approaches successfully eliminate effects of the exterior GDL surface, the derived contact angles still account for the internal pore morphology of the GDL. For microstructure-resolving pore-scale methods such as LBM, on the other hand, the contact angle should be free of any geometric influences since any structural effects (e.g., capillary valve effect) ideally arises from the lattice representation of the porous microstructure (see also Section 3.2.3). Hence, assumption of a graphite contact angle for the modeling of carbon fiber wettability appears to be an obvious choice to simulations of liquid water transport on the pore scale. However, since graphitic surfaces are in general also susceptible to contamination processes when exposed to ambient air [312, 341, 344, 345], there exists no unique literature value for its contact angle. As a result, related PSM studies on liquid water transport in GDLs have employed

a wide range of carbon fiber contact angles from 50° up to 95° [100, 322, 332, 341, 346]. In the default computational setup of this chapter, the carbon fiber contact angle is assumed with $\theta_{\mathrm{CF}} = 65°$, based on the measurement of Qiu et al. for a single carbon fiber [332]. In front of the bandwidth of reported contact angle values, however, there is a minor parametric uncertainty for the modeling of the carbon fiber wettability. Therefore, another simulation study is conducted to derive capillary hystereses for a range of possible contact angles. By comparison to the experimental data of the $p_c - S$ test bench, these curves furthermore assist in reassuring that wettability is modeled in the best possible way based on the agreement to the test bench data. Figure 4.26b shows simulated intrusion and drainage curves for carbon fiber contact angles of 65°, 75° and 90°. As apparent from first sight, the capillary hysteresis is observed to be shifted towards lower capillary pressures for increasing θ_{CF}, which is in line with related experimental [100, 260] and simulation work [139, 273]. This trend is as expected, since the capillary transport resistance for the invasion of a wetting fluid (liquid water) increases with higher hydrophobicity of a porous medium. Vice-versa and equivalently, drainage of the wetting phase is promoted by an increasing surface hydrophobicity. At $\theta_{\mathrm{CF}} = 90°$, neutral wettability is obtained and both fluids experience the same capillary resistance for pore invasion, as indicated by a simulated hysteresis curve being symmetrical around $p_c = 0\,\mathrm{kPa}$. Along with the increase in hydrophobicity, the residual saturation is furthermore found to decrease from $S^{\mathrm{res}}(\theta_{\mathrm{CF}} = 65°) \approx 10\,\%$ to $S^{\mathrm{res}}(\theta_{\mathrm{CF}} = 75°) \approx 8\,\%$ and $S^{\mathrm{res}}(\theta_{\mathrm{CF}} = 90°) \approx 3\,\%$, respectively. This observation is in agreement with Liao et al. [347] and can be explained by a reduced fluid-solid interaction strength and consequently a lower tendency for the wetting phase to become entrapped in narrow GDL pores upon drainage. In summary, this parametric study confirms the initial choice for a carbon fiber contact angle of $\theta_{\mathrm{CF}} = 65°$, as the corresponding simulated capillary hysteresis provides the best agreement with the test bench data.

4.4.8 Representativeness of the GDL subvolumes

In Section 4.2.3, three representative elementary volumes are selected for the plain fiber substrate of the H14 GDL. Based on a comparison of the porosity profiles (Figure 4.4c) and the pore size distributions (Figure 4.5a), these GDL subvolumes (Figure 4.1d-Figure 4.1e) are furthermore found to posses similar structural properties. However, while the default GDL subvolume ((Figure 4.1d) already proved to recover the experimental $p_c - S$ curves appropriately, this does not ensure representativeness for the capillary characteristics of the GDL since the agreement could be as well coincidental. Therefore, capillary hysteresis has to be simulated and compared for all three GDL subvolumes. In case of similarity,

the chosen domains are then confirmed to serve as REVs not just for the structural properties but also for the capillary characteristics of the GDL as well. Figure 4.27 shows the simulated capillary intrusion and drainage curves for the three different plain fiber subvolumes. Even though minor deviations are observable, the overall curvature and width of capillary hysteresis as well as the residual saturation are very similar among all three GDL subvolumes. The remaining small variance in the simulated $p_c - S$ curves can be furthermore related to the local structural heterogeneity across the GDL subvolumes, as indicated by the porosity profiles ((Figure 4.4c) and the pore size distributions (Figure 4.5a). Eventually, this investigation confirms that the selected GDL subvolumes effectively serve as REVs in being not just representative for the structural properties but the capillary characteristics of the GDL as well. At this point, the computational setup for the simulation of capillary liquid water transport in the plain fiber substrate of the H14 GDL is considered to be successfully validated by satisfactory agreement with experimental $p_c - S$ data.

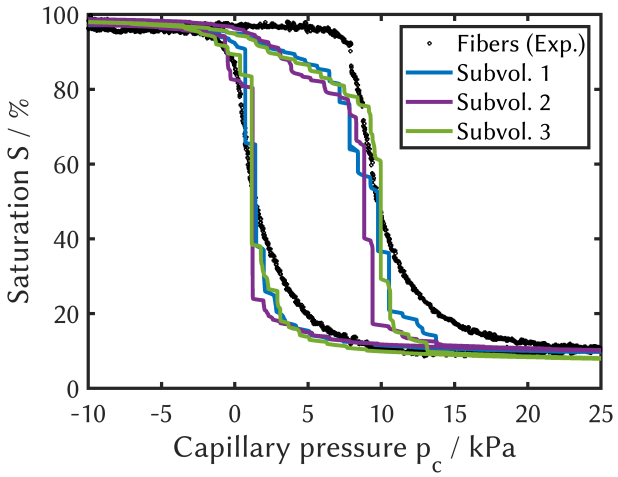

Figure 4.27: Simulated capillary hysteresis for three different subvolumes (Figure 4.1d-Figure 4.1e) of the GDL microstructure reconstruction for the plain fiber substrate.

4.4.9 Impact of mixed wettability

GDLs are commonly wet-proofed with hydrophobic agents such as PTFE in order to improve their water management capabilities (see Section 2.2.2). As a result of the hydrophobizing treatment, the partially impregnated carbon fibers exhibit surfaces with locally variable hydrophilicity. While many PSM studies on GDL wettability neglect this aspect by limiting their investigations to uniform contact angles [55, 93, 139, 340, 348–350], mixed wettability reportedly has a significant influence on the capillary transport characteristics in porous media [90, 261, 263, 270, 273, 312, 339, 351]. In this work, however, an algorithm is developed as introduced in Section 4.2.5, which models the

spatial PTFE distribution within the GDL in a realistic fashion according to experimental observations. While quantitative experimental surface analysis is still difficult and beyond the scope of this work, the modeled mixed wettability can be only validated indirectly based on the comparison of simulated capillary hysteresis curves with test bench data. In order to investigate the impact of mixed wettability on the GDL liquid water transport, capillary intrusion and drainage is simulated for the GDL subvolume of the impregnated H14 fiber substrate, as shown in Figure 4.2b. A heterogeneous spatial additive distribution is therefore realized as described in Section 4.2.4 and Section 4.2.5, with an overall PTFE surface coverage of $\chi = 50\,\%$. For the LB simulations, the computational setup is the same as for the plain fiber substrate, i.e., with a domain size of $500 \times 200 \times 156$ voxels and a lattice resolution of $\Delta x^{\text{phys}} = 0.96\,\mu\text{m}$ per voxel. Mixed wettability is furthermore modeled with contact angles of $\theta_{\text{CF}} = 65°$ and $\theta_{\text{PTFE}} = 115°$ for the carbon fibers and PTFE, respectively.

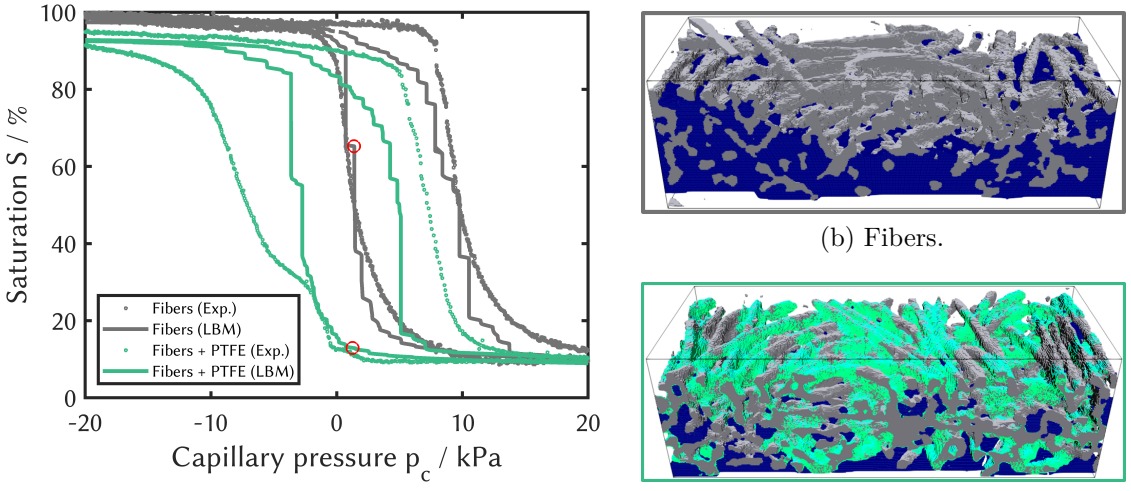

(a) $p_c - S$ curve.

(b) Fibers.

(c) Fibers+PTFE.

Figure 4.28: (a) Simulated capillary hysteresis for the plain (Figure 4.1d) and impregnated (Figure 4.12) fiber substrate. (b)-(c) Simulation snapshots visualize the liquid water distribution in the respective intrusion curve, as indicated by red circles in (a). The different phases are colored as follows: Carbon fiber (grey), PTFE (green), liquid water (dark-blue).

Figure 4.28a shows the simulated capillary hysteresis for both the plain and impregnated fiber substrate in comparison to the test bench data. In both simulation and experiment, a distinct shift of the capillary hysteresis towards lower capillary pressures can be seen for the impregnated fiber substrate. This observation is as expected and comparable to the findings in Section 4.4.7, since impregnation with a hydrophobic additive leads to an increase of the average GDL contact angle, resulting in a higher capillary transport resistance for the invading wetting fluid. This impeding effect of the PTFE-impregnation

on the liquid water transport is also contrasted by two simulation snapshots visualizing the wetting phase distribution during intrusion into the plain (Figure 4.28b) and impregnated (Figure 4.28c) fiber substrate. While the former is with $S \approx 65\,\%$ by almost two thirds saturated, the hydrophobized fiber substrate is with $S \approx 13\,\%$ still comparably dry (red circles in Figure 4.28a). Different to the capillary hysteresis for a uniform contact angle, however, the saturation in the impregnated fiber substrate never reaches a maximum of $100\,\%$, which is in line with Niu et al. [270]. In addition, the residual saturation S^{res} appears to be unaltered by hydrophobization of the carbon fibers. These two observations can be both explained by the heterogeneous additive distribution (Figure 4.13e), which renders the GDL surfaces more hydrophobic than the core region. As a result, liquid water encounters elevated capillary barriers already in the surface region of the wetting phase inlet side and consequently enters the GDL via fewer invasion paths. Approaching the GDL core region, liquid water intrusion is then driven by a positive (hydrophobic to hydrophilic) wettability gradient before it is hampered again by an increasing PTFE surface coverage towards the GDL surface region of the gas inlet side. This accelerated capillary filling of the core region leads to an increased gas phase entrapment in the GDL surface region near the liquid phase inlet, eventually lowering the maximum saturation. For the invasion of the non-wetting gas phase (i.e., during liquid water drainage), the capillary bottleneck remains in the GDL core region, as the major portion of the hydrophobic additive is located in the GDL surface regions. Therefore, entrapment of the wetting phase and thus the residual saturation S^{res} is similar in both the plain and impregnated fiber substrate. With respect to the width of the capillary hysteresis, on the other hand, the experimental data deviate significantly for the two GDL samples. While at lower saturations the shift towards lower capillary pressure is similar for both the intrusion and drainage curve, an intermediate change in curvature is observed for the former between $30\,\% < S < 40\,\%$. As a result, the width of the capillary hysteresis for the impregnated fiber substrate is measured to be significantly broader and of different shape in comparison to the test bench data for the plain fiber substrate. According to Tranter et al. [352], this characteristic 'shoulder' in the intrusion curve is a measurement artifact which stems from improper hydraulic contact between the GDL sample and the enclosing semipermeable membranes. Gostick et al. [261] reported similar observations and related the 'shoulder' to effects of limited domain sizes in thin GDLs, which would vanish for increased sample thicknesses. In contrast to the experimental observations, the LB simulations show for the impregnated fibers a capillary hysteresis of similar width and shape as for the plain fiber substrate, which is in agreement with findings of related experimental [261] and simulative [263] studies. In spite of affirmation by related literature and the strong indication of an experimental artifact, further simulations for varying additive distributions are carried out subsequently

to assure that the observed deviation from the experiment is not caused by improper modeling of mixed wettability.

4.4.10 Variation of the spatial additive distribution

As quantitative experimental analysis of additive distributions remains a major challenge (see Section 4.2.5), the overall PTFE surface coverage is so far estimated with $\chi^{\mathrm{est}} = 50\,\%$. In front of this parametric insecurity, liquid water intrusion and drainage are therefore in the following also simulated for different additive surface coverages to investigate their effect on the capillary hysteresis of the impregnated fiber substrate. Whereas χ is varied in this parametric study, the spatial distribution of the additive is kept heterogeneous along the GDL thickness, according to the through-plane profiles in Figure 4.14.

Figure 4.29a shows the simulated capillary hysteresis for the impregnated fiber substrate subvolumes (Figure 4.14) with PTFE surface coverages of 25 % and 75 % in comparison to the default of $\chi = 50\,\%$. As expected, for a higher additive surface coverage of $\chi = 75\,\%$ the capillary hysteresis is found to be progressively shifted towards lower capillary pressures, owing to the increasing hydrophobicity of the carbon fiber surface. For a lower additive surface coverage of $\chi = 25\,\%$, on the other hand, the maximum saturation is observed to increase. This is reasonable and consistent with Figure 4.28, as for declining χ the GDL microstructure approaches the wetting properties of the plain fiber substrate. Interestingly, the maximum saturation furthermore appears to be rather constant for PTFE surface coverages of $\chi \geq 50\,\%$. A possible explanation for this could be that the wettability gradient from the GDL surface to the core region potentially reaches a maximum for $\chi \geq 50\,\%$, resulting in similar gas phase entrapment (see Section 4.4.9). The residual saturation on the other side is observed to be reduced from $S^{\mathrm{res}} \approx 9\,\%$ to 4 % for the highest additive surface coverage of $\chi = 75\,\%$. This trend is similar to the one observed for the change $65° \rightarrow 90°$ in the uniform carbon fiber contact angle θ_{CF} of the plain fiber substrate (Figure 4.26b), indicating a vanishing effect of mixed wettability. According to these observations for a change in the average contact angle, one may expect that for an additive surface coverage of $\chi = 25\,\%$ the residual saturation would be at least as high as for $\chi = 50\,\%$. However, the residual saturation resides around $S^{\mathrm{res}} \approx 6\,\%$ and thus between the ones observed for $\chi = 75\,\%$ and $\chi = 50\,\%$. This observation demonstrates that not just the overall content of the hydrophobic additive but rather its spatial distribution is decisive for the residual saturation in mixed-wetting porous media. With respect to the capillary hysteresis, on the other hand, no distinct variation is observable as all three PTFE surface coverages yield capillary hystereses of similar shape and width.

In a final parametric study, capillary transport of liquid water is therefore simulated for a homogeneous additive distribution (Figure 4.17 and Figure 4.16) and compared to the default heterogeneous profile to investigate if a different spatial additive distribution could induce an increase in the capillary hysteresis width. Figure 4.29b shows that this is not the case as both the heterogeneous and homogeneous PTFE distribution yield very similar capillary intrusion and drainage curves. Furthermore, also the maximum saturation is found to be comparable. The only notable difference is observed for the residual saturation, which decreases to $S^{\mathrm{res}} \approx 4\,\%$ (comparable to $\theta_{\mathrm{CF}} = 90°$ and $\chi = 75\,\%$) for the homogeneous additive profile. This finding can be explained by a more hydrophobic GDL core region and lower wettability gradients along the through-plane direction, both reducing liquid phase entrapment.

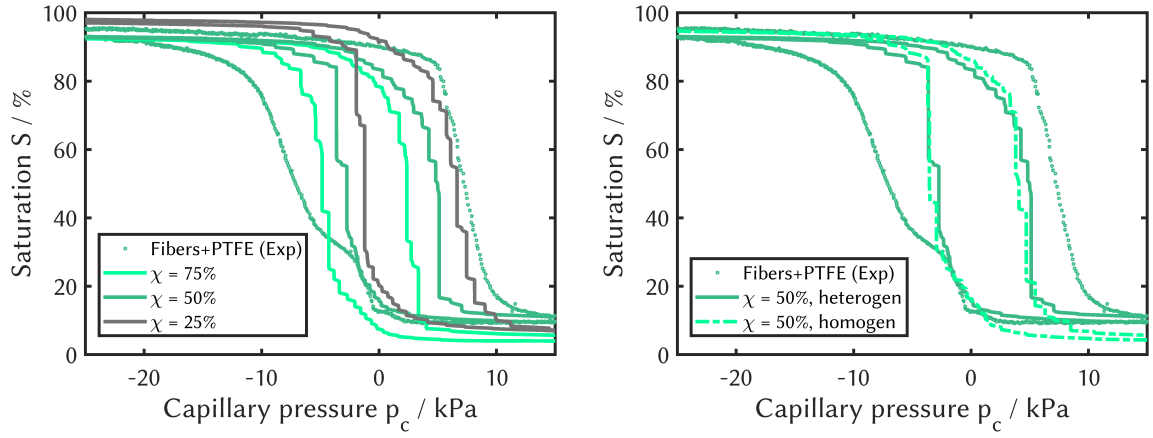

(a) PTFE surface coverage.

(b) Spatial PTFE distribution.

Figure 4.29: Simulated capillary hysteresis for the impregnated fiber substrate under variation of the spatial PTFE distribution with respect to (a) degree of fiber surface coverage (Figure 4.15) and (b) heterogeneity along the GDL thickness (Figure 4.17).

In summary, above simulative studies show that even moderate variations in the spatial distribution of PTFE do not have a significant impact on the width of the capillary hysteresis. Thus, parametric insecurity in the modeling of mixed wettability can be largely excluded as an explanation for the remaining deviation between simulation and measurement. At this point, the LB model validation for the capillary liquid water transport in the impregnated fiber substrate is considered to be completed as partly successful. Whereas the simulations reproduce the impeding effect of a hydrophobic additive on the wetting phase transport in general, a mismatch remains between the simulated and measured intrusion curve. Eventually, this discrepancy is assumed to arise from limited reliability of the test bench data, as the measurement of the impregnated H14 fiber substrate is presumably distorted by an experimental artifact.

4.4.11 Derivation of novel $p_c - S$ relations

After the (partially successful) validation of the simulated capillary hystereses for the plain and impregnated H14 fiber substrate in the previous subsections, novel $p_c - S$ relations are in the following derived by nonlinear curve-fitting. Later on, these expressions can be used in, e.g., cell-level simulation models for the prediction of capillary characteristics for the intrusion and drainage of liquid water. For the plain fiber substrate (Figure 4.30a), the simulated intrusion curve is found to be described almost perfectly by an inverse tangent relation

$$S_{\mathrm{H14}}^{\mathrm{Intr}}\left(p_c\right) = S_{\mathrm{H14}}^{\mathrm{res}} + \left[\frac{\pi}{2} - \arctan\left(A_{\mathrm{H14}}^{\mathrm{Intr}} \cdot p_c + B_{\mathrm{H14}}^{\mathrm{Intr}}\right)\right] \frac{\Delta S_{\mathrm{H14}}}{\pi} \tag{4.13}$$

with the residual saturation $S_{\mathrm{H14}}^{\mathrm{res}} = 9.72\,\%$, maximum saturation $S_{\mathrm{H14}}^{\mathrm{max}} = 98.79\,\%$, maximum saturation change $\Delta S_{\mathrm{H14}} = S_{\mathrm{H14}}^{\mathrm{max}} - S_{\mathrm{H14}}^{\mathrm{res}} = 89.06\,\%$. By nonlinear regression, the two fit parameters $A_{\mathrm{H14}}^{\mathrm{Intr}}$ and $B_{\mathrm{H14}}^{\mathrm{Intr}}$ are furthermore determined as listed in Table 4.3. For the drainage of liquid water, a similar fit function

$$S_{\mathrm{H14}}^{\mathrm{Drain}}\left(p_c\right) = S_{\mathrm{H14}}^{\mathrm{res}} + \left[\frac{\pi}{2} - \arctan\left(A_{\mathrm{H14}}^{\mathrm{Drain}} \cdot p_c + B_{\mathrm{H14}}^{\mathrm{Drain}}\right)\right] \frac{\Delta S_{\mathrm{H14}}}{\pi} \tag{4.14}$$

is observed to describe the simulated $p_c - S$ curve over a wide saturation range accurately as well (yellow solid line in Figure 4.30a). In the low and high capillary pressure region, on the other hand, equation (4.14) is found to over-/underestimate the minimum and maximum saturation, respectively. By slight adjustment, however, a modified second fit function (with the same fit parameters $A_{\mathrm{H14}}^{\mathrm{Drain}}$ and $B_{\mathrm{H14}}^{\mathrm{Drain}}$) can be obtained with

$$S_{\mathrm{H14}}^{\mathrm{Drain}}\left(p_c\right) = \left(S_{\mathrm{H14}}^{\mathrm{res}} - 0.0275\right) + \left[\frac{\pi}{2} - \arctan\left(A_{\mathrm{H14}}^{\mathrm{Drain}} \cdot p_c + B_{\mathrm{H14}}^{\mathrm{Drain}}\right)\right] \frac{1.05\Delta S_{\mathrm{H14}}}{\pi} \tag{4.15}$$

which then predicts the drainage curve of the plain fiber substrate over the whole saturation range very well (yellow dashed line in Figure 4.30a). On the other hand, the widely-used Leverett relation (*cf.* equations (2.20)-(2.22)) may provide an acceptable description for the capillary characteristics only in the intermediate saturation range (approx. 20 to 80 %) but is otherwise incapable of predicting both the intrusion and drainage curve in the low and high saturation region. Similar observations have been also reported by Hao et al. [263].

For the impregnated H14 fiber substrate (Figure 4.30b) an inverse tangent relation is as well determined to appropriately describe the $p_c - S$ characteristics for the intrusion

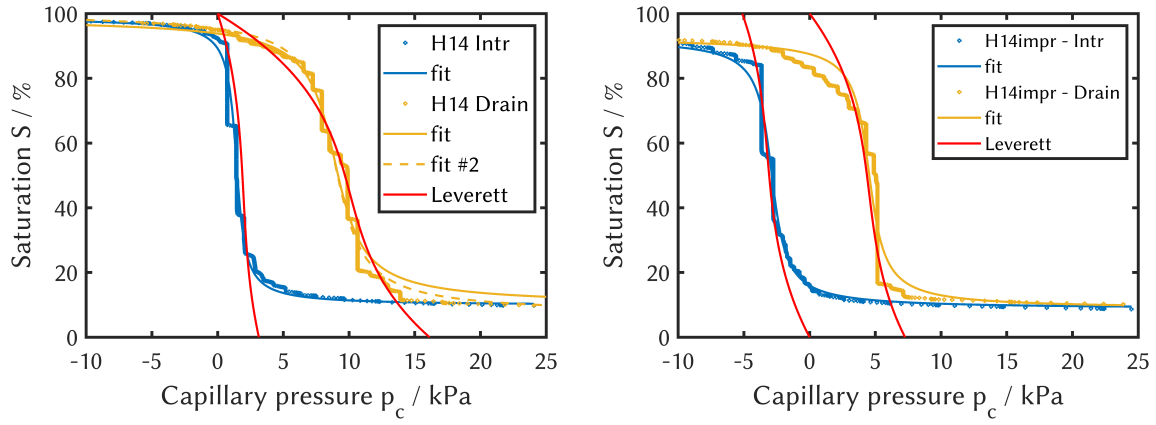

(a) Plain H14 fiber substrate

(b) Impregnated H14 fiber substrate.

Figure 4.30: Simulated capillary hysteresis for the plain and impregnated H14 fiber substrate and corresponding $p_c - S$ fit functions. The Leverett relation (*cf.* equations (2.20)-(2.22)) was fitted to the respective drainage curves.

$$S^{\mathrm{Intr}}_{\mathrm{H14impr}}\left(p_c\right) = S^{\mathrm{res}}_{\mathrm{H14impr}} + \left[\frac{\pi}{2} - \arctan\left(A^{\mathrm{Intr}}_{\mathrm{H14impr}} \cdot p_c + B^{\mathrm{Intr}}_{\mathrm{H14impr}}\right)\right] \frac{\Delta S_{\mathrm{H14impr}}}{\pi} \tag{4.16}$$

and drainage curve

$$S^{\mathrm{Drain}}_{\mathrm{H14impr}}\left(p_c\right) = S^{\mathrm{res}}_{\mathrm{H14impr}} + \left[\frac{\pi}{2} - \arctan\left(A^{\mathrm{Drain}}_{\mathrm{H14impr}} \cdot p_c + B^{\mathrm{Drain}}_{\mathrm{H14impr}}\right)\right] \frac{\Delta S_{\mathrm{H14impr}}}{\pi} \tag{4.17}$$

most appropriately with the residual saturation $S^{\mathrm{res}}_{\mathrm{H14impr}} = 8.68\,\%$, maximum saturation $S^{\mathrm{max}}_{\mathrm{H14impr}} = 92.67\,\%$, maximum saturation change $\Delta S_{\mathrm{H14impr}} = S^{\mathrm{max}}_{\mathrm{H14impr}} - S^{\mathrm{res}}_{\mathrm{H14impr}} = 83.99\,\%$. The two parameters $A^{\mathrm{Intr}}_{\mathrm{H14}}$ and $B^{\mathrm{Intr}}_{\mathrm{H14}}$ are again fitted by nonlinear regression with values as listed in Table 4.3. As apparent from Figure 4.30b, the Leverett relation describes also in this case the $p_c - S$ characteristics in the intermediate saturation range (approx. 20 to 80 %) well but otherwise fails to provide any accurate predicting in the low and high saturation region for both the intrusion and drainage curve. As clearly illustrated by the above comparison, widely-used empirical relations do not necessarily provide appropriate predictions for the $p_c - S$ characteristics of GDLs, irrespective of their popularity. Consequently, novel $p_c - S$ relations (as provided by this work) are needed to improve future models for the GDL liquid water transport. However, whereas the newly derived $p_c - S$ of this section are in general ready-to-use for cell-level simulation models, there also still remains the question about the reasonable coupling of two $p_c - S$ relations (intrusion/drainage) and thus appropriate modeling of capillary hysteresis on the cell-level.

Table 4.3: Fit parameters for the new $p_c - S$ relations (equations (4.13)-(4.15)) derived for the plain and impregnated H14 fiber substrate (Figure 4.30)

$A^{\mathrm{Intr}}_{\mathrm{H14}}$ kPa	$B^{\mathrm{Intr}}_{\mathrm{H14}}$ –	$A^{\mathrm{Drain}}_{\mathrm{H14}}$ kPa	$B^{\mathrm{Drain}}_{\mathrm{H14}}$ –	$A^{\mathrm{Intr}}_{\mathrm{H14impr}}$ kPa	$B^{\mathrm{Intr}}_{\mathrm{H14impr}}$ –	$A^{\mathrm{Drain}}_{\mathrm{H14impr}}$ kPa	$B^{\mathrm{Drain}}_{\mathrm{H14impr}}$ –
2	−2.86	0.64	−5.67	1.24	3.57	1.13	−5.1

4.5 Conclusion

In this chapter, capillary hysteresis was investigated for the plain and PTFE-impregnated fiber substrate by simulation of capillary intrusion and drainage of liquid water. At first, GDL microstructures were reconstructed by segmentation of CT images with a high resolution of $\Delta x^{\mathrm{phys}} = 0.96\,\mu$m per pixel. Smaller GDL subvolumes were then selected as representative elementary volumes (REV) for further investigation and following a novel approach based on the analysis of in-plane porosity profiles. Representativeness of these elementary volumes was then confirmed by structural properties (local porosity profiles and pore size distributions) similar to the macroscopic properties of the overall GDL microstructure. In addition, an in-house algorithm was developed to differentiate carbon fibers and PTFE in the impregnated fiber substrate. The routine was then employed to localize additive near fiber intersections according to experimental observations and based on a heterogeneous PTFE loading profile as derived from µCT images. Subsequently, a computational setup was generated with boundary conditions similar to a test bench for the measurement of $p_c - S$ curves. Corresponding to the experimental measurement procedure, capillary invasion and drainage of liquid water was then simulated using an adaptive gas phase pressure ramp in the computational setup. The derived capillary hysteresis curves were then compared with test bench data to validate the simulation model for the capillary liquid water transport in GDL microstructures. In order to provide new insights on key influencing parameters for capillary hysteresis, liquid water transport was furthermore studied for a variety of different model and simulation parameters, leading to the following prime observations:

- Boundary effects can have a major impact on the structural properties of the GDL, owing to the highly-porous surface regions. In order to simulate capillary characteristics as experimentally observed, boundary conditions have to be chosen with care and as close as possible to the corresponding test bench setup. In the simulations of this chapter, GDL microstructures therefore had to be modeled as sandwiched between two semipermeable membranes, according to the boundary conditions of a test bench for the measurement of $p_c - S$ curves. Whereas neglect of this aspect resulted in

an overestimation in the residual saturation, a more sophisticated membrane model allowed to achieve a good agreement with the experimental data. This finding also raises a general question on the transferability of *ex situ* wettability characterization to *in situ* conditions in fuel cell operation.

- A sufficiently high spatial discretization is indispensable for the validity of microstructure-resolved simulations. In this chapter, a lattice resolution of at least 0.96 µm per voxel was required to resolve all relevant structural details of GDL microstructure reconstructions in order to appropriately recover their capillary hysteresis. While higher resolutions were inaccessible to the µCT imaging device available in this work, the value 0.96 µm per voxel is not guaranteed to be already sufficiently high and should be therefore interpreted as a lower resolution limit.

- The contact angle is a fundamental parameter to surface wettability in both experiment and simulation. Whereas in the former case several standard characterization methods exist, the resulting measured values usually not only account for wetting but structural properties such as surface roughness as well. For wettability modeling in LB simulations, on the other hand, the contact angle ideally only accounts for wetting properties, as geometric effects should arise from a sufficiently resolved simulation geometry itself. Owing to the parametric insecurity due to a wide range of literature values, capillary intrusion and drainage was simulated for carbon fiber contact angles of 65°, 75° and 90°. As expected, capillary transport of liquid water was observed to be hampered for increasing contact angles, owing to decreasing hydrophilicity of the GDL fiber substrate. Whereas this effect was clearly indicated by a linear shift towards lower capillary pressures, the overall width of the hysteresis remained unaltered. Furthermore, the residual saturation was found to be significantly reduced for a neutrally wetting fiber substrate with 90°. Eventually, a contact angle of 65° proved to yield the best agreement between simulation and experiment. Based on the obtained results, the LB model is considered to be validated for the capillary transport of liquid water in the plain fiber substrate of the H14 GDL.

- For the simulation of the capillary hysteresis in the impregnated fiber substrate, mixed wettability was modeled with contact angles of $\theta_{\mathrm{CF}} = 65°$ and $\theta_{\mathrm{PTFE}} = 115°$ for the carbon fibers and PTFE, respectively. While the simulated capillary intrusion and drainage curves showed the expected shift towards lower capillary pressures due the impeding effect of the hydrophobic additive, the width of the capillary hysteresis remained unaffected. Furthermore, the simulations illustrated that unlike a uniform contact angle, mixed wettability can lead to wettability gradients in

the GDL microstructure. These influence the entrapment of both the wetting and non-wetting phase, resulting in different maximum and residual liquid water saturations upon intrusion and drainage. Apart a similar shift of the capillary hysteresis towards higher capillary pressures, the experiment on the other hand showed an intrusion curve with a different curvature in the intermediate saturation range between 30 to 40 %. As a result, the capillary hysteresis of the impregnated fibers was measured to be significantly broader than for the plain fiber substrate. However, even for variations in the content and spatial distribution of PTFE, such characteristic could not be recovered in the simulations. Supported by related research works, this discrepancy between experiment and simulation is eventually assumed to be caused by an experimental artifact and not by deficiencies in the wettability modeling. For completeness, it is at this point noted that despite a high resolution in the µCT images, primary PTFE particles with a commonly reported size of 0.5 µm [292, 318, 353] likely remained unresolved in the GDL microstructure reconstruction. Therefore, local heterogeneity could be in principle underrepresented in the underlying modeling of mixed wettability. However, it is assumed that, if even quantifiable, this aspect would have a much smaller effect on the capillary hysteresis than the indicated experimental artifact. At this point, the LB model is considered to be only partly validated for the capillary transport of liquid water in the impregnated fiber substrate of the H14 GDL. While the LB simulations have in general demonstrated appropriate modeling of mixed wettability by reproducing expected trends, a satisfactory agreement with the experiment was not achievable.

- In order to describe the capillary characteristics of the plain and impregnated H14 fiber substrate, novel $p_c - S$ relations were derived from the respective simulated intrusion and drainage curves. As a result, fit functions were obtained by nonlinear regression, which accurately described the saturation in inverse tangent relation to the capillary pressure. Employing the widely-used Leverett relation, on the other hand, the predictions were found to be only suitable in the intermediate saturation range between approximately and 20 to 80 % but otherwise failed to achieve reasonable agreement with the simulated $p_c - S$ curves in the low and high saturation regions.

5 Impact of gas diffusion and microporous layer degradation on effective transport properties

5.1 Aging phenomena for diffusion layer degradation during fuel cell operation

As introduced in Section 1.1, durability is to this day still considered as one of the remaining barriers for widespread commercialization of PEM fuel cells. Since the GDL and MPL have to fulfill several essential tasks such as effective gas distribution and efficient water removal, degradation of these porous cell components can result in severe performance losses or even failure during operation. As evidenced by a multitude of experiments, aging of the GDL and MPL is generally embodied in structural changes and/or alteration of the surface wettability [354]. The former degradation effect is typically accompanied by changes in structural properties such as porosity, permeability or tortuosity and has therefore direct consequences for the effective mass transport and thereby the overall cell performance. Wettability changes, on the other hand, impair the water removal capabilities of the porous media, which can lead to liquid water accumulation and thereby a severe deterioration of the gas transport due to increasing pore blockage. While the repercussions of wettability alteration on the fuel cell performance are only indirect, the consequences of a degrading water management can be drastic, as flooding of the porous electrodes may result in complete failure of fuel cell operation. These concerns are in particular present in mobile PEMFC use cases such as automotive application, where aging is accelerated by the harsh operating conditions [355].

According to Pan et al. [356], the different scenarios for GDL/MPL degradation can be assigned to three basic operation modes: idling at open-circuit voltage (OCV), start-up/shutdown (SUSD) and ordinary operation with static/dynamic load demands. At open-circuit voltage (OCV) present in idling periods, hydrogen peroxide (H_2O_2) may be formed at the anode due to gas crossover (O_2) from the cathode [357]. Catalyzed in the

presence of transition metal ions (primarily contaminations from membrane fabrication or degradation of metallic cell components [358]), radicals may then be formed in Fenton reactions [359]. After formation, these free radicals then attack weak chemical bonds of surrounding cell components. Whereas studies on this type of chemical degradation focused in the past primarily on the ionomer membrane [360], similar aging behavior was later also reported for the catalyst layer [361]. In recent years, researchers also studied potential radical attack degradation of the GDL and MPL. Owing to the difficulty of isolating superposing aging effects, however, degradation was, to the author's knowledge, so far solely investigated in *ex situ* experiments by immersion of porous samples into peroxide solutions [32–36]. As a result of the oxidative conditions in these baths, researchers have reported carbon mass loss, which was higher in the presence of a MPL, and increased surface hydrophilicity. Liu et al. [362] furthermore attributed the quantified mass loss partly to PTFE degradation. In subsequent *in situ* cell tests, the observed performance decay was then primarily accredited to a worsening of the water management related to the wettability changes due to surface oxidation.

A similar degradation route for the oxidation of carbonaceous surfaces can occur in the start-up or shutdown phase of a PEM fuel cell. With a standard potential of 0.207 V, carbon is under fuel cell conditions a thermodynamically unstable cathode material susceptible to electrochemical oxidation. Whereas electrochemical carbon corrosion occurs in general during ordinary FC operation, this process is typically negligible due to the very slow reaction kinetics. At fuel cell start-up, however, the electrodes are initially filled with air and a hydrogen-air front is established in the anode by the reactant gas feed. In the passive anode zone, the absence of hydrogen then creates a high interfacial potential difference of up to 1.44 V, which strongly promotes carbon corrosion in the cathode. As firstly introduced and explained by Reiser et al. [363], this reverse-current mechanism is expected to be present not just at start-up but at shutdown or any other similar scenario of local fuel starvation as well. Therefore, electrochemical carbon corrosion can become also relevant in normal fuel cell operation, e.g., in anode flooding [364]. Whereas originally primarily investigated as a degradation mechanism for catalyst layers, researchers have in recent years also observed comparable yet less pronounced electrochemical carbon corrosion in the GDL and MPL as well [365–370]. Similar to the degradation by radial attack, aging was reported to result in loss of carbon material and surface oxidation. Observed performance losses were again related to the aggravation of water management upon wettability changes.

Another degradation scenario strongly associated with the start-up period arises from fuel cell operation below the freezing point. As a prerequisite for automotive application, cold start from subzero temperatures poses a challenging task for FC durability due to

the formation of ice inside the cell [355]. The latter may be formed by the freezing of residual water from the previous shutdown period or newly generated water during the start-up. As the water freezes in the porous layers, the effective gas transport and the electrochemically active surface area (ECSA) may be strongly reduced, potentially causing complete operation failure. Furthermore, the volumetric expansion due to the phase change upon ice formation exerts mechanical stress on the porous MEA components, which may undergo irreversible structural changes [371]. In order to investigate potential degradation effects in fuel cell cold start, researchers have therefore artificially aged GDLs and MPLs primarily by (thermal) freeze-thaw cycling in *ex situ* experiments [37–40]. According to Pan et al. [356], the observed aging phenomena can be categorized primarily into three different structural alterations: crack formation in the GDL carbon fibers and the MPL, loss of hydrophobic additive (detachment of PTFE) and delamination of MEA components (e.g., GDL/MPL and CL). Based on the reported findings, microstructure aging during FC cold start may be therefore in general expected to have a detrimental impact on the mechanical strength, water management as well as electrical and thermal conductivity of the GDL and MPL.

In addition to the cold start scenario, mechanical stress can occur during normal fuel cell operation as well. Whereas in general a certain clamping pressure is required for air-tight cell assembly and proper electrical and thermal contacting, elevated mechanical loads can reduce the effective mass transport in the diffusion media [372]. Furthermore, an overly compressed cell assembly may also lead to irreversible structural alterations of the GDL and MPL with additional adverse effects on the FC performance. Performing static compression tests as well as dynamic load cycling (e.g., vibrations or membrane shrinking/swelling due to (de-)hydration [356]), researchers have reported that mechanical degradation can result in carbon fiber breakage [373, 374], additive detachment (PTFE loss) [375] and MPL cracking [79]. Owing to its mechanical properties, presence of the MPL was furthermore observed to dampen GDL deformation upon compression [376]. Beyond the aforementioned structural alterations, however, mechanical degradation of the GDL and MPL may affect the structural integrity of adjacent MEA components as well, thereby compromising the cell performance even further [377].

Another mechanical aging scenario during ordinary FC operation is commonly postulated to occur due to erosion at high gas velocities. In order to investigate potential degradation effects, researchers have therefore exposed dummy cell assemblies (without catalyst layer) to high gas flow rates. Aging impacts were then amongst others assessed in single cell performance tests. Whereas all studies reported material loss and performance decay in the high current region, these findings were primarily related to changes in the MPL morphology [78, 378] or a decrease in GDL surface hydrophobicity due to loss of PTFE

[379] in the degraded samples. The observed performance losses were furthermore mostly accredited to increased mass transport resistances due to an aggravated water management. As pointed out by Lapicque et al. [380], however, the reported aging effects might stem to a certain degree from a superposition of different aging mechanism, since the experiments also involved other stressors such as elevated temperatures or high gas humidity.

In the presence of liquid water in an air-rich environment during normal fuel cell operation, the cathode side diffusion layers might be as well exposed to oxidative conditions, which could cause material dissolution. Researchers have therefore conducted *ex situ* leaching tests, immersing the GDL and MPL into deionized water at elevated temperatures in order to study potential degradation effects. While all investigations reported a decreasing hydrophobicity, this was primarily accredited to dissolution of hydrophobic carbonized resin (binder) [366, 381–383]. Sparging the water bath with air, however, Burheim et al. [384] observed wettability alteration, which they related to the loss of PTFE. In order to accelerate the aforementioned aging effects, researchers also conducted leaching tests using sulfuric acid (H_2SO_4) to intensify the oxidative conditions. Once again, the studies showed hydrophobicity loss which was explained by the dissolution of carbonized resin [378, 382] or, when purged with air, loss of PTFE [385]. Considering the eventual aging impact on the MPL, researchers furthermore come to equivocal conclusions. Whereas some studies reported that the wettability alteration in the MPL was less than in the GDL [366, 384], others observed in addition to a decreasing surface hydrophobicity also morphological changes in the aged MPL, resulting in the formation of new or enlargement of preexisting larger openings (i.e., holes, fractures, cracks) [382, 383, 385]. Irrespective of the eventual degradation path, however, dissolution of the GDL/MPL resulted in performance losses due to mass transport limitations, which were primarily related to changes in the water management capabilities. In summary and according to Pan et al. [356], GDL and MPL aging inside an (automotive) PEM fuel cell may occur via a total of six different degradation mechanisms in dependence of the operating mode. In the course of operation, the diffusion layers may thus experience morphological changes by mechanical failure (GDL fiber breakage or MPL crack/fracture formation) or loss of support material and wettability alterations due to oxidation of the solid surfaces or loss of additive (PTFE). Impairing the gas transport properties and the water management, these aging effects will then lead to mass transport limitations and ultimately to performance losses.

Whereas the aforementioned degradation phenomena are in general expected to be present in long-term static [315, 386, 387] or dynamic [388] PEM fuel cell operation, occurrence of significant aging may require durability tests with thousands of operating hours. In addition, when cycling through different operating modes, a fuel cell will potentially undergo several degradation routes and the observed effects will be thus a

superposition of different aging phenomena. In order to investigate well-defined degradation scenarios in shorter periods of time, researchers have therefore developed accelerated stress tests (ASTs) speeding up the aging process under extreme operating conditions. Over the past decades, various *in situ* AST protocols have been designed to accelerate *operando* degradation by PEM fuel cell operation at elevated stress conditions. In these ASTs, distinct aging stressors are imposed, amongst others, by OCV holding [27–29], SU/SD cycling [30, 31], gas humidity cycling [389, 390], or dynamic load profiles (e.g., the New European Driving Cycle (NEDC) [391, 392]). While the well-defined operating conditions in these *in situ* stress tests enable to promote specific degradation mechanisms, the latter usually occurs in several cell components at a time (e.g., carbon corrosion in the CL, MPL and GDL). Consequently, observed aging effects may result from a superposition of simultaneous degradation processes in different cell components, thereby obviating a precise root cause analysis for performance decay upon aging.

In order to isolate the degradation phenomena of different other cell components, *ex situ* ASTs have been therefore excessively employed to exclusively accelerate aging of the GDL/MPL. Realizing similar but harsher conditions than in real FC operation, researchers have conducted, amongst others, immersion tests with oxidizing solutions (typically H_2O_2) [32–36] to study radical attack during idling, freeze-thaw cycling [37–40] to mimic mechanical stress in start-up/shutdown periods or leaching tests (typically DI water [366, 381–384] or H_2SO_4 [378, 382, 385]) to investigate material dissolution during ordinary operation. In contrast to *in situ* ASTs, these test protocols allow for a targeted degradation of single cell components in even shorter periods of time. Due to the accelerated aging under extreme test conditions, however, *ex situ* ASTs may on the other hand exhibit limited transferability to *operando* degradation during real fuel cell operation.

In front of the aforementioned limitations for experimental degradation studies, modelling and simulation of aging phenomena have in recent years increasingly attracted researchers' attention, as these virtual approaches allow time-efficient investigations under precisely-defined conditions. In the context of GDL/MPL degradation inside the PEMFC, in particular pore-scale methods have gained popularity, as they allow to investigate local aging effects on the multiphase transport at the pore-scale. PSMs have been therefore increasingly utilized to study potential impacts of GDL/MPL microstructure degradation on the PEMFC water management and thereby on the cell performance as well. In order to investigate the repercussions of GDL hydrophobicity loss on the water management, researchers have carried out several simulative studies on the liquid water transport in aged GDLs.

Assuming loss of hydrophobic additive as the main degradation mechanism, Seidenberger et al. [393] performed 3D Monte Carlo simulations on the liquid water transport through

stochastic GDL reconstructions with PTFE fiber surface coverages between 85 % and 55 %. A MPL was considered as well, thereby restricting the liquid water invasion sites into the GDL. In order to investigate the effect of varying amounts of a hydrophobic additive on the liquid water transport through the GDL, mixed wettability was accounted for by assigning different surface energies to the support (carbon fibers) and additive (PTFE), respectively. Reducing the additive content upon aging, the authors observed water cluster growth resulting in a nonlinear saturation increase owing to the decreasing hydrophobicity of the GDL surface. Along with proceeding GDL degradation, the simulations furthermore showed increasing merging of formerly disconnected water clusters until for a PTFE coverage of 55 % major portions of the GDL became hydrated. At this point, it is acknowledged that Seidenberger et al. assumed in their study even for the completely degraded GDL a still higher PTFE surface coverage than the default of $\chi = 50\,\%$ estimated in this work for the pristine GDL (see also Section 4.2.5). Whereas a higher fiber surface coverage cannot be (yet) ruled out *per se*, it may appear rather overestimated considering the often-reported observation of inhomogeneous additive deposition preferentially in vicinity of fiber intersections (Section 4.2.5) and towards the GDL surface (Section 4.2.4). Pauchet et al. [41] utilized a pore network model to investigate liquid water transport and effective gas diffusion in aged GDLs. Considering loss of PTFE as the primary degradation scenario, mixed wettability was accounted for by increasing the fraction of hydrophilic pores and throats in the pore network. When the hydrophilic fraction was below a percolation threshold, the PNM simulations showed similar liquid water invasion patterns with only slightly increasing breakthrough saturations. Above the percolation threshold, on the other hand, the breakthrough saturation was observed to increase suddenly and non-linearly, resulting in severe deterioration of the effective gas transport. By performance modeling, a link was eventually established between hydrophobicity loss upon GDL degradation and decay of cell performance. Bosomoiu et al. [350] studied the effect of hydrophobicity loss on the effective transport in partially wetted and aged GDLs. Employing a pore morphology model (see also Section 3.1), liquid water intrusion was simulated for the microstructure of a SGL 34BC as reconstructed from µCT imaging data. Since carbon fibers and PTFE were not differentiated, mixed wettability was not considered and loss of hydrophobicity was therefore modeled as an increase of a uniform solid surface contact angle. For proceeding stages of aging (i.e., decreasing hydrophobicity), the simulations then predicted increasing accumulation of liquid water in the GDL. This increasing flooding tendency furthermore resulted in a considerable aggravation of the effective gas transport, as indicated by a decreasing diffusivity and permeability inside the partially saturated GDL. In a rather general study, Yu et al. [321] investigated the impact of varying PTFE loadings and distributions on the GDL liquid water transport. Using a 3D Lattice Boltzmann

model, liquid water invasion was simulated for stochastic reconstructions of a Toray TGP090 with variable PTFE surface coverages. The authors reported that higher additive loads can shorten breakthrough time and increase the number of breakthrough locations. Furthermore, a more hydrophobic GDL inlet region (adjacent to the CL) was found to be beneficial for fuel cell operation by sustaining more empty pores for the gas transport. Wang et al. [43] used a 2D pseudopotential multiphase LB model to study liquid water transport in fresh and aged carbon fiber-type GDLs. The latter were reconstructed with a stochastic algorithm and employing PTFE contents of 5 wt%, 10 wt% and 15 wt%. For the reconstruction of aged GDLs, loss of carbon by corrosion and PTFE detachment were assumed as the main degradation mechanisms. Based on the simulation results, the authors concluded that GDL aging diminishes the water removal capability, as indicated by increasing breakthrough times and saturations. Furthermore, this degradation effect was found to be more pronounced by PTFE detachment than by carbon loss, owing to the hydrophobic nature of the additive. In order to counteract the increasing flooding tendency upon aging, higher PTFE loadings were suggested as they raise the capillary pressure and an additive content of 10 wt% was found to yield the highest effective porosity.

In addition to PSM studies on varying GDL structural properties, researchers have in recent years also increasingly investigated the effect of a MPL on the liquid water transport. Whereas not necessarily explicitly considering degradation phenomena, most of these works nonetheless focused on MPL defects (e.g., cracks or fractures) and their impact on the liquid water invasion into the GDL. Wu et al. [394] employed a pore net work model to investigate the effect of a MPL crack on the liquid water invasion into the GDL. Permitting liquid water transport exclusively through the crack, presence of the MPL was observed to significantly decrease the saturation at the MPL/GDL interface. At liquid water breakthrough, the GDL saturation depended furthermore on the crack location (under channel or land). Cetinbas et al. [395] developed a dynamic pore-scale model to investigate the liquid water flow through GDL and MPL microstructure reconstructions from micro and nano tomographic data. Comparing the liquid water transport in a SGL24BA and a SGL25BC, the simulations showed that a crack-free MPL significantly reduced the GDL breakthrough saturation due to the high capillary pressures inside the MPL nanopores. Whereas a high capillary transport resistance may cause anode back-diffusion during cell operation, the authors found that a cracked MPL was more beneficial for water management as the cracks provided preferential liquid water removal paths. Similar observations were made by Hou et al. [396], who utilized a 3D pseudopotential LB model to study liquid water transport in a stochastically reconstructed GDL and MPL. Whereas a single GDL showed typical flooding behavior, presence of a crack-free MPL required very high capillary pressures for breakthrough, which could potentially cause CL

flooding during cell operation. On the other hand, a MPL with randomly distributed cracks as preferential liquid water pathways was again found to offer superior water management. As MPL crack appearance might be difficult to control in reality, the authors furthermore suggested an alternative concept of a laser-perforated GDL/MPL, which showed an even further optimized water management. The effect of ordered microstructures on the liquid water transport characteristics was also investigated by Niblett et al. [42]. Employing a 3D VoF model, two-phase flow was simulated for stochastic reconstructions of ordered and disordered GDLs embedded between a MPL and the gas channel. Whereas a crack-free MPL strongly restricted liquid water entry sites to the GDL, MPL defects (i.e., cracks) were again found to provide preferential water pathways. However, introduction of MPL apertures also lead to lateral redistribution of liquid water in the disordered GDL. The authors therefore concluded that an optimal water management can be achieved with a cracked MPL and an anisotropically ordered GDL favoring liquid water transport in the through-plane direction. In a later study, Niblett et al. [397] examined the impact of MPL aging on the liquid water distribution in a microstructure reconstruction from µCT images of a Toray TGP-H 060. Assuming crack dilation as main mechanism of MPL degradation (based on an *in situ* carbon corrosion AST in [398]), the VoF simulations showed increasing in-plane connectivity of liquid water clusters at breakthrough. While these observations indicated increasing flooding upon proceeding MPL aging, the authors furthermore pointed out the importance to reduce the in-plane distribution of liquid water in order to enhance the effective gas transport to the CL.

In the subsequent sections of this chapter, liquid water transport is investigated for a carbon felt GDL at varying stages of aging and under conditions similar to fuel cell operation. At first, the microstructure reconstruction of the PTFE-impregnated Freudenberg H14 from Chapter 4 is therefore virtually compressed to account for a typical clamping pressure of fuel cell stack assembly. A single slice of a microporous layer is furthermore reconstructed by segmentation of representative MPL macropores from µCT images for a PTFE-impregnated and MPL-coated Freudenberg H14. In order to mimic *operando* conditions during fuel cell operation, a computational domain is then generated by assembling the GDL and MPL microstructures between a liquid and gas phase buffer region corresponding to the adjacent cathode catalyst layer and the gas channel, respectively. Subsequently, GDL microstructure reconstructions are virtually aged assuming loss of hydrophobic PTFE as the primary degradation path. According to Pan et al. [356], this scenario potentially occurs due to radical attacks while idling, freeze-thaw cycles due to SU/SD periods or material dissolution during normal cell operation. At this point, however, it is noted that an in-depth investigation of aging mechanisms is beyond the scope of this study as it focuses on the impact of degradation on the water management and effective gas transport

during cell operation. In addition to the GDL, degradation of the MPL is considered in this work as well. Whereas several works found that MPL aging could lead to fracture formation or crack propagation (e.g., due to carbon corrosion [369], compression [79], erosion [78, 378] or material dissolution [382, 383, 385]), Freudenberg MPLs are reported to be rather crack-free but partly macroporous [68]. Therefore, degradation of the MPL is in this work assumed to result in an increasing macroporosity. Hence, MPL macropores are reconstructed for proceeding stages of aging and adjusting the macroporosity accordingly. Combining different stages of artificially aged GDL and MPL reconstructions, liquid water intrusion is then simulated using the 3D Color-Gradient Lattice Boltzmann model introduced in Chapter 3. Once the liquid phase has reached the gas channel, the liquid water invasion patterns are characterized for their breakthrough characteristics to analyze the impact of degradation on the liquid water transport. In order to characterize the impact of liquid water accumulation on the effective mass transport, gas transport through the partially wetted and aged GDLs is furthermore simulated to determine effective gas diffusivities and permeabilities. Eventually, empirical relations are derived for the liquid water saturation and the effective gas transport properties in dependence of the stage of GDL/MPL degradation. At last, the major outcomes of this chapter have been published in a second scientific article in Sarkezi-Selsky et al.[399].

5.2 Geometry generation for *operando* GDLs

5.2.1 Compression of GDL reconstructions

Starting point for the modeling of structural GDL degradation is the microstructure reconstruction of the impregnated fiber substrate (Figure 4.12) with a PTFE surface coverage of $\chi = 50\,\%$ used as default in the previous chapter. Contrary to the model validation against an experimental *ex situ* reference ($p_c - S$ test bench), however, this chapter intents to mimic *in situ* conditions during PEM fuel cell operation. Therefore, the model for the semipermeable membranes is abandoned for the subsequent simulative studies. Instead, the GDL microstructures are considered to be in the compressed state, since fuel cells are commonly operated under a certain assembly/clamping pressure to prevent leakage and establish good electrical contact [400, 401]. Taking this *in situ* condition into account, the reconstruction workflow from Section 4.2 could be in principle repeated for µCT images of GDL samples under compression. However, while technically feasible, installation of a compression unit to the µCT scanning device introduces an extra component for X-ray interference and thereby an additional source for noise in the recorded images. In this work, a different route is therefore taken by compressing the

yet reconstructed GDL microstructures artificially. This virtual operation is carried out with the GeoDict tool 'Compress', which compacts a structure geometrically along its through-plane direction up to a predefined compression ratio (CR)

$$\mathrm{CR} = 1 - \frac{d_{\mathrm{compr}}}{d_0} \tag{5.1}$$

of reduced d_{compr} to initial thickness d_0. At this point, it is noted that while GDL compression is known to be different under the channel and rib/land regions of the bipolar plates [372, 402], distinction of multiple compression scenarios is beyond the scope of this work. For the subsequent studies of this chapter the GDL is therefore at this point assumed to be homogeneously compressed. While manufacturer specification sheets provide compressibility data for the plain H14 [403] and related impregnated and MPL-coated variants (prefix H14C) [404] up to 1 MPa, information is in general missing for higher compression pressures. Therefore, a compression ratio is derived based on comparison of Freudenberg-internal compression curves for an untreated and an impregnated and MPL-coated H14, assuming a common clamping pressure of 2 MPa [64, 401, 405]. With CR $\approx$ 0.22, this estimate resides in the typical range of 20 to 25 % GDL compression [406]. According to equation (5.1) and based on a nominal thickness of $d_0 = 150\,\mu\mathrm{m}$ (156 voxel) for the uncompressed GDL, the reduced thickness of the compressed H14 is then obtained as $d_{\mathrm{compr}} = 117\,\mu\mathrm{m}$ (122 voxel). With the aforementioned compression ratio, the default microstructure reconstruction of the impregnated fiber substrate is then eventually compacted virtually with the GeoDict routine 'Compress', as illustrated in Figure 5.1. In the context of the subsequent degradation studies, the compressed microstructure reconstruction from Figure 5.1b will be referred to as the 'pristine' GDL.

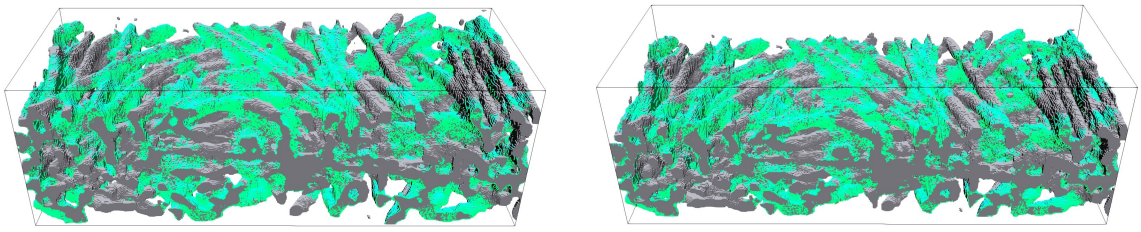

(a) Uncompressed. (b) Compressed.

Figure 5.1: Virtual compaction of (a) the default impregnated H14 fiber substrate reconstruction with the GeoDict tool 'Compress' yields the (b) compressed GDL microstructure with approximately 22 % thickness reduction. In the subsequent degradation studies, the latter is referred to as the 'pristine' GDL.

As apparent from Figure 5.2, GDL compression has repercussions on both the pore morphology and wettability. With the compaction of the pore space, the local porosity is

observed to decrease all along the GDL thickness (Figure 5.2a), resulting in a decrease of the void volume fraction from 73.22 to 65.8 %. Furthermore, the PTFE surface coverage is found to be reduced from 50 to 47 % upon compression. This observation can be related to the circumstance that while the fiber surface area decreases all throughout the GDL, such compaction effect is more pronounced in the highly porous GDL surface regions where the additive is predominantly deposited. Apart the aforementioned changes and despite being jolted, however, the through-plane profiles of both ϵ^{local} and χ^{local} remain similar after compression. This may be related to the moderate compression ratio of approximately 22 % and the modeling approach of linear geometric compaction. At this point, it is noted that whereas a physics-based modeling of compression effects may provide a more accurate approach, complex structural mechanics simulations are beyond the scope of the underlying work. Furthermore, this is also not strictly necessary, as for lower compression rates sample compaction is reported to be primarily embodied in a reduction of the pore volume [407].

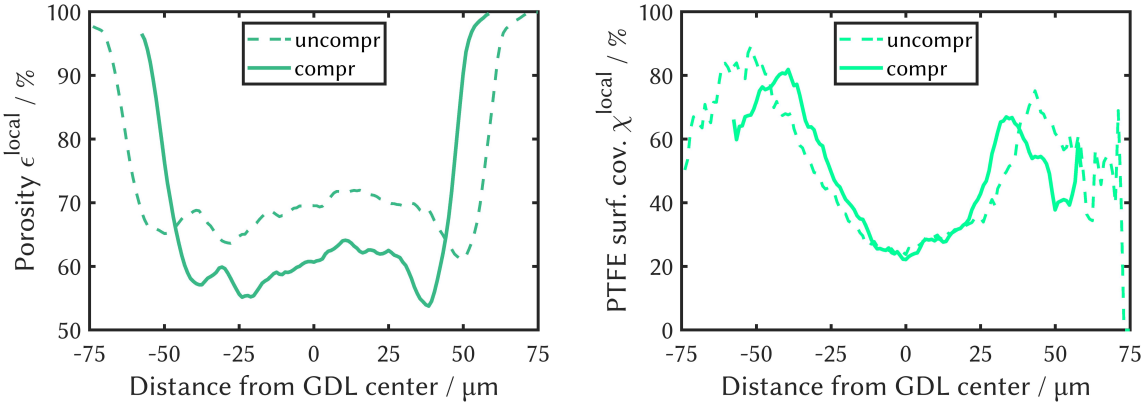

(a) Porosity. (b) PTFE surface coverage.

Figure 5.2: Virtual compaction of the impregnated H14 fiber substrate reconstruction with the GeoDict tool 'Compress'. A compression ratio of approximately 22 % leads to an alteration of the pore space, as indicated by the changes in the through-plane profiles of (a) porosity and (b) PTFE surface coverage.

5.2.2 Reconstruction of a microporous layer

Owing to their hydrophobicity and small pore sizes, MPLs introduce additional capillary barriers to the MEA, which (on the cathode side) strongly restricts the liquid water invasion paths into the GDL and thereby also helps to retain water near the PEM. Given these aforementioned characteristics, microporous layers have been reported to promote PEMFC water management by preventing both GDL flooding [77, 408, 409] and membrane dehydration [73, 74] (see also Section 2.2.2). As MPLs can have a decisive impact on the

capillary transport in GDLs, a microporous layer is therefore considered as well in the subsequent degradation studies of this chapter.

In the most straightforward approach, a MPL could be accounted for by direct reconstruction from µCT images for an impregnated and MPL-coated Freudenberg H14 GDL. However, joint reconstruction of the GDL carbon fibers and the carbonaceous MPL powder would require segmentation into three phases (i.e., void, fibers, powder), as their different chemical composition would lead to unequal grayscale values in µCT images. In addition, the MPL is known to penetrate the highly porous GDL surface region to variable depths depending on the coating procedure [67–72]. As a result, there is usually no sharp interface but rather a smooth transition between GDL and MPL, which aggravates clear distinction of the two porous media. These circumstances render segmentation by trinarization a disparately more difficult task as compared to binarization (void, solid) of the plain and impregnated fiber substrate. In the frame of this work, such a multiple thresholding approach is additionally aggravated by a lack of manufacturer specifications on, e.g., MPL thickness or porosity. Consequently, a thresholding routine would be required, whose performance depends in general on the quality of the input images and which would have to be validated first [285]. Therefore, an alternative approach is pursued in this work, in which GDL and MPL are first reconstructed separately from µCT images of different samples and then combined after binarization.

In this work, complete reconstruction of the MPL is obstructed by the µCT resolution limitations, as nanostructural details cannot be resolved. While nanoCT or SEM offer the technical capabilities for sufficiently high sample resolution, simulation of liquid water transport through both GDL and MPL would require a multiscale modeling approach, for which computation times would exceed the practical limit. On the other hand, this is also not strictly necessary, as liquid water is reported to be primarily transported through the largest MPL openings with least capillary resistance [80–82]. Depending on the MPL manufacturer, these hollows are generally represented by either cracks or macropores [68, 80, 410, 411], of which the latter are visualized by SEM images of an impregnated and MPL-coated H14 in Figure 5.3. Presuming that these macrostructures are decisive for the effective liquid water transport through the GDL, a reconstruction of the MPL restricted to its macropores should therefore suffice for the subsequent degradation investigations of this work.

While the nanostructural details of the MPL are beyond the resolution limit of the given µCT device, larger pores are still visible, as illustrated for an impregnated and MPL-coated H14 in Figure 5.4a. Following the same procedure as for GDL reconstruction (Section 4.2.1 and Section 4.2.2), MPL macropores are then reconstructed from µCT images of an impregnated and MPL-coated H14 by Freudenberg with 0.96 µm per pixel. However,

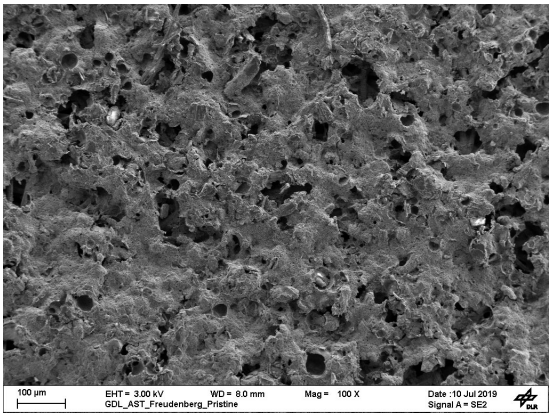

(a) 100x magnification.

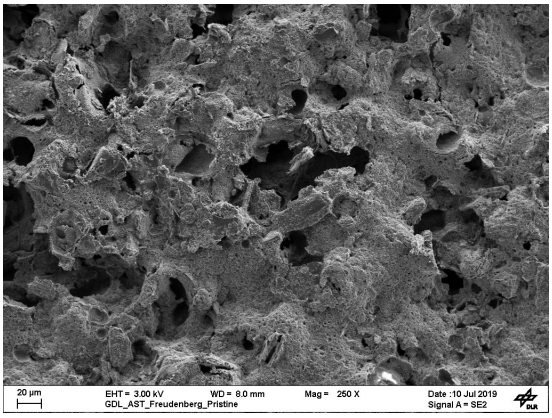

(b) 250x magnification.

Figure 5.3: SEM images of the microporous layer surface of an impregnated and MPL-coated H14 GDL by Freudenberg. Image recorded by Pia Aßmann (Department for Electrochemical Energy Technology, Institute of Engineering Thermodynamics, DLR Stuttgart) in the frame of the EU project ID-FAST.

since the subsequent degradation studies focus on transport phenomena in the GDL and not in the MPL, and due to the unknown depth of MPL penetration into the GDL, the MPL reconstruction is furthermore intentionally limited to a single layer from the MPL bulk. After filtering, a single slice is then selected from the center of the µCT image stack and binarized via manual thresholding, assuming a porosity of 20 % [412]. The resulting microstructure reconstruction for the MPL macropores is illustrated in Figure 5.4b. In the context of the subsequent degradation studies, the latter will be referred to as the 'pristine' MPL. Whereas the microporous layer is commonly a compound material with varying composition of a carbonaceous powder and a hydrophobic additive [413], this aspect is not considered in this work. Instead, the MPL is assumed to be composed of a single solid component. Furthermore, sample compression is assumed to be negligible, as the MPL in general exhibits a lower thickness and higher stiffness than the GDL [62, 75, 76].

At this point, it is noted that the given MPL porosity of 20 % is lower than commonly reported literature values [68, 414, 415]. Whereas these works typically refer to the overall porosity including the nanostructural properties, the MPL porosity has to be interpreted in this work as a macroporosity ($\epsilon_{\mathrm{MPL}}^{\mathrm{macro}} = 19.97\,\%$), since the microporosity on the nanoscale cannot be resolved by the µCT imaging device. For this means of structural characterization, Fishman and Bazylak reported macroporosities as low as 14 % for MPL-coated SGL GDLs [416]. Notwithstanding the aforementioned reference, however, the MPL macroporosity remains an estimate within this work, whose parametric uncertainty is acknowledged. As will be shown in Section 5.7.4, however, the liquid water transport characteristics appear to be insensitive to $\epsilon_{\mathrm{MPL}}^{\mathrm{macro}}$ beyond a certain threshold.

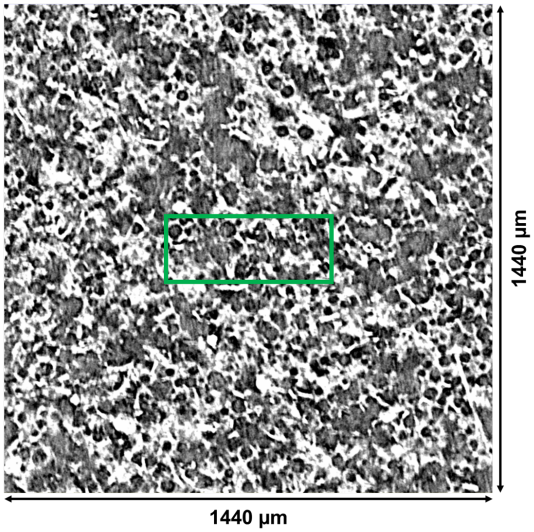

(a) Grayscale µCT image.

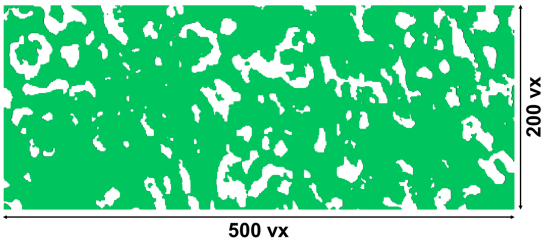

(b) Binarized MPL macropores.

Figure 5.4: MPL macropore reconstruction from a µCT image with a resolution of $\Delta x^{\mathrm{phys}} = 0.96\,\mu\mathrm{m}$ per pixel. The (a) grayscale data is binarized by manual thresholding and assuming a macroporosity of $\epsilon_{\mathrm{MPL}}^{\mathrm{macro}} = 19.97\,\%$ (b). In the subsequent degradation studies, the latter is referred to as the 'pristine' MPL.

5.3 Computational setup

5.3.1 Modeling of the transition zone between GDL and MPL

Whereas Section 4.3 aimed at realizing the *ex situ* boundary conditions of the $p_c - S$ test bench, this paragraph intends to generate a computational setup, which mimics the *in situ* GDL liquid water transport during PEM fuel cell operation. Therefore, the GDL microstructure is considered to be in the compressed state and sandwiched between the catalyst layer (CL) and the bipolar plate (BPP). Between the CL and the GDL, a MPL is furthermore included, albeit in a simplified manner. As already mentioned in the previous section, coated GDLs commonly exhibit a MPL-sided surface region with a smooth transition from micro- to macroporous layers. Consequently, definition of a distinct interface separating the two diffusion media is in general not possible. Furthermore, as the underlying thesis focuses on the capillary transport in the GDL, full account of the MPL is beyond the scope of this work. Therefore, the transition zone between GDL and MPL is not considered in detail but simplified to a single representative interface layer instead. At first, the MPL penetration depth and thus the width of the transition zone is estimated based on the through-plane porosity profiles for the binarized uncompressed microstructures of the impregnated fiber substrate of the H14 GDL with and without MPL. For this comparison, the impregnated and MPL-coated fiber substrate is once more (firstly

in Section 5.2.2) reconstructed via binarization from µCT images. Since both samples contain the same impregnated carbon fibers, the manual thresholding is furthermore conducted in the same way as for the reconstruction of the impregnated fiber substrate without MPL (Section 4.2.2). At this point, it is acknowledged that binarization only allows for a qualitative analysis of the impregnated and MPL-coated H14 fiber substrate, as full reconstruction by segmentation into pore space, GDL fibers and MPL would require trinarization. For identification of the transition zone, however, a qualitative porosity analysis based on binarized microstructures is at this point expected to be sufficient.

Figure 5.5a shows the through-plane porosity profiles for the uncompressed microstructure reconstructions of the impregnated H14 with and without MPL. As expected, the porosity of both samples is qualitatively for the most part very similar. While slight deviations are visible in the GDL core region, these may be related to batch variations within the production tolerances of GDL manufacturers [293]. From the GDL core towards the surface region on the MPL side, however, the porosity of the MPL-coated impregnated H14 exhibits an intermediate change in curvature which is not present for the sample without MPL. More precisely, the porosity increase towards the GDL surface is dampened, suggesting appearance of a denser material. This conjecture is confirmed by visual inspection of the raw µCT images, which furthermore reveals presence of the MPL throughout the whole GDL surface region. As a result of this analysis, the complete GDL surface region is thus identified as the transition zone between GDL and MPL, as indicated in Figure 5.5b. This definition of the transition zone is therefore similar to Chevalier et al. [69] and Lee et al. [67].

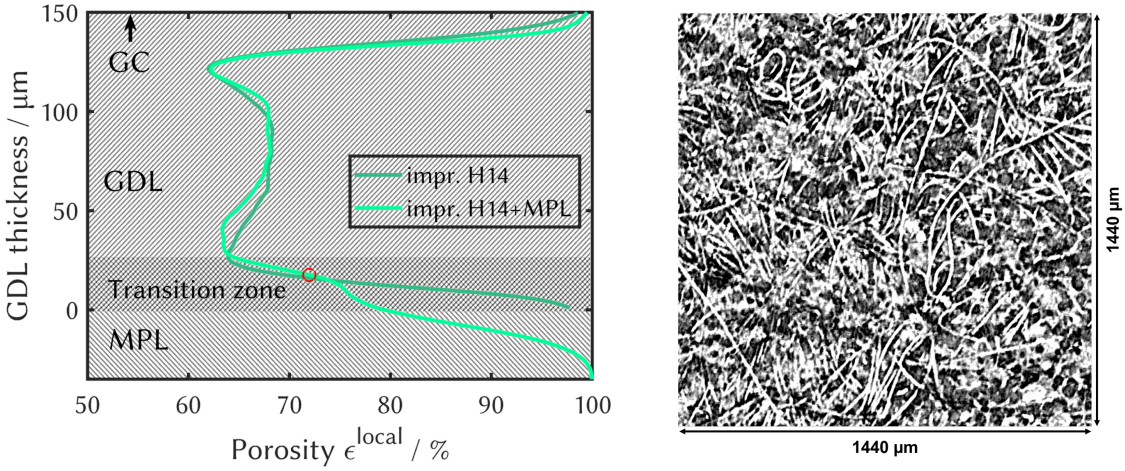

(a) Porosity profiles.

(b) GDL/MPL transition zone.

Figure 5.5: (a) Due to the coating procedure, the MPL penetrates the highly porous GDL surface with variable depth, resulting in a transition zone in between both porous domains. (b) µCT image of a GDL surface region (red circle in (a)) with the MPL inside large pores.

Since above porosity analysis is conducted for the uncompressed GDL microstructure but the subsequent simulative studies consider *in situ* conditions, above definition for the transition zone GDL/MPL is transferred to the compressed microstructure reconstruction of the impregnated H14 fibers, as shown in Figure 5.1b. Identifying one GDL surface region as transition zone, this portion with a thickness of $d_{\text{trans}} = 21$ voxels is then cut off the binarized microstructure, reducing the overall domain size to $500 \times 200 \times 101$ voxels. With an overall thickness $d_{\text{compr}} = 122$ voxels for the compressed GDL microstructure (see Section 5.2.1), the ratio $d_{\text{trans}}/d_{\text{compr}} \approx 0.17$ is then in good agreement with MPL penetration depth ratios between 15 to 25 % reported in literature [71, 256, 417]

In order to represent the restraining effect on the liquid water transport, the reconstructed MPL monolayer from Section 5.2.2 is then appended to the cut open side of the GDL, as shown in Figure 5.6. At this point, it is noted that the MPL monolayer is effectively no real 3D porous domain, as it exhibits a thickness of only one voxel. Instead it has to be rather interpreted as a GDL/MPL interface serving as an additional liquid water inlet condition to the GDL. In this regard, the computational setup is therefore comparable to the studies of Niblett et al. [42] and Zhou et al. [418].

5.3.2 Boundary conditions

Corresponding to the cell setup in PEMFC operation, the unified porous GDL/MPL domain is then considered to be sandwiched between the catalyst layer and the gas channel. Buffer zones with thicknesses of 10 and 30 voxels are therefore defined at the CL and GC side, respectively. In summary, the computational domain then comprises a total of $500 \times 200 \times 142$ voxels. Furthermore, both the porous media and the GC buffer zone are considered to be initially dry, i.e., completely occupied with the gas phase. On the other side, the buffer zone at the CL is set to be initially filled with liquid water.

Assuming stationary cell operation and mimicking a constant water production rate by the ORR in the cathode catalyst, liquid water invasion into the computational domain is then enforced by a inlet velocity boundary condition at the lowermost layer of the CL buffer zone. At the opposite domain end, a pressure boundary condition is utilized to the topmost layer of the GC buffer zone in order to maintain a gas pressure of $p_g = 1\,\text{bar}$. Both aforementioned external boundary conditions are again employed based on the original formulation of Zou and He [203, 204], the remaining in-plane domain ends are governed by periodic boundary conditions. The final computational domain for the combined GDL/MPL microstructure reconstruction sandwiched in between the CL and GC buffer zones is sketched in Figure 5.6.

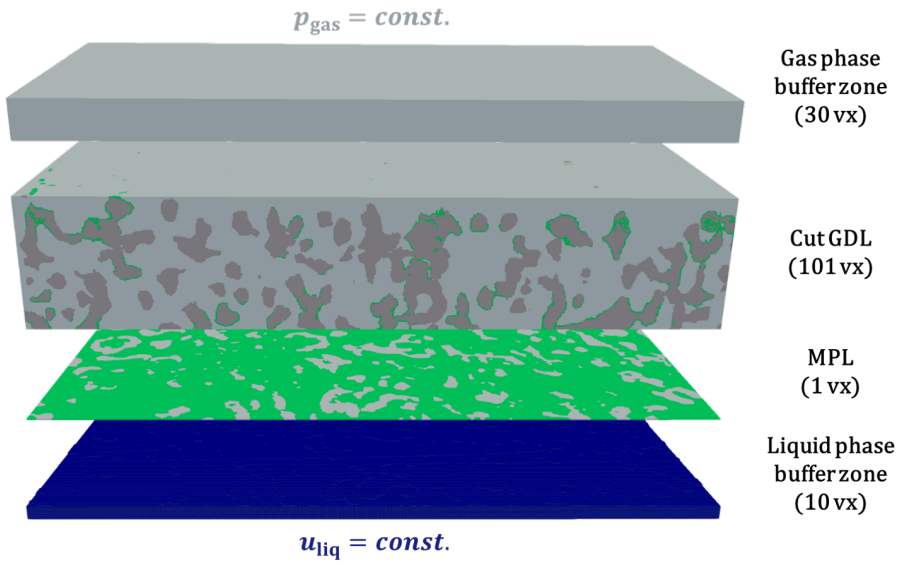

Figure 5.6: Computational domain for the simulative studies on liquid water transport in combined GDL/MPL microstructure reconstructions with *in situ* boundary conditions of PEM fuel cell operation. The GDL surface region towards the MPL side is cut off the porous domain and replaced by a monolayer representing the MPL macropores.

Analogous to the computational setup in Section 4.3.3, fluid properties are initialized with $\rho_l^0 = \rho_g^0 = 1$ and $\nu_l = 1/6$ and $\nu_g = 1/12$ in order to set the density and dynamic viscosity ratio to $\gamma = 1$ and $M = 2$, respectively. While for a typical PEMFC operation temperature of 80 °C the real ratios would reside around $\gamma^{\text{phys}} \sim 970$ [326, 327] and $M^{\text{phys}} \sim 17$ [328, 329], they are again neglected under assumption of a capillary-dominated flow. Mixed wettability is once more modeled with liquid water contact angles of $\theta_{\text{CF}} = 65°$ and $\theta_{\text{PTFE}} = 115°$ for the carbon fibers and PTFE, respectively. In addition, the MPL is assumed to exhibit a wetting behavior similar to the hydrophobic additive, i.e., $\theta_{\text{MPL}} = \theta_{\text{PTFE}} = 115°$. The surface tension is again set to $\sigma = 0.125$. In order to warrant dominance of capillary forces, however, the capillary number $\text{Ca} = u_l \rho_l^0 \nu_l / \sigma$ (see also eq. (2.8)) has to be sufficiently low as well. With the proportionality $\text{Ca} \propto u_l$, this will be ensured by determination of an adequately small liquid inlet velocity u_l in a sensitivity study in Section 5.7.2.

With the aforementioned computational setup, liquid water invasion into the initially dry GDL is then simulated until it reaches the upper end of the porous domain on the GC side and breaks through to the gas channel buffer zone, i.e., at 'breakthrough'. With above computational setup and assuming a typical PEMFC operation temperature of 80 °C, the relevant conversion factors (see also Section 3.2.4) for the subsequent simulations in this chapter are furthermore given as listed in Table 5.1.

Table 5.1: Conversion factors (*cf.* Section 3.2.4) for the LB simulation of *operando* GDL liquid water transport at a typical PEMFC operation temperature of 80 °C.

Quantity	**Value**		**Conversion factor**
X	phys	LBM	$C_X = {}^{X^{\text{phys}}}/_{X^{\text{LBM}}}$
Length l	0.96 µm	1	$C_l = 0.96\,\mu\text{m}$
Viscosity ν_l	$3.64\text{e}^{-7}\,\text{m}^2/\text{s}$ [326]	1/6	$C_\nu = 2.18\text{e}^{-6}\,\text{m}^2/\text{s}$
Time t	$4.22\text{e}^{-7}\,\text{s}$	1	$C_t = {}^{C_l^2}/_{C_\nu} = 4.22\text{e}^{-7}\,\text{s}$
Velocity u_l			$C_u = C_l/C_t = 2.27\,\text{m/s}$

5.4 Characterization of liquid water distributions at breakthrough

In the capillary-dominated regime, the liquid water invasion patterns into the GDL are in general a result of the pore morphology and wettability (see also $p_c = f(R_i, \theta)$ as given by the Young-Laplace equation (2.19)). Depending on the spatial variation of the structural properties, the resulting saturation profiles in the GDL can be rather uniform or non-uniform. García-Salaberri et al. [419] have furthermore shown that the spatial distribution of liquid water can lead to vastly different effective gas transport properties in partially saturated GDLs. Consequently, the characterization of liquid water distributions at different stages of GDL/MPL aging is of high relevance for the assessment of degradation effects on the water management capabilities and the repercussions on the effective gas transport. Furthermore, as the liquid water invasion paths are reported to be quasi-stationary after breakthrough occurrence [42, 86, 93, 346, 420], these characteristics can be considered as representative for stationary fuel cell operating conditions. In the subsequent degradation studies, partially saturated GDL microstructures at varying stages of aging are characterized for their liquid water distributions at breakthrough. After simulating liquid water invasion up to breakthrough, simulation snapshots of the partially saturated GDL microstructures are therefore extracted and further postprocessed. With the local voxel-wise saturation S^{vx} according to equation (4.11), saturation profiles are then derived by averaging along the 'in-plane X'

$$S_x^{\text{BT}}(x) = \frac{1}{n_y^p n_z^p} \sum_{iy} \sum_{iz} S^{\text{vx}}(x, iy, iz)\,, \tag{5.2}$$

'in-plane Y'

$$S_y^{\text{BT}}(y) = \frac{1}{n_x^p n_z^p} \sum_{ix} \sum_{iz} S^{\text{vx}}(ix, y, iz) \tag{5.3}$$

and 'through-plane Z' direction

$$S_z^{\mathrm{BT}}(z) = \frac{1}{n_x^p n_y^p} \sum_{ix} \sum_{iy} S^{\mathrm{vx}}(ix, iy, z) \tag{5.4}$$

of the GDL. Similar to equation (4.12), the overall saturation at breakthrough is eventually determined as the global average over all three spatial dimensions:

$$S^{\mathrm{BT}} = \frac{1}{n_x^p n_y^p n_z^p} \sum_{ix} \sum_{iy} \sum_{iz} S^{\mathrm{vx}}(ix, iy, iz) \tag{5.5}$$

5.5 Determination of effective gas transport properties

One of the principal tasks of GDLs during cell operation is an efficient and homogeneous gas distribution to the catalyst layers. However, as liquid product water is formed in the CCL pores and discharged through the MPL and GDL, it blocks available paths for the gas transport to the catalyst. In order to investigate, how the liquid water distributions at breakthrough affect the gas transport in the GDL, effective gas transport properties are therefore determined for the partially saturated GDLs in the subsequent simulative studies of this chapter. With the small gas velocities present in PEM fuel cell operation, the convective gas transport through the GDL is typically described using Darcy's law [421, 422] with

$$\mathbf{u}_g = -\frac{\kappa_g}{\mu_g} \nabla p_g \tag{5.6}$$

and the dynamic viscosity μ_g and permeability κ_g of the fluid. In a single-phase system (i.e., only gas), the latter is equal to the absolute permeability κ as a fluid-independent material property for porous media. As of such, the permeability is typically described in a constitutive relation

$$\kappa_g = f(\epsilon) \tag{5.7}$$

as a function of the material's porosity. One of the most widely used relations for the porosity-dependence of a material's permeability was proposed by Kozeny [423] and Carman [424] with

$$\kappa^{\mathrm{Kozeny-Carman}} = \frac{\Phi_s^2 d_p^2}{180} \frac{\epsilon^3}{(1-\epsilon)^2} \tag{5.8}$$

and the average diameter d_p and sphericity Φ_s of particles in a packed bed. However, whereas the GDL generally consists of fibers and not particles, the aforementioned two geometric properties are in this case not well-defined. According to Nam and Kaviany

[425], however, above equation can be adopted to fibrous porous media such as GDLs with

$$\kappa^{\text{Kozeny-Carman}} = \frac{d_f^2}{16 k_\text{K}} \frac{\epsilon^3}{(1-\epsilon)^2}, \tag{5.9}$$

the fiber diameter d_f and the Kozeny constant k_K. While the authors furthermore suggest $k_\text{K} = 6$ for porosities around $50\,\% < \epsilon < 70\,\%$, this parameter will be used as a fitting parameter for nonlinear regression of permeabilities for the dry GDL in the degradation studies in Section 5.7. Due to consumption (H_2, O_2) and production (H_2O) by the reactions in the catalyst layers, local concentrations of gaseous species in general vary throughout the porous diffusion layers of the cell. As a result, the gas transport through the GDL is also driven by concentration gradients. According to Fick's law, the diffusive flux of a species j occurs with

$$\boldsymbol{J}_j = -D \nabla c_j \tag{5.10}$$

due to a concentration gradient ∇c_j and proportional to a diffusion coefficient D. For the bulk of a gas, the latter equals the self-diffusion coefficient D_0 as a fluid property. In a porous medium, however, this intrinsic diffusivity is constricted to an effective diffusion coefficient

$$D^\text{eff} = D_0 \frac{\epsilon}{\tau} \tag{5.11}$$

due to the pore morphology, which is commonly assumed to be characterized by the porosity ϵ and tortuosity factor τ. Whereas D_0 is a fluid-dependent quantity, it is practical to define with

$$D^* = \frac{D^\text{eff}}{D_0} = \frac{\epsilon}{\tau} \tag{5.12}$$

a dimensionless effective diffusivity as a material-specific property. As a measure for the diffusion resistance due to the curvature of the pore walls, the tortuosity factor is then given with

$$\tau = \frac{\epsilon}{D^*} = f(\epsilon) \tag{5.13}$$

and is commonly assumed to be only dependent on the porosity of a porous medium. In 1935, Bruggeman [426] derived with

$$\tau = \frac{1}{\sqrt{\epsilon}} \tag{5.14}$$

a relation between the tortuosity factor and porosity of a porous medium, which is presumably to this day the most-utilized in the modeling of porous media diffusive transport. Despite its simplicity, however, Bruggeman's relation has been widely reported (and as will be shown in Section 5.7) to overestimate the effective diffusivity or equivalently underestimate the effective tortuosity in different porous media [69, 316, 427, 428]. In the

past, various research works have been therefore dedicated to find alternative and improved expressions for the porosity-dependence of the tortuosity in porous media. However, as this work focuses on the repercussions of liquid water accumulation on the effective gas transport in partially aged GDLs, a review of these alternative formulations is omitted here. Therefore, the interested reader is at this point referred to the recent summary by Bao et al. [76]. Whereas Fick's law (eq. (5.10)) describes the bulk diffusion of gaseous species due to interparticle collisions, diffusive gas transport can also occur due to collision of the gas molecules with the pore walls. However, this Knudsen diffusion becomes only relevant for large Knudsen numbers

$$\mathrm{Kn} := \frac{\text{mean interparticle distance}}{\text{mean particle} - \text{wall distance}} = \frac{\lambda}{L_{\mathrm{char}}}, \tag{5.15}$$

i.e., when the mean free path λ is much larger than the characteristic length L_{char} of the porous medium. For macroporous media such as the GDL with a median pore diameter of around $d_{p(50)}^{\mathrm{phys}} \approx 21\,\mu\mathrm{m}$ (see also Section 4.2.2) as the characteristic length, this is not the case as for a molecular free path of $\lambda_{\mathrm{air}} = 68\,\mathrm{nm}$ [429] the Knudsen number is with $\mathrm{Kn} << 1$ very low. Therefore, Knudsen diffusion is not considered in the subsequent simulative studies of this work. At this point, however, it is noted that for studies of gas transport phenomena in the nanoporous MPL, Knudsen diffusion in general cannot be neglected anymore due to the much smaller characteristic length.

In the previous paragraphs, the gas transport was described under the assumption of a dry GDL microstructure. In the presence of liquid product water, however, the pore volume of the partially saturated GDL is reduced, which evidently affects its gas transport properties. In terms of volume-averaged quantities, the liquid saturation S in the GDL causes a reduction of the pore space fraction ϵ

$$\epsilon_{\mathrm{eff}} = \epsilon\,(1 - S) \tag{5.16}$$

to an effective porosity ϵ_{eff} available for the gas transport. According to equation (5.7), the effective gas permeability in a partially saturated medium can be then formulated with

$$\kappa_g^{\mathrm{wet}} = f\,(\epsilon_{\mathrm{eff}})\,. \tag{5.17}$$

Presuming that the effects of the unsaturated porosity ϵ and the liquid water saturation S on the gas transport can be separated, above relation can be decomposed into

$$\kappa_g^{\mathrm{wet}} = f\,(\epsilon)\,g\,(S)\,. \tag{5.18}$$

Furthermore, a relative permeability can be then defined with

$$\kappa_g^{\mathrm{rel}} = \frac{\kappa_g^{\mathrm{wet}}}{\kappa_g^{\mathrm{dry}}} = \frac{f(\epsilon)\, g(S)}{f(\epsilon)} = g(S), \tag{5.19}$$

which describes the gas permeability as a sole function of the liquid saturation S. Above definition presents a widely taken approach for the characterization of effective gas permeabilities in partially saturated porous media such as GDLs. While the expression $g(S)$ is commonly assumed to follow a power law relation with

$$g_\kappa(S) = (1-S)^{n_\kappa}, \tag{5.20}$$

research works have determined different values for the typically fitted exponent parameter, resulting in a wide range of approximately $n_\kappa = 2$ to 8 reported in literature [20, 101, 113, 430, 431].

In analogous fashion to equation (5.19), the diffusive transport in partially saturated porous media is typically characterized with a relative diffusivity

$$D_g^{\mathrm{rel}} = \frac{D_g^{\mathrm{eff,wet}}}{D_g^{\mathrm{eff,dry}}} = g_D(S) = (1-S)^{n_D} \tag{5.21}$$

as the ratio of effective diffusivities in the dry and partially saturated porous medium, respectively. As already for the permeability, the derived exponent is again reported with a wide range of approximately $n_D = 2$ to 5 [69, 113, 419, 425, 427, 428, 432–434].

At this point, it is noted for completeness that some studies (e.g., [419]) also investigated the in-plane effective gas transport in partially saturated GDL. However, since in operating fuel cells the transport of gas (and liquid) occurs primarily from the gas channels to the catalyst layers (and vice-versa), the subsequent studies of this work focus exclusively on the characterization of the through-plane gas transport in the GDL. Accordingly, Darcy's law (eq. (5.6)) simplifies to

$$u_g^z = -\frac{\kappa_g}{\mu_g}\frac{\Delta p_g}{\Delta z} \tag{5.22}$$

and Fick's law (eq. (5.10)) becomes

$$J_j^z = -D\frac{\Delta c_j}{\Delta z} \tag{5.23}$$

with the spatial coordinate z along the thickness Δz of the GDL.

In the subsequent simulative studies of this chapter, the effective gas transport is characterized for partially saturated GDL microstructures at different stages of aging. After simulation of liquid water invasion and evaluation of the breakthrough liquid water distributions (see Section 5.4), the simulation snapshots of the partially saturated GDL

microstructures are thus further postprocessed. Whereas in LBM approximated as a diffuse layer, the interface between two immiscible fluids (here: liquid water and air) is in reality rather sharp and with a thickness beyond the lattice resolution of the simulation domains. Therefore, prior to the subsequent gas transport simulations, the two-phase regions in the simulation snapshots of the partially saturated GDL microstructures have to be differentiated into the bulk phases of the respective fluids. With the voxel-based phase-field parameter

$$\varphi^{\mathrm{vx}}(x,y,z) = \frac{\rho_l(x,y,z) - \rho_g(x,y,z)}{\rho_l(x,y,z) + \rho_g(x,y,z)} \tag{5.24}$$

denoting the position of the fluid-fluid interface at $\varphi^{\mathrm{vx}} = 0$ (see also eq. (3.59)), pore space voxels are assigned to either the liquid ($\varphi^{\mathrm{vx}} \geq 0$) or the gas phase bulk ($\varphi^{\mathrm{vx}} < 0$), according to their relative position to the fluid-fluid interface. In addition to this phase binarization, the liquid phase is assumed to act as an immobile phase blocking the gas transport and is therefore treated as an additional solid component. Postulating furthermore that gas can pass unhindered through the unresolved nanostructure of the MPL, its solid material voxels are defined as void space voxels. Following these postprocessing steps, the simulation snapshots of the partially saturated GDL microstructures are transformed into binarized solid-void matrices. Employing the GeoDict modules 'FlowDict' and 'DiffuDict', convective and diffusive gas transport is then simulated for these binary porous structures by imposition of a concentration and a pressure gradient in the GDL through-plane direction, respectively. Eventually, effective gas phase diffusivities and permeabilities are then determined by solving Fick's (eq. (5.10)) and Darcy's law (eq. (5.6)) for D_g^{eff} and k_g.

5.6 Modeling of structural degradation effects

5.6.1 GDL microstructure aging due to PTFE loss

As previously described in Section 5.1, several degradation routes for GDL aging have been identified over the past decades. However, experimental investigation of *in situ* GDL aging is mostly limited to qualitative analysis, as isolation of superposing degradation effects of different fuel cell components remains a challenging task. This shortfall of experimental research applies in particular to GDL aging due to loss of hydrophobic additive, which is, however, in the main focus of the subsequent degradation studies. Lacking preexisting studies for quantitative experimental analysis of PTFE loss in aged GDLs, an in-house algorithm is therefore developed in this work to generate virtually

degraded GDL microstructure reconstructions. In this in-house aging routine, GDL degradation by loss of additive is realized by voxel-wise removal of PTFE from the fiber surfaces within the microstructure. Assuming that the elimination of superficial additive is proportional to its local abundance, PTFE voxels are then selected through the GDL thickness according to a probability based on the surface coverage profile in Figure 5.2b. Defining the compressed default impregnated fiber reconstruction (Figure 5.1b) as the 'pristine' GDL, this microstructure is then gradually aged by incremental additive elimination with the in-house degradation algorithm. As a result of this procedure, degraded GDL microstructures are obtained for 11 stages of progressive aging, which correspond to PTFE surface coverages ranging from $\chi = 47\,\%$ (pristine) to $\chi = 0\,\%$ (completely aged). Following this approach, two different structural degradation effects can be recognized. Firstly, as the more hydrophobic solid component ($\theta_{\mathrm{PTFE}} > \theta_{\mathrm{CF}}$) is successively removed, the porous medium becomes more hydrophilic. Secondly, since PTFE removal is equivalent to a selective erosion of solid material, the overall porosity of the microstructure will increase upon aging. With a maximum PTFE volume fraction of $\phi = 3.68\,\mathrm{vol}\%$ (see Section 4.2.4), however, the latter degradation effect is expected to have a subordinate impact on the multiphase transport characteristics in the GDL, as will be shown in Section 5.7. In Figure 5.7, the two structural degradation effects of increasing surface hydrophilicity and decreasing solid volume fraction are illustrated by the through-plane profiles for the local PTFE surface coverage χ^{local} and the local porosity $\epsilon^{\mathrm{local}}$. Furthermore, loss of additive is also illustrated for three different stages of GDL aging in Figure 5.8. A summary of the porosity and the PTFE surface coverage for all the 11 different stages of modeled GDL aging is furthermore provided in Table 5.2 (columns 'compr.'). In a final preprocessing step prior to simulations, the different representations of the aged GDL microstructure are cropped by clipping of the GDL/MPL transition zone to comply to the computational setup as presented in Section 5.3 Evidently, this operation slightly alters both the porosity and additive surface coverage, as shown in Table 5.2 (columns 'compr.+cut').

5.6.2 MPL microstructure degradation due to increase in macroporosity

Analogous to the research on GDL aging, most mechanisms of MPL degradation are presumably already identified (see Section 5.1) but yet only rarely quantified in detail. In order to consider effects of MPL aging on the GDL liquid water transport as well, different MPL macropore reconstructions are therefore virtually generated for the subsequent degradation studies. For this modeling of structural aging effects, degradation of the

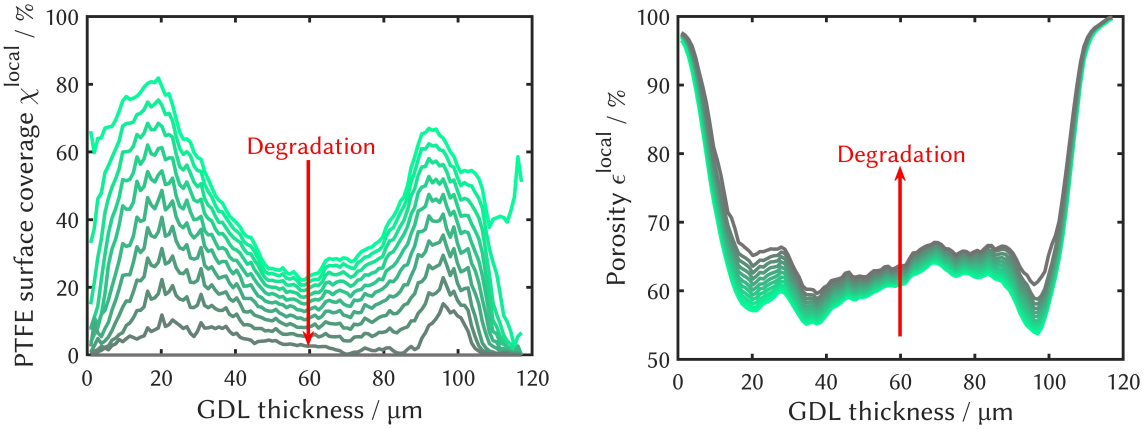

(a) Hydrophobicity decrease. (b) Porosity increase.

Figure 5.7: Virtual degradation of impregnated H14 microstructure reconstructions with an in-house algorithm for 11 stages of PTFE loss: Additive depletion on the fiber surface results in (a) lower hydrophobicity and (b) higher porosity for the degraded GDL samples.

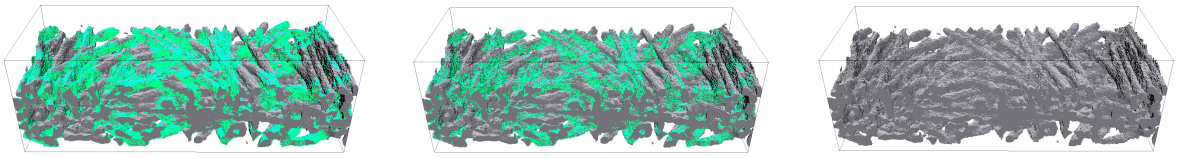

(a) Pristine ($\chi = 47\,\%$). (b) Partially aged ($\chi = 25.9\,\%$). (c) Completely aged ($\chi = 0\,\%$).

Figure 5.8: Virtually degraded microstructure reconstructions for the impregnated H14 microstructure reconstruction at three different stages of PTFE loss. Starting from the pristine state (a), the microstructure is artificially degraded with an in-house algorithm by voxel-wise additive removal up to full PTFE depletion (c).

MPL is assumed to result in an increase of its macroporosity (e.g., due to high gas flow rates [378]). The postulated main MPL aging effect of macropore growth is therefore comparable to the material-specific crack dilation modeled by Niblett et al. [397]. In the frame of the subsequent degradation studies, the microstructure representations for both the pristine GDL (Figure 5.1b) and MPL (Figure 5.4b) are already generated in similar fashion via binarization of µCT images (Section 4.2.2 and Section 5.2.2). In order to obtain microstructure representations of aged samples, however, different approaches are taken for structure generation. Whereas the GDL microstructure reconstruction from µCT image data is carried out only once for the pristine state, all degraded microstructure representations are derived by virtual aging of this unique reconstruction (Figure 4.12). Macropore representations for different stages of MPL degradation on the other hand are not obtained by alteration of the reconstruction for the pristine MPL. Instead, the raw µCT image data is repeatedly binarized for each stage of aging and assuming increasing macroporosities for proceeding degradation. At this point, it is acknowledged that with

Table 5.2: Structural properties for virtually aged GDL microstructure reconstructions at progressive stages of PTFE loss, ranging from pristine (#1) to completely degraded (#11). The column headers 'compr' and 'compr+cut' refer to the artificially compressed reconstructions before and after clipping of the GDL/MPL transition zone.

No	Porosity ϵ_{GDL}/%		PTFE surface coverage χ/%	
#	compr	compr+cut	compr	compr+cut
1	65.76	64.14	47.03	42.83
2	66.10	64.43	43.25	39.65
3	66.47	64.76	39.31	36.29
4	66.87	65.12	35.09	32.62
5	67.29	65.51	30.62	28.66
6	67.72	65.91	25.92	24.52
7	68.19	66.35	20.92	19.98
8	68.68	66.81	15.73	15.19
9	69.17	67.27	10.41	10.17
10	69.67	67.75	5.03	4.93
11	70.46	68.41	0.00	0.00

this approach all microstructure representations of the degraded MPL are eventually derived from the same µCT image data of a pristine impregnated and MPL-coated H14 GDL. As a consequence, the modeling of structural aging effects in the MPL is, analogous to the GDL, again purely virtual. Following the aforementioned approach, 9 different MPL macropore reconstructions are thus generated ranging from $\epsilon_{MPL}^{macro} = 20\,\%$ (pristine) to $\epsilon_{MPL}^{macro} = 100\,\%$ (completely aged/no MPL). This structural degradation effect of an increasing MPL macroporosity is illustrated for two different stages of aging in Figure 5.9. A summary of the macroporosities for all the MPL reconstructions is furthermore provided in Table 5.3.

(a) Pristine ($\epsilon_{MPL}^{macro} = 19.97\,\%$). (b) Partially aged ($\epsilon_{MPL}^{macro} = 59.99\,\%$).

Figure 5.9: Different macropore reconstructions as surrogates for degraded MPLs. Proceeding stages of aging are generated via binarization of µCT image data for the impregnated and MPL-coated H14 and setting successively higher macroporosities ϵ_{MPL}^{macro}.

Table 5.3: Increasing macroporosities for proceeding stages of MPL degradation.

No #	MPL macroporosity $\epsilon_{\mathrm{MPL}}^{\mathrm{macro}}$ / %
1	19.97
2	29.95
3	40.16
4	50.10
5	59.99
6	70.14
7	80.08
8	86.27
9	100.00

5.7 Simulation of breakthrough characteristics in degraded GDLs and MPLs

5.7.1 Liquid water transport in a pristine GDL and MPL

In a first numerical study of this chapter, *in situ* liquid water transport is simulated for the pristine GDL (Figure 5.1b) and pristine MPL (Figure 5.4b). For this purpose, liquid water invasion into the GDL is simulated employing the computational setup as described in Section 5.3.2. However, while in ordinary PEM fuel cell operation liquid water velocities in the GDL are expected to be very low ($u_l \sim 10^{-6}\,\mathrm{m/s}$, see Section 2.2.3), breakthrough may occur only after longer time spans of up to several minutes [276, 435]. For computationally expensive pore-scale methods such as the LBM, these time scales typically result in simulation durations beyond accesibility. In order to obtain a reasonable level of computational expense in this first study, the liquid water inlet velocity in the simulations is therefore set to a higher value of $u_l = 1e^{-5}$, which corresponds to a physical velocity of $u_l^{\mathrm{phys}} = 2.27e^{-5}\,\mathrm{m/s}$ (see Table 5.4) for a typical PEMFC operation temperature of 80 °C. According to Faraday's law (see equation (2.6)), this liquid water flow rate can then be related to a current density of $i \approx 23.7\,\mathrm{A/cm^2}$, which is significantly higher than common PEMFC current densities of typically $i < 3\,\mathrm{A/cm^2}$ [84, 85]. As will be demonstrated in Section 5.7.2, however, the fluid invasion patterns in porous media are to some extend invariant to the flow rate (and thus the current density) of the invading phase as long as a capillary-dominated flow regime is ensured.

After $t^{\mathrm{BT}} = 2.68\mathrm{e}^{6}$ time steps, breakthrough is reached for a liquid water distribution in the pristine GDL/MPL microstructure as shown in Figure 5.10a. At breakthrough, large amounts of liquid water are observable in the right-hand side half of the microstructure. As illustrated by Figure 5.11a, two thirds of the domain (right-hand sided) exhibit strong liquid water accumulation with an average saturation of $S_x^{\mathrm{BT}} \approx 57\,\%$, whereas the left-hand sided third remains almost completely dry. This observation may be related to the local distribution of pore sizes offering lower capillary transport resistances on the right-hand side of the domain. Figure 5.11b on the other hand shows a relatively homogeneous saturation profile in the in-plane y-direction with $S_y^{\mathrm{BT}} \approx 39\,\%$. In the through-plane z-direction, the local saturation slightly increases from the liquid inlet side (left) towards the GDL core and then decreases again towards the gas channel side (right). With an average saturation of $S_z^{\mathrm{BT}} \approx 42\,\%$, this saturation profile can be related to the through-plane porosity profile shown in Figure 5.5a. In total, the overall saturation sums up to $S^{\mathrm{BT}} = 39.4\,\%$, which is significantly higher than typically reported values of less than 25 % [23, 36, 139, 409]. In summary, these findings are contrary to expectations as *operando* liquid water transport in the GDL is commonly assumed to proceed along single percolation paths of lowest capillary resistance, corresponding to the flow regime of capillary fingering [23, 88, 91]. In the simulation, on the other hand, the liquid water distribution exhibits a rather broad invasion front, resembling more of stable displacement [89], a flow regime which is not anymore capillary dominated ($\mathrm{Ca} \gtrsim 10^{-3}$ [349]). With an inlet velocity of $u_l = 1\mathrm{e}^{-5}$, however, liquid water invasion was simulated for a capillary number of $\mathrm{Ca} = 1.33\mathrm{e}^{-5}$ (see eq. (2.8)), which should be sufficiently low to ensure dominance of capillary forces. At this point, however, it is noted that Lenormand et al. [89] derived their capillary flow regimes of viscous fingering, stable displacement and capillary fingering for the invasion of a nonwetting fluid. Here, however, the invading liquid water is with $\theta_{\mathrm{CF}} = 65°$ on the carbon fiber surface *per se* a primarily wetting fluid. Whereas this wetting capability is to a some degree locally reduced by the hydrophobic additive ($\theta_{\mathrm{PTFE}} = 115°$ and the capillary valve effect (see Section 3.2.5), the liquid water appears to remain effectively a wetting fluid in the right-hand side half of the GDL, where it is thus found to be imbibed. This observation raises the question if the mixed wettability of the impregnated fiber substrate is accurately modeled for the simulations. Under the assumption that the contact angles for the carbon fibers and PTFE are appropriately chosen, it appears natural to rework the additive distribution in the GDL microstructure, in particular as the latter could not be successfully validated against the experimental reference in Section 4.4.9-Section 4.4.10. Acknowledging the parametric uncertainty in the estimate $\chi^{\mathrm{est}} \approx 50\,\%$, one could therefore think about raising the PTFE surface coverage even further in order to increase the average hydrophobicity in the GDL microstructure reconstruction. However, lacking clear

evidence from literature, at least to the author's knowledge, overly high PTFE surface coverages are expected to contradict the often reported primary additive deposition near fiber intersections [53, 54, 316, 317, 320]. Furthermore, for $\chi \to 100\,\%$ the average fiber surface contact angle would approach $\theta_{\mathrm{PTFE}} = 115°$ and could be then modeled by just using a single uniform contact angle for both carbon fibers and additive, thereby neglecting the effect of mixed wettability.

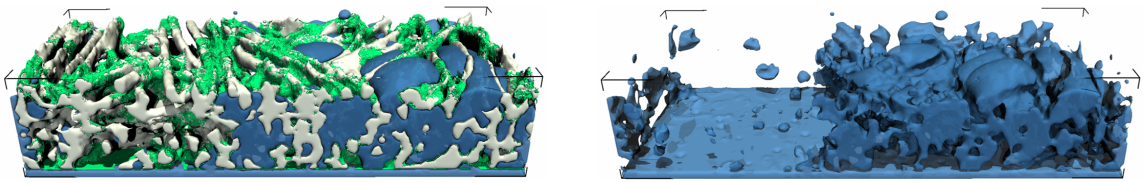

(a) $\theta_{\mathrm{CF}} = 65°$.

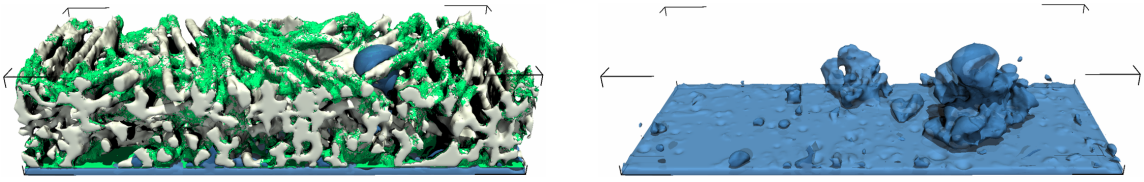

(b) $\theta_{\mathrm{CF}} = 90°$.

Figure 5.10: Simulated liquid water breakthrough in the microstructure reconstruction of the pristine impregnated H14 GDL/MPL (Figure 5.1b/Figure 5.4b) for a liquid inlet velocity of $u_l = 1\mathrm{e}^{-5}$. The liquid water distribution is shown for two different carbon fiber contact angles θ_{CF} of a (a) hydrophilic and (b) neutrally wetting support material.

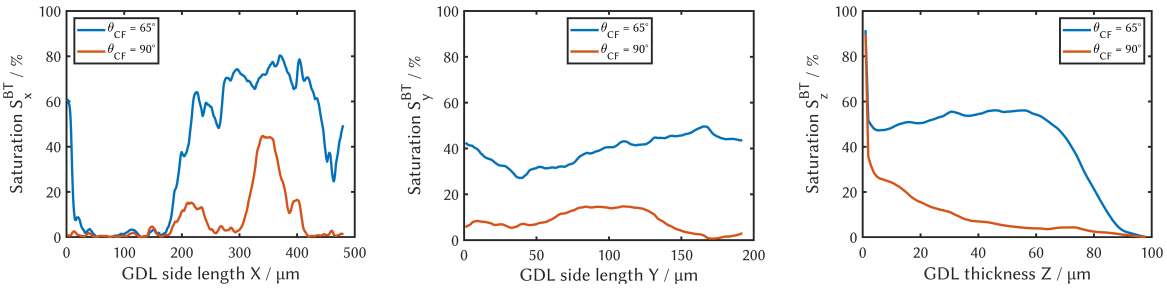

(a) In-plane X. (b) In-plane Y. (c) Through-plane Z.

Figure 5.11: Saturation profiles for the simulated liquid water breakthrough in the microstructure reconstruction of the pristine impregnated H14 GDL/MPL (Figure 5.1b, Figure 5.4b), assuming a liquid inlet velocity of $u_l = 1\mathrm{e}^{-5}$ and variable carbon fiber contact angles θ_{CF}.

At this point, it is therefore assumed that the original choice of $\theta_{\mathrm{CF}} = 65°$ may be inappropriate for the subsequent simulations of *operando* GDL liquid water transport, despite providing the best agreement with the experimental $p_c - S$ data (see Figure 4.26b

in Section 4.4.7). This conjecture is supported by two possible explanations: On the one hand, the measurement of the $p_c - S$ relations for the impregnated H14 fiber substrate appears to be most likely distorted by an artifact from improper hydraulic contacting (see Figure 4.28a in Section 4.4.9). Therefore, the test bench is assumed to provide experimental data with limited reliability, not excluding additional unknown sources of measurement errors. Under the premise that the recorded capillary pressure is subject to an unknown measurement offset as well, the simulations and thus θ_{CF} could have been validated against a false reference. On the other hand, liquid water contact angles on graphitic surfaces have been reported to increase up to 90° when exposed to ambient air, owing to hydrocarbon contamination [312, 341, 344, 345]. Thus, it is in general possible that the *ex situ* wettability characterization at the $p_c - S$ test bench was conducted shortly after exfoliation and for uncontaminated graphitic fiber surfaces with $\theta_{\mathrm{CF}} = 65°$. In cell operation, on the other side, the GDL may then after an initial contamination period in general already have become more hydrophobic.

Aiming to recover the *operando* flow regime of capillary fingering, the previous liquid water invasion simulation is therefore repeated with a carbon fiber contact angle of as high as $\theta_{\mathrm{CF}} = 90°$, which is still in the reported wide range of 50° to 95° [100, 322, 332, 341, 346]. Owing to the now neutrally wetting carbon fiber substrate, the overall breakthrough liquid water accumulation is found to be significantly reduced, as shown in Figure 5.10b. The broad liquid invasion front has vanished and instead single capillary percolation paths are visible at breakthrough. While the actual breakthrough site is still the same (see also peak in Figure 5.11a), the amount of accumulated liquid water has significantly decreased along all three principal directions of the GDL, as illustrated by the saturation profiles in Figure 5.11. Furthermore, the through-plane saturation profile has not just changed quantitatively but also qualitatively, as the local saturation is now found to decrease continuously from the liquid inlet side to the GC side. This observation indicates that the liquid water has no more tendency to occupy additional pore space on the way to breakthrough, as it effectively has become a nonwetting fluid percolating along paths of least capillary transport resistance. As a consequence, breakthrough is already reached after $t^{\mathrm{BT}} = 6.01\mathrm{e}^5$ time steps with an overall saturation of as low as $S^{\mathrm{BT}} = 8.4\,\%$, which complies to commonly reported values of less than 25 %[23, 36, 139, 409].

In summary, these observations provide strong indications for the presence of capillary fingering as the flow regime one would expect for *operando* liquid water transport in the GDL. Therefore, a new carbon fiber contact angle of $\theta_{\mathrm{CF}} = 90°$ will be used as default for all subsequent liquid water breakthrough simulations of this chapter.

5.7.2 Sensitivity of the liquid water invasion pattern on the inlet velocity

In ordinary fuel cell operation with current densities of $i < 3\,\mathrm{A/cm^2}$ [84, 85], liquid water production rates and thus GDL inlet velocities are quite low, as indicated by low capillary numbers in the range of $\mathrm{Ca} \sim 10^{-5} - 10^{-8}$ [23, 88]. With GDL thicknesses of typically 100 to 400 µm [19], liquid water breakthrough is often observed to require up to several minutes [23, 276, 435]. In microstructure-resolving PSM simulations, on the other hand, high spatial resolutions necessitate small time step sizes in order provide consistent results. Moreover, domain sizes for the simulation geometries have to be large enough to serve as REVs (see Section 4.2.3), rendering pore-scale models with heavy computational expense. As a consequence, PSM simulations on the time scale of minutes would require large numbers of time steps, for which the computation time is often beyond the practical limit. However, this is also not strictly necessary as long as the flow regime is invariant to the boundary conditions, which can be in this case ensured by a sufficiently low capillary number [42, 90, 397]. Therefore, a sensitivity study is conducted prior to the subsequent degradation simulations in order to determine the highest liquid water inlet velocity still yielding the same invasion pattern of a capillary-dominated flow, as expected under *operando* conditions. Presuming that the liquid water transport remains in the capillary-dominated regime and that the time to breakthrough scales reciprocally with the liquid inlet velocity, computational cost could be significantly reduced for higher u_l, while the findings of the simulations would still be transferable to cell operation. Employing the computational setup from Section 5.3, liquid water invasion into the pristine GDL/MPL is simulated for seven different liquid inlet velocities u_l (Table 5.4) until breakthrough occurs. Based on the obtained liquid water invasion patterns, the flow regimes are then characterized by evaluation of the through-plane saturation profiles and the time to breakthrough.

Figure 5.12 illustrates the resulting liquid water distributions at three different inlet velocities. At the lowest flow rate of $u_l = 5\mathrm{e}^{-6}$, liquid water invades primarily via two percolation paths with an invasion pattern similar to the liquid water distribution for the twice higher velocity of $u_l = 1\mathrm{e}^{-5}$ (Figure 5.10b). This similarity in the breakthrough characteristics is confirmed by the saturation profiles in Figure 5.13 and an overall saturation of $S^{\mathrm{BT}} = 8.17\,\%$ (cf. $8.4\,\%$ for $u_l = 1\mathrm{e}^{-5}$). Increasing the velocity by two orders of magnitude, i.e., $u_l = 5\mathrm{e}^{-4}$, on the other hand, the liquid water distribution at breakthrough has significantly changed. Whereas for the lower inlet velocity only two capillary fingers were observed, liquid water invasion now occurs broadly all over the cross-sectional area of the X-Y plane in the GDL domain. As a consequence, significantly

larger amounts of liquid water have accumulated in the two in-plane directions as well as along the thickness of the GDL, resulting in an overall breakthrough saturation of $S^{\mathrm{BT}} = 28.10\,\%$. For the even higher velocity of $u_l = 1\mathrm{e}^{-3}$, this change in flow characteristics is observed to be continued with an even broader liquid water invasion front and an overall saturation of as high as $S^{\mathrm{BT}} = 40.38\,\%$.

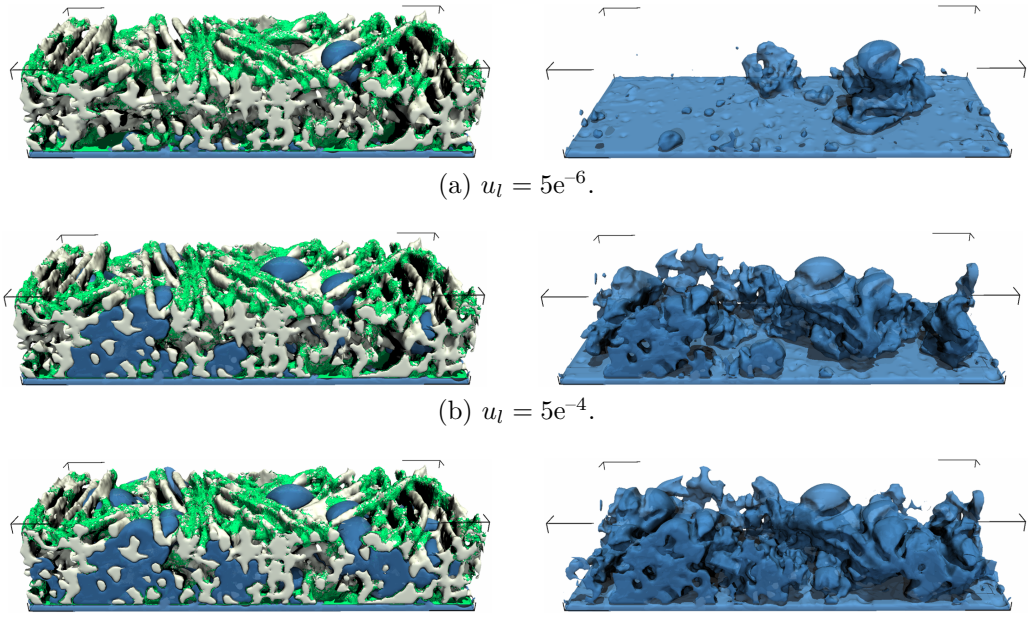

(a) $u_l = 5\mathrm{e}^{-6}$.

(b) $u_l = 5\mathrm{e}^{-4}$.

(c) $u_l = 1\mathrm{e}^{-3}$.

Figure 5.12: Simulated liquid water breakthrough in the microstructure reconstruction of the pristine impregnated H14 GDL/MPL (Figure 5.1b/Figure 5.4b) for three different liquid inlet velocities u_l.

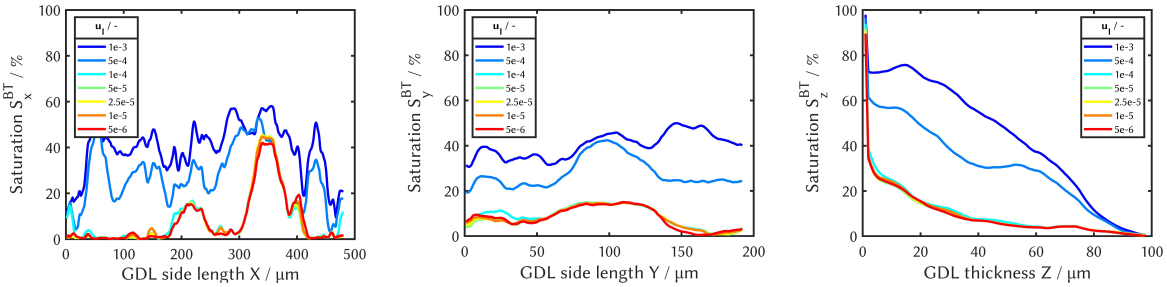

(a) In-plane X. (b) In-plane Y. (c) Through-plane Z.

Figure 5.13: Breakthrough saturation profiles for the microstructure reconstruction of the pristine impregnated H14 GDL/MPL (Figure 5.1b, Figure 5.4b) at varying liquid phase inlet velocities u_l.

Above findings suggest that the flow regime is for higher u_l not anymore fully capillary-dominated but instead in the transition from capillary fingering to stable displacement

[89], where inertial effects start to become relevant. This conjecture is supported by the change in the time required for breakthrough occurrence. Whereas viscous and inertial forces are negligible in the capillary-dominated regime, liquid invasion patterns in capillary fingering are expected to be independent of the invading fluid's velocity. Hence, the time to breakthrough should therefore exhibit an approximately reciprocal dependence on the liquid inlet velocity, i.e., $t^{\mathrm{BT}} \sim 1/u_l$. However, as Figure 5.14b shows this relation evidently does not hold for $u_l \geq 1\mathrm{e}^{-4}$ resp. $\mathrm{Ca} \geq 1.33\mathrm{e}^{-4}$ (see Table 5.4). This finding is in line with Lenormand et al. [89], who classify flow regimes for $\mathrm{Ca} < 1\mathrm{e}^{-4}$ ($M > 1$) as capillary fingering. For $\mathrm{Ca} > 1\mathrm{e}^{-4}$, on the other hand, the liquid invasion patterns are then expected to be in a transitional state between capillary fingering and stable displacement. Taking the breakthrough simulations for all seven u_l into account, the time dependence of the breakthrough occurrence is observed to hold very well for $u_l \leq 5\mathrm{e}^{-5}$ (Figure 5.14b). This indication of an upper boundary at $\mathrm{Ca} \leq 6.67\mathrm{e}^{-5}$ for the flow regime of capillary fingering is eventually confirmed by the quasi-stationarity in both the local (Figure 5.13) and overall saturation (Figure 5.14a) at breakthrough.

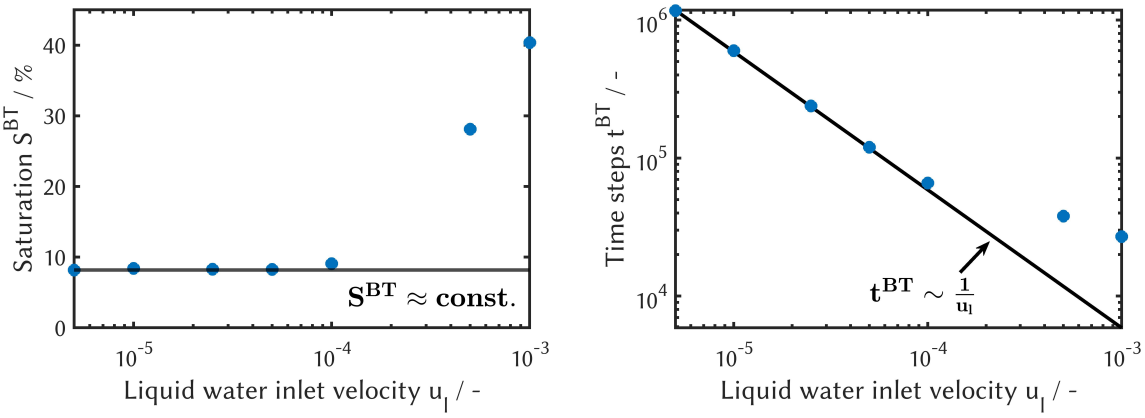

(a) Breakthrough saturation.

(b) Time to breakthrough.

Figure 5.14: Breakthrough characteristics for the microstructure reconstruction of the pristine impregnated H14 GDL/MPL (Figure 5.1b, Figure 5.4b) at varying liquid water inlet velocities u_l.

Based on above sensitivity study, a liquid water inlet velocity of $u_l \leq 5\mathrm{e}^{-5}$ is determined to yield a capillary number sufficiently low to warrant the flow regime of capillary fingering. Furthermore, providing similar breakthrough characteristics as the initial value of $u_l \leq 1\mathrm{e}^{-5}$ in one fifth of the computation time, this larger liquid inlet velocity of $u_l \leq 5\mathrm{e}^{-5}$ is therefore set as default for all subsequent simulative degradation studies of this work. At this point, it is furthermore noted that the physical time $t^{\mathrm{BT,phys}}$ to breakthrough in Table 5.4 is with hundredths to tenths of a second apparently very short. Here, one has to recall that these values relate to very high current densities, which are not expected to occur in ordinary

PEM fuel cell operation. However, under the assumption that the similarity of capillary-dominated liquid water invasion patterns holds for all $u_l \leq 5\text{e}^{-5}$ and thus $i \leq 118.5\,\text{A/cm}^2$ and with $t^{\text{BT,phys}} \sim 1/u_l \propto 1/i$, on the other hand, the time to breakthrough can be extrapolated down to realistic current densities via

$$t^{\text{BT,phys}}(i) = \left(\frac{i_{\text{ref}}}{i}\right) t^{\text{BT,phys}}(i_{\text{ref}}) = \left(\frac{118.5\,\text{A/cm}^2}{i}\right) t^{\text{BT,phys}}(i_{\text{ref}}) \tag{5.25}$$

and the reference current density of $i_{\text{ref}}(u_l = 5\text{e}^{-5}) = 118.5\,\text{A/cm}^2$. Assuming, e.g., an intermediate current density of $1\,\text{A/cm}^2$ for ordinary PEMFC operation and with $t^{\text{BT,phys}}(i_{\text{ref}}) = 0.05\,\text{s}$ from Table 5.4, the time to breakthrough would then amount to $t^{\text{BT,phys}}(1\,\text{A/cm}^2) \approx 5.9\,\text{s}$, which is in the range of seconds [23, 436] to minutes [276, 435] reported in literature.

Table 5.4: Simulation parameters and resulting breakthrough characteristics from the sensitivity study on liquid water invasion patterns for varying inlet velocities. The corresponding physical counterparts u_l^{phys} and $t^{\text{BT,phys}}$ are obtained with the conversion factors from Table 5.1 and the capillary number Ca is calculated from the lattice-based fluid properties as given in Section 5.3. According to equation (2.6), the liquid inlet velocity can be furthermore related to a current density in PEMFC operation.

Liquid inlet velocity		Capillary number	Current density	Breakthrough characteristics		
u_l	u_l^{phys}	$\text{Ca} = \frac{\rho_l \nu_l u_l}{\sigma}$	i	t^{BT}	$t^{\text{BT,phys}}$	S^{BT}
l.u./l.t.	m/s	-	A/cm^2	–	s	%
1e^{-3}	$2.27e^{-3}$	1.33e^{-3}	2369.92	2.7e^{4}	0.01	40.38
5e^{-4}	$1.14e^{-3}$	6.67e^{-4}	1184.96	3.8e^{4}	0.02	28.10
1e^{-4}	$2.27e^{-4}$	1.33e^{-4}	236.99	6.6e^{4}	0.03	9.08
5e^{-5}	$1.14e^{-4}$	6.67e^{-5}	118.50	1.2e^{5}	0.05	8.26
2.5e^{-5}	$5.69e^{-5}$	3.33e^{-5}	59.25	2.4e^{5}	0.10	8.30
1e^{-5}	$2.27e^{-5}$	1.33e^{-5}	23.70	6.0e^{5}	0.25	8.40
5e^{-6}	$1.14e^{-5}$	6.67e^{-6}	11.58	1.2e^{6}	0.49	8.17

5.7.3 Effect of GDL aging on breakthrough characteristics

In a first degradation study, the impact of GDL aging on the liquid water transport characteristics is investigated. Assuming loss of PTFE as the main degradation path, liquid water invasion is simulated for the microstructure reconstruction of the impregnated GDL/MPL at a total of 11 stages of proceeding GDL aging (see also Section 5.6.1), as summarized in Table 5.2. Whereas difficult to asses in experiments, the effects of GDL aging are furthermore isolated from structural changes of the MPL presuming that the latter remains in the pristine state (Figure 5.4b) throughout this investigation. Setting the inlet velocity to $u_l = 5\text{e}^{-5}$, liquid water invasion into the GDL is then simulated and

stopped at breakthrough. Figure 5.15 shows the resulting liquid water distributions at breakthrough for the pristine, partially degraded and completely degraded GDL. Even though the average surface hydrophobicity is clearly altered by a reduction of the PTFE surface coverage χ from 42.83 to 0 %, no significant difference in the liquid water invasion patterns is observable across the three different microstructures. This visual impression is confirmed by the profiles in Figure 5.16 showing very similar local saturations across all stages of GDL aging.

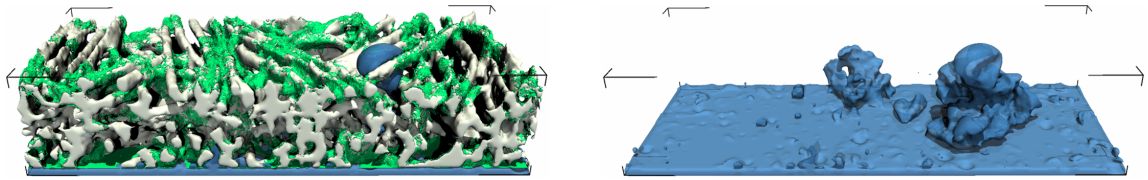

(a) Pristine ($\chi = 42.83\,\%$).

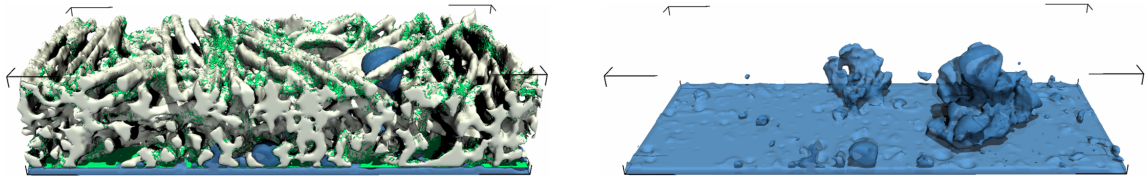

(b) Partially degraded ($\chi = 24.52\,\%$).

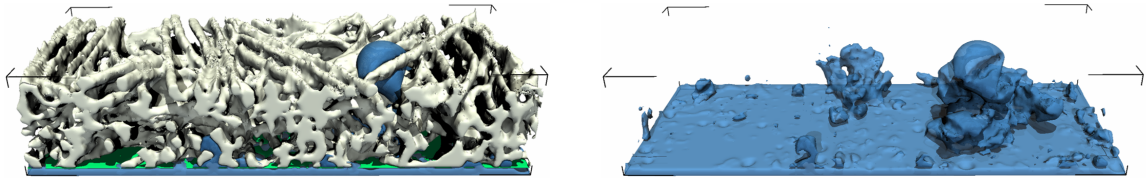

(c) Completely degraded ($\chi = 0.00\,\%$).

Figure 5.15: Simulated liquid water breakthrough in the microstructure reconstruction of the impregnated H14 GDL/MPL for varying stages of GDL aging by loss of hydrophobic additive. The degradation results in a reduction of the PTFE surface coverage χ. In these aging studies, the MPL is assumed to remain in the pristine state with a macroporosity of $\epsilon_{\mathrm{MPL}}^{\mathrm{macro}} = 19.97\,\%$ (Figure 5.4b).

As a result, the overall saturation at breakthrough (Figure 5.17) appears to be constant and unaffected by the loss of PTFE. Based on these observations, the absence of any significant aging effect on the liquid water transport is attributed to a dominant impact of the pristine MPL on the breakthrough characteristics [437]. With a macroporosity of only $\epsilon_{\mathrm{macro}}^{\mathrm{MPL}} = 19.97\,\%$ (Table 5.2), the MPL drastically reduces the liquid water entry sites into the GDL. In addition, the median macropore of the MPL reconstruction is with around 8.57 µm approximately half the size of the median pore (18.06 µm) of the GDL reconstruction (compressed and cut). Furthermore, the MPL is also assumed to be more hydrophobic with $\theta_{\mathrm{MPL}} = \theta_{\mathrm{PTFE}} = 115°$. Eventually, these properties may render the

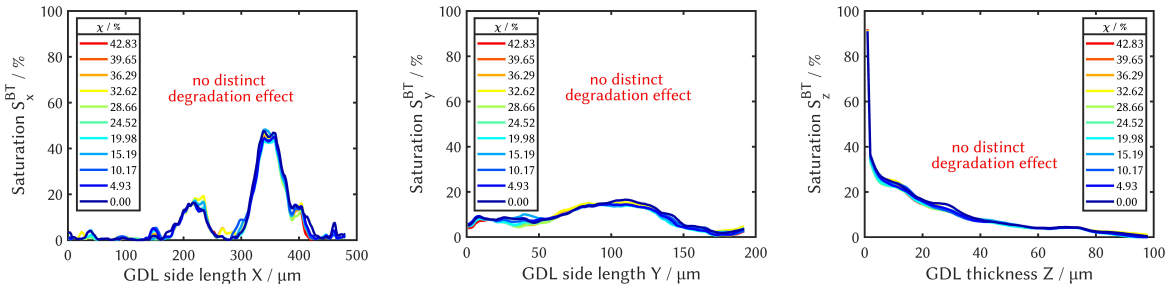

(a) In-plane X. (b) In-plane Y. (c) Through-plane Z.

Figure 5.16: Breakthrough saturation profiles for the impregnated H14 GDL/MPL at varying stages of GDL aging by loss of hydrophobic additive. The degradation results in a reduction of the PTFE surface coverage χ. In these aging studies, the MPL is assumed to remain in the pristine state with a macroporosity of $\epsilon_{\mathrm{MPL}}^{\mathrm{macro}} = 19.97\,\%$ (Figure 5.4b).

MPL a dominant capillary barrier, which could therefore superpose any impact of GDL wettability alteration on the breakthrough characteristics. Owing to the lack of significant GDL aging effects, a subsequent investigation of the repercussion on the effective gas transport properties is at this point omitted due to the invariance of the liquid water breakthrough distribution upon GDL degradation.

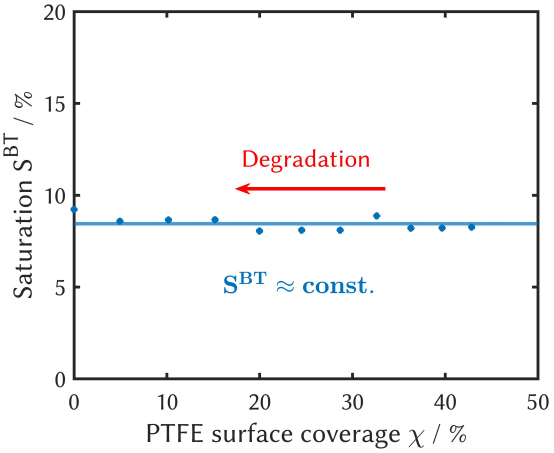

Figure 5.17: Breakthrough characteristics for the impregnated H14 GDL/MPL at varying stages of GDL aging by loss of hydrophobic additive. The degradation results in a reduction of the PTFE surface coverage χ. In these aging studies, the MPL is assumed to remain in the pristine state with a macroporosity of $\epsilon_{\mathrm{MPL}}^{\mathrm{macro}} = 19.97\,\%$ (Figure 5.4b).

5.7.4 Influence of MPL aging on breakthrough characteristics

In a second degradation study, the effect of MPL degradation on the liquid water transport within the GDL is investigated. Under the assumption that MPL aging is primarily embodied in an increase in macroporosity, liquid water invasion is simulated for the

microstructure reconstruction of the impregnated GDL/MPL at a total of 9 stages of proceeding MPL degradation (see also Section 5.6.2), as summarized in Table 5.3. In order to isolate the effects of MPL aging, the GDL microstructure reconstruction is assumed to remain in the pristine state with a PTFE surface coverage of $\chi = 42.83\,\%$ (Figure 5.1b). Invasion of liquid water into the GDL is then simulated for different stages of MPL degradation and halted upon breakthrough for further analysis of the effective gas transport properties. Figure 5.18 shows the breakthrough liquid water distribution in the GDL for three different stages of MPL degradation. Evidently, larger amounts of liquid water accumulate within the GDL when the MPL is degraded, indicating that MPL aging has a significant impact on the breakthrough characteristics. This observation is as expected since the size and number of liquid water entry sites increases with higher macroporosities, which promotes liquid water transport as larger and new percolation paths become accessible. Consequently, the liquid water invasion patterns become increasingly broader, as depicted by the saturation profiles in Figure 5.19.

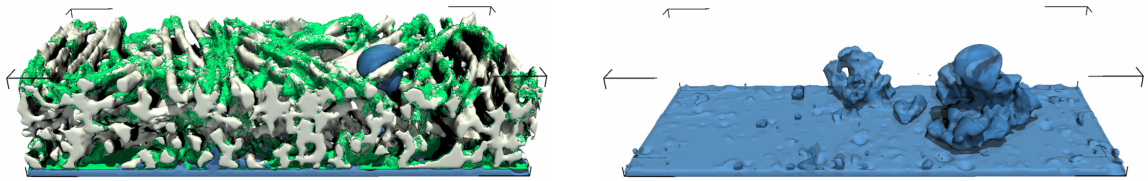

(a) Pristine ($\epsilon_{\mathrm{MPL}}^{\mathrm{macro}} = 19.97\,\%$).

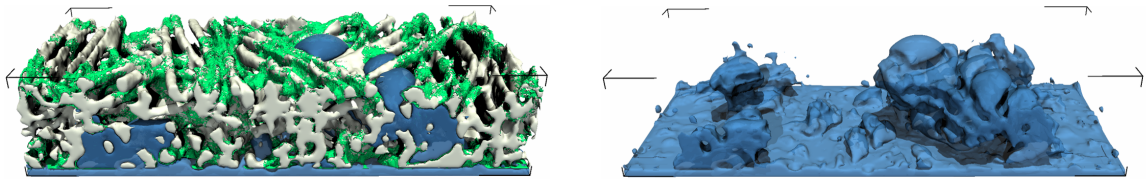

(b) Partially degraded ($\epsilon_{\mathrm{MPL}}^{\mathrm{macro}} = 59.99\,\%$).

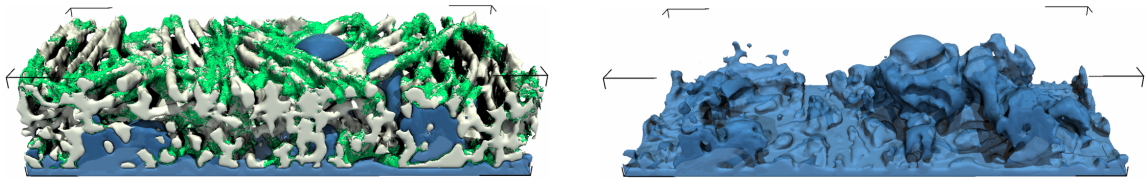

(c) Completely degraded ($\epsilon_{\mathrm{MPL}}^{\mathrm{macro}} = 100\,\%$).

Figure 5.18: Liquid water distribution in the microstructure reconstruction of the impregnated H14 GDL/MPL at breakthrough for varying stages of MPL aging by increase in macroporosity. In these aging studies, the GDL is assumed to remain in the pristine state with a PTFE surface coverage of $\chi = 42.83\,\%$ (Figure 5.1b).

A more detailed comparison of the local saturations for all 9 stages of MPL aging furthermore reveals that the breakthrough liquid water distribution remains quite similar for $\epsilon_{\mathrm{MPL}}^{\mathrm{macro}} \leq 40.16\,\%$ and $\epsilon_{\mathrm{MPL}}^{\mathrm{macro}} \geq 80.08\,\%$, but increases significantly in between. This

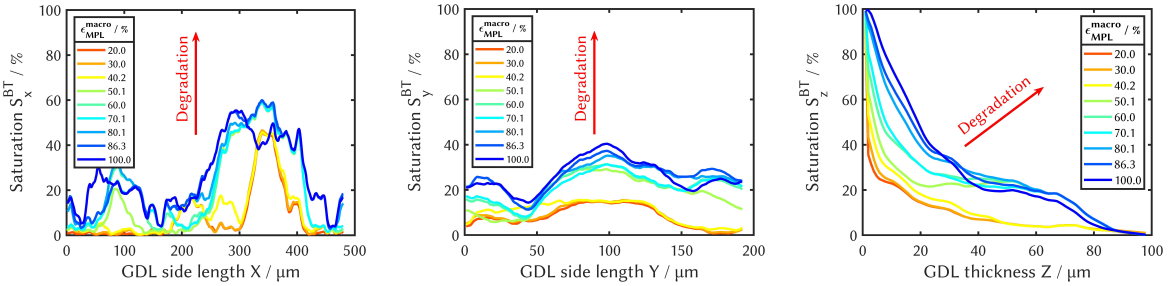

(a) In-plane X. (b) In-plane Y. (c) Through-plane Z.

Figure 5.19: Breakthrough saturation profiles for the impregnated H14 GDL/MPL at varying stages of MPL aging by increase in macroporosity. In these aging studies, the GDL is assumed to remain in the pristine state with a PTFE surface coverage of $\chi = 42.8\,\%$ (Figure 5.1b).

intermediate transition zone with a steep gradient is also clearly visible in the breakthrough characteristics shown in Figure 5.20. For the breakthrough saturation S^{BT}, the overall dependence on the MPL macroporosity $\epsilon_{\mathrm{MPL}}^{\mathrm{macro}}$ is determined to follow an inverse tangent relation. By nonlinear regression, a fit function is obtained with

$$S^{\mathrm{BT}} = 0.09 + 0.07\left\{1 + \arctan\left[8.22\left(\epsilon_{\mathrm{MPL}}^{\mathrm{macro}} - 0.5\right)\right]\right\}. \tag{5.26}$$

For the time t^{BT} to breakthrough a similar dependence is identified with

$$t^{\mathrm{BT}} = 1.29\mathrm{e}^{5} + 1.02\mathrm{e}^{5}\left\{1 + \arctan\left[7.58\left(\epsilon_{\mathrm{MPL}}^{\mathrm{macro}} - 0.5\right)\right]\right\}, \tag{5.27}$$

which is anticipated, since the amount of liquid water in the GDL is expected to be proportional to the constant liquid inlet velocity, i.e., $S^{\mathrm{BT}} \propto u_l t^{\mathrm{BT}}$. With $C_t = 4.22\mathrm{e}^{-7}\,\mathrm{s}$ (see Table 5.1), the physical time $t^{\mathrm{BT,phys}}$ to breakthrough can be furthermore denoted as

$$t^{\mathrm{BT,phys}} = C_t \cdot t^{\mathrm{BT}} = 0.05\,\mathrm{s} + 0.04\,\mathrm{s}\left\{1 + \arctan\left[7.58\left(\epsilon_{\mathrm{MPL}}^{\mathrm{macro}} - 0.5\right)\right]\right\} \tag{5.28}$$

and similar to eq. (5.25) the current density-dependent breakthrough time can then be estimated to

$$t^{\mathrm{BT,phys}}(i) = \left(\frac{i_{\mathrm{ref}}}{i}\right) t^{\mathrm{BT,phys}}(i_{\mathrm{ref}}) \tag{5.29}$$

$$= \left(\frac{118.5\,\mathrm{A/cm^2}}{i}\right)\left(0.05\,\mathrm{s} + 0.04\,\mathrm{s}\left\{1 + \arctan\left[7.58\left(\epsilon_{\mathrm{MPL}}^{\mathrm{macro}} - 0.5\right)\right]\right\}\right) \tag{5.30}$$

$$= \left(\frac{\mathrm{A/cm^2}}{i}\right)\left(6.45\,\mathrm{s} + 5.1\,\mathrm{s}\left\{1 + \arctan\left[7.58\left(\epsilon_{\mathrm{MPL}}^{\mathrm{macro}} - 0.5\right)\right]\right\}\right). \tag{5.31}$$

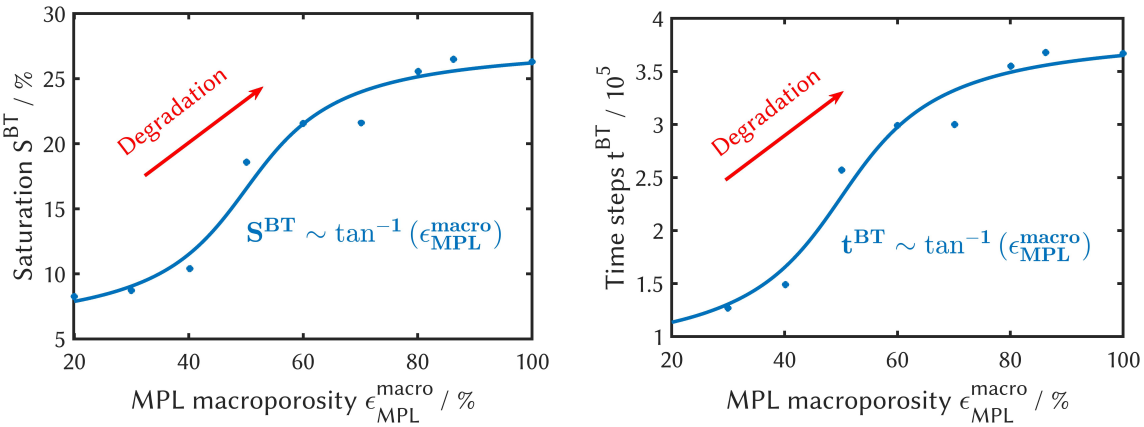

(a) Breakthrough saturation.

(b) Time to breakthrough.

Figure 5.20: Breakthrough characteristics for the impregnated H14 GDL/MPL at varying stages of MPL aging by increase in macroporosity. In these aging studies, the GDL is assumed to remain in the pristine state with a PTFE surface coverage of $\chi = 42.83\,\%$ (Figure 5.1b).

Above observation of a nonlinear intermediate transition zone for S^{BT} and t^{BT} with high sensitivity on $\epsilon_{\mathrm{MPL}}^{\mathrm{macro}}$ can be explained by the circumstance that degradation of the MPL does not just result in an enlargement of existing GDL invasion sites but also in the creation of new macropores. Whereas the latter may be of small diameter at first, they can represent capillary barriers which are too high for liquid water invasion into the GDL. In this case, the smaller macropores have to grow further upon proceeding MPL aging until their capillary resistance is low enough to eventually offer additional percolation paths into the GDL. In addition, the MPL macropores have a dominant but not exclusive impact on the liquid water transport (see also Section 5.7.4), as the fluid has to percolate through an effective GDL/MPL cross-sectional area. Therefore, a larger or new MPL macropore opening does not necessarily infer new invasion paths into the GDL if not adjacent to the pore space of the neighboring GDL surface layer. In summary, the observed degradation trend with regions of low and high sensitivity on the MPL macroporosity eventually supports the conjecture from Section 5.2.2 that the parametric uncertainty for the estimate $\epsilon_{\mathrm{MPL}}^{\mathrm{macro}} = 19.97\,\%$ of the pristine MPL's macroporosity is no relevant impact factor in the underlying investigations. Beyond that, above degradation characteristic is also interesting with respect to health monitoring in long-term fuel cell operation: For a longer initial period, MPL degradation may occur without any observable impact on the cell performance and would thus remain unnoticed. After certain time of operation and aging, however, a strong degradation behavior could then occur suddenly and without prior announcement.

Occupying pore space, liquid water accumulation evidently has repercussions on the gas transport within the GDL. In order to investigate how MPL aging impacts the gas transport at breakthrough, effective gas tortuosities and permeabilities are therefore derived for the partially saturated GDL microstructure reconstructions at proceeding stages of MPL degradation and as described in Section 5.5. As evident from Figure 5.21, the effective gas transport at breakthrough is deteriorated upon progressing MPL aging due to the increasing saturation (Figure 5.20a) and thus pore blockage in the GDL. For the pristine MPL ($\epsilon_{\mathrm{MPL}}^{\mathrm{macro}} = 19.97\,\%$), the effective gas tortuosity is with $\tau_g^{\mathrm{wet}} = 1.72$ still very similar to $\tau_g^{\mathrm{dry}} = 1.58$ of the dry GDL. This indicates that the liquid water transport occurs primarily along the GDL thickness with only minor in-plane distribution (see Section 5.7.3), a characteristic of Freudenberg GDLs which has been also reported by Zhang et al. [275]. With advancing MPL degradation, the effective tortuosity is then observed to increase nonlinearly. For this dependence on the MPL macroporosity, a fit function is derived with

$$\tau_g^{\mathrm{wet}} = \tau_g^{\mathrm{dry}} \cdot 0.5 \left[1 + \frac{1}{1 - \epsilon_{\mathrm{MPL}}^{\mathrm{macro}}}\right]^{0.93} \tag{5.32}$$

by nonlinear regression using only one fit parameter and the tortuosity τ_g^{dry} of the dry GDL. The effective permeability on the other hand is already for the pristine MPL with $\kappa_g^{\mathrm{wet}} = 3.06\mathrm{e}^{-12}\,\mathrm{m}^2$ significantly different to $\kappa_g^{\mathrm{dry}} = 4.06\mathrm{e}^{-12}\,\mathrm{m}^2$ of the dry GDL. Along proceeding MPL aging, the permeability is then found to further decline in linear fashion. By nonlinear regression, a fit function is determined which describes this linear dependence on $\epsilon_{\mathrm{MPL}}^{\mathrm{macro}}$ with

$$\kappa_g^{\mathrm{wet}} = \kappa_g^{\mathrm{dry}} \cdot [1 - 1.05\epsilon_{\mathrm{MPL}}^{\mathrm{macro}}] \tag{5.33}$$

using only one fit parameter and the permeability κ_g^{dry} of the dry GDL. When the MPL is completely degraded with $\epsilon_{\mathrm{MPL}}^{\mathrm{macro}} = 100\,\%$, the MPL monolayer at the GDL inlet side is entirely flooded with liquid water (see $S^{\mathrm{BT}} \to 100\,\%$ for $Z = 0\,\mu\mathrm{m}$ in Figure 5.19c). As a result, there is no more through-path for the gas transport along the GDL thickness as indicated by $\tau_g^{\mathrm{dry}} = \infty$ and $\kappa_g^{\mathrm{dry}} = 0$ (beyond the scale of the graphs in Figure 5.21). This transport limitation is as well recovered by above fit functions.

Whereas above analysis already illustrates the distorting impact of MPL aging on the effective gas transport in the GDL, the MPL macroporosity $\epsilon_{\mathrm{MPL}}^{\mathrm{macro}}$ might be in general cumbersome to assess in experimental works. The same applies to the tortuosity, which is typically derived from diffusivity measurements and $\tau = \epsilon/D^*$ (compare eq. (5.13)). In addition, the relation between the GDL gas transport and the MPL macroporosity is only indirect, as the pore blockage due to liquid water accumulation is eventually responsible for the deterioration of the effective transport properties. Therefore, it is

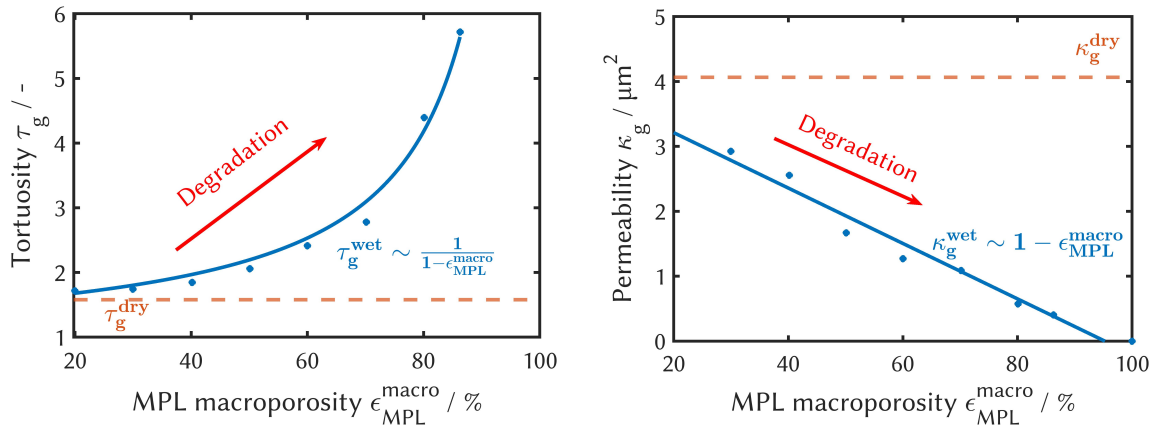

(a) Tortuosity. (b) Permeability.

Figure 5.21: Effective gas transport properties for the partially saturated impregnated H14 GDL/MPL at breakthrough and varying stages of MPL aging by increase in macroporosity. In these aging studies, the GDL is assumed to remain in the pristine state with a PTFE surface coverage of $\chi = 42.83\,\%$ (Figure 5.1b).

commonly more convenient to investigate the dependence of the relative effective diffusivity $D_g^{rel} = D_g^{wet}/D_g^{dry} = g_D(S)$ and relative effective permeability $\kappa_g^{rel} = \kappa_g^{wet}/\kappa_g^{dry} = g_\kappa(S)$ as functions of the GDL saturation (see also Section 5.5). For the saturation dependence of the relative effective diffusivity, numerous works report a power law relation $D_g^{rel} = (1-S)^{n_D}$ with a fitted exponent parameter n_D mostly ranging from 2 to 5 [69, 113, 419, 425, 427, 428, 432–434]. In this second degradation study, however, a different saturation dependence of the diffusive transport is observed, as shown in Figure 5.22a. Whereas the relative effective diffusivity remains comparably high ($n_D \approx 2$) for $S^{BT} < 20\,\%$, it increasingly declines towards higher breakthrough saturations. Nonetheless, the observed trend can be still described by a power law relation with

$$D_g^{rel} = \left(1 - 3.74 \cdot S^{BT}\right)^{0.45} \tag{5.34}$$

albeit with an exponent of $n_D = 0.45$ lower than typically reported values. This observation of a different saturation dependence for the diffusivity can be related to the fact that the GDL saturation is in this degradation study a function of the varying MPL macroporosity (see also eq. (5.26)). In related studies, on the other hand, saturation relations of the form $g(S) = (1-S)^n$ are usually derived for the same invariant GDL microstructure by variation of, e.g., the capillary pressure during liquid water injection. In this work, however, variations in the GDL saturation result from microstructural changes (here: ϵ_{MPL}^{macro}). Controlling the liquid water invasion sites, the MPL delays flooding of the liquid inlet site and thereby supports in sustaining gas transport paths through the

thickness of the GDL up to higher saturations. For proceeding aging of the MPL, however, the number of macropores/invasion sites will grow and single liquid water percolation paths through the GDL will begin to merge, resulting in increasing pore blockage and thus decrease in the effective diffusivity. A comparable characteristic is also reported by Hwang and Weber [427] for different Toray TGP-H-120 and SGL10 series GDLs, however, only for PTFE-treated samples. In their work, the authors relate their observations to different saturation profiles within the GDLs due to the heterogeneous distribution of the hydrophobic additive. Thereby, hydrophilic through-plane percolation paths would be invaded first, whereas additive-rich regions could remain accessible to gas transport up to a certain higher average global saturation. In a similar work, García-Salaberri et al. [419] come to the broader conclusion that the effective diffusivity in partially saturated GDLs is in general not just dependent on the average saturation but its local distribution as well. According to the authors, this circumstance is given by the fact that high local saturations can act as a bottleneck for the global effective gas transport. As apparent from Figure 5.22b, pore blockage by liquid water affects the relative permeability as well. By curve-fitting, an almost linear saturation dependence is determined to

$$\kappa_g^{\mathrm{rel}} = \left(1 - 3.64 \cdot S^{\mathrm{BT}}\right)^{0.82}, \tag{5.35}$$

which is thus significantly different to the power law relations $\kappa_g^{\mathrm{rel}} = (1-S)^{n_\kappa}$ widely reported with $n_\kappa > 1$ [20, 101, 106, 107, 113, 430, 431]. As for the relative effective diffusivity, this finding can be again related to the circumstance that the GDL saturation varies due to microstructural changes, i.e., $S^{\mathrm{BT}} = f\left(\epsilon_{\mathrm{MPL}}^{\mathrm{macro}}\right)$ (see also eq. (5.26)). In summary, both D_g^{rel} and κ_g^{rel} provide yet again clear indicators for the deteriorating effect of pore blockage by liquid water on the effective gas transport in the GDL. Furthermore, with respect to the underlying MPL aging study it is again emphasized that for a completely degraded MPL both the diffusive ($D_g^{\mathrm{rel}} \to 0$) and convective gas transport ($\kappa_g^{\mathrm{rel}} \to 0$) are found to be entirely inhibited in the partially saturated GDL. Eventually, these results clearly illustrate the beneficial impact of the MPL on the water management and in turn the effective gas transport in the GDL.

5.7.5 Effect of GDL aging on the breakthrough characteristics for a partially degraded MPL

In a third and final degradation study, GDL aging is investigated again and similar to the first degradation study in Section 5.7.3 (11 stages of proceeding PTFE loss, see also Table 5.2) but for a partially degraded MPL with a macroporosity of $\epsilon_{\mathrm{MPL}}^{\mathrm{macro}} = 59.99\,\%$ (Figure 5.9b). Whereas for a pristine MPL, loss of PTFE did not lead to any distinct

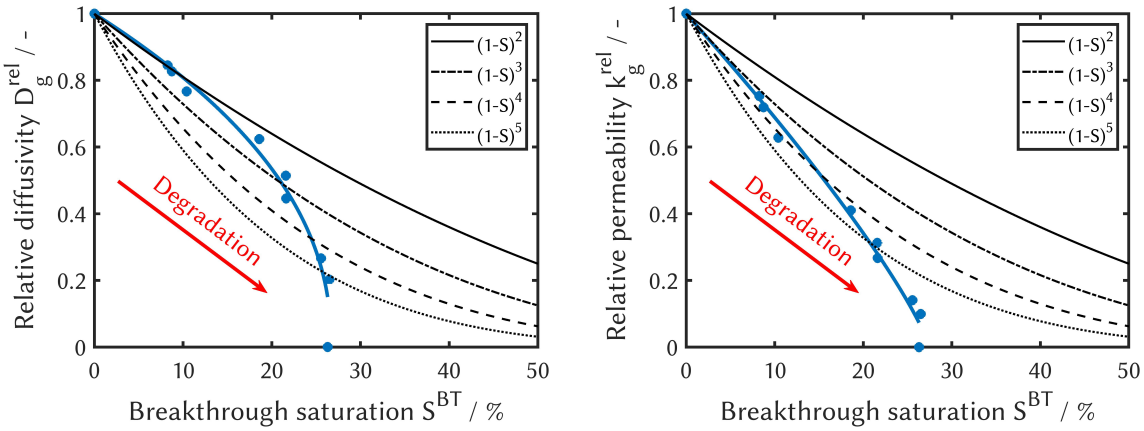

(a) Diffusivity. (b) Permeability.

Figure 5.22: Relative effective gas transport properties in the partially saturated impregnated H14 GDL/MPL at breakthrough for varying stages of MPL aging by increase in macroporosity. In these aging studies, the GDL is assumed to remain in the pristine state with a PTFE surface coverage of $\chi = 42.83\,\%$ (Figure 5.1b).

alteration in the liquid water transport (see Section 5.7.3), GDL aging is now observed to have a significant impact on the invasion patterns up to breakthrough. As illustrated by Figure 5.23, loss of hydrophobic additive now evidently leads to a broader liquid invasion front into the GDL, indicating the expected promoting effect on the overall accumulation of liquid water. Apparently, the impact of GDL degradation is enhanced by partial aging of the MPL, suggesting for the latter a diminishing capillary dominance on the liquid water transport (see also Section 5.7.3) by offering progressively more and larger invasion sites to the GDL. A more detailed analysis of the saturation profiles in Figure 5.24 furthermore reveals that the increase of liquid water accumulation is locally different, which might be related to the heterogeneous distribution of the hydrophobic additive PTFE.

On average, however, local liquid water accumulation is enhanced by a decreasing PTFE surface coverage and the overall breakthrough saturation S^{BT} increases from 21.57 to 29.80 % (Figure 5.25a). By curve-fitting, the breakthrough saturation is determined to exhibit a reciprocal dependence with

$$S^{\mathrm{BT}} = 0.18 \left[1 + \frac{0.12}{\chi + 0.18} \right] \tag{5.36}$$

on the PTFE surface coverage χ. Analogous to the studies on MPL aging (Figure 5.20), the time to breakthrough is again observed to follow a very similar degradation trend. As a result, the same type of fit function is derived with

$$t^{\mathrm{BT}} = 2.26\mathrm{e}^5 \left[1 + \frac{0.2}{\chi + 0.21} \right] \tag{5.37}$$

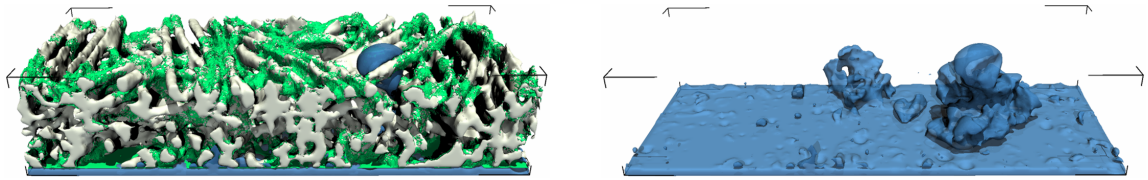

(a) Pristine ($\chi = 42.83\,\%$).

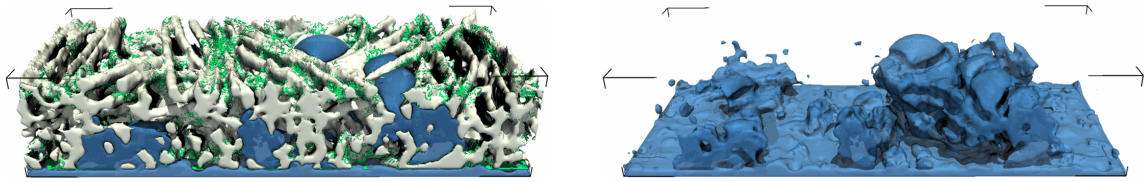

(b) Partially degraded ($\chi = 24.52\,\%$).

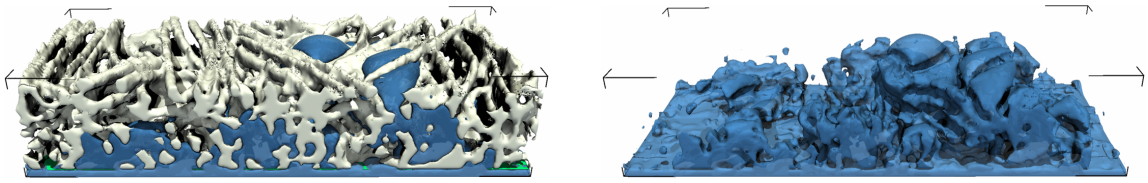

(c) Completely degraded ($\chi = 0.00\,\%$).

Figure 5.23: Liquid water distribution in the microstructure reconstruction of the impregnated H14 GDL/MPL at breakthrough for varying stages of GDL aging by loss of hydrophobic additive. The degradation results in a reduction of the PTFE surface coverage χ. In these aging studies, the MPL is assumed to be partially degraded with a macroporosity of $\epsilon_{\text{macro}}^{\text{MPL}} = 59.99\,\%$(Figure 5.9).

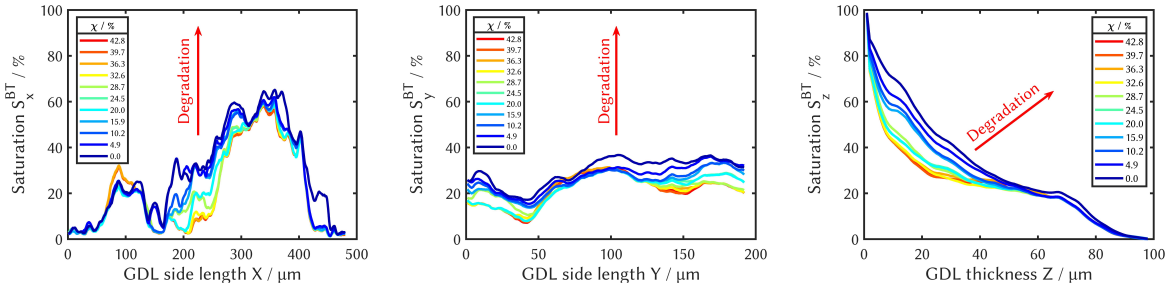

(a) In-plane X. (b) In-plane Y. (c) Through-plane Z.

Figure 5.24: Breakthrough saturation profiles for the impregnated H14 GDL/MPL at varying stages of GDL aging by loss of hydrophobic additive. The degradation results in a reduction of the PTFE surface coverage χ. In these aging studies, the MPL is assumed to be partially degraded with a macroporosity of $\epsilon_{\text{macro}}^{\text{MPL}} = 59.99\,\%$ (Figure 5.9).

by nonlinear regression and three fit parameters. With $C_t = 4.22\text{e}^{-7}\,\text{s}$ (see Table 5.1), the physical time $t^{\text{BT,phys}}$ to breakthrough can be furthermore denoted as

$$t^{\text{BT,phys}} = C_t \cdot t^{\text{BT}} = 0.095\,\text{s}\left[1 + \frac{0.2}{\chi + 0.21}\right] \tag{5.38}$$

and similar to eq. (5.25) the current density-dependent breakthrough time can then be estimated to

$$t^{\mathrm{BT,phys}}(i) = \left(\frac{i_{\mathrm{ref}}}{i}\right) t^{\mathrm{BT,phys}}(i_{\mathrm{ref}}) \tag{5.39}$$

$$= \left(\frac{118.5\,\mathrm{A/cm^2}}{i}\right) 0.095\,\mathrm{s}\left[1 + \frac{0.2}{\chi + 0.21}\right] \tag{5.40}$$

$$= \left(\frac{\mathrm{A/cm^2}}{i}\right) 11.3\,\mathrm{s}\left[1 + \frac{0.2}{\chi + 0.21}\right]. \tag{5.41}$$

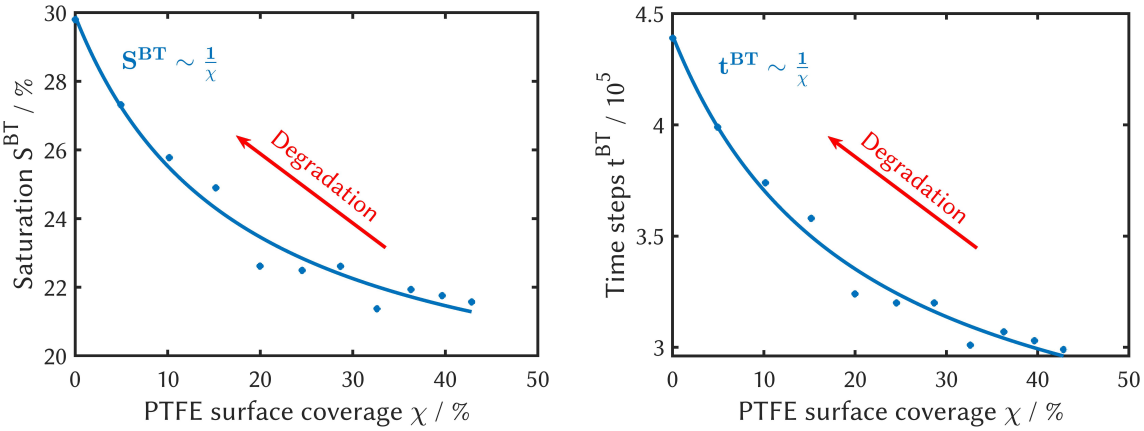

(a) Breakthrough saturation.

(b) Time to breakthrough.

Figure 5.25: Breakthrough characteristics for the impregnated H14 GDL/MPL at varying stages of GDL aging by loss of hydrophobic additive. The degradation is embodied in a reduction of the PTFE surface coverage χ. In these aging studies, the MPL is assumed to be partially degraded with a macroporosity of $\epsilon_{\mathrm{macro}}^{\mathrm{MPL}} = 59.99\,\%$ (Figure 5.9).

Above relations for S^{BT} and t^{BT} are amongst others in line with the LB simulations of Wang et al. [346], who derived similar breakthrough characteristics, albeit for the dependence on the overall PTFE loading. In addition, the trend of the breakthrough saturation is also in general qualitative agreement with the Monte Carlo simulations by Seidenberger et al. [393], even though the latter investigated liquid water distributions for higher PTFE surface coverages. A comparison of above findings with the breakthrough characteristics in Section 5.7.3 furthermore confirms that the dominant role of the MPL on the capillary transport has indeed lessened upon its partial degradation. Consequently, aging of the GDL now has a notable effect on the liquid water distribution and thereby on the effective gas transport at breakthrough as well.

Figure 5.26a shows that due to the pore blockage by liquid water, the effective gas tortuosity of the partially saturated pristine GDL is with $\tau_g^{\mathrm{wet}} = 2.41$ by more than a factor of 1.5 higher than $\tau_g^{\mathrm{dry}} = 1.58$ of the dry state. For progressive stages of aging,

the tortuosity then further increases in nonlinear fashion along with the breakthrough saturation (Figure 5.25a). By curve fitting, this degradation effect is identified to follow a reciprocal dependence

$$\tau_g^{\mathrm{wet}} = 2.12 \left[1 + \frac{0.06}{\chi + 0.09}\right] \tag{5.42}$$

on the PTFE surface coverage χ, which is thus similar to the relation for the breakthrough saturation (*cf.* eq. (5.36) and Figure 5.25a). With above nonlinear dependence, the tortuosity then eventually increases along progressive GDL aging up to $\tau_g^{\mathrm{wet}} = 3.43$ for the completely degraded GDL, which is by more than a factor of 2.2 higher as compared to $\tau_g^{\mathrm{dry}} = 1.51$. For the dry GDL, a reverse degradation trend is furthermore identified as a slight tortuosity decline

$$\tau_g^{\mathrm{dry}} = \tau_g^{\mathrm{dry,0}} \frac{1}{\sqrt{1 - 0.21\chi}} \tag{5.43}$$

in reciprocal square root-dependence on the additive surface coverage. In above equation, $\tau_g^{\mathrm{dry,0}} = 1.51$ refers to the tortuosity of the dry impregnated GDL in the completely degraded state or equivalently the untreated fiber substrate. Whereas wettability alterations are irrelevant to the effective gas transport in the dry GDL, this effect can be related to the porosity increase as a secondary aging effect from the erosion of the hydrophobic additive (see also Figure 5.7b). For the dependence of the porosity on the additive surface coverage, a linear relation is identified with

$$\epsilon_{\mathrm{GDL}} = \epsilon_{\mathrm{GDL}}^0 \left(1 - 0.15\chi\right) \tag{5.44}$$

and the porosity $\epsilon_{\mathrm{GDL}}^0 = 68.41\,\%$ of the completely degraded/untreated GDL. Combining equations (5.43) and (5.44) then yields

$$\tau_g^{\mathrm{dry}} = \tau_g^{\mathrm{dry,0}} \frac{1}{\sqrt{1.4\left(\epsilon_{\mathrm{GDL}}/\epsilon_{\mathrm{GDL}}^0 - 0.29\right)}} \tag{5.45}$$

for the tortuosity of the dry GDL as a function of its porosity. Above dependence is similar to the well-known Bruggeman relation with $\tau^{\mathrm{Bruggeman}} = 1/\sqrt{\epsilon_{\mathrm{GDL}}}$. However, as evident from Figure 5.26a, the latter underestimates the tortuosity of the dry GDL, as has been also reported in several other related works [69, 316, 427]. This deviation may be amongst others explained by the circumstance that Bruggeman derived his relation for a granular isotropic system of spherical particles, whereas the GDL is in general an anisotropic fibrous porous medium.

The effective gas permeability is impaired from the pore blockage by liquid water as well and is observed to decrease by a factor of more than 3 from $\kappa_g^{\mathrm{dry}} = 4.06\mathrm{e}^{-12}\,\mathrm{m}^2$ to

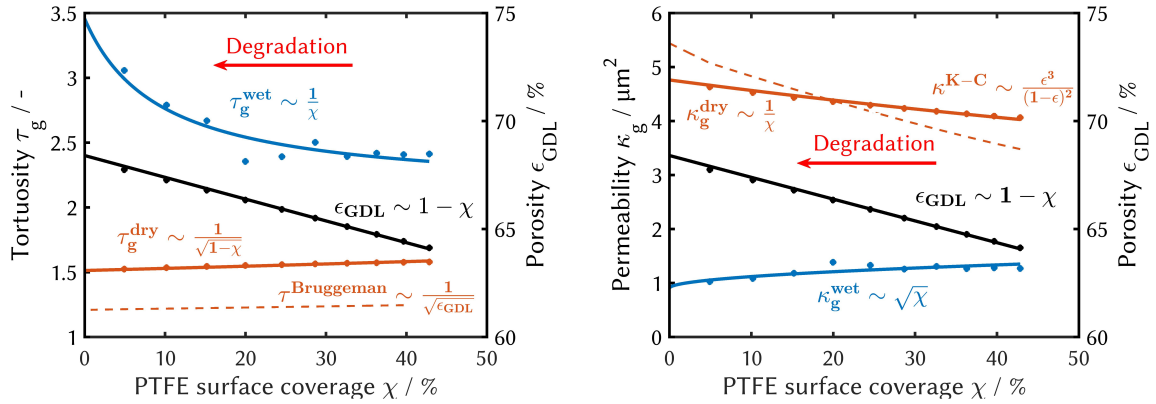

(a) Tortuosity. (b) Permeability.

Figure 5.26: Effective gas transport properties for the partially saturated impregnated H14 GDL/MPL at breakthrough and varying stages of GDL aging by loss of hydrophobic additive. The degradation is embodied in a reduction of the PTFE surface coverage χ. In these aging studies, the MPL is assumed to be partially degraded with a macroporosity of $\epsilon_{macro}^{MPL} = 59.99\,\%$ (Figure 5.9).

$\kappa_g^{wet} = 1.27e^{-12}\,m^2$ for the pristine GDL. For proceeding stages of aging, the effective gas permeability then declines further in square root-dependence

$$\kappa_g^{wet} = \left[1 + \sqrt{0.57\chi}\right] 0.9e^{-12}\,m^2 \tag{5.46}$$

on the PTFE surface coverage χ. For the completely degraded GDL, a minimum is eventually reached for $\kappa_g^{wet} = 8.65e^{-13}\,m^2$, which is by more than a factor of 5.5 lower than $\kappa_g^{dry} = 4.76e^{-12}\,m^2$ of the corresponding dry state. In the latter case, a reverse degradation effect is again observed with increasing effective gas permeabilities along proceeding PTFE erosion and with a reciprocal dependence

$$\kappa_g^{dry} = \kappa_g^{dry,0} \frac{1}{1 + 0.42\chi} \tag{5.47}$$

on the additive surface coverage. This trend can be again related to the secondary GDL degradation effect of an increasing porosity promoting the effective gas transport. For the description of the permeability in dependence of the porosity, the Kozeny-Carman relation (eq. (5.9)) is determined to

$$\kappa^{Kozeny-Carman} = \frac{d_f^2}{16 k_K} \frac{\epsilon_{GDL}^3}{(1-\epsilon_{GDL})^2} = 1.7e^{-12}\,m^2 \frac{\epsilon_{GDL}^3}{(1-\epsilon_{GDL})^2} \tag{5.48}$$

assuming an average fiber diameter of $d_f = 10\,\mu m$ [51]. The Kozeny constant is fitted to $k_K \approx 3.68$, which is not far from the value of $k_K = 6$ suggested by Nam and Kaviany [425], in particular considering that GDL permeabilities can range from 10^{-13} to $10^{-10}\,m^2$.

However, as apparent from Figure 5.27b, the fitted Kozeny-Carman relation is eventually incapable of providing a qualitative description of the observed permeability trend. As for the Bruggeman relation, this observation may be again explained by the fact that the GDL is an anisotropic fibrous porous medium and not an isotropic granular system.

With the above-presented effective tortuosities and permeabilities for the dry and partially saturated GDL, the relative effective gas transport properties are then obtained as shown in Figure 5.27. For the relative effective diffusivity, the saturation dependence is determined to follow a linear relation with

$$D_g^{\mathrm{rel}} = 1 - 2.18 \cdot S^{\mathrm{BT}} \tag{5.49}$$

and is hence different from the commonly reported power law relation $D_g^{\mathrm{rel}} = (1 - S)^{n_D}$ with $n_D = 2$ to 5 [69, 113, 419, 425, 427, 428, 432–434]. As for the MPL degradation study in Section 5.7.4, this observation of a different relation can be again related to the fact that the saturation is in this work a function of microstructural alterations (here: a changing PTFE surface coverage, see also eq. (5.36)). Figure 5.27a illustrates that already for the pristine GDL, the effective diffusivity is with $D_g^{\mathrm{rel}} = 0.51$ almost halved due to the pore blockage by liquid water. Along proceeding GDL aging, this deterioration of the diffusive gas transport is further amplified until for the completely degraded GDL D_g^{rel} has decreased by two thirds down to 0.34. The convective gas transport, on the other hand, appears to be even more sensitive to liquid water accumulation within the GDL. As apparent from Figure 5.27a, the relative effective gas permeability drops in the presence of liquid water down to as low as $\kappa_g^{\mathrm{rel}} = 0.31$ already for the pristine GDL. With progressing PTFE loss, the permeability is then reduced further with a power law dependence of

$$\kappa_g^{\mathrm{rel}} = \left(1 - S^{\mathrm{BT}}\right)^{4.5} \tag{5.50}$$

on the breakthrough saturation. For the completely degraded GDL, a minimum of $\kappa_g^{\mathrm{rel}} = 0.21$ is eventually reached, indicating that pore blockage by liquid water has decreased the effective gas permeability down to one fifth of κ_g^{dry}. Analogous to D_g^{rel}, above saturation dependence for the relative permeability appears to follow again a power law relation, whose exponent is with 4.5 well in the wide range of $n_\kappa = 2$ to 8 reported in literature [20, 101, 113, 430, 431]. At this point, however, it is recalled that a direct comparison of equation (5.50) with commonly reported relations from literature is in general difficult, as the saturation changes as a function of the PTFE surface coverage (see $S^{\mathrm{BT}} = f(\chi)$ in eq. (5.36)).

Lastly, it is worth noting that loss of PTFE (Figure 5.27) is observed to have a significantly different and less pronounced impact on the effective gas transport in the

GDL at breakthrough as compared to aging of the MPL (Figure 5.22). On the one hand, this circumstance may be partly related to the parametric uncertainty in the similar choices for the carbon fiber ($\theta_{\mathrm{CF}} = 90°$) and PTFE ($\theta_{\mathrm{CF}} = 115°$) contact angles (see also Section 5.7.1), potentially underestimating mixed wettability. On the other hand, however, full inhibition of the effective gas transport in the partially saturated and aged GDL was eventually only observed, when the MPL was completely degraded. This strongly suggests that, even when partly degraded with $\epsilon_{\mathrm{MPL}}^{\mathrm{macro}} = 59.99\,\%$, the MPL retains major influence on the capillary transport in the GDL and thereby potentially superposes effects of GDL aging on the liquid water and effective gas transport at breakthrough.

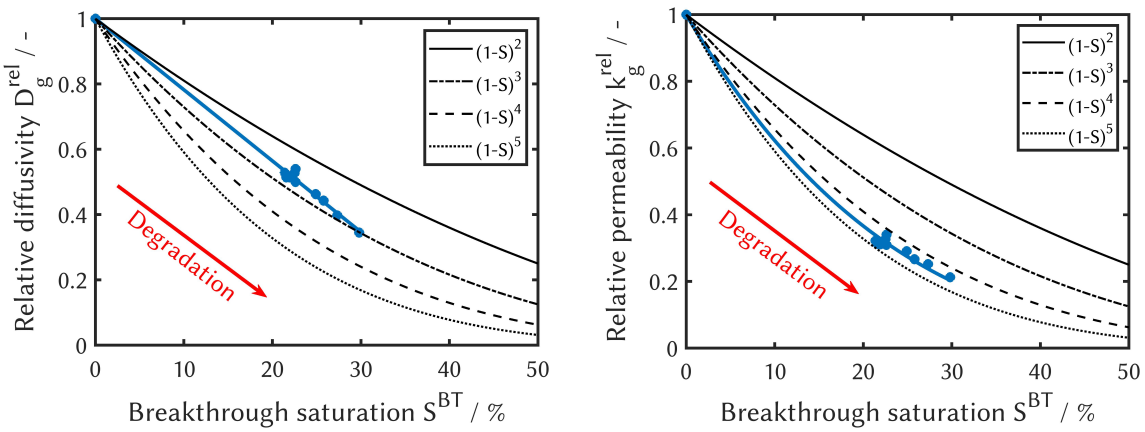

(a) Diffusivity.

(b) Permeability.

Figure 5.27: Relative effective gas transport properties for the partially saturated impregnated H14 GDL/MPL at breakthrough and varying stages of GDL aging by loss of hydrophobic additive. The degradation is embodied in a reduction of the PTFE surface coverage χ. In these aging studies, the MPL is assumed to be partially degraded with a macroporosity of $\epsilon_{\mathrm{macro}}^{\mathrm{MPL}} = 59.99\,\%$ (Figure 5.9).

5.8 Conclusion

In this chapter, the impact of microstructure degradation on the capillary transport was investigated by Lattice Boltzmann simulation of liquid water invasion into reconstructions of a PTFE-impregnated and MPL-coated Freudenberg H14 GDL at different stages of aging. Corresponding to boundary conditions of real fuel cell operation, the partially degraded GDL microstructures were therefore virtually compressed by approximately 22 %, mimicking common cell assembly clamping pressures. Furthermore, a MPL was considered as well by segmentation of a representative layer within the high resolution µCT image stack of a PTFE-impregnated and MPL-coated Freudenberg H14. Owing to the limited resolution of the µCT scanning device, however, the reconstruction of the

MPL was restricted to its macropores. Subsequent to generation, the microstructure reconstructions of the MPL and GDL were merged. While the penetration depth of the MPL into the GDL surface is in general inhomogeneous, the commonly observed region of continuous transition from GDL to MPL was simplified by replacement of one GDL surface region with the representative MPL macropore reconstruction. Since consideration of transport phenomena is obviated by a thickness of only one layer, the single slices of MPL macropore reconstructions were therefore utilized as internal boundary for the subsequent simulation of liquid water invasion into the GDL. Mimicking *operando* conditions, a computational setup was furthermore created, in which the GDL/MPL domain was sandwiched between a liquid and gas phase buffer zone representative for the catalyst layer (CL) and gas channel (GC), respectively. With this setup, liquid water invasion was then simulated with a constant liquid inlet velocity corresponding to stationary fuel cell operation while the gas pressure was set to be constant. The simulations were stopped when the liquid water reached the opposite GDL surface towards the gas channel (i.e., at breakthrough) and the resulting invasion patterns were analyzed with respect to local and overall saturation and the time to breakthrough. In order to investigate the impact of liquid water accumulation on the effective gas transport, effective gas diffusivities and permeabilities were furthermore determined for the partially saturated and degraded GDL/MPL microstructures. For the degradation studies, partially degraded GDL and MPL reconstructions were furthermore generated by purely virtual alteration of the underlying microstructural data. In order to account for structural aging effects in the GDL, loss of PTFE was assumed as the primary degradation route. Defining the GDL microstructure reconstruction from Figure 4.12 as the pristine state, proceeding stages of aging were then generated by voxel-wise removal of hydrophobic additive. Employing an in-house degradation routine, this incremental and artificial PTFE elimination was carried out in a realistic fashion as a stochastic process based on the local abundance of additive. Following this approach, GDL microstructure reconstructions were obtained for 11 stages of proceeding aging with PTFE surface coverages ranging from $\chi = 42.83$ to 0 %. While the removal of hydrophobic additive evidently affects the surface wettability of the carbon fibers, an increase in the GDL porosity was identified as a secondary structural degradation effect due to additive erosion. Assuming an increase in macroporosity as the main degradation path, aging of the MPL was considered as well by repeated segmentation of the representative µCT image layer, targeting for increasingly higher macroporosities. In this way, 9 different reconstructions of a single MPL macropore slice were obtained with macroporosities ranging from $\epsilon_{\mathrm{MPL}}^{\mathrm{maro}} = 19.99$ to 100 %. Combining varying stages of GDL and MPL aging, liquid water invasion into the degraded microstructure reconstruction was then simulated up to breakthrough, where the effective gas transport in the partially

saturated GDL was then analyzed. Based on the results of the simulative degradation studies in this chapter, the following main conclusions were drawn:

- A first breakthrough simulation for the pristine GDL/MPL showed for a carbon fiber contact angle as low as $\theta_{\mathrm{CF}} = 65°$ a broad liquid phase invasion front. This observation was contrary to expectations, since capillary transport of liquid water in the GDL is commonly assumed to occur primarily along single percolation paths of lowest capillary resistance, a flow regime commonly referred to as capillary fingering. As demonstrated in a second simulation, such a flow regime can be obtained for a significantly higher carbon fiber contact angle of $\theta_{\mathrm{CF}} = 90°$. Whereas this drastic change in the carbon fiber wettability can be justified by the large parametric uncertainty from a vast range of reported contact angles, a contradiction remains to the simulated capillary hysteresis in Section 4.4.7 providing for $\theta_{\mathrm{CF}} = 65°$ the best agreement with experimental data. While remaining unresolved, this discrepancy may be explained with unknown measurement artifacts at the $p_c - S$ test bench (see also Section 4.4.9) or to a variable carbon fiber wettability due to surface contamination under air exposure. Based on the observed flow regimes, a carbon fiber contact angle of $\theta_{\mathrm{CF}} = 90°$ was assumed to provide a more realistic liquid water invasion behavior for the subsequent degradation studies and was thus eventually set as default.

- With typically low water production rates in fuel cell operation, occurrence of breakthrough can take up to several minutes. Due to the small time step sizes common to PSM methods such as LBM, on the other hand, computational expense for reaching the aforementioned time scales may rise beyond accessibility. However, in order to simulate *operando* liquid water transport through the GDL, utilization of realistically low liquid velocities is not strictly necessary as long as dominance of capillary forces is ensured. In a sensitivity study, a liquid flow velocity of as high as $u_l = 1.14e^{-4}\,\mathrm{m/s}$ was determined to still provide liquid water invasion patterns in the capillary-dominated regime and thus, similar to actual cell operation. For the subsequent simulative degradation studies, this velocity served as an upper threshold for a flow regime dominated by capillary forces, below which capillary transport is invariant to the flow velocity. Consequently, *operando* capillary flow characteristics can be recovered by liquid water invasion simulations using significantly higher flow velocities. This resulted in a massive reduction of computational expense by at least an order of magnitude, while the simulation results retained transferability to real fuel cell operation.

- When the MPL was pristine, loss of PTFE did not lead to any noticeable GDL aging effect on the liquid water transport at breakthrough. These findings were related

to a dominating influence of the MPL on the capillary transport, as liquid water entry sites to the GDL were strongly restricted by the MPL macropores ($\epsilon_{\mathrm{MPL}}^{\mathrm{maro}} = 19.99\,\%$).Therefore, the overall impact of the hydrophobic additive on the liquid water transport was delimited to a few percolation paths which are apparently not significantly affected by the loss of PTFE. Eventually, the strong impact of the pristine MPL on the capillary transport superposed any detectable GDL degradation effect.

- Aging of the MPL had a significant impact on the liquid water transport at breakthrough, since an increasing macroporosity lead to larger and new MPL macropores promoting further liquid invasion into the GDL. As a result, both local and overall breakthrough saturation were observed to increase upon MPL aging. Whereas this degradation effect was at first only minor, a steep intermediate gradient in the breakthrough saturation was then observable for MPL macroporosities around $40\,\% < \epsilon_{\mathrm{MPL}}^{\mathrm{macro}} < 50\,\%$ before the saturation increase weakened again for even higher macroporosities. This aging characteristic is very interesting with respect to health monitoring in long-term PEM fuel cell operation, as component degradation could first proceed unnoticed until after a certain time of operation a significant aging effect and consequently performance loss would occur without prior warning. Due to the increasing pore blockage by liquid water accumulation, the effective gas transport in the partially saturated GDL was progressively disturbed, as indicated by a nonlinear tortuosity increase and a linear permeability decrease along with crescent MPL macroporosities. When the MPL was completely degraded ($\epsilon_{\mathrm{MPL}}^{\mathrm{macro}} = 100\,\%$), the gas transport was eventually completely inhibited. By normalization with the respective gas transport property of the dry GDL, relative diffusivities and permeabilities were furthermore derived and their saturation dependence was identified to follow a power law relation with $g\,(S) \sim (1 - S)^n$. While the general form for the saturation dependence was as expected, the exponents for the relative diffusivity ($n_D = 0.45$) and permeability ($n_\kappa = 0.82$) were determined to be significantly lower as compared to commonly reported values of $n_i > 1$ [20, 69, 101, 113, 113, 419, 425, 427, 428, 430–434]. This finding was related to the circumstance that the saturation dependence $g\,(S)$ of relative effective gas transport properties is in this work a result of microstructural alterations, whereas it is elsewhere typically determined for an invariant GDL microstructure by imposition of variable capillary pressures.

- When the MPL was partially degraded ($\epsilon_{\mathrm{MPL}}^{\mathrm{macro}} = 59.99\,\%$), aging effects of the GDL on the liquid water transport became perceivable. As the former dominance of the MPL on the capillary transport faded, loss of PTFE lead to a notable nonlinear increase in the breakthrough saturations due to a decreasing hydrophobicity of the carbon fiber

surfaces. Consequently, the effective gas transport in the partially saturated GDL was progressively distorted with decreasing PTFE surface coverage, resulting in a nonlinear tortuosity increase and a slight nonlinear permeability decrease. Whereas already halved for the pristine GDL, the relative diffusivity and permeability were evidently further decreasing along with degradation due to increasing pore blockage by liquid water. This saturation dependence was determined to follow the expected power law relation with $g(S) = (1 - S)^n$. As opposed to the previous MPL degradation study, the exponents for the relative diffusivity ($n_D = 2.7$) and relative permeability ($n_\kappa = 4.5$) were furthermore well in the wide range of reported values with $n_D = 2-5$ [69, 113, 419, 425, 427, 428, 432–434] and $n_\kappa = 2 - 8$ [20, 101, 113, 430, 431]. At this point, however, it is reminded again that a direct comparison of the derived new saturation dependencies with relations from literature is difficult, as the latter usually do not consider microstructural alterations. For the porosity dependence of the effective gas transport properties in the dry GDL, the most widely used Bruggeman relation for the diffusivity and the Kozeny-Carman relation for the permeability were lastly both identified to be incapable of providing appropriate predictions.

6 Summary and Outlook

6.1 Summary

In this work, liquid water transport through carbon felt GDLs was thoroughly studied using 3D multiphase pore-scale simulations and real microstructural tomographic data.

For the simulation of capillary fluid flow in porous media, a 3D multiphase Color-Gradient Lattice Boltzmann model was therefore introduced in Chapter 3. Furthermore, in order to ensure an adequate description of fluid-fluid and fluid-solid interactions, the model was validated against analytical references of three numerical test cases (see Jurin's law, Washburn's law and the capillary valve effect in Section 3.2.5).

In Chapter 4, this model was then employed to study capillary transport characteristics of GDLs under variation of different model and simulation parameters. For this, GDL microstructures of plain and PTFE-impregnated carbon fiber substrates of a Freudenberg H14 were reconstructed by segmentation of µCT images with a high resolution of 0.96 µm per pixel. In order to reduce computational expense in the subsequent simulations, smaller GDL subvolumes were then selected from the microstructure reconstructions and their representativeness was ensured with respect to porosity profiles and pore size distributions. For the reconstruction of the PTFE-treated fiber substrate, an in-house routine was developed to distinguish PTFE from carbon fibers. Corresponding to experimental observations, this algorithm identified the additive component primarily near fiber intersections. Along the thickness of the GDL, the PTFE was furthermore localized according to a heterogeneous PTFE loading profile as it was derived from µCT image data. Aiming to validate the simulated capillary characteristics of the GDL to an experimental reference, a computational setup was then generated, mimicking the boundary conditions of a test bench for the measurement of capillary pressure-saturation ($p_c - S$) curves. Corresponding to the test bench conditions, two semipermeable membranes were therefore explicitly modeled for the simulations. Subsequently, capillary intrusion of liquid water into initially dry GDL microstructure reconstruction was then simulated by control of the gas pressure according to the experimental test bench procedure. By reversal of this process, also capillary drainage was simulated in order to recover the full capillary hysteresis. In several simulation studies, the capillary transport characteristics of the GDLs were then

investigated for key influencing parameters. A comparison of two different approaches for the modeling of the semipermeable membranes showed that the highly porous surface regions of the GDL can have a major impact on the overall capillary hysteresis. As a result, the capillary characteristics of an experimental reference can only be recovered in simulations by appropriate accounting of the real boundary conditions. This conclusion summons again the often avoided debate on the transferability of *ex situ* (and also *in situ*) testing to *operando* conditions of actual cell operation. Furthermore, simulation of capillary hysteresis at two different resolutions of the GDL microstructures highlighted the importance of spatial discretization for microstructure-resolving methods such as LBM. Based on the results of this study, at least a resolution of less than 2 µm per pixel is therefore required to account for all relevant structural details in order to accurately recover capillary characteristics. Owing to a wide range of reported literature values, the carbon fiber contact angle introduced some parametric uncertainty to the wettability modeling in this work. Simulating capillary hysteresis for varying carbon fiber wettabilities, the best agreement with test bench data of the plain H14 fiber substrate was achieved for a contact angle of 65°. In order to account for mixed wettability in the PTFE-impregnated fiber substrate, the contact angle of PTFE was furthermore set to 115°. However, the experimental $p_c - S$ curves showed an unexpectedly wide capillary hysteresis which could not be recovered in the simulations, even under multiple variation of the additive distribution. Whereas parametric uncertainty in the modelling of mixed wettability cannot be completely excluded as a reason for the observed discrepancy, the experimental capillary intrusion curve exhibited features which have been elsewhere reported as a measurement artifact from improper sample contacting. Eventually, the Lattice Boltzmann model could be validated for the simulation of capillary characteristics in the plain fiber substrate but not the PTFE-impregnated variant of the H14 carbon felt GDL. Subsequent to the parametric studies and validation, novel $p_c - S$ relations were derived from the simulated capillary hystereses for the plain and impregnated fiber substrate. By nonlinear regression, fit functions were derived for the intrusion and drainage curve of each substrate variant, which described the saturation in inverse tangent relation to the capillary pressure. Whereas these newly derived $p_c - S$ provided accurate predictions over the entire saturation range, the widely-used Leverett relation was incapable of describing capillary characteristics in the low and high saturation region appropriately. As a consequence, the newly derived $p_c - S$ relations of this work can be readily employed in, e.g., cell-level simulation suites and can thereby help to improve the modeling accuracy of the GDL liquid water transport and eventually the PEMFC water management.

In Chapter 5, the impact of microstructural degradation on the liquid water transport in the GDL was investigated as it may occur in long-term PEM fuel cell operation. Corre-

sponding to the *operando* conditions of cell assembly, the microstructure reconstruction of the PTFE-impregnated fiber substrate was therefore virtually compressed according to typical clamping pressures. Corresponding to state-of-the-art diffusion layers, a MPL was reconstructed as well by segmentation of µCT images of a PTFE-impregnated and MPL-coated Freudenberg H14. However, delimited by the resolution of the µCT scanning technique, the reconstruction was restricted to the MPL macropores. Assuming that liquid water is primarily transported through the larger MPL openings, this macropore reconstruction was expected to be sufficient for further investigations. Subsequently, the reconstructions of the MPL and GDL were unified. Whereas the MPL is commonly observed to penetrate the GDL surface at variable depths, a simpler approach was chosen for this work in replacing one GDL surface region by the MPL macropore reconstruction. While one layer in thickness did not allow to recover capillary transport phenomena in the MPL itself, the single representative MPL macropore layer was employed to define an interface for liquid water invasion sites into the GDL. Similar to cell assembly, a computational setup was then generated by sandwiching the GDL/MPL domain between a liquid and a gas phase buffer zone, which represented the catalyst layer (CL) and the gas channel (GC), respectively. Mimicking steady state cell operation, liquid water invasion into the GDL was then simulated for a constant liquid inlet velocity at the CL and a constant phase gas pressure at the GC. At breakthrough (to the GC), the resulting liquid water distributions in the GDL were then analyzed by means of local and global saturation. In order to characterize the impact of pore blockage by liquid water on the gas transport, effective gas diffusivities and permeabilities were furthermore derived for the partially saturated GDL.

In a first simulation, the liquid water distribution at breakthrough exhibited a broad invasion front. This finding was against the common expectation of a capillary-dominated flow along single percolation paths according to the flow regime of capillary fingering. Whereas a second simulation could recover the expected capillary-dominated flow regime for a carbon fiber contact angle of 90°, the unexpected first simulation results were explained with an overestimation of the carbon fiber wettability for an initial contact angle of 65°. While a higher contact angle of 90° is still in the range of reported literature values, it contradicts the findings in Chapter 4, where a lower contact angle of 65° yielded the best agreement between simulated and measured capillary hysteresis curve. Even though remaining unresolved, this contradiction was partly related to limited reliability of the test bench data and temporary variable GDL properties, thereby justifying a higher carbon fiber contact angle of 90° for all subsequent simulations of Chapter 5. Owing to the low liquid water flow rates during ordinary PEMFC operation, breakthrough may take up to several minutes. For computationally expensive pore-scale methods such as LBM, this

time scale is typically beyond accessibility. However, the same liquid water breakthrough characteristics can be recovered by simulations at significantly higher velocities as long as a capillary-dominated flow regime is ensured. In this work, a maximum liquid water inlet velocity of $1.14e^{-4}$ m/s was determined to still yield a capillary-dominated flow regime as expected for actual fuel cell operation. This upper threshold velocity therefore enabled to reduce the computational expense by at least an order of magnitude while maintaining transferability to *operando* conditions. For the investigation of microstructual aging effects on the liquid water and effective gas transport, GDL and MPL reconstructions were furthermore virtually degraded assuming loss of PTFE and increase in macroporosity as the respective primary aging paths. Combining GDL and MPL microstructure reconstructions at different stages of aging, liquid water transport to breakthrough was then simulated and effective gas transport properties were determined in three degradation studies. For a pristine MPL, loss of PTFE was observed to have no notable impact on the liquid water transport in the degrading GDL. This finding was accredited to the dominant role of the MPL on the capillary transport in the GDL by controlling the liquid water invasion sites.

When the MPL was subject to degradation, distinct aging effects were detectable as increasing breakthrough saturations, owing to increasing sizes and numbers of macropores. Whereas in the beginning and at the end of the proceeding stages of MPL degradation this effect was rather minor, breakthrough saturations were observed to increase strongly in the intermediate macroporosity range between 40 % to 50 %. This characteristic was explained by the fact that new MPL macropores do not necessarily promote further liquid water invasion into the GDL when they are small and thus present high capillary barriers. As a result of increasing pore blockage by liquid water, the effective gas transport was observed to be progressively disturbed along proceeding MPL degradation. This was indicated by a nonlinear increase of the effective tortuosity and a linear decrease of the effective permeability in the partially saturated GDL towards higher MPL macroporosities. For a completely degraded MPL, the effective gas transport was observed to be completely inhibited. Relative effective gas transport properties were furthermore found to change in dependence of the breakthrough saturation according to the commonly assumed power law relation $g(S) = (1 - S)^n$. As opposed to most related works, however, the exponents for the relative diffusivity and permeability were determined to $n_D = 0.45$ and $n_\kappa = 0.82$, which were thus significantly lower than commonly reported values of $n_D = 2 - 5$ [69, 113, 419, 425, 427, 428, 432–434] and $n_\kappa = 2 - 8$ [20, 101, 113, 430, 431]. This finding of quite different saturation dependencies can be related to the fact that the relations of the form $g(S) = (1 - S)^n$ are in most studies determined for invariant GDL microstructures, whereas they are in this work a result of microstructural changes (here, the MPL macroporosity $\epsilon_{\mathrm{MPL}}^{\mathrm{macro}}$).

When the MPL was partially degraded, loss of PTFE from the GDL was then observed to result in significant aging effects on the liquid water transport, as indicated by nonlinear increases in the breakthrough saturation. In consequence, the effective gas transport was increasingly hampered, resulting in a nonlinear increase in the tortuosity and a nonlinear decrease of the permeability along with proceeding PTFE loss. The dependence of the relative effective diffusivity and permeability on the breakthrough saturation was again determined to follow the power law relation $g(S) = (1 - S)^n$ with exponents of $n_D = 2.7$ and $n_\kappa = 4.5$, which are thus well in the range of $n_D = 2{-}5$ [69, 113, 419, 425, 427, 428, 432–434] and $n_\kappa = 2 - 8$ [20, 101, 113, 430, 431] for commonly reported values. At this point, however, it is reminded that a direct comparison of the saturation dependencies from this work with relations in literature is rather difficult, as the latter are usually derived for invariant GDL microstructures. For the prediction of the effective diffusivity and permeability in the dry GDL, the well-known relations of Bruggeman and Kozeny-Carman were furthermore eventually found to be inappropriate.

Above findings on the simulative degradation studies of this chapter provide novel insights on the impact of microstructural degradation on the GDL liquid water transport. The presented results thereby support a deeper understanding of aging effects in PEM fuel cell water management. Investigating various combinations of partially degraded microstructures, breakthrough characteristics were furthermore studied for both GDL and MPL aging. Whereas hardly realizable in experiments, degradation effects of GDL and MPL were thus isolated. For the latter, a strong dominance on the capillary transport was observed in the pristine state, superposing any notable GDL aging effect. Along proceeding degradation, the dominant role of the MPL then faded with an intermediate strong increase in the breakthrough saturation and aging effects of the GDL then became visible. These findings present an interesting aspect and challenge for health monitoring in fuel cell operation, as degradation processes could remain undetected for a certain time until a sudden strong aging effect would occur. Eventually, an abrupt increase in the breakthrough saturation could then lead to an unexpected flooding and consequently failure of the fuel cell without prior notice. The changing role of the aging MPL in the capillary liquid water transport through the GDL furthermore illustrates the importance of isolating superposing degradation effects as a prerequisite for proper root cause analysis and targeted material development. The findings of these simulative degradation studies may therefore as well provide inspiration and motivation for the development of future experimental aging procedures. The derived degradation trends for the effective gas transport in the partially saturated and aged GDLs furthermore illustrated the repercussions of increasing pore blockage by liquid water accumulation, thereby highlighting the indirect impact of GDL water management on the eventual cell performance. In the end, the

presented relations for the breakthrough characteristics and the effective gas transport properties in dependence of the aging process in the GDL/MPL can be used in cell-level models and thereby foster future simulation studies on fuel cell degradation.

In summary, the comprehensive simulative studies of this work provide new insights into the capillary characteristics of GDLs, aging effects on the liquid water transport and the repercussions of pore blockage by liquid water on the effective gas transport in the GDL. The presented findings therefore contribute to a better understanding of capillary phenomena in general, the impact of aging on the GDL water management and how this may indirectly affect the cell performance. By this, the underlying thesis supports further material development for optimal water management and provides incentives for subsequent degradation studies in order to achieve the ultimate goal of stable and reliable long-term PEM fuel cell operation.

6.2 Outlook

This work provided interesting new insights on the water management in carbon felt GDLs for PEM fuel cell operation. Owing to the complexity of the underlying capillary multiphase transport phenomena, however, further research is necessary to improve both the understanding of underlying mechanisms and the predictive power of pore-scale simulation methods for the GDL liquid water transport.

In this work, the Lattice Boltzmann model was successfully validated for the simulation of capillary pressure-saturation characteristics in the plain fiber substrate of a Freudenberg H14 carbon felt GDL. For the PTFE-impregnated fiber substrate, on the other hand, a satisfactory agreement with an experimental reference could not be achieved. Whereas the remaining discrepancy was primarily accredited to a measurement artifact, more experimental $p_c - S$ data is needed to verify or falsify this hypothesis. A reliable experimental reference would thereby also allow to largely eliminate the parametric uncertainty for the carbon fiber contact angle.

In order to validate the modeling of additive distributions in microstructure reconstructions, further studies on experimental surface analysis are required, which provide not just qualitative but also quantitative information on additive deposition. Furthermore, tomographic imaging of GDLs at even higher resolutions (i.e., nanoCT) would allow to ensure that all relevant structural features of the GDL are recovered and to review if a resolution of less than 2 µm per pixel is in fact sufficiently high.

For the simulation of *operando* liquid water transport through the GDL, several amendments can be made to the model in order to improve its predictive capabilities. Whereas

the GDL microstructure reconstruction was in this work virtually compacted according to a homogeneous load, GDL sample compression in real cell assembly is known to be heterogeneous due to the alternating channel-land structures of the bipolar plate flow fields (see Figure 2.1 and ref. [438]). In order to properly account for these compression effects, one would therefore have to consider the complete channel-land geometry, which will increase the computational expense of 3D PSM simulations significantly.

In general, the product water in the cathode CL has to be assumed to not exclusively remain in the liquid state but also evaporate or at subfreezing temperatures even desublimate. Whereas water vapor can be as well discharged from the cell via diffusion through the MPL and GDL to the gas channel, it may as well condensate along the way in dependence of the local temperature field. As a result, phase-change phenomena can have a non-negligible impact on the effective water management in PEM fuel cells [439] and should be therefore in principle included in pore-scale models on the GDL liquid water transport. Since phase-change phenomena are in general dictated by the local temperature, an energy balance should then be included as well.

The effective gas transport was in this work simulated assuming a single-component gas phase. For reasons of practicability, however, PEM fuel cells are typically operated not with pure oxygen by with air, i.e., a gas mixture. In addition, oxygen will be consumed at the cathode CL which leads to local concentration gradients as a driving force for the diffusion of gas species. Furthermore, the product water will be formed where oxygen is depleted and will thus in general not be homogeneously distributed across the CL/MPL interface. Eventually, the predictive accuracy of the PSM model on both the liquid water and gas transport in partially saturated GDLs could be therefore improved further by consideration of gas mixtures and definition of a concentration-dependent reaction rate for the consumption and formation of reactands at the CL/MPL interface. Such a concept was for example realized by Zhang et al. [440], however, the 3D LB simulations were conducted on a rather small GDL domain due to the massive computational expense.

Bibliography

[1] W. M. O. (WMO), State of the Global Climate 2021 (WMO-No. 1290), WMO (2022).

[2] F. D. Albuquerque, M. A. Maraqa, R. Chowdhury, T. Mauga, M. Alzard, Greenhouse gas emissions associated with road transport projects: current status, benchmarking, and assessment tools, Transportation Research Procedia 48 (2020) 2018–2030. doi:10.1016/j.trpro.2020.08.261.

[3] H. Ritchie, M. Roser, P. Rosado, CO_2 and Greenhouse Gas Emissions, Our World in Data (2020).
URL https://ourworldindata.org/co2-and-greenhouse-gas-emissions

[4] S. Verma, S. Mishra, A. Gaur, S. Chowdhury, S. Mohapatra, G. Dwivedi, P. Verma, A comprehensive review on energy storage in hybrid electric vehicle, Journal of Traffic and Transportation Engineering (English Edition) 8 (5) (2021) 621–637. doi:10.1016/j.jtte.2021.09.001.

[5] X. Han, F. Li, T. Zhang, T. Zhang, K. Song, Economic energy management strategy design and simulation for a dual-stack fuel cell electric vehicle, International Journal of Hydrogen Energy 42 (16) (2017) 11584–11595. doi:10.1016/j.ijhydene.2017.01.085.

[6] K. Song, F. Li, X. Hu, L. He, W. Niu, S. Lu, T. Zhang, Multi-mode energy management strategy for fuel cell electric vehicles based on driving pattern identification using learning vector quantization neural network algorithm, Journal of Power Sources 389 (2018) 230–239. doi:10.1016/j.jpowsour.2018.04.024.

[7] A. Ferrara, S. Jakubek, C. Hametner, Energy management of heavy-duty fuel cell vehicles in real-world driving scenarios: Robust design of strategies to maximize the hydrogen economy and system lifetime, Energy Conversion and Management 232 (2021) 113795. doi:10.1016/j.enconman.2020.113795.

[8] D. Cullen, K. Neyerlin, R. Ahluwalia, New roads and challenges for fuel cells in heavy-duty transportation, Nat Energy 6 (2021) 462–474. doi:10.1038/s41560-021-00775-z.

[9] J. Wang, Barriers of scaling-up fuel cells: Cost, durability and reliability, Energy 80 (2015) 509–521. doi:10.1016/j.energy.2014.12.007.

[10] R. L. Borup, A. Kusoglu, K. C. Neyerlin, R. Mukundan, R. K. Ahluwalia, D. A. Cullen, K. L. More, A. Z. Weber, D. J. Myers, Recent developments in catalyst-related pem fuel cell durability, Current Opinion in Electrochemistry 21 (2020) 192–200. doi:10.1016/j.coelec.2020.02.007.

[11] Y. Wang, D. F. Ruiz Diaz, K. S. Chen, Z. Wang, X. C. Adroher, Materials, technological status, and fundamentals of PEM fuel cells – A review, Materials Today 32 (2020) 178–203. doi:10.1016/j.mattod.2019.06.005.

[12] Q. Liu, F. Lan, J. Chen, C. Zeng, J. Wang, A review of proton exchange membrane fuel cell water management: Membrane electrode assembly, Journal of Power Sources 517 (2022) 230723. doi:10.1016/j.jpowsour.2021.230723.

[13] J. Milewski, K. Badyda, Z. Misztal, M. Wolowicz, Combined Heat and Power unit based on polymeric electrolyte Membrane Fuel Cell in a hotel application, Rynek Energii 90 (2010) 118–123.

[14] S. Park, J.-W. Lee, B. N. Popov, A review of gas diffusion layer in PEM fuel cells: Materials and designs, International Journal of Hydrogen Energy 37 (7) (2012) 5850–5865. doi:10.1016/j.ijhydene.2011.12.148.

[15] M. Prasanna, H. Ha, E. Cho, S.-A. Hong, I.-H. Oh, Influence of cathode gas diffusion media on the performance of the PEMFCs, Journal of Power Sources 131 (1) (2004) 147–154. doi:10.1016/j.jpowsour.2004.01.030.

[16] J. Zhang, B. Wang, J. Jin, S. Yang, G. Li, A review of the microporous layer in proton exchange membrane fuel cells: Materials and structural designs based on water transport mechanism, Renewable and Sustainable Energy Reviews 156 (2022) 111998. doi:10.1016/j.rser.2021.111998.

[17] S. Park, J.-W. Lee, B. N. Popov, Effect of PTFE content in microporous layer on water management in PEM fuel cells, Journal of Power Sources 177 (2) (2008) 457–463. doi:10.1016/j.jpowsour.2007.11.055.

[18] J. Sim, M. Kang, K. Min, Effects of basic gas diffusion layer components on PEMFC performance with capillary pressure gradient, International Journal of Hydrogen Energy 46 (54) (2021) 27731–27748. doi:10.1016/j.ijhydene.2021.05.205.

[19] A. El-kharouf, T. J. Mason, D. J. Brett, B. G. Pollet, Ex-situ characterisation of gas diffusion layers for proton exchange membrane fuel cells, Journal of Power Sources 218 (2012) 393–404. doi:10.1016/j.jpowsour.2012.06.099.

[20] X. Liu, F. Peng, G. Lou, Z. Wen, Liquid water transport characteristics of porous diffusion media in polymer electrolyte membrane fuel cells: A review, Journal of Power Sources 299 (2015) 85–96. doi:10.1016/j.jpowsour.2015.08.092.

[21] C. Si, X.-D. Wang, W.-M. Yan, T.-H. Wang, A comprehensive review on measurement and correlation development of capillary pressure for two-phase modeling of proton exchange membrane fuel cells, Journal of Chemistry 2015 (2015) 876821. doi:10.1155/2015/876821.

[22] Q. Chen, Z. Niu, H. Li, K. Jiao, Y. Wang, Recent progress of gas diffusion layer in proton exchange membrane fuel cell: Two-phase flow and material properties, International Journal of Hydrogen Energy 46 (12) (2021) 8640–8671. doi:10.1016/j.ijhydene.2020.12.076.

[23] Z. Lu, M. M. Daino, C. Rath, S. G. Kandlikar, Water management studies in pem fuel cells, part iii: Dynamic breakthrough and intermittent drainage characteristics from gdls with and without mpls, International Journal of Hydrogen Energy 35 (9) (2010) 4222–4233. doi:10.1016/j.ijhydene.2010.01.012.

[24] A. Forner-Cuenca, J. Biesdorf, A. Lamibrac, V. Manzi-Orezzoli, F. N. Büchi, L. Gubler, T. J. Schmidt, P. Boillat, Advanced water management in pefcs: Diffusion layers with patterned wettability ii. measurement of capillary pressure characteristic with neutron and synchrotron imaging, Journal of The Electrochemical Society 163 (9) (2016) F1038. doi:10.1149/2.0511609jes.

[25] A. Forner-Cuenca, J. Biesdorf, V. Manzi-Orezzoli, L. Gubler, T. J. Schmidt, P. Boillat, Advanced Water Management in PEFCs: Diffusion Layers with Patterned Wettability III. Operando Characterization with Neutron Imaging, Journal of The Electrochemical Society 163 (13) (2016) F1389. doi:10.1149/2.0891613jes.

[26] S. Cleghorn, D. Mayfield, D. Moore, J. Moore, G. Rusch, T. Sherman, N. Sisofo, U. Beuscher, A polymer electrolyte fuel cell life test: 3 years of continuous operation,

Journal of Power Sources 158 (1) (2006) 446–454. doi:10.1016/j.jpowsour.2005.09.062.

[27] S. Zhang, X.-Z. Yuan, J. N. C. Hin, H. Wang, J. Wu, K. A. Friedrich, M. Schulze, Effects of open-circuit operation on membrane and catalyst layer degradation in proton exchange membrane fuel cells, Journal of Power Sources 195 (4) (2010) 1142–1148. doi:10.1016/j.jpowsour.2009.08.070.

[28] N. Zhao, Y. Chu, Z. Xie, K. Eggen, F. Girard, Z. Shi, Effects of fuel cell operating conditions on proton exchange membrane durability at open-circuit voltage, Fuel Cells 20 (2) (2020) 176–184. doi:10.1002/fuce.201900173.

[29] S. R. Choi, D. Y. Kim, W. Y. An, S. Choi, K. Park, S.-D. Yim, J.-Y. Park, Assessing the degradation pattern and mechanism of membranes in polymer electrolyte membrane fuel cells using open-circuit voltage hold and humidity cycle test protocols, Materials Science for Energy Technologies 5 (2022) 66–73. doi:10.1016/j.mset.2021.12.001.

[30] T. Mittermeier, A. Weiß, F. Hasché, H. A. Gasteiger, Pem fuel cell start-up/shut-down losses vs relative humidity: The impact of water in the electrode layer on carbon corrosion, Journal of The Electrochemical Society 165 (16) (2018) F1349. doi:10.1149/2.0931816jes.

[31] J. N. Schwämmlein, P. J. Rheinländer, Y. Chen, K. T. Freyer, H. A. Gasteiger, Anode aging during pemfc start-up and shut-down: H2-air fronts vs voltage cycles, Journal of The Electrochemical Society 165 (16) (2018) F1312. doi:10.1149/2.0611816jes.

[32] T. Arlt, M. Klages, M. Messserschmidt, H. Riesemeier, J. Scholta, J. Banhart, I. Manke, Influence of artificial aging of gas diffusion layers on the water management of pem fuel cells, ECS Electrochemistry Letters 3 (2) (2014) F7. doi:10.1149/2.004402eel.

[33] J. Kätzel, H. Markötter, T. Arlt, M. Klages, J. Haußmann, M. Messerschmidt, N. Kardjilov, J. Scholta, J. Banhart, I. Manke, Effect of ageing of gas diffusion layers on the water distribution in flow field channels of polymer electrolyte membrane fuel cells, Journal of Power Sources 301 (2016) 386–391. doi:10.1016/j.jpowsour.2015.10.004.

[34] T. Arlt, M. Klages, M. Messerschmidt, J. Scholta, I. Manke, Influence of artificially aged gas diffusion layers on the water management of polymer electrolyte membrane

fuel cells analyzed with in-operando synchrotron imaging, Energy 118 (2017) 502–511. doi:10.1016/j.energy.2016.10.061.

[35] H. Liu, M. G. George, R. Banerjee, N. Ge, J. Lee, D. Muirhead, P. Shrestha, S. Chevalier, J. Hinebaugh, R. Zeis, M. Messerschmidt, J. Scholta, A. Bazylak, Accelerated degradation of polymer electrolyte membrane fuel cell gas diffusion layers, Journal of The Electrochemical Society 164 (7) (2017) F704. doi:10.1149/2.0081707jes.

[36] H. Liu, M. G. George, N. Ge, D. Muirhead, P. Shrestha, J. Lee, R. Banerjee, R. Zeis, M. Messerschmidt, J. Scholta, P. Krolla, A. Bazylak, Microporous layer degradation in polymer electrolyte membrane fuel cells, Journal of The Electrochemical Society 165 (6) (2018) F3271. doi:10.1149/2.0291806jes.

[37] S. Kim, B. K. Ahn, M. Mench, Physical degradation of membrane electrode assemblies undergoing freeze/thaw cycling: Diffusion media effects, Journal of Power Sources 179 (1) (2008) 140–146. doi:10.1016/j.jpowsour.2007.12.114.

[38] K.-Y. Song, H.-T. Kim, Effect of air purging and dry operation on durability of pemfc under freeze/thaw cycles, International Journal of Hydrogen Energy 36 (19) (2011) 12417–12426. doi:10.1016/j.ijhydene.2011.06.095.

[39] Y. Lee, B. Kim, Y. Kim, X. Li, Degradation of gas diffusion layers through repetitive freezing, Applied Energy 88 (12) (2011) 5111–5119. doi:10.1016/j.apenergy.2011.07.011.

[40] A. Ozden, S. Shahgaldi, J. Zhao, X. Li, F. Hamdullahpur, Degradations in porous components of a proton exchange membrane fuel cell under freeze-thaw cycles: Morphology and microstructure effects, International Journal of Hydrogen Energy 45 (5) (2020) 3618–3631. doi:10.1016/j.ijhydene.2018.10.209.

[41] J. Pauchet, M. Prat, P. Schott, S. P. Kuttanikkad, Performance loss of proton exchange membrane fuel cell due to hydrophobicity loss in gas diffusion layer: Analysis by multiscale approach combining pore network and performance modelling, International Journal of Hydrogen Energy 37 (2) (2012) 1628–1641. doi:10.1016/j.ijhydene.2011.09.127.

[42] D. Niblett, A. Mularczyk, V. Niasar, J. Eller, S. Holmes, Two-phase flow dynamics in a gas diffusion layer - gas channel - microporous layer system, Journal of Power Sources 471 (2020) 228427. doi:10.1016/j.jpowsour.2020.228427.

[43] Y. Wang, H. Xu, W. He, Y. Zhao, X. Wang, Lattice boltzmann simulation of the structural degradation of a gas diffusion layer for a proton exchange membrane fuel cell, Journal of Power Sources 556 (2023) 232452. doi:10.1016/j.jpowsour.2022.232452.

[44] L. Carrette, K. A. Friedrich, U. Stimming, Fuel cells: Principles, types, fuels, and applications, ChemPhysChem 1 (4) (2000) 162–193. doi:10.1002/1439-7641(20001215)1:4<162::AID-CPHC162>3.0.CO;2-Z.

[45] M. Al-Zaidi, R. Qussay, D. Al-Zubaidy, M. Mahmood, A review: Fuel cells types and their applications 7 (2021) 375–390.

[46] A. Kusoglu, A. Z. Weber, New insights into perfluorinated sulfonic-acid ionomers, Chemical Reviews 117 (3) (2017) 987–1104. doi:10.1021/acs.chemrev.6b00159.

[47] K.-H. Kim, K.-Y. Lee, S.-Y. Lee, E. Cho, T.-H. Lim, H.-J. Kim, S. P. Yoon, S. H. Kim, T. W. Lim, J. H. Jang, The effects of relative humidity on the performances of pemfc meas with various nafion® ionomer contents, International Journal of Hydrogen Energy 35 (23) (2010) 13104–13110. doi:10.1016/j.ijhydene.2010.04.082.

[48] Z. Luo, Z. Chang, Y. Zhang, Z. Liu, J. Li, Electro-osmotic drag coefficient and proton conductivity in nafion® membrane for pemfc, International Journal of Hydrogen Energy 35 (7) (2010) 3120–3124. doi:10.1016/j.ijhydene.2009.09.013.

[49] W. Dai, H. Wang, X.-Z. Yuan, J. J. Martin, D. Yang, J. Qiao, J. Ma, A review on water balance in the membrane electrode assembly of proton exchange membrane fuel cells, International Journal of Hydrogen Energy 34 (23) (2009) 9461–9478. doi:10.1016/j.ijhydene.2009.09.017.

[50] E. Majlan, D. Rohendi, W. Daud, T. Husaini, M. Haque, Electrode for proton exchange membrane fuel cells: A review, Renewable and Sustainable Energy Reviews 89 (2018) 117–134. doi:10.1016/j.rser.2018.03.007.

[51] M. F. Mathias, J. Roth, J. Fleming, W. Lehnert, Diffusion media materials and characterisation, John Wiley & Sons, Ltd, 2010. doi:10.1002/9780470974001.f303046.

[52] R. Schweiss, C. Meiser, T. Damjanovic, I. Galbiati, N. Haak, Sigracet® gas diffusion layers for pem fuel cells, electrolyzers and batteries (white paper) (02 2016).

[53] C. Tötzke, G. Gaiselmann, M. Osenberg, T. Arlt, H. Markötter, A. Hilger, A. Kupsch, B. Müller, V. Schmidt, W. Lehnert, I. Manke, Influence of hydrophobic treatment

on the structure of compressed gas diffusion layers, Journal of Power Sources 324 (2016) 625–636. doi:10.1016/j.jpowsour.2016.05.118.

[54] G. Gaiselmann, D. Froning, C. Tötzke, C. Quick, I. Manke, W. Lehnert, V. Schmidt, Stochastic 3d modeling of non-woven materials with wet-proofing agent, International Journal of Hydrogen Energy 38 (20) (2013) 8448–8460. doi:10.1016/j.ijhydene.2013.04.144.

[55] M. Göbel, M. Godehardt, K. Schladitz, Multi-scale structural analysis of gas diffusion layers, Journal of Power Sources 355 (2017) 8–17. doi:10.1016/j.jpowsour.2017.03.086.

[56] R. Banerjee, S. Chevalier, H. Liu, J. Lee, R. Yip, K. Han, B. K. Hong, A. Bazylak, A Comparison of Felt-Type and Paper-Type Gas Diffusion Layers for Polymer Electrolyte Membrane Fuel Cell Applications Using X-Ray Techniques, Journal of Electrochemical Energy Conversion and Storage 15 (1) (2017) 011002. doi:10.1115/1.4037766.

[57] H. Xu, M. Bührer, F. Marone, T. J. Schmidt, F. N. Büchi, J. Eller, Effects of gas diffusion layer substrates on PEFC water management: Part i. operando liquid water saturation and gas diffusion properties, Journal of The Electrochemical Society 168 (7) (2021) 074505. doi:10.1149/1945-7111/ac1035.

[58] A. Vikram, P. R. Chowdhury, R. K. Phillips, M. Hoorfar, Measurement of effective bulk and contact resistance of gas diffusion layer under inhomogeneous compression – part i: Electrical conductivity, Journal of Power Sources 320 (2016) 274–285. doi:10.1016/j.jpowsour.2016.04.110.

[59] D. Qiu, H. Janßen, L. Peng, P. Irmscher, X. Lai, W. Lehnert, Electrical resistance and microstructure of typical gas diffusion layers for proton exchange membrane fuel cell under compression, Applied Energy 231 (2018) 127–137. doi:10.1016/j.apenergy.2018.09.117.

[60] E. Sadeghi, N. Djilali, M. Bahrami, Effective thermal conductivity and thermal contact resistance of gas diffusion layers in proton exchange membrane fuel cells. part 2: Hysteresis effect under cyclic compressive load, Journal of Power Sources 195 (24) (2010) 8104–8109. doi:https://doi.org/10.1016/j.jpowsour.2010.07.051.

[61] J. Yablecki, A. Bazylak, Determining the effective thermal conductivity of compressed pemfc gdls through thermal resistance modelling, Journal of Power Sources 217 (2012) 470–478. doi:10.1016/j.jpowsour.2012.06.011.

[62] S. Escribano, J.-F. Blachot, J. Ethève, A. Morin, R. Mosdale, Characterization of pemfcs gas diffusion layers properties, Journal of Power Sources 156 (1) (2006) 8–13. doi:10.1016/j.jpowsour.2005.08.013.

[63] V. Norouzifard, M. Bahrami, Deformation of pem fuel cell gas diffusion layers under compressive loading: An analytical approach, Journal of Power Sources 264 (2014) 92–99. doi:10.1016/j.jpowsour.2014.04.057.

[64] J. Millichamp, T. J. Mason, T. P. Neville, N. Rajalakshmi, R. Jervis, P. R. Shearing, D. J. Brett, Mechanisms and effects of mechanical compression and dimensional change in polymer electrolyte fuel cells – a review, Journal of Power Sources 284 (2015) 305–320. doi:10.1016/j.jpowsour.2015.02.111.

[65] H. Guo, L. Chen, S. A. Ismail, L. Jiang, S. Guo, J. Gu, X. Zhang, Y. Li, Y. Zhu, Z. Zhang, D. Han, Gas diffusion layer for proton exchange membrane fuel cells: A review, Materials 15 (24) (2022). doi:10.3390/ma15248800.

[66] A. Ozden, S. Shahgaldi, X. Li, F. Hamdullahpur, A review of gas diffusion layers for proton exchange membrane fuel cells—with a focus on characteristics, characterization techniques, materials and designs, Progress in Energy and Combustion Science 74 (2019) 50–102. doi:10.1016/j.pecs.2019.05.002.

[67] J. Lee, H. Liu, M. George, R. Banerjee, N. Ge, S. Chevalier, T. Kotaka, Y. Tabuchi, A. Bazylak, Microporous layer to carbon fibre substrate interface impact on polymer electrolyte membrane fuel cell performance, Journal of Power Sources 422 (2019) 113–121. doi:10.1016/j.jpowsour.2019.02.099.

[68] Y.-C. Chen, C. Karageorgiou, J. Eller, T. J. Schmidt, F. N. Büchi, Determination of the porosity and its heterogeneity of fuel cell microporous layers by x-ray tomographic microscopy, Journal of Power Sources 539 (2022) 231612. doi:10.1016/j.jpowsour.2022.231612.

[69] S. Chevalier, J. Lee, N. Ge, R. Yip, P. Antonacci, Y. Tabuchi, T. Kotaka, A. Bazylak, In operando measurements of liquid water saturation distributions and effective diffusivities of polymer electrolyte membrane fuel cell gas diffusion layers, Electrochimica Acta 210 (2016) 792–803. doi:10.1016/j.electacta.2016.05.180.

[70] R. Banerjee, J. Hinebaugh, H. Liu, R. Yip, N. Ge, A. Bazylak, Heterogeneous porosity distributions of polymer electrolyte membrane fuel cell gas diffusion layer materials with rib-channel compression, International Journal of Hydrogen Energy 41 (33) (2016) 14885–14896. doi:10.1016/j.ijhydene.2016.06.147.

[71] J. Sim, M. Kang, K. Min, Effects of ratio variation in substrate and micro porous layer penetration on polymer exchange membrane fuel cell performance, International Journal of Hydrogen Energy 46 (35) (2021) 18615–18629. doi:10.1016/j.ijhydene.2021.03.029.

[72] R. Bock, A. Shum, X. Xiao, H. Karoliussen, F. Seland, I. Zenyuk, O. Burheim, Thermal conductivity and compaction of gdl-mpl interfacial composite material, Journal of The Electrochemical Society 165 (2018) F514–F525. doi:10.1149/2.0751807jes.

[73] A. Z. Weber, J. Newman, Effects of microporous layers in polymer electrolyte fuel cells, Journal of The Electrochemical Society 152 (4) (2005) A677. doi:10.1149/1.1861194.

[74] S. G. Kandlikar, M. L. Garofalo, Z. Lu, Water management in a pemfc: Water transport mechanism and material degradation in gas diffusion layers, Fuel Cells 11 (6) (2011) 814–823. doi:10.1002/fuce.201000172.

[75] M. S. Ismail, A. Hassanpour, D. B. Ingham, L. Ma, M. Pourkashanian, On the compressibility of gas diffusion layers in proton exchange membrane fuel cells, Fuel Cells 12 (3) (2012) 391–397. doi:10.1002/fuce.201100054.

[76] Z. Bao, Y. Li, X. Zhou, F. Gao, Q. Du, K. Jiao, Transport properties of gas diffusion layer of proton exchange membrane fuel cells: Effects of compression, International Journal of Heat and Mass Transfer 178 (2021) 121608. doi:10.1016/j.ijheatmasstransfer.2021.121608.

[77] Y. Tabe, Y. Aoyama, K. Kadowaki, K. Suzuki, T. Chikahisa, Impact of micro-porous layer on liquid water distribution at the catalyst layer interface and cell performance in a polymer electrolyte membrane fuel cell, Journal of Power Sources 287 (2015) 422–430. doi:10.1016/j.jpowsour.2015.04.095.

[78] J. H. Chun, D. H. Jo, S. G. Kim, S. H. Park, C. H. Lee, S. H. Kim, Improvement of the mechanical durability of micro porous layer in a proton exchange membrane fuel cell by elimination of surface cracks, Renewable Energy 48 (2012) 35–41. doi:10.1016/j.renene.2012.04.011.

[79] R. W. I. Atkinson, Y. Garsany, B. D. Gould, K. E. Swider-Lyons, I. V. Zenyuk, The role of compressive stress on gas diffusion media morphology and fuel cell performance, ACS Applied Energy Materials 1 (1) (2018) 191–201. doi:10.1021/acsaem.7b00077.

[80] Y. Nagai, J. Eller, T. Hatanaka, S. Yamaguchi, S. Kato, A. Kato, F. Marone, H. Xu, F. N. Büchi, Improving water management in fuel cells through microporous layer modifications: Fast operando tomographic imaging of liquid water, Journal of Power Sources 435 (2019) 226809. doi:10.1016/j.jpowsour.2019.226809.

[81] P. Deevanhxay, T. Sasabe, S. Tsushima, S. Hirai, Observation of dynamic liquid water transport in the microporous layer and gas diffusion layer of an operating pem fuel cell by high-resolution soft x-ray radiography, Journal of Power Sources 230 (2013) 38–43. doi:10.1016/j.jpowsour.2012.11.140.

[82] H. Markötter, J. Haußmann, R. Alink, C. Tötzke, T. Arlt, M. Klages, H. Riesemeier, J. Scholta, D. Gerteisen, J. Banhart, I. Manke, Influence of cracks in the microporous layer on the water distribution in a pem fuel cell investigated by synchrotron radiography, Electrochemistry Communications 34 (2013) 22–24. doi:10.1016/j.elecom.2013.04.006.

[83] F. Barbir, PEM Fuel Cells: Theory and Practice, 2nd Edition, Elsevier Inc., 2013.

[84] M. M. Tellez-Cruz, J. Escorihuela, O. Solorza-Feria, V. Compañ, Proton exchange membrane fuel cells (pemfcs): Advances and challenges, Polymers 13 (18) (2021). doi:10.3390/polym13183064.

[85] K. Jiao, J. Xuan, Q. Du, Z. Bao, B. Xie, B. Wang, Y. Zhao, L. Fan, H. Wang, Z. Hou, S. Huo, N. P. Brandon, Y. Yin, M. D. Guiver, Designing the next generation of proton-exchange membrane fuel cells, Nature 595 (2021) 361–369. doi:10.1038/s41586-021-03482-7.

[86] L. Hao, P. Cheng, Lattice boltzmann simulations of water transport in gas diffusion layer of a polymer electrolyte membrane fuel cell, Journal of Power Sources 195 (12) (2010) 3870–3881. doi:10.1016/j.jpowsour.2009.11.125.

[87] W. Chen, F. Jiang, Impact of ptfe content and distribution on liquid–gas flow in pemfc carbon paper gas distribution layer: 3d lattice boltzmann simulations, International Journal of Hydrogen Energy 41 (20) (2016) 8550–8562. doi:10.1016/j.ijhydene.2016.02.159.

[88] P. P. Mukherjee, C.-Y. Wang, Q. Kang, Mesoscopic modeling of two-phase behavior and flooding phenomena in polymer electrolyte fuel cells, Electrochimica Acta 54 (27) (2009) 6861–6875. doi:10.1016/j.electacta.2009.06.066.

[89] R. Lenormand, E. Touboul, C. Zarcone, Numerical models and experiments on immiscible displacement in porous media, Journal of Fluid Mechanics 189 (1988) 165 – 187. doi:10.1017/S0022112088000953.

[90] P. K. Sinha, P. P. Mukherjee, C.-Y. Wang, Impact of gdl structure and wettability on water management in polymer electrolyte fuel cells, J. Mater. Chem. 17 (2007) 3089–3103. doi:10.1039/B703485G.

[91] S. Litster, D. Sinton, N. Djilali, Ex situ visualization of liquid water transport in PEM fuel cell gas diffusion layers, Journal of Power Sources 154 (1) (2006) 95–105. doi:10.1016/j.jpowsour.2005.03.199.

[92] J. Eller, J. Roth, F. Marone, M. Stampanoni, A. Wokaun, F. N. Büchi, Towards Ultra-Fast X-ray Tomographic Microscopy of Liquid Water in PEFC, ECS Transactions 41 (1) (2011) 387. doi:10.1149/1.3635572.

[93] D. H. Jeon, H. Kim, Effect of compression on water transport in gas diffusion layer of polymer electrolyte membrane fuel cell using lattice boltzmann method, Journal of Power Sources 294 (2015) 393–405. doi:10.1016/j.jpowsour.2015.06.080.

[94] T. Young, III. An essay on the cohesion of fluids, Philosophical Transactions of the Royal Society of London 95 (1805) 65–87. doi:10.1098/rstl.1805.0005.

[95] F. Behroozi, A Fresh Look at the Young-Laplace Equation and Its Many Applications in Hydrostatics, The Physics Teacher 60 (5) (2022) 358–361. doi:10.1119/5.0045605.

[96] J. Jurin, II. An account of some experiments shown before the Royal Society; with an enquiry into the cause of the ascent and suspension of water in capillary tubes, Philos. Trans. R. Soc. Lond. 30 (1719) 739–747. doi:doi.org/10.1098/rstl.1717.0026.

[97] W. He, J. S. Yi, T. Van Nguyen, Two-phase flow model of the cathode of pem fuel cells using interdigitated flow fields, AIChE Journal 46 (10) (2000) 2053–2064. doi:10.1002/aic.690461016.

[98] M. C. Leverett, Capillary behavior in porous solids, Transactions of the AIME 142 (1941) 152–169. doi:10.2118/941152-G.

[99] K. S. Udell, Heat transfer in porous media considering phase change and capillarity—the heat pipe effect, International Journal of Heat and Mass Transfer 28 (2) (1985) 485–495. doi:10.1016/0017-9310(85)90082-1.

[100] J. Gostick, M. Ioannidis, M. Fowler, M. Pritzker, Characterization of the Capillary Properties of Gas Diffusion Media, Vol. 49, 2010, pp. 225–254. doi:10.1007/978-0-387-98068-3_7.

[101] N. Zamel, X. Li, J. Becker, A. Wiegmann, Effect of liquid water on transport properties of the gas diffusion layer of polymer electrolyte membrane fuel cells, International Journal of Hydrogen Energy 36 (9) (2011) 5466–5478. doi:10.1016/j.ijhydene.2011.01.146.

[102] Z. Niu, Y. Wang, K. Jiao, J. Wu, Two-phase flow dynamics in the gas diffusion layer of proton exchange membrane fuel cells: Volume of fluid modeling and comparison with experiment, Journal of The Electrochemical Society 165 (9) (2018) F613. doi:10.1149/2.0261809jes.

[103] E. C. Kumbur, K. V. Sharp, M. M. Mench, Validated leverett approach for multiphase flow in pefc diffusion media: I. hydrophobicity effect, Journal of The Electrochemical Society 154 (12) (2007) B1295. doi:10.1149/1.2784283.

[104] E. C. Kumbur, K. V. Sharp, M. M. Mench, Validated leverett approach for multiphase flow in pefc diffusion media: Ii. compression effect, Journal of The Electrochemical Society 154 (12) (2007) B1305. doi:10.1149/1.2784285.

[105] E. C. Kumbur, K. V. Sharp, M. M. Mench, Validated leverett approach for multiphase flow in pefc diffusion media: Iii. temperature effect and unified approach, Journal of The Electrochemical Society 154 (12) (2007) B1315. doi:10.1149/1.2784286.

[106] R. H. Brooks, A. T. Corey, Properties of porous media affecting fluid flow, Journal of the Irrigation and Drainage Division 92 (2) (1966) 61–88. doi:10.1061/JRCEA4.0000425.

[107] M. T. van Genuchten, A closed-form equation for predicting the hydraulic conductivity of unsaturated soils, Soil Science Society of America Journal 44 (5) (1980) 892–898. doi:10.2136/sssaj1980.03615995004400050002x.

[108] H. Szűcs, B. Vehovszky, B. Sanders, A comprehensive review of the simulation methods for analysis at the pore-scale, Periodica Polytechnica Transportation Engineering 51 (2) (2023) 105–116. doi:10.3311/PPtr.18452.

[109] I. Fatt, The network model of porous media, Transactions of the AIME 207 (01) (1956) 144–181. doi:10.2118/574-G.

[110] R. Lenormand, C. Zarcone, Role of roughness and edges during imbibition in square capillaries 13 (09 1984). doi:10.2118/13264-MS.

[111] M. Blunt, P. King, Macroscopic parameters from simulations of pore scale flow, Phys. Rev. A 42 (1990) 4780–4787. doi:10.1103/PhysRevA.42.4780.

[112] M. A. Ioannidis, I. Chatzis, Network modelling of pore structure and transport properties of porous media, Chemical Engineering Science 48 (5) (1993) 951–972. doi:10.1016/0009-2509(93)80333-L.

[113] J. T. Gostick, M. A. Ioannidis, M. W. Fowler, M. D. Pritzker, Pore network modeling of fibrous gas diffusion layers for polymer electrolyte membrane fuel cells, Journal of Power Sources 173 (1) (2007) 277–290. doi:10.1016/j.jpowsour.2007.04.059.

[114] J. N. Roberts, L. M. Schwartz, Grain consolidation and electrical conductivity in porous media, Phys. Rev. B 31 (1985) 5990–5997. doi:10.1103/PhysRevB.31.5990.

[115] S. Bryant, M. Blunt, Prediction of relative permeability in simple porous media, Phys. Rev. A 46 (1992) 2004–2011. doi:10.1103/PhysRevA.46.2004.

[116] S. L. Bryant, P. R. King, D. W. Mellor, Network model evaluation of permeability and spatial correlation in a real random sphere packing, Transport in Porous Media 11 (1993) 53–70. doi:10.1007/BF00614635.

[117] S. Bakke, P.-E. Øren, 3-d pore-scale modelling of sandstones and flow simulations in the pore networks, SPE Journal - SPE J 2 (1997) 136–149. doi:10.2118/35479-PA.

[118] J. T. Gostick, Random pore network modeling of fibrous pemfc gas diffusion media using voronoi and delaunay tessellations, Journal of The Electrochemical Society 160 (8) (2013) F731. doi:10.1149/2.009308jes.

[119] Robust Determination of the Pore Space Morphology in Sedimentary Rocks, Vol. All Days of SPE Annual Technical Conference and Exhibition. doi:10.2118/84296-MS.

[120] W. B. Lindquist, S.-M. Lee, D. A. Coker, K. W. Jones, P. Spanne, Medial axis analysis of void structure in three-dimensional tomographic images of porous media, Journal of Geophysical Research: Solid Earth 101 (B4) (1996) 8297–8310. doi:10.1029/95JB03039.

[121] Application of a New Grain-Based Reconstruction Algorithm to Microtomography Images for Quantitative Characterization and Flow Modeling, Vol. All Days of SPE Annual Technical Conference and Exhibition. doi:10.2118/95887-MS.

[122] A. Sheppard, R. Sok, H. Averdunk, V. Robins, A. Ghous, Analysis of rock microstructure using high-resolution x-ray tomography, Society of Core Analysts, Paper No. 26 (01 2006).

[123] Q. Xiong, T. G. Baychev, A. P. Jivkov, Review of pore network modelling of porous media: Experimental characterisations, network constructions and applications to reactive transport, Journal of Contaminant Hydrology 192 (2016) 101–117. doi:10.1016/j.jconhyd.2016.07.002.

[124] T. Bultreys, W. De Boever, V. Cnudde, Imaging and image-based fluid transport modeling at the pore scale in geological materials: A practical introduction to the current state-of-the-art, Earth-Science Reviews 155 (2016) 93–128. doi:10.1016/j.earscirev.2016.02.001.

[125] M. J. Blunt, Flow in porous media — pore-network models and multiphase flow, Current Opinion in Colloid & Interface Science 6 (3) (2001) 197–207. doi:10.1016/S1359-0294(01)00084-X.

[126] A. Ryazanov, M. van Dijke, K. Sorbie, Two-phase pore-network modelling: Existence of oil layers during water invasion, Transport in Porous Media 80 (2009) 79–99. doi:10.1007/s11242-009-9345-x.

[127] V. Joekar-Niasar, M. Prodanović, D. Wildenschild, S. M. Hassanizadeh, Network model investigation of interfacial area, capillary pressure and saturation relationships in granular porous media, Water Resources Research 46 (6) (2010). doi:10.1029/2009WR008585.

[128] V. Joekar-Niasar, F. Doster, R. T. Armstrong, D. Wildenschild, M. A. Celia, Trapping and hysteresis in two-phase flow in porous media: A pore-network study, Water Resources Research 49 (7) (2013) 4244–4256. doi:10.1002/wrcr.20313.

[129] V. Joekar-Niasar, S. M. Hassanizadeh, Analysis of fundamentals of two-phase flow in porous media using dynamic pore-network models: A review, Critical Reviews in Environmental Science and Technology 42 (18) (2012) 1895–1976. doi:10.1080/10643389.2011.574101.

[130] Q. Sheng, K. Thompson, Dynamic coupling of pore-scale and reservoir-scale models for multiphase flow, Water Resources Research 49 (9) (2013) 5973–5988. doi:10.1002/wrcr.20430.

[131] A. Aghaei, M. Piri, Direct pore-to-core up-scaling of displacement processes: Dynamic pore network modeling and experimentation, Journal of Hydrology 522 (2015) 488–509. doi:10.1016/j.jhydrol.2015.01.004.

[132] H.-J. Vogel, J. Tölke, V. P. Schulz, M. Krafczyk, K. Roth, Comparison of a lattice-boltzmann model, a full-morphology model, and a pore network model for determining capillary pressure–saturation relationships, Vadose Zone Journal 4 (2) (2005) 380–388. doi:10.2136/vzj2004.0114.

[133] A. Golparvar, Y. Zhou, K. Wu, J. Ma, Z. A. Yu, Comprehensive review of pore scale modeling methodologies for multiphase flow in porous media, Advances in Geo-Energy Research 2 (2018) 418–440. doi:10.26804/ager.2018.04.07.

[134] H. Huang, L. Wang, X. yun Lu, Evaluation of three lattice boltzmann models for multiphase flows in porous media, Computers & Mathematics with Applications 61 (12) (2011) 3606–3617. doi:10.1016/j.camwa.2010.06.034.

[135] X. Huang, W. Zhou, D. Deng, Effective diffusion in fibrous porous media: A comparison study between lattice boltzmann and pore network modeling methods, Materials 14 (2021) 756. doi:10.3390/ma14040756.

[136] R. D. Hazlett, Simulation of capillary-dominated displacements in microtomographic images of reservoir rocks, Transport in Porous Media 20 (1995) 21–35. doi:10.1007/BF00616924.

[137] M. Hilpert, C. T. Miller, Pore-morphology-based simulation of drainage in totally wetting porous media, Advances in Water Resources 24 (3) (2001) 243–255. doi:10.1016/S0309-1708(00)00056-7.

[138] T. Agaesse, A. Lamibrac, F. N. Büchi, J. Pauchet, M. Prat, Validation of pore network simulations of ex-situ water distributions in a gas diffusion layer of proton exchange membrane fuel cells with x-ray tomographic images, Journal of Power Sources 331 (2016) 462–474. doi:10.1016/j.jpowsour.2016.09.076.

[139] M. Sabharwal, J. T. Gostick, M. Secanell, Virtual liquid water intrusion in fuel cell gas diffusion media, Journal of The Electrochemical Society 165 (7) (2018) F553. doi:10.1149/2.0921807jes.

[140] C. Maliska, Fundamentals of Computational Fluid Dynamics: The Finite Volume Method, 2023. doi:10.1007/978-3-031-18235-8.

[141] W. F. Noh, P. Woodward, Slic (simple line interface calculation), in: A. I. van de Vooren, P. J. Zandbergen (Eds.), Proceedings of the Fifth International Conference on Numerical Methods in Fluid Dynamics June 28 – July 2, 1976 Twente University, Enschede, Springer Berlin Heidelberg, Berlin, Heidelberg, 1976, pp. 330–340.

[142] M. Ketabdari, Free Surface Flow Simulation Using VOF Method, 2016. doi:10.5772/64161.

[143] C. Mulbah, C. Kang, N. Mao, W. Zhang, A. R. Shaikh, S. Teng, A review of vof methods for simulating bubble dynamics, Progress in Nuclear Energy 154 (2022) 104478. doi:10.1016/j.pnucene.2022.104478.

[144] H. El Baamrani, L. Bammou, A. Ahmed, B. Abdallah, Volume of fluid (vof) modeling of liquid film evaporation in mixed convection flow through a vertical channel, Mathematical Problems in Engineering 2021 (2021) 1–12. doi:10.1155/2021/9934593.

[145] A. Q. Raeini, M. J. Blunt, B. Bijeljic, Modelling two-phase flow in porous media at the pore scale using the volume-of-fluid method, Journal of Computational Physics 231 (17) (2012) 5653–5668. doi:10.1016/j.jcp.2012.04.011.

[146] Y. Yin, T. Wu, P. He, Q. Du, K. Jiao, Numerical simulation of two-phase cross flow in microstructure of gas diffusion layer with variable contact angle, International Journal of Hydrogen Energy 39 (28) (2014) 15772–15785. doi:10.1016/j.ijhydene.2014.07.162.

[147] M. Dianat, M. Skarysz, A. Garmory, A coupled level set and volume of fluid method for automotive exterior water management applications, International Journal of Multiphase Flow 91 (2017) 19–38. doi:10.1016/j.ijmultiphaseflow.2017.01.008.

[148] S. Osher, J. A. Sethian, Fronts propagating with curvature-dependent speed: Algorithms based on hamilton-jacobi formulations, Journal of Computational Physics 79 (1) (1988) 12–49. doi:10.1016/0021-9991(88)90002-2.

[149] V. Boniou, T. Schmitt, A. Vié, Comparison of interface capturing methods for the simulation of two-phase flow in a unified low-mach framework, International Journal of Multiphase Flow 149 (2022) 103957. doi:10.1016/j.ijmultiphaseflow.2021.103957.

[150] M. Sussman, E. G. Puckett, A coupled level set and volume-of-fluid method for computing 3d and axisymmetric incompressible two-phase flows, Journal of Computational Physics 162 (2) (2000) 301–337. doi:10.1006/jcph.2000.6537.

[151] L. B. Lucy, A numerical approach to the testing of the fission hypothesis., The Astronomical Journal 82 (1977) 1013–1024. doi:10.1086/112164.

[152] R. A. Gingold, J. J. Monaghan, Smoothed particle hydrodynamics: theory and application to non-spherical stars, Monthly Notices of the Royal Astronomical Society 181 (3) (1977) 375–389. doi:10.1093/mnras/181.3.375.

[153] J. J. Monaghan, Smoothed particle hydrodynamics, Annual Review of Astronomy and Astrophysics 30 (1) (1992) 543–574. doi:10.1146/annurev.aa.30.090192.002551.

[154] Z.-B. Wang, R. Chen, H. Wang, Q. Liao, X. Zhu, S.-Z. Li, An overview of smoothed particle hydrodynamics for simulating multiphase flow, Applied Mathematical Modelling 40 (23) (2016) 9625–9655. doi:10.1016/j.apm.2016.06.030.

[155] M. Shadloo, G. Oger, D. Le Touzé, Smoothed particle hydrodynamics method for fluid flows, towards industrial applications: Motivations, current state, and challenges, Computers & Fluids 136 (2016) 11–34. doi:10.1016/j.compfluid.2016.05.029.

[156] H.-G. Lyu, P. Sun, X.-T. Huang, S.-Y. Zhong, Y.-X. Peng, T. Jiang, C. Ji, A review of sph techniques for hydrodynamic simulations of ocean energy devices, Energies 15 (01 2022). doi:10.3390/en15020502.

[157] M. Liu, G. Liu, Smoothed particle hydrodynamics (sph): an overview and recent developments, Archives of Computational Methods in Engineering 17 (2010) 25–76. doi:10.1007/s11831-010-9040-7.

[158] T. Ye, D. Pan, C. Huang, M. Liu, Smoothed particle hydrodynamics (sph) for complex fluid flows: Recent developments in methodology and applications, Physics of Fluids 31 (01 2019). doi:10.1063/1.5068697.

[159] A. Tartakovsky, P. Meakin, Modeling of surface tension and contact angles with smoothed particle hydrodynamics, Phys. Rev. E 72 (2005) 026301. doi:10.1103/PhysRevE.72.026301.

[160] A. Tartakovsky, N. Trask, K. Pan, B. Jones, W. Pan, J. Williams, Smoothed particle hydrodynamics and its applications for multiphase flow and reactive transport in porous media, Computational Geosciences 20 (03 2015). doi:10.1007/s10596-015-9468-9.

[161] R. Gingold, J. Monaghan, Kernel estimates as a basis for general particle methods in hydrodynamics, Journal of Computational Physics 46 (3) (1982) 429–453. doi:10.1016/0021-9991(82)90025-0.

[162] X. Y. Hu, N. A. Adams, Angular-momentum conservative smoothed particle dynamics for incompressible viscous flows, Physics of Fluids 18 (10) (2006) 101702. doi:10.1063/1.2359741.

[163] A.-M. Zhang, P. Sun, F. Ming, A. Colagrossi, Smoothed particle hydrodynamics and its applications in fluid-structure interactions, Journal of Hydrodynamics, Ser. B 29 (2017) 187–216. doi:10.1016/S1001-6058(16)60730-8.

[164] J. Su, L. Wang, Z. Gu, Y. Zhang, C. Chen, Advances in pore-scale simulation of oil reservoirs, Energies 11 (5) (2018). doi:10.3390/en11051132.

[165] S. J. Lind, B. D. Rogers, P. K. Stansby, Review of smoothed particle hydrodynamics: towards converged lagrangian flow modelling, Proceedings of the Royal Society A: Mathematical, Physical and Engineering Sciences 476 (2241) (2020) 20190801. doi:10.1098/rspa.2019.0801.

[166] U. Frisch, B. Hasslacher, Y. Pomeau, Lattice-gas automata for the navier-stokes equation, Phys. Rev. Lett. 56 (1986) 1505–1508. doi:10.1103/PhysRevLett.56.1505.

[167] G. R. McNamara, G. Zanetti, Use of the boltzmann equation to simulate lattice-gas automata, Phys. Rev. Lett. 61 (1988) 2332–2335. doi:10.1103/PhysRevLett.61.2332.

[168] S. Chen, G. D. Doolen, Lattice boltzmann method for fluid flows, Annual Review of Fluid Mechanics 30 (1) (1998) 329–364. doi:10.1146/annurev.fluid.30.1.329.

[169] W. SHAO, J. LI, Review of lattice boltzmann method applied to computational aeroacoustics, Archives of Acoustics 44 (2) (2019). doi:10.24425/aoa.2019.128486.

[170] Z.-X. Tong, M.-J. Li, T. Xie, Z. Gu, Lattice boltzmann method for conduction and radiation heat transfer in composite materials, Journal of Thermal Science (03 2022). doi:10.1007/s11630-022-1524-x.

[171] S. Kumar, D. Panda, P. Ghodke, K. Gangawane, Lattice boltzmann method for heat transfer in phase change materials: a review, Journal of Thermal Analysis and Calorimetry (02 2023). doi:10.1007/s10973-023-12014-6.

[172] A. C. Pattnaik, R. Samanta, H. Chattopadhyay, A brief on the application of multiphase lattice boltzmann method for boiling and evaporation, Journal of Thermal Analysis and Calorimetry 148 (2022) 2869–2904. doi:10.1007/s10973-022-11820-8.

[173] R. Samanta, H. Chattopadhyay, C. Guha, A review on the application of lattice boltzmann method for melting and solidification problems, Computational Materials Science 206 (2022) 111288. doi:10.1016/j.commatsci.2022.111288.

[174] H. Liu, Q. Kang, C. Leonardi, B. Jones, S. Schmieschek, A. Narváez, J. Williams, A. Valocchi, J. Harting, Multiphase lattice boltzmann simulations for porous media applications – a review, Computational Geosciences (04 2014).

[175] D. J. Holdych, D. Rovas, J. G. Georgiadis, R. O. Buckius, An Improved Hydrodynamics Formulation for Multiphase Flow Lattice-Boltzmann Models, International Journal of Modern Physics C 09 (08) (1998) 1393–1404. doi:10.1142/S0129183198001266.

[176] X. B. Nie, X. Shan, H. Chen, Galilean invariance of lattice Boltzmann models, EPL (Europhysics Letters) 81 (3) (2008) 34005. doi:10.1209/0295-5075/81/34005.

[177] P. Lallemand, L.-S. Luo, Theory of the lattice Boltzmann method: Dispersion, dissipation, isotropy, Galilean invariance, and stability, Phys. Rev. E 61 (2000) 6546–6562. doi:10.1103/PhysRevE.61.6546.

[178] S. H. Kim, H. Pitsch, On the lattice boltzmann method for multiphase flows with large density ratios, Journal of Computational Physics 303 (2015) 19–27. doi:10.1016/j.jcp.2015.09.029.

[179] M. L. Porter, E. T. Coon, Q. Kang, J. D. Moulton, J. W. Carey, Multicomponent interparticle-potential lattice boltzmann model for fluids with large viscosity ratios, Phys. Rev. E 86 (2012) 036701. doi:10.1103/PhysRevE.86.036701.

[180] G. G. Pereira, Pseudo-potential lattice Boltzmann model for large density and viscosity ratio fluids, AIP Advances 12 (4) (2022) 045314. doi:10.1063/5.0087468.

[181] A. J. Wagner, The origin of spurious velocities in lattice boltzmann, International Journal of Modern Physics B 17 (01 & 02) (2003) 193–196. doi:10.1142/S0217979203017448.

[182] K. Connington, T. Lee, A review of spurious currents in the lattice boltzmann method for multiphase flows, Journal of Mechanical Science and Technology 26 (12 2012). doi:10.1007/s12206-012-1011-5.

[183] L. Zheng, S. Zheng, Q. Zhai, Eliminating spurious currents in phase-field-theory-based lattice Boltzmann equation for two-phase flows, Physics of Fluids 33 (9) (2021) 092102. doi:10.1063/5.0060398.

[184] Q. Li, Y. Yu, R. Z. Huang, Achieving thermodynamic consistency in a class of free-energy multiphase lattice boltzmann models, Phys. Rev. E 103 (2021) 013304. doi:10.1103/PhysRevE.103.013304.

[185] Z. Guo, Well-balanced lattice Boltzmann model for two-phase systems, Physics of Fluids 33 (3) (2021) 031709. doi:10.1063/5.0041446.

[186] Z. Qin, W. Chen, C. Qin, X. Xu, B. Wen, Spurious currents suppression by accurate difference schemes in multiphase lattice boltzmann method, Computers & Fluids 261 (2023) 105917. doi:10.1016/j.compfluid.2023.105917.

[187] T. Douillet-Grellier, S. Leclaire, D. Vidal, F. Bertrand, F. De Vuyst, Comparison of multiphase sph and lbm approaches for the simulation of intermittent flows, Computational Mechanics (2019) 1–doi:10.1007/s40571-019-00250-3.

[188] T. Danner, Modeling and experimental investigation of transport processes in the porous cathode of aqueous Li-air batteries, dissertation, University of Stuttgart (2015). doi:10.18419/opus-2361.

[189] D. H. Rothman, J. M. Keller, Immiscible cellular-automaton fluids, Journal of Statistical Physics 52 (1988) 1119–1127. doi:10.1007/BF01019743.

[190] A. K. Gunstensen, D. H. Rothman, S. Zaleski, G. Zanetti, Lattice boltzmann model of immiscible fluids, Phys. Rev. A 43 (1991) 4320–4327. doi:10.1103/PhysRevA.43.4320.

[191] T. Krüger, H. Kusumaatmaja, A. Kuzmin, O. Shardt, G. Silva, E. M. Viggen, The Lattice Boltzmann Method: Principles and Practice, Springer Nature, 2017.

[192] S. Chapman, T. G. Cowling, The Mathematical Theory of Non-uniform Gases, Cambridge University Press, Cambridge, 1952.

[193] X. He, L.-S. Luo, Lattice boltzmann model for the incompressible navier–stokes equation, Journal of Statistical Physics 88 (1997) 927–944. doi:10.1023/B:JOSS.0000015179.12689.e4.

[194] J. Li, Appendix: Chapman-Enskog Expansion in the Lattice Boltzmann Method (2015). doi:10.48550/ARXIV.1512.02599.

[195] P. L. Bhatnagar, E. P. Gross, M. Krook, A model for collision processes in gases. i. small amplitude processes in charged and neutral one-component systems, Phys. Rev. 94 (1954) 511–525. doi:10.1103/PhysRev.94.511.

[196] H. Huang, J.-J. Huang, X.-Y. Lu, Study of immiscible displacements in porous media using a color-gradient-based multiphase lattice boltzmann method, Computers & Fluids 93 (2014) 164–172. doi:10.1016/j.compfluid.2014.01.025.

[197] C. Pan, L.-S. Luo, C. T. Miller, An evaluation of lattice Boltzmann schemes for porous medium flow simulation, Computers & Fluids 35 (8) (2006) 898–909. doi:10.1016/j.compfluid.2005.03.008.

[198] D. D'Humières, I. Ginzburg, M. Krafczyk, P. Lallemand, L.-S. Luo, Multiple-relaxation-time Lattice Boltzmann Models in 3D, Philos. Trans. A Math. Phys. Eng. Sci. 360 (1792) (2002) 437–51. doi:10.1098/rsta.2001.0955.

[199] S. Leclaire, A. Parmigiani, O. Malaspinas, B. Chopard, J. Latt, Generalized three-dimensional lattice boltzmann color-gradient method for immiscible two-phase pore-scale imbibition and drainage in porous media., Physical review. E 95 3-1 (2017) 033306. doi:10.1103/physreve.95.033306.

[200] Y. Yu, Q. Li, Z. X. Wen, R. Z. Huang, Investigation on boundary schemes in lattice Boltzmann simulations of boiling heat transfer involving curved surfaces, Physics of Fluids 32 (6) (2020) 063305. doi:10.1063/5.0011282.

[201] Y. Yu, Q. Li, Z. Wen, Modified curved boundary scheme for two-phase lattice Boltzmann simulations, Computers & Fluids 208 (2020) 104638. doi:10.1016/j.compfluid.2020.104638.

[202] A. J. C. Ladd, Numerical simulations of particulate suspensions via a discretized Boltzmann equation. Part 1. Theoretical foundation, Journal of Fluid Mechanics 271 (1994) 285 – 309. doi:10.1017/S0022112094001771.

[203] Q. Zou, X. He, On pressure and velocity boundary conditions for the lattice Boltzmann BGK model, Physics of Fluids 9 (6) (1997) 1591–1598. doi:10.1063/1.869307.

[204] M. Hecht, J. Harting, Implementation of on-site velocity boundary conditions for D3Q19 lattice Boltzmann simulations, Journal of Statistical Mechanics: Theory and Experiment 2010 (01) (2010) P01018. doi:10.1088/1742-5468/2010/01/p01018.

[205] B. Ahrenholz, J. Tölke, P. Lehmann, A. Peters, A. Kaestner, M. Krafczyk, W. Durner, Prediction of capillary hysteresis in a porous material using lattice-boltzmann methods and comparison to experimental data and a morphological pore network model, Advances in Water Resources 31 (9) (2008) 1151–1173. doi:10.1016/j.advwatres.2008.03.009.

[206] H. HUANG, J.-J. HUANG, X.-Y. LU, M. C. SUKOP, On simulations of high-density ratio flows using color-gradient multiphase lattice boltzmann models, International Journal of Modern Physics C 24 (04) (2013) 1350021. doi:10.1142/S0129183113500216.

[207] X. Shan, H. Chen, Lattice boltzmann model for simulating flows with multiple phases and components, Phys. Rev. E 47 (1993) 1815–1819. doi:10.1103/PhysRevE.47.1815.

[208] X. Shan, H. Chen, Simulation of nonideal gases and liquid-gas phase transitions by the lattice boltzmann equation, Phys. Rev. E 49 (1994) 2941–2948. doi:10.1103/PhysRevE.49.2941.

[209] L. Chen, Q. Kang, Y. Mu, Y.-L. He, W.-Q. Tao, A critical review of the pseudopotential multiphase lattice boltzmann model: Methods and applications, International Journal of Heat and Mass Transfer 76 (2014) 210–236. doi:10.1016/j.ijheatmasstransfer.2014.04.032.

[210] M. R. Swift, W. R. Osborn, J. M. Yeomans, Lattice boltzmann simulation of nonideal fluids, Phys. Rev. Lett. 75 (1995) 830–833. doi:10.1103/PhysRevLett.75.830.

[211] M. R. Swift, E. Orlandini, W. R. Osborn, J. M. Yeomans, Lattice boltzmann simulations of liquid-gas and binary fluid systems, Phys. Rev. E 54 (1996) 5041–5052. doi:10.1103/PhysRevE.54.5041.

[212] X. He, X. Shan, G. Doolen, Discrete boltzmann equation model for nonideal gases, Physical Review E 57 (01 1998). doi:10.1103/PhysRevE.57.R13.

[213] J. W. Cahn, J. E. Hilliard, Free energy of a nonuniform system. i. interfacial free energy, The Journal of Chemical Physics 28 (2) (1958) 258–267. doi:10.1063/1.1744102.

[214] J. W. Cahn, J. E. Hilliard, Free Energy of a Nonuniform System, III. Nucleation in a Two-Component Incompressible Fluid, John Wiley & Sons, Ltd, 1998, pp. 39–50. doi:10.1002/9781118788295.ch5.

[215] H. Liu, Q. Kang, C. Leonardi, S. Schmieschek, A. Narváez, B. Jones, J. Williams, A. Valocchi, J. Harting, Multiphase lattice boltzmann simulations for porous media applications, Computational Geosciences 20 (2016) 777–805. doi:10.1007/s10596-015-9542-3.

[216] D. Grunau, S. Chen, K. Eggert, A lattice boltzmann model for multiphase fluid flows, Physics of Fluids A: Fluid Dynamics 5 (1993) 2557–2562. doi:10.1063/1.858769.

[217] T. Reis, T. N. Phillips, Lattice boltzmann model for simulating immiscible two-phase flows, Journal of Physics A: Mathematical and Theoretical 40 (14) (2007) 4033–4053. doi:10.1088/1751-8113/40/14/018.

[218] H. Liu, A. J. Valocchi, Q. Kang, Three-dimensional lattice boltzmann model for immiscible two-phase flow simulations, Phys. Rev. E 85 (2012) 046309. doi:10.1103/PhysRevE.85.046309.

[219] J. Tölke, Lattice boltzmann simulations of binary fluid flow through porous media, Phil. Trans. R. Soc. A 360 (2002) 535–545. doi:10.1098/rsta.2001.0944.

[220] M. Latva-Kokko, D. H. Rothman, Diffusion properties of gradient-based lattice boltzmann models of immiscible fluids, Phys. Rev. E 71 (2005) 056702. doi:10.1103/PhysRevE.71.056702.

[221] S. Leclaire, M. Reggio, J.-Y. Trépanier, Numerical evaluation of two recoloring operators for an immiscible two-phase flow lattice boltzmann model, Applied Mathematical Modelling 36 (5) (2012) 2237–2252. doi:10.1016/j.apm.2011.08.027.

[222] X. Shan, Analysis and reduction of the spurious current in a class of multiphase lattice boltzmann models, Physical review. E, Statistical, nonlinear, and soft matter physics 73 (2006) 047701. doi:10.1103/PhysRevE.73.047701.

[223] M. Sbragaglia, R. Benzi, L. Biferale, S. Succi, K. Sugiyama, F. Toschi, Generalized lattice boltzmann method with multirange pseudopotential, Phys. Rev. E 75 (2007) 026702. doi:10.1103/PhysRevE.75.026702.

[224] S. Leclaire, M. El-Hachem, J.-Y. Trépanier, M. Reggio, High order spatial generalization of 2d and 3d isotropic discrete gradient operators with fast evaluation on gpus, Journal of Scientific Computing 59 (2014) 545–573. doi:10.1007/s10915-013-9772-2.

[225] S. Leclaire, M. Reggio, J.-Y. Trépanier, Isotropic color gradient for simulating very high-density ratios with a two-phase flow lattice boltzmann model, Computers & Fluids 48 (1) (2011) 98–112. doi:10.1016/j.compfluid.2011.04.001.

[226] S. Leclaire, N. Pellerin, M. Reggio, J.-Y. Trépanier, An approach to control the spurious currents in a multiphase lattice boltzmann method and to improve the implementation of initial condition, International Journal for Numerical Methods in Fluids 77 (12) (2015) 732–746. doi:10.1002/fld.4002.

[227] J. Yang, E. S. Boek, A comparison study of multi-component lattice boltzmann models for flow in porous media applications, Computers & Mathematics with Applications 65 (6) (2013) 882–890. doi:10.1016/j.camwa.2012.11.022.

[228] K. P. N. Datadien, G. Di Staso, H. M. A. Wijshoff, F. Toschi, A quantitative comparison of physical accuracy and numerical stability of lattice boltzmann color gradient and pseudopotential multicomponent models for microfluidic applications (2021). doi:10.48550/ARXIV.2110.05197.

[229] Y. Ba, H. Liu, Q. Li, Q. Kang, J. Sun, Multiple-relaxation-time color-gradient lattice boltzmann model for simulating two-phase flows with high density ratio, Phys. Rev. E 94 (2016) 023310. doi:10.1103/PhysRevE.94.023310.

[230] Z. X. Wen, Q. Li, Y. Yu, K. H. Luo, Improved three-dimensional color-gradient lattice boltzmann model for immiscible two-phase flows, Phys. Rev. E 100 (2019) 023301. doi:10.1103/PhysRevE.100.023301.

[231] S. M. S. Noori, M. T. Rahni, S. S. Taleghani, Multiple-relaxation time color-gradient lattice boltzmann model for simulating contact angle in two-phase flows with high density ratio, Eur. Phys. J. Plus 134 (2019) 399. doi:10.1140/epjp/i2019-12759-x.

[232] S. Leclaire, N. Pellerin, M. Reggio, J.-Y. Trépanier, Enhanced equilibrium distribution functions for simulating immiscible multiphase flows with variable density ratios in a class of lattice Boltzmann models, International Journal of Multiphase Flow 57 (2013) 159–168. doi:10.1016/j.ijmultiphaseflow.2013.07.001.

[233] R. Sadeghi, M. Shadloo, M. Hopp-Hirschler, A. Hadjadj, U. Nieken, Three-dimensional lattice boltzmann simulations of high density ratio two-phase flows in porous media, Computers & Mathematics with Applications 75 (7) (2018) 2445–2465. doi:10.1016/j.camwa.2017.12.028.

[234] W. R. Osborn, E. Orlandini, M. R. Swift, J. M. Yeomans, J. R. Banavar, Lattice Boltzmann Study of Hydrodynamic Spinodal Decomposition, Phys. Rev. Lett. 75 (1995) 4031–4034. doi:10.1103/PhysRevLett.75.4031.

[235] S. Leclaire, K. Abahri, R. Belarbi, R. Bennacer, Modeling of static contact angles with curved boundaries using a multiphase lattice boltzmann method with variable density and viscosity ratios, International Journal for Numerical Methods in Fluids 82 (8) (2016) 451–470. doi:10.1002/fld.4226.

[236] H. Liu, Y. Zhang, Modelling thermocapillary migration of a microfluidic droplet on a solid surface, Journal of Computational Physics 280 (2015) 37–53. doi:10.1016/j.jcp.2014.09.015.

[237] H. DING, P. D. M. SPELT, Onset of motion of a three-dimensional droplet on a wall in shear flow at moderate reynolds numbers, Journal of Fluid Mechanics 599 (2008) 341–362. doi:10.1017/S0022112008000190.

[238] H. Liu, Y. Ju, N. Wang, G. Xi, Y. Zhang, Lattice boltzmann modeling of contact angle and its hysteresis in two-phase flow with large viscosity difference, Phys. Rev. E 92 (2015) 033306. doi:10.1103/PhysRevE.92.033306.

[239] F. Qin, J.-l. Zhao, Q. Kang, D. Derome, J. Carmeliet, Lattice boltzmann modeling of drying of porous media considering contact angle hysteresis, Transport in Porous Media 140 (2021) 1–26. doi:10.1007/s11242-021-01644-9.

[240] M. Latva-Kokko, D. H. Rothman, Static contact angle in lattice boltzmann models of immiscible fluids, Phys. Rev. E 72 (2005) 046701. doi:10.1103/PhysRevE.72.046701.

[241] B. Fornberg, Generation of finite difference formulas on arbitrarily spaced grids, Math. Comput. 51 (1988) 699–706. doi:10.1090/S0025-5718-1988-0935077-0.

[242] S. P. Sutera, R. Skalak, The History of Poiseuille's Law, Annual Review of Fluid Mechanics 25 (1) (1993) 1–20. doi:10.1146/annurev.fl.25.010193.000245.

[243] E. W. Washburn, The dynamics of capillary flow, Phys. Rev. 17 (1921) 273–283. doi:10.1103/PhysRev.17.273.

[244] R. Lucas, Ueber das Zeitgesetz des kapillaren Aufstiegs von Flüssigkeiten, Kolloid-Zeitschrift 23 (1918) 15–22. doi:10.1007/BF01461107.

[245] J. C. Melrose, Wettability as related to capillary action in porous media, Society of Petroleum Engineers Journal 5 (1965) 259–271.

[246] F. A. L. Dullien, Two-phase flow in porous media, Chemical Engineering & Technology 11 (1) (1988) 407–424. doi:10.1002/ceat.270110153.

[247] R. Wu, A. Kharaghani, E. Tsotsas, Two-phase flow with capillary valve effect in porous media, Chemical Engineering Science 139 (2016) 241–248. doi:10.1016/j.ces.2015.09.028.

[248] Z. Xu, H. Liu, A. J. Valocchi, Lattice boltzmann simulation of immiscible two-phase flow with capillary valve effect in porous media, Water Resources Research 53 (5) (2017) 3770–3790. doi:https://doi.org/10.1002/2017WR020373.

[249] J. Jang, Z. Sun, J. C. Santamarina, Capillary pressure across a pore throat in the presence of surfactants, Water Resources Research 52 (12) (2016) 9586–9599. doi:10.1002/2015WR018499.

[250] W. R. Purcell, Interpretation of capillary pressure data, Journal of Petroleum Technology 2 (1950) 11–12. doi:10.2118/950369-G.

[251] W. B. Haines, Studies in the physical properties of soils: Iv. a further contribution to the theory of capillary phenomena in soil, The Journal of Agricultural Science 17 (2) (1927) 264–290. doi:10.1017/S0021859600018499.

[252] W. B. Haines, Studies in the physical properties of soil. v. the hysteresis effect in capillary properties, and the modes of moisture distribution associated therewith, The Journal of Agricultural Science 20 (1) (1930) 97–116. doi:10.1017/S002185960008864X.

[253] Z. Sun, J. C. Santamarina, Haines jumps: Pore scale mechanisms, Phys. Rev. E 100 (2019) 023115. doi:10.1103/PhysRevE.100.023115.

[254] A. Maqsoud, B. Bussière, M. Aubertin, M. Mbonimpa, Predicting hysteresis of the water retention curve from basic properties of granular soils, Geotechnical and Geological Engineering 30 (10 2012). doi:10.1007/s10706-012-9529-y.

[255] B. Eral, D. 't Mannetje, J. Oh, Contact angle hysteresis: a review of fundamentals and applications, Colloid and polymer science 291 (2) (2013) 247–260. doi:10.1007/s00396-012-2796-6.

[256] J. T. Gostick, M. W. Fowler, M. A. Ioannidis, M. D. Pritzker, Y. Volfkovich, A. Sakars, Capillary pressure and hydrophilic porosity in gas diffusion layers for polymer electrolyte fuel cells, Journal of Power Sources 156 (2) (2006) 375–387. doi:10.1016/j.jpowsour.2005.05.086.

[257] J. D. Fairweather, P. Cheung, J. St-Pierre, D. T. Schwartz, A microfluidic approach for measuring capillary pressure in pemfc gas diffusion layers, Electrochemistry Communications 9 (9) (2007) 2340–2345. doi:10.1016/j.elecom.2007.06.042.

[258] T. V. Nguyen, G. Lin, H. Ohn, X. Wang, Measurement of Capillary Pressure Property of Gas Diffusion Media Used in Proton Exchange Membrane Fuel Cells, Electrochemical and Solid-State Letters 11 (8) (2008) B127. doi:10.1149/1.2929063.

[259] K. G. Gallagher, R. M. Darling, T. W. Patterson, M. L. Perry, Capillary pressure saturation relations for pem fuel cell gas diffusion layers, Journal of The Electrochemical Society 155 (11) (2008) B1225. doi:10.1149/1.2979145.

[260] I. Harkness, N. Hussain, L. Smith, J. Sharman, The use of a novel water porosimeter to predict the water handling behaviour of gas diffusion media used in polymer electrolyte fuel cells, Journal of Power Sources 193 (1) (2009) 122–129. doi:doi.org/10.1016/j.jpowsour.2008.11.055.

[261] J. T. Gostick, M. A. Ioannidis, M. W. Fowler, M. D. Pritzker, Wettability and capillary behavior of fibrous gas diffusion media for polymer electrolyte membrane fuel cells, Journal of Power Sources 194 (1) (2009) 433–444. doi:10.1016/j.jpowsour.2009.04.052.

[262] S. Dwenger, G. Eigenberger, U. Nieken, Measurement of capillary pressure–saturation relationships under defined compression levels for gas diffusion media of pem fuel cells, Transport in Porous Media 91 (2011) 281–294. doi:10.1007/s11242-011-9844-4.

[263] L. Hao, P. Cheng, Capillary pressures in carbon paper gas diffusion layers having hydrophilic and hydrophobic pores, International Journal of Heat and Mass Transfer 55 (1) (2012) 133–139. doi:10.1016/j.ijheatmasstransfer.2011.08.049.

[264] B. Ramos-Alvarado, J. D. Sole, A. Hernandez-Guerrero, M. W. Ellis, Experimental characterization of the water transport properties of pem fuel cells diffusion media, Journal of Power Sources 218 (2012) 221–232. doi:10.1016/j.jpowsour.2012.05.069.

[265] P. A. García-Salaberri, G. Hwang, M. Vera, A. Z. Weber, J. T. Gostick, Effective diffusivity in partially-saturated carbon-fiber gas diffusion layers: Effect of through-plane saturation distribution, International Journal of Heat and Mass Transfer 86 (2015) 319–333. doi:10.1016/j.ijheatmasstransfer.2015.02.073.

[266] V. P. Schulz, J. Becker, A. Wiegmann, P. P. Mukherjee, C.-Y. Wang, Modeling of two-phase behavior in the gas diffusion medium of pefcs via full morphology approach, Journal of The Electrochemical Society 154 (4) (2007) B419. doi:10.1149/1.2472547.

[267] T. Agaesse, A. Lamibrac, F. N. Büchi, J. Pauchet, M. Prat, Validation of pore network simulations of ex-situ water distributions in a gas diffusion layer of proton exchange membrane fuel cells with x-ray tomographic images, Journal of Power Sources 331 (2016) 462–474. doi:10.1016/j.jpowsour.2016.09.076.

[268] N. K. Palakurthi, S. Konangi, A. Kishore, K. Comer, U. Ghia, Prediction of capillary pressure-saturation relationship for primary drainage in a 3d fibrous porous medium using volume-of-fluid method, European Journal of Mechanics - B/Fluids 67 (2018) 357–365. doi:10.1016/j.euromechflu.2017.10.008.

[269] P. Satjaritanun, S. Hirano, A. D. Shum, I. V. Zenyuk, A. Z. Weber, J. W. Weidner, S. Shimpalee, Fundamental understanding of water movement in gas diffusion layer under different arrangements using combination of direct modeling and experimental visualization, Journal of The Electrochemical Society 165 (13) (2018) F1115–F1126. doi:10.1149/2.0201814jes.

[270] Z. Niu, Z. Bao, J. Wu, Y. Wang, K. Jiao, Two-phase flow in the mixed-wettability gas diffusion layer of proton exchange membrane fuel cells, Applied Energy 232 (2018) 443–450. doi:10.1016/j.apenergy.2018.09.209.

[271] X. Zhou, Z. Niu, Z. Bao, J. Wang, Z. Liu, Y. Yin, Q. Du, K. Jiao, Two-phase flow in compressed gas diffusion layer: Finite element and volume of fluid modeling, Journal of Power Sources 437 (2019) 226933. doi:10.1016/j.jpowsour.2019.226933.

[272] T. G. Tranter, P. Boillat, A. Mularczyk, V. Manzi-Orezzoli, P. R. Shearing, D. J. L. Brett, J. Eller, J. T. Gostick, A. Forner-Cuenca, Pore network modelling of capillary transport and relative diffusivity in gas diffusion layers with patterned wettability, Journal of The Electrochemical Society 167 (11) (2020) 114512. doi:10.1149/1945-7111/ab9d61.

[273] J. Yang, L. Fei, X. Zhang, X. Ma, K. H. Luo, S. Shuai, Improved pseudopotential lattice boltzmann model for liquid water transport inside gas diffusion layers, International Journal of Hydrogen Energy 46 (29) (2021) 15938–15950. doi:10.1016/j.ijhydene.2021.02.067.

[274] L. Zhu, H. Zhang, L. Xiao, A. Bazylak, X. Gao, P.-C. Sui, Pore-scale modeling of gas diffusion layers: Effects of compression on transport properties, Journal of Power Sources 496 (2021) 229822. doi:10.1016/j.jpowsour.2021.229822.

[275] H. Zhang, L. Zhu, H. B. Harandi, K. Duan, R. Zeis, P.-C. Sui, P. A. Chuang, Microstructure reconstruction of the gas diffusion layer and analyses of the anisotropic transport properties, Energy Conversion and Management 241 (2021) 114293. doi:10.1016/j.enconman.2021.114293.

[276] Y. Shao, L. Xu, J. Li, Z. Hu, Y. Ding, W. Zheng, M. Ouyang, Polymer electrolyte membrane fuel cell transient voltage characteristic considering liquid water imbibition and drainage in gas diffusion layer, Journal of Power Sources 493 (2021) 229683. doi:10.1016/j.jpowsour.2021.229683.

[277] T. Tranter, J. Gostick, A. Burns, W. Gale, Capillary hysteresis in neutrally wettable fibrous media: A pore network study of a fuel cell electrode, Transport in Porous Media 121 (02 2018). doi:10.1007/s11242-017-0973-2.

[278] P. Sarkezi-Selsky, H. Schmies, A. Kube, A. Latz, T. Jahnke, Lattice Boltzmann simulation of liquid water transport in gas diffusion layers of proton exchange membrane fuel cells: Parametric studies on capillary hysteresis, Journal of Power Sources 535 (2022) 231381. doi:10.1016/j.jpowsour.2022.231381.

[279] M. Shojaeefard, G. Molaeimanesh, M. Nazemian, M. Moqaddari, A review on microstructure reconstruction of pem fuel cells porous electrodes for pore scale simulation, International Journal of Hydrogen Energy 41 (44) (2016) 20276–20293. doi:10.1016/j.ijhydene.2016.08.179.

[280] S. De, S. Bhattacharyya, S. Chakraborty, P. Dutta, Image Segmentation: A Review, Springer International Publishing, Cham, 2016, pp. 29–40. doi:10.1007/978-3-319-47524-0_2.

[281] S. Abdulateef, M. Salman, A comprehensive review of image segmentation techniques, Iraqi Journal for Electrical and Electronic Engineering 17 (2021) 166–175. doi:10.37917/ijeee.17.2.18.

[282] G. Davis, J. Elliott, Artefacts in x-ray microtomography of materials, Materials Science and Technology 22 (2006) 1011–1018. doi:10.1179/174328406X114117.

[283] G. Siroky, Introduction to x-ray microtomography (08 2018). doi:10.13140/RG.2.2.17687.42407.

[284] N. Otsu, A threshold selection method from gray-level histograms, IEEE Transactions on Systems, Man, and Cybernetics 9 (1) (1979) 62–66. doi:10.1109/TSMC.1979.4310076.

[285] M. Sezgin, B. Sankur, Survey over image thresholding techniques and quantitative performance evaluation, Journal of Electronic Imaging 13 (2004) 146–168. doi:10.1117/1.1631315.

[286] GeoDict simulation software Release 2022, by Math2Market GmbH, Germany (2022). doi:10.30423/release.geodict2022.

[287] L. Levi, Unsharp masking and related image enhancement techniques, Computer Graphics and Image Processing 3 (2) (1974) 163–177. doi:10.1016/S0146-664X(74)80005-5.

[288] Y. Zhu, C. Huang, An improved median filtering algorithm for image noise reduction, Physics Procedia 25 (2012) 609–616. doi:10.1016/j.phpro.2012.03.133.

[289] Freudenberg gas diffusion layers technical data, https://fuelcellcomponents.freudenberg-pm.com/-/media/Files/fuelcellcomponents,-d-,freudenbergpm,-d-,com/FPM_technical_data_sheet_gdl_ENG_2018-07-04.pdf (2021).

[290] R. R. Rashapov, J. Unno, J. T. Gostick, Characterization of PEMFC gas diffusion layer porosity, Journal of The Electrochemical Society 162 (6) (2015) F603–F612. doi:10.1149/2.0921506jes.

[291] H. Ito, T. Iwamura, S. Someya, T. Munakata, A. Nakano, Y. Heo, M. Ishida, H. Nakajima, T. Kitahara, Effect of through-plane polytetrafluoroethylene distribution in gas diffusion layers on performance of proton exchange membrane fuel cells, Journal of Power Sources 306 (2016) 289–299. doi:10.1016/j.jpowsour.2015.12.020.

[292] A. Rofaiel, J. Ellis, P. Challa, A. Bazylak, Heterogeneous through-plane distributions of polytetrafluoroethylene in polymer electrolyte membrane fuel cell gas diffusion layers, Journal of Power Sources 201 (2012) 219–225. doi:10.1016/j.jpowsour.2011.11.005.

[293] Z. Fishman, A. Bazylak, Heterogeneous through-plane porosity distributions for treated PEMFC GDLs i. PTFE effect, Journal of The Electrochemical Society 158 (8) (2011) B841. doi:10.1149/1.3594578.

[294] V. Manzi-Orezzoli, A. Mularczyk, P. Trtik, J. Halter, J. Eller, T. J. Schmidt, P. Boillat, Coating distribution analysis on gas diffusion layers for polymer electrolyte

fuel cells by neutron and x-ray high-resolution tomography, ACS Omega 4 (17) (2019) 17236–17243. doi:10.1021/acsomega.9b01763.

[295] S. Odaya, R. Phillips, Y. Sharma, J. Bellerive, A. Phillion, M. Hoorfar, X-ray tomographic analysis of porosity distributions in gas diffusion layers of proton exchange membrane fuel cells, Electrochimica Acta 152 (2015) 464–472. doi:10.1016/j.electacta.2014.11.143.

[296] M. J. Shojaei, B. Bijeljic, Y. Zhang, M. J. Blunt, Minimal surfaces in porous materials: X-ray image-based measurement of the contact angle and curvature in gas diffusion layers to design optimal performance of fuel cells, ACS Applied Energy Materials 5 (4) (2022) 4613–4621. doi:10.1021/acsaem.2c00023.

[297] Z. Fishman, J. Hinebaugh, A. Bazylak, Microscale tomography investigations of heterogeneous porosity distributions of PEMFC GDLs, Journal of The Electrochemical Society 157 (11) (2010) B1643. doi:10.1149/1.3481443.

[298] N. Parikh, J. S. Allen, R. S. Yassar, Microstructure of gas diffusion layers for pem fuel cells, Fuel Cells 12 (3) (2012) 382–390. doi:10.1002/fuce.201100014.

[299] A. Kongkanand, W. Gu, M. F. Mathias, Proton-Exchange Membrane Fuel Cells with Low-Pt Content, Springer New York, New York, NY, 2019, pp. 323–342. doi:10.1007/978-1-4939-7789-5_1022.

[300] J. Bear, C. Braester, On the flow of two immscible fluids in fractured porous media, in: IAHR (Ed.), Fundamentals of Transport Phenomena in Porous Media, Vol. 2 of Developments in Soil Science, Elsevier, 1972, pp. 177–202. doi:10.1016/S0166-2481(08)70538-5.

[301] J. Bear, Fundamentals of transport phenomena in porous media, Journal of Fluid Mechanics 61 (1973) 206–208. doi:10.1017/S0022112073210662.

[302] J. Bear, Y. Bachmat, Introduction to modeling of transport phenomena in porous media, Geological Magazine 129 (1992) 373–374. doi:10.1017/S0016756800019336.

[303] G. O. Brown, H. T. Hsieh, D. A. Lucero, Evaluation of laboratory dolomite core sample size using representative elementary volume concepts, Water Resources Research 36 (5) (2000) 1199–1207. doi:10.1029/2000WR900017.

[304] I. V. Zenyuk, D. Y. Parkinson, L. G. Connolly, A. Z. Weber, Gas-diffusion-layer structural properties under compression via x-ray tomography, Journal of Power Sources 328 (2016) 364–376. doi:10.1016/j.jpowsour.2016.08.020.

[305] P. Satjaritanun, S. Shimpalee, I. V. Zenyuk, Gas diffusion layers: Experimental and modeling approach for morphological and transport properties, Accounts of Materials Research 3 (4) (2022) 416–425. doi:10.1021/accountsmr.1c00125.

[306] P. A. García-Salaberri, I. V. Zenyuk, A. D. Shum, G. Hwang, M. Vera, A. Z. Weber, J. T. Gostick, Analysis of representative elementary volume and through-plane regional characteristics of carbon-fiber papers: diffusivity, permeability and electrical/thermal conductivity, International Journal of Heat and Mass Transfer 127 (2018) 687–703. doi:10.1016/j.ijheatmasstransfer.2018.07.030.

[307] J. Roth, J. Eller, F. Marone, F. N. Büchi, Investigation of the representative area of the water saturation in gas diffusion layers of polymer electrolyte fuel cells, The Journal of Physical Chemistry C 117 (49) (2013) 25991–25999. doi:10.1021/jp4057169.

[308] S. Hasanpour, M. Hoorfar, A. Phillion, Characterization of transport phenomena in porous transport layers using x-ray microtomography, Journal of Power Sources 353 (2017) 221–229. doi:10.1016/j.jpowsour.2017.03.153.

[309] J. Hinebaugh, Z. Fishman, A. Bazylak, Unstructured pore network modeling with heterogeneous pemfc gdl porosity distributions, Journal of The Electrochemical Society 157 (2010) B1651–B1657. doi:10.1149/1.3486095.

[310] C. Lim, C. Wang, Effects of hydrophobic polymer content in gdl on power performance of a pem fuel cell, Electrochimica Acta 49 (24) (2004) 4149–4156. doi:10.1016/j.electacta.2004.04.009.

[311] F. Lee, M. Ismail, D. Ingham, K. Hughes, L. Ma, S. Lyth, M. Pourkashanian, Alternative architectures and materials for pemfc gas diffusion layers: A review and outlook, Renewable and Sustainable Energy Reviews 166 (2022) 112640. doi:10.1016/j.rser.2022.112640.

[312] H. Deng, Y. Hou, K. Jiao, Lattice boltzmann simulation of liquid water transport inside and at interface of gas diffusion and micro-porous layers of pem fuel cells, International Journal of Heat and Mass Transfer 140 (2019) 1074–1090. doi:10.1016/j.ijheatmasstransfer.2019.05.097.

[313] A. D. Santamaria, P. K. Das, J. C. MacDonald, A. Z. Weber, Liquid-water interactions with gas-diffusion-layer surfaces, Journal of The Electrochemical Society 161 (12) (2014) F1184–F1193. doi:10.1149/2.0321412jes.

[314] M. Minus, S. Kumar, The processing, properties, and structure of carbon fibers, JOM 57 (2005) 52–58. doi:10.1007/s11837-005-0217-8.

[315] Y. Hiramitsu, H. Sato, K. Kobayashi, M. Hori, Controlling gas diffusion layer oxidation by homogeneous hydrophobic coating for polymer electrolyte fuel cells, Journal of Power Sources 196 (13) (2011) 5453–5469. doi:10.1016/j.jpowsour.2011.01.099.

[316] N. Zamel, X. Li, J. Shen, Correlation for the effective gas diffusion coefficient in carbon paper diffusion media, Energy & Fuels 23 (12) (2009) 6070–6078. doi:10.1021/ef900653x.

[317] M. Sarker, M. A. Rahman, F. Mojica, S. Mehrazi, W. J. Kort-Kamp, P.-Y. A. Chuang, Experimental and computational study of the microporous layer and hydrophobic treatment in the gas diffusion layer of a proton exchange membrane fuel cell, Journal of Power Sources 509 (2021) 230350. doi:10.1016/j.jpowsour.2021.230350.

[318] H. Ito, K. Abe, M. Ishida, A. Nakano, T. Maeda, T. Munakata, H. Nakajima, T. Kitahara, Effect of through-plane distribution of polytetrafluoroethylene in carbon paper on in-plane gas permeability, Journal of Power Sources 248 (2014) 822–830. doi:10.1016/j.jpowsour.2013.10.009.

[319] V. Radhakrishnan, S. Seshadri, P. Haridoss, Gas diffusion layer with ptfe gradients for effective water management in pem fuel cells, Transactions of The Indian Institute of Metals - TRANS INDIAN INST MET 64 (2011) 175–179. doi:10.1007/s12666-011-0034-4.

[320] A. J. Mendoza, M. A. Hickner, J. Morgan, K. Rutter, C. Legzdins, Raman spectroscopic mapping of the carbon and ptfe distribution in gas diffusion layers, Fuel Cells 11 (2) (2011) 248–254. doi:10.1002/fuce.201000096.

[321] J. Yu, D. Froning, U. Reimer, W. Lehnert, Polytetrafluorethylene effects on liquid water flowing through the gas diffusion layer of polymer electrolyte membrane fuel cells, Journal of Power Sources 438 (2019) 226975. doi:10.1016/j.jpowsour.2019.226975.

[322] D. L. Wood, C. Rulison, R. L. Borup, Surface properties of PEMFC gas diffusion layers, Journal of The Electrochemical Society 157 (2) (2010) B195. doi:10.1149/1.3261850.

[323] J. Serra, Introduction to mathematical morphology, Computer Vision, Graphics, and Image Processing 35 (3) (1986) 283–305. doi:10.1016/0734-189X(86)90002-2.

[324] SGL Carbon, Material Properties SIGRACET® GDL 28AA (2020).
URL https://ion-power.com/wp-content/uploads/2020/05/GDL-28-AA.pdf

[325] Z. Fishman, A. Bazylak, Heterogeneous through-plane distributions of tortuosity, effective diffusivity, and permeability for pemfc gdls, Journal of The Electrochemical Society 158 (2) (2010) B247. doi:10.1149/1.3524284.

[326] Engineering ToolBox, Water - Density, Specific Weight and Thermal Expansion Coefficients (2003).
URL https://www.engineeringtoolbox.com/water-density-specific-weight-d_595.html

[327] Engineering ToolBox, Air - Density, Specific Weight and Thermal Expansion Coefficient vs. Temperature and Pressure (2003).
URL https://www.engineeringtoolbox.com/air-density-specific-weight-d_600.html

[328] Engineering ToolBox, Water - Dynamic (Absolute) and Kinematic Viscosity vs. Temperature and Pressure (2004).
URL https://www.engineeringtoolbox.com/water-dynamic-kinematic-viscosity-d_596.html

[329] Engineering ToolBox, Air - Dynamic and Kinematic Viscosity (2003).
URL https://www.engineeringtoolbox.com/air-absolute-kinematic-viscosity-d_601.html

[330] L. Chen, H.-B. Luan, Y.-L. He, W.-Q. Tao, Numerical investigation of liquid water transport and distribution in porous gas diffusion layer of a proton exchange membrane fuel cell using lattice boltzmann method, Russian Journal of Electrochemistry 48 (07 2012). doi:10.1134/S1023193512070026.

[331] Engineering ToolBox, Surface Tension of Water in contact with Air (2004).
URL https://www.engineeringtoolbox.com/water-surface-tension-d_597.html

[332] S. Qiu, C. A. Fuentes, D. Zhang, A. W. V. Vuure, D. Seveno, Wettability of a single carbon fiber, Langmuir 32 (2016) 9697–9705. doi:10.1021/acs.langmuir.6b02072.

[333] A. Diana, M. Castillo, D. Brutin, T. Steinberg, Sessile drop wettability in normal and reduced gravity, Microgravity - Science and Technology 24 (2012) 195–202. doi:10.1007/s12217-011-9295-0.

[334] S. W. Fitriani, S. Ikeda, M. Tani, H. Yajima, H. Furuta, A. Hatta, Hydrophilization of polytetrafluoroethylene using an atmospheric-pressure plasma of argon gas with

water–ethanol vapor, Materials Chemistry and Physics 282 (2022) 125974. doi:10.1016/j.matchemphys.2022.125974.

[335] Y. D. Wang, Q. Meyer, K. Tang, J. Mcclure, R. White, S. Kelly, M. Crawford, F. Iacoviello, D. Brett, P. Shearing, P. Mostaghimi, C. Zhao, R. Armstrong, Large-scale physically accurate modelling of real proton exchange membrane fuel cell with deep learning, Nature Communications 14 (02 2023). doi:10.1038/s41467-023-35973-8.

[336] A. Arvay, E. Yli-Rantala, C.-H. Liu, X.-H. Peng, P. Koski, L. Cindrella, P. Kauranen, P. Wilde, A. Kannan, Characterization techniques for gas diffusion layers for proton exchange membrane fuel cells – a review, Journal of Power Sources 213 (2012) 317–337. doi:10.1016/j.jpowsour.2012.04.026.

[337] X. Wang, W. Wang, Z. Qu, G. Ren, H. Wang, Surface roughness dominated wettability of carbon fiber in gas diffusion layer materials revealed by molecular dynamics simulations, International Journal of Hydrogen Energy 46 (52) (2021) 26489–26498. doi:10.1016/j.ijhydene.2021.05.121.

[338] P. K. Das, A. Grippin, A. Kwong, A. Z. Weber, Liquid-water-droplet adhesion-force measurements on fresh and aged fuel-cell gas-diffusion layers, Journal of The Electrochemical Society 159 (5) (2012) B489. doi:10.1149/2.052205jes.

[339] A. Forner-Cuenca, V. Manzi-Orezzoli, J. Biesdorf, M. E. Kazzi, D. Streich, L. Gubler, T. J. Schmidt, P. Boillat, Advanced water management in pefcs: Diffusion layers with patterned wettability i. synthetic routes, wettability tuning and thermal stability, Journal of The Electrochemical Society 163 (8) (2016) F788. doi:10.1149/2.0271608jes.

[340] J. Yu, D. Froning, U. Reimer, W. Lehnert, Apparent contact angles of liquid water droplet breaking through a gas diffusion layer of polymer electrolyte membrane fuel cell, International Journal of Hydrogen Energy 43 (12) (2018) 6318–6330. doi:10.1016/j.ijhydene.2018.01.168.

[341] A. Kozbial, F. Zhou, Z. Li, H. Liu, L. Li, Are graphitic surfaces hydrophobic?, Acc. Chem. Res. 49 (2016) 2765–2773. doi:10.1021/acs.accounts.6b00447.

[342] V. Gurau, M. J. Bluemle, E. S. De Castro, Y.-M. Tsou, J. A. Mann, T. A. Zawodzinski, Characterization of transport properties in gas diffusion layers for proton exchange membrane fuel cells: 1. Wettability (internal contact angle to water and surface

energy of GDL fibers), Journal of Power Sources 160 (2) (2006) 1156–1162. doi:10.1016/j.jpowsour.2006.03.016.

[343] C. P. Liu, P. Saha, Y. Huang, S. Shimpalee, P. Satjaritanun, I. V. Zenyuk, Measurement of contact angles at carbon fiber–water–air triple-phase boundaries inside gas diffusion layers using x-ray computed tomography, ACS Applied Materials & Interfaces 13 (17) (2021) 20002–20013. doi:10.1021/acsami.1c00849.

[344] A. Kozbial, Z. Li, J. Sun, X. Gong, F. Zhou, Y. Wang, H. Xu, H. Liu, L. Li, Understanding the intrinsic water wettability of graphite, Carbon 74 (2014) 218–225. doi:10.1016/j.carbon.2014.03.025.

[345] Z. Li, Y. Wang, A. Kozbial, G. Shenoy, F. Zhou, R. McGinley, P. Ireland, B. Morganstein, A. Kunkel, S. Surwade, L. li, H. Liu, Effect of airborne contaminants on the wettability of supported graphene and graphite, Nature materials 12 (07 2013). doi:10.1038/nmat3709.

[346] Y. Wang, H. Xu, Z. Zhang, H. Li, X. Wang, Lattice boltzmann simulation of a gas diffusion layer with a gradient polytetrafluoroethylene distribution for a proton exchange membrane fuel cell, Applied Energy 320 (2022) 119248. doi:10.1016/j.apenergy.2022.119248.

[347] J. Liao, G. Yang, Q. Shen, S. Li, Z. Jiang, H. Wang, G. Zhang, Z. Li, J. Sun, Simulation of liquid water removal in the gas diffusion layer with polytetrafluoroethylene random shedding using lattice boltzmann method, Materials Today Communications 34 (2023) 105293. doi:10.1016/j.mtcomm.2022.105293.

[348] W.-Z. Fang, Y.-Q. Tang, L. Chen, Q.-J. Kang, W.-Q. Tao, Influences of the perforation on effective transport properties of gas diffusion layers, International Journal of Heat and Mass Transfer 126 (2018) 243–255. doi:10.1016/j.ijheatmasstransfer.2018.05.016.

[349] S. Sakaida, Y. Tabe, T. Chikahisa, Large scale simulation of liquid water transport in a gas diffusion layer of polymer electrolyte membrane fuel cells using the lattice boltzmann method, Journal of Power Sources 361 (2017) 133–143. doi:10.1016/j.jpowsour.2017.06.054.

[350] M. Bosomoiu, G. Tsotridis, T. Bednarek, Study of effective transport properties of fresh and aged gas diffusion layers, Journal of Power Sources 285 (2015) 568–579. doi:10.1016/j.jpowsour.2015.03.132.

[351] Y. Ira, Y. Bakhshan, J. Khorshidimalahmadi, Effect of wettability heterogeneity and compression on liquid water transport in gas diffusion layer coated with microporous layer of pemfc, International Journal of Hydrogen Energy 46 (33) (2021) 17397–17413. doi:10.1016/j.ijhydene.2021.02.160.

[352] T. G. Tranter, J. T. Gostick, A. D. Burns, W. F. Gale, Capillary hysteresis in neutrally wettable fibrous media: A pore network study of a fuel cell electrode, Transp Porous Med 121 (2018) 597–620. doi:10.1007/s11242-017-0973-2.

[353] M. M. Daino, S. G. Kandlikar, 3d phase-differentiated gdl microstructure generation with binder and ptfe distributions, International Journal of Hydrogen Energy 37 (6) (2012) 5180–5189. doi:10.1016/j.ijhydene.2011.12.050.

[354] J. Park, H. Oh, T. Ha, Y. I. Lee, K. Min, A review of the gas diffusion layer in proton exchange membrane fuel cells: Durability and degradation, Applied Energy 155 (2015) 866–880. doi:10.1016/j.apenergy.2015.06.068.

[355] P. Ren, P. Pei, Y. Li, Z. Wu, D. Chen, S. Huang, Degradation mechanisms of proton exchange membrane fuel cell under typical automotive operating conditions, Progress in Energy and Combustion Science 80 (2020) 100859. doi:10.1016/j.pecs.2020.100859.

[356] Y. Pan, H. Wang, N. P. Brandon, Gas diffusion layer degradation in proton exchange membrane fuel cells: Mechanisms, characterization techniques and modelling approaches, Journal of Power Sources 513 (2021) 230560. doi:10.1016/j.jpowsour.2021.230560.

[357] A. A. Shah, T. R. Ralph, F. C. Walsh, Modeling and simulation of the degradation of perfluorinated ion-exchange membranes in pem fuel cells, Journal of The Electrochemical Society 156 (4) (2009) B465. doi:10.1149/1.3077573.

[358] X. Cheng, Z. Shi, N. Glass, L. Zhang, J. Zhang, D. Song, Z.-S. Liu, H. Wang, J. Shen, A review of pem hydrogen fuel cell contamination: Impacts, mechanisms, and mitigation, Journal of Power Sources 165 (2) (2007) 739–756. doi:10.1016/j.jpowsour.2006.12.012.

[359] L. Gubler, S. M. Dockheer, W. H. Koppenol, Radical (ho•, h• and hoo•) formation and ionomer degradation in polymer electrolyte fuel cells, Journal of The Electrochemical Society 158 (7) (2011) B755. doi:10.1149/1.3581040.

[360] M. Zatoń, J. Rozière, D. Jones, Current understanding of chemical degradation mechanisms of perfluorosulfonic acid membranes and their mitigation strategies: A review, Sustainable Energy and Fuels 1 (3) (2017) 409 – 438. doi:10.1039/c7se00038c.

[361] A. El Kaddouri, L. Flandin, C. Bas, Chemical degradation of pfsa ionomer binder in pemfc's catalyst layer, International Journal of Hydrogen Energy 43 (32) (2018) 15386–15397. doi:10.1016/j.ijhydene.2018.06.049.

[362] H. Liu, M. G. George, M. Messerschmidt, R. Zeis, D. Kramer, J. Scholta, A. Bazylak, Accelerated degradation of polymer electrolyte membrane fuel cell gas diffusion layers, Journal of The Electrochemical Society 164 (7) (2017) F695. doi:10.1149/2.0071707jes.

[363] C. A. Reiser, L. Bregoli, T. W. Patterson, J. S. Yi, J. D. Yang, M. L. Perry, T. D. Jarvi, A reverse-current decay mechanism for fuel cells, Electrochemical and Solid-State Letters 8 (6) (2005) A273. doi:10.1149/1.1896466.

[364] N. Macauley, D. D. Papadias, J. Fairweather, D. Spernjak, D. Langlois, R. Ahluwalia, K. L. More, R. Mukundan, R. L. Borup, Carbon corrosion in pem fuel cells and the development of accelerated stress tests, Journal of The Electrochemical Society 165 (6) (2018) F3148. doi:10.1149/2.0061806jes.

[365] G. Chen, H. Zhang, H. Ma, H. Zhong, Electrochemical durability of gas diffusion layer under simulated proton exchange membrane fuel cell conditions, International Journal of Hydrogen Energy 34 (19) (2009) 8185–8192. doi:10.1016/j.ijhydene.2009.07.085.

[366] J. D. Fairweather, B. Li, R. Mukundan, J. Fenton, R. L. Borup, In situ and ex situ characterization of carbon corrosion in pemfcs, ECS Transactions 33 (1) (2010) 433. doi:10.1149/1.3484542.

[367] T. Ha, J. Cho, J. Park, K. Min, H.-S. Kim, E. Lee, J.-Y. Jyoung, Experimental study on carbon corrosion of the gas diffusion layer in polymer electrolyte membrane fuel cells, International Journal of Hydrogen Energy 36 (19) (2011) 12436–12443. doi:10.1016/j.ijhydene.2011.06.098.

[368] D. Spernjak, J. Fairweather, R. Mukundan, T. Rockward, R. L. Borup, Influence of the microporous layer on carbon corrosion in the catalyst layer of a polymer electrolyte membrane fuel cell, Journal of Power Sources 214 (2012) 386–398. doi:10.1016/j.jpowsour.2012.04.086.

[369] S. Yu, X. Li, S. Liu, J. Hao, Z. Shao, B. Yi, Study on hydrophobicity loss of the gas diffusion layer in pemfcs by electrochemical oxidation, RSC Advances 4 (8) (2014) 3852 – 3856. doi:10.1039/c3ra45770b.

[370] X. Zhang, Y. Yang, X. Zhang, H. Liu, Identification of performance degradations in catalyst layer and gas diffusion layer in proton exchange membrane fuel cells, Journal of Power Sources 449 (2020) 227580. doi:10.1016/j.jpowsour.2019.227580.

[371] Y. Luo, K. Jiao, Cold start of proton exchange membrane fuel cell, Progress in Energy and Combustion Science 64 (10 2017). doi:10.1016/j.pecs.2017.10.003.

[372] I. Nitta, T. Hottinen, O. Himanen, M. Mikkola, Inhomogeneous compression of pemfc gas diffusion layer: Part i. experimental, Journal of Power Sources 171 (1) (2007) 26–36. doi:10.1016/j.jpowsour.2006.11.018.

[373] T. Matsuura, M. Kato, M. Hori, Study on metallic bipolar plate for proton exchange membrane fuel cell, Journal of Power Sources 161 (1) (2006) 74–78. doi:10.1016/j.jpowsour.2006.04.064.

[374] V. Radhakrishnan, P. Haridoss, Effect of cyclic compression on structure and properties of a gas diffusion layer used in pem fuel cells, International Journal of Hydrogen Energy 35 (20) (2010) 11107–11118. doi:10.1016/j.ijhydene.2010.07.009.

[375] A. Bazylak, D. Sinton, Z.-S. Liu, N. Djilali, Effect of compression on liquid water transport and microstructure of pemfc gas diffusion layers, Journal of Power Sources 163 (2) (2007) 784–792. doi:10.1016/j.jpowsour.2006.09.045.

[376] F. Aldakheel, M. Ismail, K. Hughes, D. Ingham, L. Ma, M. Pourkashanian, D. Cumming, R. Smith, Gas permeability, wettability and morphology of gas diffusion layers before and after performing a realistic ex-situ compression test, Renewable Energy 151 (2020) 1082–1091. doi:10.1016/j.renene.2019.11.109.

[377] K. D. Baik, S. I. Kim, B. K. Hong, K. Han, M. S. Kim, Effects of gas diffusion layer structure on the open circuit voltage and hydrogen crossover of polymer electrolyte membrane fuel cells, International Journal of Hydrogen Energy 36 (16) (2011) 9916–9925. doi:10.1016/j.ijhydene.2011.05.088.

[378] S. Latorrata, P. Gallo Stampino, C. Cristiani, G. Dotelli, Development of an optimal gas diffusion medium for polymer electrolyte membrane fuel cells and assessment of its degradation mechanisms, International Journal of Hydrogen Energy 40 (42) (2015) 14596–14608. doi:10.1016/j.ijhydene.2015.05.100.

[379] J. Wu, J. J. Martin, F. P. Orfino, H. Wang, C. Legzdins, X.-Z. Yuan, C. Sun, In situ accelerated degradation of gas diffusion layer in proton exchange membrane fuel cell: Part i: Effect of elevated temperature and flow rate, Journal of Power Sources 195 (7) (2010) 1888–1894. doi:10.1016/j.jpowsour.2009.10.022.

[380] F. Lapicque, M. Belhadj, C. Bonnet, J. Pauchet, Y. Thomas, A critical review on gas diffusion micro and macroporous layers degradations for improved membrane fuel cell durability, Journal of Power Sources 336 (2016) 40–53. doi:10.1016/j.jpowsour.2016.10.037.

[381] R. Borup, J. Davey, F. Garzon, D. Wood, P. Welch, K. More, Pem fuel cell durability with transportation transient operation, ECS Transactions 3 (1) (2006) 879. doi:10.1149/1.2356206.

[382] T. Ha, J. Cho, J. Park, K. Min, H.-S. Kim, E. Lee, J.-Y. Jyoung, Experimental study of the effect of dissolution on the gas diffusion layer in polymer electrolyte membrane fuel cells, International Journal of Hydrogen Energy 36 (19) (2011) 12427–12435. doi:10.1016/j.ijhydene.2011.06.096.

[383] J. Cho, T. Ha, J. Park, H.-S. Kim, K. Min, E. Lee, J.-Y. Jyoung, Analysis of transient response of a unit proton-exchange membrane fuel cell with a degraded gas diffusion layer, International Journal of Hydrogen Energy 36 (10) (2011) 6090–6098. doi:10.1016/j.ijhydene.2011.02.060.

[384] O. Burheim, G. Ellila, J. Fairweather, A. Labouriau, S. Kjelstrup, J. Pharoah, Ageing and thermal conductivity of porous transport layers used for pem fuel cells, Journal of Power Sources 221 (2013) 356–365. doi:10.1016/j.jpowsour.2012.08.027.

[385] S. Yu, X. Li, J. Li, S. Liu, W. Lu, Z. Shao, B. Yi, Study on hydrophobicity degradation of gas diffusion layer in proton exchange membrane fuel cells, Energy Conversion and Management 76 (2013) 301–306. doi:10.1016/j.enconman.2013.07.034.

[386] K. Fu, T. Tian, Y. Chen, S. Li, C. Cai, Y. Zhang, W. Guo, M. Pan, The durability investigation of a 10-cell metal bipolar plate proton exchange membrane fuel cell stack, International Journal of Energy Research 43 (7) (2019) 2605–2614. doi:10.1002/er.4283.

[387] J. Pang, S. Li, R. Wang, K. Zhu, S. Liu, Z. Guo, M. Pan, Durability failure analysis of proton exchange membrane fuel cell and its effect on oxygen transport in gas diffusion layer, Journal of The Electrochemical Society 166 (13) (2019) F1016. doi:10.1149/2.1101913jes.

[388] F. A. de Bruijn, V. A. T. Dam, G. J. M. Janssen, Review: Durability and degradation issues of pem fuel cell components, Fuel Cells 8 (1) (2008) 3–22. doi:10.1002/fuce.200700053.

[389] S. Vengatesan, M. W. Fowler, X.-Z. Yuan, H. Wang, Diagnosis of mea degradation under accelerated relative humidity cycling, Journal of Power Sources 196 (11) (2011) 5045–5052. doi:10.1016/j.jpowsour.2011.01.088.

[390] K. Panha, M. Fowler, X.-Z. Yuan, H. Wang, Accelerated durability testing via reactants relative humidity cycling on pem fuel cells, Applied Energy 93 (2012) 90–97. doi:10.1016/j.apenergy.2011.05.011.

[391] Y. Yang, X. Zhou, F. Tang, B. Li, P. Ming, C. Zhang, Failure behavior of gas diffusion layer in proton exchange membrane fuel cells, Journal of Power Sources 515 (2021) 230655. doi:10.1016/j.jpowsour.2021.230655.

[392] Y. Yang, X. Li, F. Tang, P. Ming, B. Li, C. Zhang, Power evolution of fuel cell stack driven by anode gas diffusion layer degradation, Applied Energy 313 (2022) 118858. doi:10.1016/j.apenergy.2022.118858.

[393] K. Seidenberger, F. Wilhelm, T. Schmitt, W. Lehnert, J. Scholta, Estimation of water distribution and degradation mechanisms in polymer electrolyte membrane fuel cell gas diffusion layers using a 3d monte carlo model, Journal of Power Sources 196 (12) (2011) 5317–5324. doi:10.1016/j.jpowsour.2010.08.068.

[394] R. Wu, X. Zhu, Q. Liao, R. Chen, G.-M. Cui, Liquid and oxygen transport in defective bilayer gas diffusion material of proton exchange membrane fuel cell, International Journal of Hydrogen Energy 38 (10) (2013) 4067–4078. doi:10.1016/j.ijhydene.2013.01.045.

[395] F. C. Cetinbas, R. K. Ahluwalia, A. D. Shum, I. V. Zenyuk, Direct simulations of pore-scale water transport through diffusion media, Journal of The Electrochemical Society 166 (7) (2019) F3001. doi:10.1149/2.0011907jes.

[396] Y. Hou, X. Li, Q. Du, K. Jiao, N. Zamel, Pore-scale investigation of the effect of microporous layer on water transport in proton exchange membrane fuel cell, Journal of The Electrochemical Society 167 (14) (2020) 144504. doi:10.1149/1945-7111/abc30a.

[397] D. Niblett, V. Niasar, S. Holmes, A. Mularczyk, J. Eller, R. Prosser, M. Mamlouk, Water cluster characteristics of fuel cell gas diffusion layers with artificial microporous layer crack dilation, Journal of Power Sources 555 (2023) 232383. doi:10.1016/j.jpowsour.2022.232383.

[398] J. Hack, L. Rasha, P. L. Cullen, J. J. Bailey, T. P. Neville, P. R. Shearing, N. P. Brandon, D. J. Brett, Use of x-ray computed tomography for understanding localised, along-the-channel degradation of polymer electrolyte fuel cells, Electrochimica Acta 352 (2020) 136464. doi:10.1016/j.electacta.2020.136464.

[399] P. Sarkezi-Selsky, H. Schmies, A. Latz, T. Jahnke, Lattice Boltzmann simulation of liquid water transport in gas diffusion layers of proton exchange membrane fuel cells: Impact of gas diffusion layer and microporous layer degradation on effective transport properties, Journal of Power Sources 556 (2023) 232415. doi:10.1016/j.jpowsour.2022.232415.

[400] W. Chang, J. Hwang, F. Weng, S. Chan, Effect of clamping pressure on the performance of a pem fuel cell, Journal of Power Sources 166 (1) (2007) 149–154. doi:10.1016/j.jpowsour.2007.01.015.

[401] T. J. Mason, J. Millichamp, P. R. Shearing, D. J. Brett, A study of the effect of compression on the performance of polymer electrolyte fuel cells using electrochemical impedance spectroscopy and dimensional change analysis, International Journal of Hydrogen Energy 38 (18) (2013) 7414–7422. doi:10.1016/j.ijhydene.2013.04.021.

[402] Y. Zhou, K. Jiao, Q. Du, Y. Yin, X. Li, Gas diffusion layer deformation and its effect on the transport characteristics and performance of proton exchange membrane fuel cell, International Journal of Hydrogen Energy 38 (29) (2013) 12891–12903. doi:10.1016/j.ijhydene.2013.05.150.

[403] Freudenberg gas diffusion layers technical data, https://fuelcellcomponents.freudenberg-pm.com/-/media/Files/fuelcellcomponents,-d-,freudenbergpm,-d-,com/FPM_technical_data_sheet_gdl_ENG_2018-07-04.pdf (2018).

[404] Freudenberg gas diffusion layers technical data, https://fuelcellcomponents.freudenberg-pm.com/-/media/Files/fuelcellcomponents,-d-,freudenbergpm,-d-,com/FPM_technical-data-sheet_electrolysis_ENG_2022-02-11.pdf (2021).

[405] P.-Y. A. Chuang, M. A. Rahman, F. Mojica, D. S. Hussey, D. L. Jacobson, J. M. LaManna, The interactive effect of heat and mass transport on water condensation in the gas diffusion layer of a proton exchange membrane fuel cell, Journal of Power Sources 480 (2020) 229121. doi:10.1016/j.jpowsour.2020.229121.

[406] C. Simon, F. Hasché, H. A. Gasteiger, Influence of the gas diffusion layer compression on the oxygen transport in pem fuel cells at high water saturation levels, Journal of The Electrochemical Society 164 (6) (2017) F591. doi:10.1149/2.0691706jes.

[407] J. Kleemann, F. Finsterwalder, W. Tillmetz, Characterisation of mechanical behaviour and coupled electrical properties of polymer electrolyte membrane fuel cell gas diffusion layers, Journal of Power Sources 190 (1) (2009) 92–102. doi:10.1016/j.jpowsour.2008.09.026.

[408] R. Omrani, B. Shabani, Gas diffusion layer modifications and treatments for improving the performance of proton exchange membrane fuel cells and electrolysers: A review, International Journal of Hydrogen Energy 42 (47) (2017) 28515–28536. doi:10.1016/j.ijhydene.2017.09.132.

[409] J. T. Gostick, M. A. Ioannidis, M. W. Fowler, M. D. Pritzker, On the role of the microporous layer in pemfc operation, Electrochemistry Communications 11 (3) (2009) 576–579. doi:10.1016/j.elecom.2008.12.053.

[410] C. Simon, D. Kartouzian, D. Müller, F. Wilhelm, H. A. Gasteiger, Impact of microporous layer pore properties on liquid water transport in pem fuel cells: Carbon black type and perforation, Journal of The Electrochemical Society 164 (14) (2017) F1697. doi:10.1149/2.1321714jes.

[411] S. Prass, S. Hasanpour, P. K. Sow, A. B. Phillion, W. Mérida, Microscale x-ray tomographic investigation of the interfacial morphology between the catalyst and micro porous layers in proton exchange membrane fuel cells, Journal of Power Sources 319 (2016) 82–89. doi:10.1016/j.jpowsour.2016.04.031.

[412] D. Muirhead, R. Banerjee, J. Lee, M. G. George, N. Ge, H. Liu, S. Chevalier, J. Hinebaugh, K. Han, A. Bazylak, Simultaneous characterization of oxygen transport resistance and spatially resolved liquid water saturation at high-current density of polymer electrolyte membrane fuel cells with varied cathode relative humidity, International Journal of Hydrogen Energy 42 (49) (2017) 29472–29483. doi:10.1016/j.ijhydene.2017.10.031.

[413] Y. Yang, X. Zhou, B. Li, C. Zhang, Recent progress of the gas diffusion layer in proton exchange membrane fuel cells: Material and structure designs of microporous layer, International Journal of Hydrogen Energy 46 (5) (2021) 4259–4282. doi:10.1016/j.ijhydene.2020.10.185.

[414] M. Andisheh-Tadbir, F. P. Orfino, E. Kjeang, Three-dimensional phase segregation of micro-porous layers for fuel cells by nano-scale x-ray computed tomography, Journal of Power Sources 310 (2016) 61–69. doi:10.1016/j.jpowsour.2016.02.001.

[415] E. Wargo, T. Kotaka, Y. Tabuchi, E. Kumbur, Comparison of focused ion beam versus nano-scale x-ray computed tomography for resolving 3-d microstructures of porous fuel cell materials, Journal of Power Sources 241 (2013) 608–618. doi:10.1016/j.jpowsour.2013.04.153.

[416] Z. Fishman, A. Bazylak, Heterogeneous through-plane porosity distributions for treated pemfc gdls. ii. effect of mpl cracks, Journal of The Electrochemical Society 158 (8) (2011) B846. doi:10.1149/1.3594636.

[417] J. Park, H. Oh, Y. I. Lee, K. Min, E. Lee, J.-Y. Jyoung, Effect of the pore size variation in the substrate of the gas diffusion layer on water management and fuel cell performance, Applied Energy 171 (2016) 200–212. doi:10.1016/j.apenergy.2016.02.132.

[418] C. Zhou, L. Guo, L. Chen, X. Tian, T. He, Q. Yang, Pore-scale modeling of air–water two phase flow and oxygen transport in gas diffusion layer of proton exchange membrane fuel cell, Energies 14 (13) (2021). doi:10.3390/en14133812.

[419] P. A. García-Salaberri, G. Hwang, M. Vera, A. Z. Weber, J. T. Gostick, Effective diffusivity in partially-saturated carbon-fiber gas diffusion layers: Effect of through-plane saturation distribution, International Journal of Heat and Mass Transfer 86 (2015) 319–333. doi:10.1016/j.ijheatmasstransfer.2015.02.073.

[420] Y. Hu, A. Patmonoaji, C. Zhang, T. Suekane, Experimental study on the displacement patterns and the phase diagram of immiscible fluid displacement in three-dimensional porous media, Advances in Water Resources 140 (2020) 103584. doi:10.1016/j.advwatres.2020.103584.

[421] S. Litster, N. Djilali, Two-phase transport in porous gas diffusion electrodes (10 2005). doi:10.2495/1-85312-840-6/05.

[422] A. Z. Weber, R. L. Borup, R. M. Darling, P. K. Das, T. J. Dursch, W. Gu, D. Harvey, A. Kusoglu, S. Litster, M. M. Mench, R. Mukundan, J. P. Owejan, J. G. Pharoah, M. Secanell, I. V. Zenyuk, A critical review of modeling transport phenomena in polymer-electrolyte fuel cells, Journal of The Electrochemical Society 161 (12) (2014) F1254. doi:10.1149/2.0751412jes.

[423] J. Kozeny, Über kapillare Leitung des Wassers im Boden (Aufstieg, Versickerung und Anwendung auf die Bewässerung), Sitzungsber Akad. Wiss., Wien 136 (2a) (1927) 271–306.

[424] P. C. Carman, Fluid flow through a granular bed, Trans. Inst. Chem. Eng. London 15 (1937) 150–156. doi:10.1016/S0263-8762(97)80003-2.

[425] J. H. Nam, M. Kaviany, Effective diffusivity and water-saturation distribution in single- and two-layer pemfc diffusion medium, International Journal of Heat and Mass Transfer 46 (24) (2003) 4595–4611. doi:10.1016/S0017-9310(03)00305-3.

[426] D. A. G. Bruggeman, Berechnung verschiedener physikalischer Konstanten von heterogenen Substanzen. I. Dielektrizitätskonstanten und Leitfähigkeiten der Mischkörper aus isotropen Substanzen, Annalen der Physik 416 (7) (1935) 636–664. doi:10.1002/andp.19354160705.

[427] G. S. Hwang, A. Z. Weber, Effective-diffusivity measurement of partially-saturated fuel-cell gas-diffusion layers, Journal of The Electrochemical Society 159 (11) (2012) F683. doi:10.1149/2.024211jes.

[428] S. Wang, Y. Wang, Investigation of the through-plane effective oxygen diffusivity in the porous media of pem fuel cells: Effects of the pore size distribution and water saturation distribution, International Journal of Heat and Mass Transfer 98 (2016) 541–549. doi:10.1016/j.ijheatmasstransfer.2016.03.060.

[429] S. Jennings, The mean free path in air, Journal of Aerosol Science 19 (2) (1988) 159–166. doi:10.1016/0021-8502(88)90219-4.

[430] I. Hussaini, C. Wang, Measurement of relative permeability of fuel cell diffusion media, Journal of Power Sources 195 (12) (2010) 3830–3840. doi:10.1016/j.jpowsour.2009.12.105.

[431] K. Jiao, X. Li, Water transport in polymer electrolyte membrane fuel cells, Progress in Energy and Combustion Science 37 (3) (2011) 221–291. doi:10.1016/j.pecs.2010.06.002.

[432] P. A. García-Salaberri, J. T. Gostick, G. Hwang, A. Z. Weber, M. Vera, Effective diffusivity in partially-saturated carbon-fiber gas diffusion layers: Effect of local saturation and application to macroscopic continuum models, Journal of Power Sources 296 (2015) 440–453. doi:10.1016/j.jpowsour.2015.07.034.

[433] T. Rosén, J. Eller, J. Kang, N. I. Prasianakis, J. Mantzaras, F. N. Büchi, Saturation dependent effective transport properties of pefc gas diffusion layers, Journal of The Electrochemical Society 159 (9) (2012) F536. doi:10.1149/2.005209jes.

[434] R. Wu, X. Zhu, Q. Liao, H. Wang, Y. dong Ding, J. Li, D. ding Ye, Determination of oxygen effective diffusivity in porous gas diffusion layer using a three-dimensional pore network model, Electrochimica Acta 55 (24) (2010) 7394–7403. doi:10.1016/j.electacta.2010.07.018.

[435] A. Mularczyk, Q. Lin, D. Niblett, A. Vasile, M. J. Blunt, V. Niasar, F. Marone, T. J. Schmidt, F. N. Büchi, J. Eller, Operando liquid pressure determination in polymer electrolyte fuel cells, ACS Applied Materials & Interfaces 13 (29) (2021) 34003–34011. doi:10.1021/acsami.1c04560.

[436] M. Mortazavi, K. Tajiri, Liquid water breakthrough pressure through gas diffusion layer of proton exchange membrane fuel cell, International Journal of Hydrogen Energy 39 (17) (2014) 9409–9419. doi:10.1016/j.ijhydene.2014.03.238.

[437] F. Jinuntuya, W. Kamsanam, Effects of a microporous layer on water transport behaviour in PEM fuel cell gas diffusion layers, IOP Conference Series: Materials Science and Engineering 886 (1) (2020) 012043. doi:10.1088/1757-899x/886/1/012043.

[438] C. Tötzke, G. Gaiselmann, M. Osenberg, J. Bohner, T. Arlt, H. Markötter, A. Hilger, F. Wieder, A. Kupsch, B. Müller, M. Hentschel, J. Banhart, V. Schmidt, W. Lehnert, I. Manke, Three-dimensional study of compressed gas diffusion layers using synchrotron x-ray imaging, Journal of Power Sources 253 (2014) 123–131. doi:10.1016/j.jpowsour.2013.12.062.

[439] H. Xu, S. Nagashima, H. P. Nguyen, K. Kishita, F. Marone, F. N. Büchi, J. Eller, Temperature dependent water transport mechanism in gas diffusion layers revealed by subsecond operando x-ray tomographic microscopy, Journal of Power Sources 490 (2021) 229492. doi:10.1016/j.jpowsour.2021.229492.

[440] D. Zhang, Q. Cai, S. Gu, Three-dimensional lattice-boltzmann model for liquid water transport and oxygen diffusion in cathode of polymer electrolyte membrane fuel cell with electrochemical reaction, Electrochimica Acta 262 (2018) 282–296. doi:10.1016/j.electacta.2017.12.189.

List of Figures

List of Tables

Acknowledgements

First of all, I want to thank Prof. Dr. K. Andreas Friedrich for the supervision of my doctorate, for supporting me in pursuit of it and for warranting me the freedom to develop and follow my own scientific curiosity.

I also thank Prof. Dr. Arnulf Latz for the co-supervision of my thesis, for giving me the opportunity to be part of his department and for sharing his extraordinary expertise on modeling aspects during reviews.

In addition, I want to thank Prof. Dr. Rainer Helmig for his willigness to act as an external examiner and for invoking my interest in fluid mechanics with his great lectures during my bachelor studies.

A special thanks goes Dr. Thomas Jahnke for his endless scientific curiosity, excellent scientific practice and availability for fruitful discussions at practically any time.

With respect to valuable experimental studies, I thank Pia Aßman for the SEM imaging, Dr. Henrike Schmies for µCT imaging and in particular Dr. Alexander Kube for the measurement of capillary pressure-saturation relations of Freudenberg GDLs.

I also want to thank all the colleagues from the Department for Computational Electrochemistry as well as the Department for Electrochemical Energy Technology at the DLR Institute for Engineering Thermodynamics in Stuttgart who supported me in various ways. Here, the following persons derserve particular mention: Fabian Bienen, Diana María Amaya-Duenas, Jonina Felbinger, Joachim Häcker, Martina Gerle and Christina Schmitt.

Moreover, I thank the European Union's Horizon 2020 research and innovation programme for receiving funding from the Fuel Cells and Hydrogen 2 Joint Undertaking under grant agreement No. 779565 (project ID-FAST). For the provision of computational resources I furthermore want to acknowledge support by the state of Baden-Württemberg

through bwHPC, Germany and the German Research Foundation (DFG) through grant no INST 40/575-1 FUGG (JUSTUS 2 cluster).

In the end, I want to express my sincere gratitude to my family and friends, who were always there for me and supported me wherever they could.

Last but not least, I thank my girlfriend who always believed in me, endured every mood I had and never gave up on me. $Εύχαριστώ\ πολύ, σ'αγαπώ$.